UNCLASSIFIED

AD 423802

DEFENSE DOCUMENTATION CENTER

FOR

SCIENTIFIC AND TECHNICAL INFORMATION

CAMERON STATION, ALEXANDRIA, VIRGINIA

UNCLASSIFIED

DISCLAIMER NOTICE

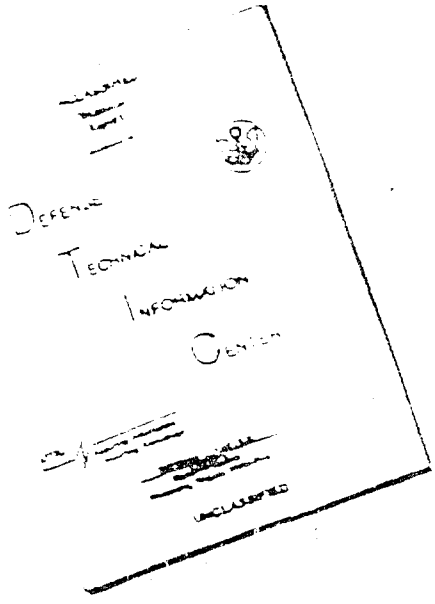

THIS DOCUMENT IS BEST QUALITY AVAILABLE. THE COPY FURNISHED TO DTIC CONTAINED A SIGNIFICANT NUMBER OF PAGES WHICH DO NOT REPRODUCE LEGIBLY.

REPRODUCED FROM BEST AVAILABLE COPY

THIS DOCUMENT CONTAINED BLANK PAGES THAT HAVE BEEN DELETED

NOTICE: When government or other drawings, specifications or other data are used for any purpose other than in connection with a definitely related government procurement operation, the U. S. Government thereby incurs no responsibility, nor any obligation whatsoever; and the fact that the Government may have formulated, furnished, or in any way supplied the said drawings, specifications, or other data is not to be regarded by implication or otherwise as in any manner licensing the holder or any other person or corporation, or conveying any rights or permission to manufacture, use or sell any patented invention that may in any way be related thereto.

nato

423802

PROCEEDINGS

OF THE

SIXTH SYMPOSIUM ON HYPERVELOCITY IMPACT

CATALOGED BY DDC
AS

423802

DDC
NOV 27 1963
TISIA B

VOLUME III

AUGUST, 1963

PROCEEDINGS
OF THE
SIXTH SYMPOSIUM ON HYPERVELOCITY IMPACT

CLEVELAND, OHIO

APRIL 30, MAY 1, 2, 1963

Sponsored by:

U.S. Army

U.S. Air Force

U.S. Navy

Tri-Service Committee:

R. J. Eichelberger, Army, BRL, Chairman

W. H. Dittrich, Air Force, Det. 4, ASD

W. W. Atkins, Navy, NRL

Contract No.
DA-31-124-ARO(D)-16

VOLUME III

AUGUST, 1963

The Firestone Tire & Rubber Co. (Conference Host)

Volume II of the Sixth Symposium on Hypervelocity Impact appears in two parts. Part 1 contains pages 1 through 336; Part 2 contains pages 337 through 709.

The views, conclusions and recommendations expressed herein do not necessarily reflect the official views or policies of either the United States Army, United States Navy or the United States Air Force.

TABLE OF CONTENTS

VOLUME I
PROJECTION TECHNIQUES

TABLE OF CONTENTS iii

UNPUBLISHED PRESENTATIONS

A CRITIQUE OF ACCELERATOR TECHNIQUES FOR HYPERVELOCITY IMPACT (Introductory Paper) 1
A. C. Charters

EXPERIMENTAL AND THEORETICAL STUDIES ON THE INTERIOR BALLISTICS OF LIGHT GAS GUNS 41
Paul G. Baer and Horace C. Smith

AN INVESTIGATION OF THE PERFORMANCE OF A COMPRESSION HEATER FOR USE WITH GUN TUNNELS OR HYPERVELOCITY LAUNCHERS 107
Bo Lemcke

COMPUTER ANALYSIS OF TWO-STAGE HYPERVELOCITY MODEL LAUNCHERS 155
R. Piacesi, D. F. Gates, and A. E. Seigel

NRL HYPERVELOCITY ACCELERATOR DEVELOPMENT 175
H. F. Swift, C. D. Porter, J. J. Condon, and J. R. Baker

PERFORMANCE OF A THREE STAGE ARC HEATED LIGHT GAS GUN 247
J. Eckerman and W. L. McKay

HYPERVELOCITY AUGMENTATION TECHNIQUES 305
William G. Howell, Rodney F. Recht, and Thomas W. Ipson

THE MAGNETOHYDRODYNAMIC HYPERVELOCITY GUN 317
R. L. Chapman, D. E. Harms, and
G. P. Sorenson

INHIBITED JET CHARGE 331
S. Kronman and A. Merendino

SPECIAL EXPLOSIVE PROJECTORS: I. SHAPED CHARGE ACCELERATOR; II. TARGET PLATE ACCELERATOR 349
K. N. Kreyenhagen, J. E. Ferguson,
R. R. Randall, and J. P. Joyce

(Confidential) ARMOUR RESEARCH FOUNDATION TRAVELING CHARGE GUN (U) Vol. IV, 395
Louis A. C. Barbarek

SUMMARY REMARKS 375
H. F. Swift

ATTENDANCE ROSTER 379

AUTHOR INDEX 387

VOLUME II - Part 1

THICK TARGET CRATERING AND IONIZATION

TABLE OF CONTENTS iii

REVIEW OF PHYSICAL PROCESSES IN HYPERVELOCITY IMPACT AND PENETRATION (Introductory Paper) 1
Robert L. Bjork

HYDRODYNAMICS OF HYPERVELOCITY IMPACT 59
J. M. Walsh and J. H. Tillotson

VISCO-PLASTIC SOLUTION OF HYPERVELOCITY IMPACT CRATERING PHENOMENON 105
T. E. Riney

THE CALCULATION OF STRESS WAVES IN SOLIDS 141
Mark L. Wilkins and Richard Giroux

A HYPERVELOCITY IMPACT MODEL FOR COMPLETELY DEFORMING PROJECTILES 157
J. L. Luttrell

A BLAST-WAVE THEORY OF CRATER FORMATION IN SEMI-INFINITE TARGETS 163
William J. Rae and Henry P. Kirchner

SPHERICAL SHOCK WAVES AND CAVITY FORMATION IN METALS 229
N. Davids, H. H. Calvit, and O. T. Johnson

PROPERTIES OF SPHERICAL SHOCK WAVES PRODUCED BY HYPERVELOCITY IMPACT 273
Ray Kinslow

SHOCK FRONT VARIATION IN TIME FOR HIGH SPEED IMPACT INTO WATER 321
James F. Heyda

VOLUME II - Part 2

HYPERVELOCITY CRATERING DATA AND A CRATER-DEPTH MODEL FOR THE REGIME OF FLUIDITY 337
Olive G. Engel

FLUID IMPACT CRATERS AND HYPERVELOCITY - - HIGH-VELOCITY IMPACT EXPERIMENTS IN METALS AND ROCKS 367
H. J. Moore, R. W. MacCormack, and D. E. Gault

ENERGY BALANCES IN HYPERVELOCITY PENETRATION 401
R. B. Pond, C. Mobley, and C. M. Glass

THE PARTITION OF ENERGY FOR HYPERVELOCITY IMPACT CRATERS FORMED IN ROCK 419
Donald E. Gault and Ezra D. Heitowit

TRANSIENT OBSERVATIONS OF CRATER FORMATION IN SEMI-INFINITE TARGETS 457
J. H. Kineke, Jr., and Richard Vitali

INFLUENCE OF TARGET STRENGTH ON HYPERVELOCITY CRATER FORMATION IN ALUMINUM 513
J. H. Kineke, Jr., and L. G. Richards

SOME PHENOMENA ASSOCIATED WITH IMPACTS INTO ALUMINUM 525
S. M. Halperson

PARTICLE-SOLID IMPACT PHENOMENA 543
E. H. Goodman and C. D. Liles

INVESTIGATION OF THE IMPACT OF COPPER FILAMENTS INTO ALUMINUM TARGETS AT VELOCITIES TO 16,000 FEET PER SECOND 577
C. Robert Nysmith, James L. Summers, and B. Pat Denardo

IONIZATION ASSOCIATED WITH HYPERVELOCITY IMPACT 591
J. F. Friichtenichtand J. C. Slattery

INVESTIGATION OF IMPACT FLASH AT LOW AMBIENT PRESSURES 613
Robert W. MacCormack

AN INVESTIGATION OF THE PHENOMENA OF IMPACT FLASH AND ITS POTENTIAL USE AS A HIT DETECTION AND TARGET DISCRIMINATION TECHNIQUE 627
J. W. Gehring and R. L. Warnica

SUMMARY: THEORETICAL AND EXPERIMENTAL STUDIES OF CRATER FORMATION 683
R. J. Eichelberger

AUTHOR INDEX 707

TABLE OF CONTENTS

VOLUME III

THIN TARGET PERFORATIONS AND PROTECTION

TABLE OF CONTENTS iii

INTRODUCTORY PAPER - EXPERIMENTATION 1
L. Zernow

TWO DIMENSIONAL ANALYSIS OF A HYPERVELOCITY IMPACT UPON A VISCO-PLASTIC PLATE 13
H. Kraus

A METEOROID BUMPER DESIGN CRITERION 41
P. E. Sandorff

EXPERIMENTAL AND THEORETICAL RESULTS CONCERNING THE PROTECTIVE ABILITY OF A THIN SHIELD AGAINST HYPERVELOCITY PROJECTILES 69
C. J. Maiden

EFFECTS OF 3 TO 12 KM/SEC IMPACTS ON FINITE TARGETS 157
R. B. Mortensen, J. E. Ferguson, J. P. Joyce, and K. N. Kreyenhagen

THIN PLATE PERFORATION STUDIES WITH PROJECTILES IN THE VELOCITY RANGE FROM 2 TO 5 KM/SEC 207
R. W. Watson, K. R. Becker, and F. C. Gibson

A NEW SYSTEM OF PROTECTION FROM HYPERVELOCITY PARTICLES 249
B. W. Reynolds and R. H. Emmons

HYPERVELOCITY PUNCTURING OF SELF-SEALING STRUCTURES 281
Philip J. D'Anna

AN INVESTIGATION OF THE PENETRATION OF HYPER-VELOCITY PROJECTILES INTO COMPOSITE LAMINATES 309
A. R. McMillan

METEOROID EFFECTS ON NUCLEAR ROCKET SPACE VEHICLE MISSION SUCCESS 357
William H. Sterbentz and Loren L. Long

SUMMARY: THIN PLATE PERFORATION AND PROTECTION 387
Dale M. Davis

AUTHOR INDEX 393

VOLUME IV
APPLICATIONS

TABLE OF CONTENTS iii

(Secret) APPLICATION ASPECTS OF HYPERVELOCITY IMPACT - 1963 (U) (Introductory Paper) 1
J. M. Brown and P. K. Margolis

(Confidential) JET PELLET PROJECTION TECHNIQUE (U) 21
S. Kronman

(Confidential) HYPERVELOCITY PROJECTILE INVESTIGATION FOR MULTIPLE THIN PLATE PENETRATION (U) 37
R. L. Chandler, T. Watmough, and F. J. Zimmerman

(Secret) LETHALITY OF HOLLOW SHAPES (U) 101
W. H. Dittrich, D. R. Christman, J. W. Gehring, K. N. Kreyenhagen, and R. B. Mortensen

(Confidential) A WARHEAD CONCEPT FOR DEFEAT OF HARD TARGETS IN SPACE (U) 151
Dale M. Davis

(Secret) AIMED WARHEAD CONCEPTS (U) 167
Samuel D. Stein, George M. Gaydos, and Edmund M. Harrity

(Confidential) HYPERVELOCITY IMPACT EXPERIMENTS WITH LAMINATED COMPLEX TARGETS (U) 193
C. M. Cox and E. S. Thorn

(Secret-No Foreign) HYPERVELOCITY IMPACTS INTO ABLATIVE MATERIALS (U) 235
Mario A. Persechino

(Confidential) DETERMINATION OF PERFORATION ENERGIES FOR COMPOSITE TARGETS (U) 271
Murray Rockowitz and Charles A. Carey

(Secret) A SHORT REVIEW OF THE STATUS OF THE AERO-THERMAL PHASE OF THE HYPERVELOCITY KILL MECHANISMS PROGRAM (U) 305
Coleman duP. Donaldson

(Secret-No Foreign) LETHALITY OF SMALL FRAGMENTS VERSUS ICBM RE-ENTRY VEHICLES (U) 329
James J. Dailey

(Secret-No Foreign) VULNERABILITY OF LARGE MISSILE SYSTEMS DURING THE LAUNCH PHASE (U) 345
H. S. Zimney, R. B. Mortensen, W. A. Rhea, and R. B. Coley

(Confidential) FREE, A HYPERVELOCITY ROCKET WEAPON (U) 373
D. C. Lane

(Secret) SUMMARY: APPLICATIONS (U) 385
W. W. Atkins

(Confidential) ARMOUR RESEARCH FOUNDATION TRAVELING CHARGE GUN (U) 395
Louis A. C. Barbarek

AUTHOR INDEX 417

ATTENDANCE ROSTER 421

Introductory Paper

EXPERIMENTATION

L. Zernow
Director of Research
Ordnance Division
Aerojet-General Corporation

Last week while gathered at the dinner table, my kids having heard that I was leaving town for a week, asked me where I was going. I informed them that I was going to attend a Symposium on Hypervelocity Impact. They asked me what a Symposium was, and I of course took great delight in indicating the dictionary definition of a Symposium as essentially a "drinking party". However, I was quick to point out that this Symposium was not going to be that kind of affair. Rather, it would consist of a group of people who would gather together to air their differences. One of my "wise-guy" kids was quick to comment that this was also what went on at a nudist camp. I was slightly nonplussed at the moment, but I must admit that the proceedings of yesterday's "rump session" were quite revealing. Enough of this.

Having been asked to discuss the historical aspects of experimental work, I will take this opportunity to make a few critical remarks about experimenters and their claims for experimental techniques. However, I will also comment on the relationship of experimenters with the theoreticians.

INTRODUCTORY PAPER - EXPERIMENTATION

I feel no qualms about some comments on theory since other introductory speakers have seen fit to intersperse their remarks with experimental comments.

A convenient way to introduce the historical aspects of the discussion is to review the proceedings of the previous (5th) Symposium. Dr. Eichelberger gave both the introductory status review and the final summary review at that symposium and since it was done so well, I will draw on his material freely. This will serve two purposes. It will give some feeling for the progress that was made at that symposium and will bring us to a point of departure from which we can assess, on the basis of the material we hear at this meeting, how much progress has been made in the interval between symposia. I don't always agree with Bob in his summary statements. Where I disagree, I will so indicate and provide reasons for my disagreement. Despite this disagreement I would like to say that Bob did an excellent job in his summarizing activities.

I have made a tabulation which briefly summarizes Bob's comments before and after the 5th Symposium. He breaks his comments down into discussions of specific aspects and this same breakdown is followed in Table I. He summarizes separately the subjects of the effects of velocity, mass, shape and density of the fragment. He also comments upon wave propagation, com-

TABLE I

SUMMARY OF EICHELBERGER'S 5TH SYMPOSIUM BEFORE AND AFTER REVIEWS CONCERNING STATE OF KNOWLEDGE IN SPECIFIED AREAS

EFFECTS OF	FOR DUCTILE, LARGE TARGETS	
	BEFORE 5TH SYMPOSIUM	AFTER 5TH SYMPOSIUM
1. PROJECTILE VELOCITY	Crater Volume $\sim V^2$ up to 10 km/sec without willingness to extrapolate above this.	Same -- but reinforced and extended to 12 km/sec.
2. PROJECTILE MASS	Linear Modeling Laws almost universally accepted.	Still same -- with caution that Linear Modeling Laws should not be used as confirmation of validity of hydrodynamic treatment without viscosity.
3. PROJECTILE SHAPE	Except for extremes such as long rods, flat discs, shape is a weak parameter at hypervelocities.	Same.
4. PROJECTILE DENSITY	Controversial -- ranging from quadratic relationship between crater volume and projectile density to no influence at all.	No improvement -- Target and projectile density both important.
5. WAVE PROPAGATION IN TARGET	Generally agreed that Wave Propagation properties of target have no influence upon crater formation.	Same -- with new reservations regarding changes in cratering mechanism as functions of velocity.
6. COMPRESSIBILITY OF TARGET	No crater parameter correlation with Hugoniot	Same.
7. STRENGTH OF PROJECTILE OR TARGET	Projectile strength ignorable. Target strength effects seen in correlation of cratering with Brinell hardness up to 10 km/sec.	Resistance of target to deformation is important -- Disappearance of strength effects at high velocities is questioned.
8. OBLIQUITY OF IMPACT	Asymmetry of crater at low velocity disappears at high velocity, with nearly hemispherical craters. Crater volume decreases with obliquity.	Same -- Quantitative confirmation of these effects found experimentally although different experimenters don't agree.

pressibility and strength in the target as well as the effects of obliquity in the impact.

I disagree in a number of places with regard to the assessment of the status after the 5th Symposium. Let me state my disagreements in the hope that further discussion may provide additional insight.

First, on effects of velocity, there still appears to be experimental data which is not in agreement with the hypothesis of crater volume being proportional to V^2. An example of such data which is of particular interest in the light of yesterday's "rump session" on theory, was obtained by Frazier and Karpov in wax targets (Ref. 1).

It is useful also to remember that theoretical considerations indicate that as velocities increase to the point where additional energy absorbing processes become important (e.g., melting, boiling and even ionization), the velocity exponent will increase further. Hence, it will become necessary to specify the velocity ranges associated with specific energy partition mechanisms.

Therefore a particular exponent reputed to represent either momentum or kinetic energy dependence may be an accident, and should not, in my

Reg. (1) Proceedings of 5th Symposium on Hypervelocity Impact, Vol. 1, Part 2, pp 371-388.

opinion, serve as an object of sentimental attachment, or be given the appearance of being innately physically logical. The theoretical treatments should be helpful in assigning the proper changes in the exponent with increasing velocity even if they don't appear to agree at the moment with respect to the exponent itself.

A second point of discussion concerns the effect of projectile density. The paper by A. E. Olshaker and R. L. Bjork (Ref. 2) in my opinion makes a very significant contribution to an improved correlation of the effects of projectile and target density upon the cratering process and I believe that Bjork in his introductory paper, earlier at this meeting, has referenced additional experimental data in support of their basic hypothesis that the target and projectile densities affect the cratering process directly at a given velocity, by fixing the initial particle velocity field in the projectile and the target. These can be specified when the Hugoniots for both target and projectile are known. Further experimental checks of the Olshaker-Bjork hypothesis should prove to be of great interest.

I am somewhat puzzled about Bob's conclusion regarding lack of correlation of crater data with target Hugoniots, under the heading of target compressibility. The theoretical methods (e. g., numerical) make full use of both the projectile and target Hugoniots. In any case, target compressibility

---

Ref. (2) Proceedings of 5th Symposium Vol. I, Part 1, p 185.

is taken into account in computational techniques reported at previous symposia by Bjork.

I find myself in agreement with Bob on the subject of strength effects, in the sense that these appear at present to persist somewhat beyond the point where one might have expected them to become negligible. However, 17 km/sec data with tiny beryllium fragments on aluminum does not really constitute as severe a check as it may appear at first glance, since the pressures induced by the tiny beryllium fragments decay rapidly and also reflect the effects of density differences. Therefore they are at a level considerably less than one associates with aluminum on aluminum impact at 17 km/sec.

Further experimental checks would clearly be very useful.

Dr. Eichelberger's general conclusions at the end of the 5th Symposium are summarizable as follows:

ON THE DIM SIDE

(1) "The purely empirical approach to the hypervelocity impact problem has been singularly unproductive."

(2) There has been a "regrettable lack of perception in the analysis of the data obtained."

(3) "It is ---- discomforting to realize the amount of effort expended for so little gain."

I think Bob has summarized the dark side of the situation with excellent insight.

ON THE BRIGHT SIDE

(1) "The future, on the other hand seems to hold particularly bright promise. Combinations of the new projectile techniques with the methods described for observing transient conditions should finally provide a definitive test of the theoretical results as well as the urgently needed empirical data."

It might be useful to mention that the new experimental techniques referred to were described at the 5th Symposium, and may be summarized as follows:

(1) A new explosive projection technique claiming 21 km/sec fragments.

(2) An improved electrostatic projection technique for micro-particles claiming 14 km/sec and 25 km/sec.

Without in any way disputing the legitimacy of these specific claims, I believe it is worth mentioning that in addition to Dr. Charter's "psychotic projection techniques", there has also been evident in the past a tendency for what I would like to characterize as "verbal projection techniques". These are not always easily recognizable but they are characterized by the use of copious amounts of "hot air" as the working substance, and they can be found over the whole field of projection techniques. Perhaps I am being unnecessarily brutal but I believe the following needs saying:

Experimentalists should be conservative in their claims; much more heavily guided by available theory; much more careful with their measurements; and should recognize an obligation not only to project material at high velocity; but to obtain useful terminal ballistic data as well.

I'm sure we will all be anxious to see how the new projection techniques described at the 5th Symposium have helped us solve our hypervelocity impact problems in the interval between these symposia.

I have one more theme to pursue before I'm finished. This concerns what I'd like to call the "less than perfect" projection techniques. Back in 1955 at the first Rand Symposium on Hypervelocity Impact, everyone was hoping that those techniques which could provide hypervelocity fragments of precisely specified mass and shape would soon become available in the very high ranges of projection velocity. With the exception of the light gas gun technique which has continued to make significant though slow progress, these hopes for a "perfect projection technique" have been largely unfulfilled. At that 1st Symposium, a number of "less than perfect" techniques were described by the speaker, and a plea made for their use pending the attainment of the "perfect" techniques. However, it was not until five years later that the realization of the failure of most of the "perfect" techniques to materialize became sufficiently apparent to permit the application of these "imperfect" but useful methods for the actual acquisition of terminal ballistic data.

Mr. Kreyenhagen (Ref. 3) has described the modified shaped charge technique which has produced terminal ballistic data in the range up to 38,000 feet per second. This is still a substantially higher velocity than is even attainable at present with the light gas gun. It is furthermore much higher than the velocity range in which a useful amount of light gas gun data has been obtained. There may even be a serious question as to whether the light gas gun technique will produce a well-defined fragment if and when it attains a projection velocity of 38,000 ft/sec. The results of an extensive set of experiments involving the projection of aluminum fragments against an aluminum target are shown in Figure 1.

I'm not sure I can assess the value of such data presented at this time, nor can I precisely evaluate its enhanced value, had it been available five years ago. I am sure, however, that the "less than perfect" techniques represent a means for attaining otherwise inaccessible velocities with fragments of useful size in the range of 10 grains. Furthermore, the very careful experimental and instrumentational techniques which are absolutely necessary to make such projection methods useful for the acquisition of data, are also desirable for even the "perfect techniques".

I therefore make an additional plea to those of you in the audience who are in a position to support work aimed at the acquisition of terminal ballistic

Ref. (3) Kreyenhagen, K. N., et al. Special Explosive Projectors. Proc. of the Sixth Hypervelocity Impact Symposium, Vol. I, p. 349, 1963.

data. By all means, continue to support the "perfect" techniques and any bright new ideas which may provide a breakthrough in attaining hypervelocities with initially specified fragments, checking of course to assure that the working substance is not "hot air". However, I urge you not to falter in your support of the "less than perfect" techniques where the velocities are well outside of the range of the "perfect" methods, or where the particular fragment shapes required are not readily projected by the perfect methods for it is in the higher velocity ranges that a basis for resolving the current theoretical dilemma can be obtained experimentally.

I am delighted to see that Mr. Kronman of BRL has succeeded in obtaining a reasonably well-defined "inhibited Jet" and also a cylindrical "long rod" jet. These are additional examples of the value of "less than perfect" techniques and their rapid application to the problem of hypervelocity impact should be encouraged.

I'd like to close by noting that it is clear that theoretical progress, despite the disagreement, is rapidly leaving the experimentalists behind. Yet, major decisions, not only regarding safety but also of tremendous fiscal impact, are going to have to be made on the basis of our efforts. The manner in which we rise to this challenge can have far-reaching effects.

CRITIQUE OF ACCELERATOR TECHNIQUES

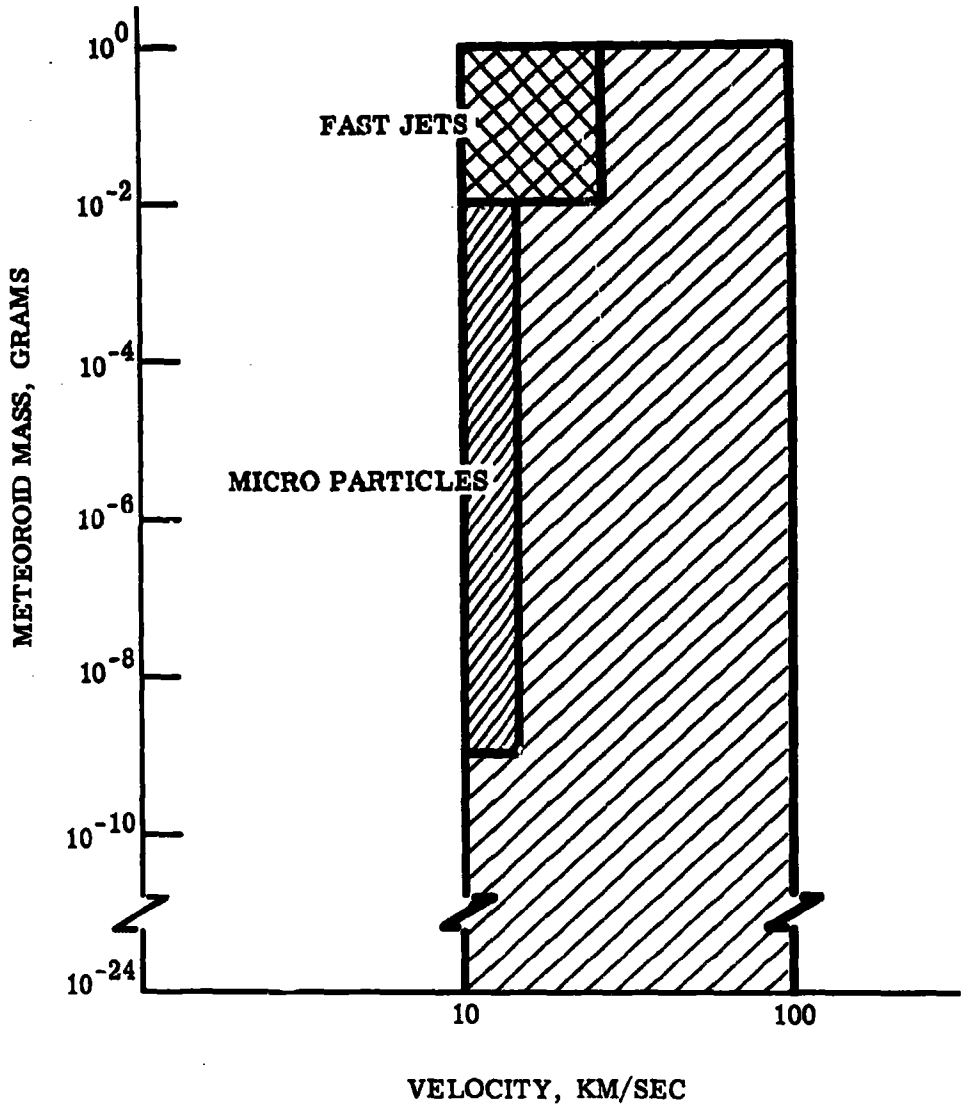

Figure 10 Accelerator Requirements for Space Missions

Two Dimensional Analysis of a Hypervelocity Impact Upon a Visco-Plastic Plate

by

H. Kraus

Scientific Staff
Pratt & Whitney Aircraft Division
United Aircraft Corporation
East Hartford, Connecticut

March 1963

TWO DIMENSIONAL ANALYSIS OF A HYPERVELOCITY IMPACT UPON A VISCO-PLASTIC PLATE

by

H. Kraus

SUMMARY

Previous, one-dimensional, analyses of this problem have assumed that no radial velocities are induced in a thin target plate by an impacting particle. They have also ignored variations of the axial velocity (and radial velocity) through the thickness. In this paper we remove these restrictions and present the results of a two-dimensional analysis of a hypervelocity impact upon a visco-plastic plate. The radial velocities are found to be quite small when compared to the axial velocities except at the edge of the impact zone. Numerical results for the radius of separation obtained with the present theory are found to be less than those obtained in the previous theory because of differences in the manner of initiation of the impact process in the two analyses.

TWO DIMENSIONAL ANALYSIS OF IMPACT

INTRODUCTION

P. C. Chou (1), (2)* has postulated that under the pressures attending a hypervelocity impact upon a thin plate, the plate behaves as an incompressible, visco-plastic (Bingham) material. He presented an analytical solution to the problem of the one dimensional perforation of such a plate by a hypervelocity particle. T. D. Riney (3) also used the concept of a visco-plastic material in his one dimensional numerical analysis of a hypervelocity impact between two semi-infinite compressible masses.

In the present investigation we are concerned with a two-dimensional analysis of the impact of a hypervelocity particle upon an incompressible visco-plastic plate. The salient features of the analysis are its inclusion of both a radial and an axial velocity component, and the satisfaction of prescribed boundary conditions on the surfaces of the plate as well as around its periphery. The previous analyses (1), (2) were restricted to one, axial, velocity component and boundary conditions could thus be prescribed only at the outer periphery of the plate and at the outer radius of a cylindrical slug of the plate material which moves as a rigid body under the influence of the incoming particle.

*Underlined numbers in parentheses denote references listed at the end.

TWO DIMENSIONAL ANALYSIS OF IMPACT

MATHEMATICAL FORMULATION OF THE PROBLEM

We consider the hypervelocity impact of a cylindrical projectile of radius r_p upon a visco-plastic plate of outer radius a and thickness 2h and we assume that the process is initiated by the pressure of impact, P_o, acting over an area of radius r_p on the forward surface ($z = -h$) of the plate. The governing equations for the visco-plastic material have been given by, among others, W. Prager (4) and appear as follows:

$$\frac{\partial \sigma_r}{\partial r} + \frac{\partial \sigma_{rz}}{\partial z} + \frac{\sigma_r - \sigma_\theta}{r} = \rho \frac{Du}{Dt} \qquad \text{(radial equilibrium)}$$

$$\frac{\partial \sigma_{rz}}{\partial r} + \frac{\partial \sigma_z}{\partial z} + \frac{\sigma_{rz}}{r} = \rho \frac{Dw}{Dt} \qquad \text{(axial equilibrium)}$$

$$\frac{1}{r}\frac{\partial}{\partial r}(ru) + \frac{\partial w}{\partial z} = 0 \qquad \text{(continuity equation)}$$

where cylindrical symmetry has been assumed. In the foregoing equations r, z, θ are, respectively, the radial, axial and tangential directions, u and w are the radial and axial velocities, ρ is the density and D/Dt is the substantial derivative. In a visco-plastic material no flow occurs until the shear yield, k, is reached, and thereafter the stresses are given by (4)

$$\sigma_r = -p + 2\left(\mu + \frac{k}{I}\right)\frac{\partial u}{\partial r}, \qquad \sigma_z = -p + 2\left(\mu + \frac{k}{I}\right)\frac{\partial w}{\partial z},$$

$$\sigma_\theta = -p + 2\left(\mu + \frac{k}{I}\right)\frac{u}{r}, \qquad \sigma_{rz} = \left(\mu + \frac{k}{I}\right)\left(\frac{\partial w}{\partial r} + \frac{\partial u}{\partial z}\right),$$

where μ is the viscosity and

$$-3p = \sigma_r + \sigma_\theta + \sigma_z ,$$

$$I = \sqrt{2\left[\left(\frac{\partial u}{\partial r}\right)^2 + \left(\frac{u}{r}\right)^2 + \left(\frac{\partial w}{\partial z}\right)^2\right] + \left(\frac{\partial w}{\partial r} + \frac{\partial u}{\partial z}\right)^2}$$

If we substitute the stress expressions into the equilibrium equations and if we assume, as did Chou, that in the initial, important, stages of the process the quantity $I\mu >> k$, making k/I negligible in comparison to μ the equations reduce to the set**

$$\frac{\partial u'}{\partial t'} + \eta\left(u'\frac{\partial u'}{\partial r'} + w'\frac{\partial u'}{\partial z'}\right) = -\frac{\partial p'}{\partial r'} + \nabla'^2 u' - \frac{u'}{r'^2} ,$$

$$\frac{\partial w'}{\partial t'} + \eta\left(u'\frac{\partial w'}{\partial r'} + w'\frac{\partial w'}{\partial z'}\right) = -\frac{\partial p'}{\partial z'} + \nabla'^2 w' ,$$

$$\frac{1}{r'}\frac{\partial}{\partial r'}(r'u') + \frac{\partial w'}{\partial z'} = 0 , \qquad \nabla'^2 \equiv \frac{\partial^2}{\partial r'^2} + \frac{1}{r'}\frac{\partial}{\partial r'} + \frac{\partial^2}{\partial z'^2} . \qquad \text{(A)}$$

In the foregoing, dimensionless (primed) quantities have been defined as

$$u = u'\left(\frac{p_0 r_p}{\mu}\right) , \quad r = r' r_p , \quad p = p' p_0 ,$$

$$w = w'\left(\frac{p_0 r_p}{\mu}\right) , \quad z = z' r_p , \quad t = t'\left(\frac{\rho r_p^2}{\mu}\right) ,$$

and if, for instance, P_0 is taken as the dynamic pressure of impact

$$\eta = \left(\frac{r_p^2 \rho}{\mu^2}\right)\left(\frac{1}{2}\rho V_0^2\right) = \frac{1}{2}(R_e)^2$$

where V_0 is the velocity of the incoming particle, and the target and particle are assumed to be of the same material.

**The assumption $I\mu >> k$ states, in effect, that initially the plate behaves as a viscous fluid.

In terms of the dimensionless variables we may also define dimensionless stresses as (recalling that $I\mu \gg k$)

$$\sigma_z' = \frac{\sigma_z}{\rho_0} = -p' + 2\frac{\partial w'}{\partial z'}, \qquad \sigma_\theta' = \frac{\sigma_\theta}{\rho_0} = -p' + 2\frac{u'}{r'},$$
$$\sigma_r' = \frac{\sigma_r}{\rho_0} = -p' + 2\frac{\partial u'}{\partial r'}, \qquad \sigma_{rz}' = \frac{\sigma_{rz}}{\rho_0} = \frac{\partial u'}{\partial z'} + \frac{\partial w'}{\partial r'}.$$

It is seen that the equations (A) are non-linear. We thus assume solutions in the form

$$\begin{aligned} u' &= u_0 + \eta u_1 + \eta^2 u_2 + \cdots + \eta^n u_n, \\ w' &= w_0 + \eta w_1 + \eta^2 w_2 + \cdots + \eta^n w_n, \\ p' &= p_0 + \eta p_1 + \eta^2 p_2 + \cdots + \eta^n p_n. \end{aligned} \qquad \text{(B)}$$

Upon substitution of the set (B) into the set (A) and collection of like powers of η we obtain (dropping primes)

$$\begin{aligned} \frac{\partial u_0}{\partial t} + \frac{\partial p_0}{\partial r} - \nabla^2 u_0 + \frac{u_0}{r^2} &= 0 \\ \frac{\partial w_0}{\partial t} + \frac{\partial p_0}{\partial z} - \nabla^2 w_0 &= 0 \\ \frac{1}{r}\frac{\partial}{\partial r}(r u_0) + \frac{\partial w_0}{\partial z} &= 0 \end{aligned} \qquad \text{(C)}$$

In terms of the dimensionless variables we may also define dimensionless stresses as (recalling that $I\mu \gg k$)

$$\sigma_z' = \frac{\sigma_z}{\rho_0} = -p' + 2\frac{\partial w'}{\partial z'}, \qquad \sigma_\theta' = \frac{\sigma_\theta}{\rho_0} = -p' + 2\frac{u'}{r'},$$
$$\sigma_r' = \frac{\sigma_r}{\rho_0} = -p' + 2\frac{\partial u'}{\partial r'}, \qquad \sigma_{rz}' = \frac{\sigma_{rz}}{\rho_0} = \frac{\partial u'}{\partial z'} + \frac{\partial w'}{\partial r'}.$$

It is seen that the equations (A) are non-linear. We thus assume solutions in the form

$$\begin{aligned} u' &= u_0 + \eta u_1 + \eta^2 u_2 + \cdots + \eta^n u_n, \\ w' &= w_0 + \eta w_1 + \eta^2 w_2 + \cdots + \eta^n w_n, \\ p' &= p_0 + \eta p_1 + \eta^2 p_2 + \cdots + \eta^n p_n. \end{aligned} \qquad \text{(B)}$$

Upon substitution of the set (B) into the set (A) and collection of like powers of η we obtain (dropping primes)

$$\begin{aligned} \frac{\partial u_0}{\partial t} + \frac{\partial p_0}{\partial r} - \nabla^2 u_0 + \frac{u_0}{r^2} &= 0 \\ \frac{\partial w_0}{\partial t} + \frac{\partial p_0}{\partial z} - \nabla^2 w_0 &= 0 \\ \frac{1}{r}\frac{\partial}{\partial r}(r u_0) + \frac{\partial w_0}{\partial z} &= 0 \end{aligned} \qquad \text{(C)}$$

and

$$\begin{aligned} \frac{\partial u_1}{\partial t} + \frac{\partial p_1}{\partial r} - \nabla^2 u_1 + \frac{u_1}{r^2} &= -u_0 \frac{\partial u_0}{\partial r} - w_0 \frac{\partial u_0}{\partial z} \\ \frac{\partial w_1}{\partial t} + \frac{\partial p_1}{\partial z} - \nabla^2 w_1 &= -u_0 \frac{\partial w_0}{\partial r} - w_0 \frac{\partial w_0}{\partial z} \qquad \text{(D)} \\ \frac{1}{r}\frac{\partial}{\partial r}(r u_1) + \frac{\partial w_1}{\partial z} &= 0 \end{aligned}$$

and so on for the higher terms. The solution of the set (C) represents a "first approximation" in which the convective terms are ignored. The "second approximation" is obtained by solving the inhomogeneous set (D) and so on.

As stated at the outset, the process is initiated by the dynamic pressure of impact, acting suddenly over an area of radius r_p, on the forward surface (z = -h) of the target plate. The initial conditions of the problem thus are

$$u(r, z, o) = w(r, z, o) = p(r, z, o) = o$$

and the boundary conditions (for $t > o$) are

$$\begin{aligned} &p(a, z, t) = 0, \quad -h \le z \le h \qquad && p(r, -h, t) = p_0, \quad 0 \le r \le r_p \\ &p(r, h, t) = 0, \quad 0 \le r \le a \qquad && \frac{dw}{dz}(r, \pm h, t) = 0, \quad 0 \le r \le a. \\ &p(r, -h, t) = 0, \quad r_p \le r \le a \end{aligned}$$

These conditions are sufficient to solve the problem completely and will insure, through its definition, that the axial stress vanishes at the surfaces of the plate except over the portion where the pressure P_o acts; there, the axial stress is equal to the negative of the applied

pressure. The implications of these boundary conditions and of the present formulation will be discussed more fully at the end.

SOLUTION

In the present analysis we restrict ourselves to the "first approximation" wherein the non-linear terms are neglected. We are thus concerned with the solution of the set of equations (C). To begin we apply a Laplace transformation (6) with respect to time to equations (C) and thus convert these to the set

$$s\bar{u} = -\frac{\partial \bar{p}}{\partial r} + \nabla^2 \bar{u} - \frac{\bar{u}}{r^2},$$

$$s\bar{w} = -\frac{\partial \bar{p}}{\partial z} + \nabla^2 \bar{w},$$

$$\frac{1}{r}\frac{\partial}{\partial r}(r\bar{u}) + \frac{\partial \bar{w}}{\partial z} = 0,$$

where the barred quantities are the transformed dependent variables, s is the Laplace transform parameter and the initial conditions have been utilized in the transformation of the time derivatives. If, now, we assume that the space variables are separable; that is, $\bar{u} = R_1(r)\,Z_1(z)$, $\bar{w} = R_2(r)\,Z_2(z)$ and $\bar{p} = R_3(r)\,Z_3(z)$, then the equations can be decomposed as follows (5):

$$\frac{d^2R_1}{dr^2} + \frac{1}{r}\frac{dR_1}{dr} + \left(\alpha_n^2 - \frac{1}{r^2}\right)R_1 = 0, \qquad \frac{d^2Z_1}{dz^2} - (s+\alpha_n^2)Z_1 = \frac{Z_3}{R_1}\frac{dR_3}{dr},$$

$$\frac{d^2R_2}{dr^2} + \frac{1}{r}\frac{dR_2}{dr} + \alpha_n^2 R_2 = 0, \qquad \frac{d^2Z_2}{dz^2} - (s+\alpha_n^2)Z_2 = \frac{R_3}{R_2}\frac{dZ_3}{dz},$$

$$Z_1\frac{1}{r}\frac{d}{dr}(rR_1) + R_2\frac{dZ_3}{dz} = 0,$$

where α_n is a separation constant. It follows that for bounded results at r = O the solutions to the first two equations above are the Bessel functions $R_2(r) = R_3(r) = J_o(\alpha_n r)$, $R_1(r) = J_1(\alpha_n r)$.

The separation constant α_n is found from the requirement that the pressure vanish at r = a. This gives α_n as the roots of the equation

$$J_0(\alpha_n a) = 0,$$

where n = 1, 2.....

The remaining, z dependent, solutions are then obtained from ***

$$\frac{d^2 Z_1}{dz^2} - (5+\alpha_n^2) Z_1 = -\alpha_n Z_3,$$

$$\frac{d^2 Z_3}{dz^2} - (5+\alpha_n^2) Z_3 = \frac{dZ_3}{dz}, \qquad \alpha_n Z_1 + \frac{dZ_3}{dz} = 0$$

If Z_1 and Z_3 are eliminated in the preceding equations there is obtained the following differential equation in Z_2:

$$\frac{d^4 Z_2}{dz^4} - (5+2\alpha_n^2)\frac{d^2 Z_2}{dz^2} + \alpha_n^2(5+\alpha_n^2) Z_2 = 0.$$

***Note, for future reference , that the third of these equations indicates that the vanishing of the z derivative of the axial velocity implies the vanishing of the radial velocity.

The general solution to the above equation can be shown, by standard methods, to be

$$Z_2 = \sum_{n=1}^{\infty} \left(A_n \cosh \alpha_n z + B_n \sinh \alpha_n z + C_n \cosh z\sqrt{s+\alpha_n^2} + D_n \sinh z\sqrt{s+\alpha_n^2} \right),$$

and, furthermore,

$$Z_3 = -s \sum_{n=1}^{\infty} \frac{1}{\alpha_n} \left(A_n \sinh \alpha_n z + B_n \cosh \alpha_n z \right),$$

$$Z_1 = -\sum_{n=1}^{\infty} \left[A_n \sinh \alpha_n z + B_n \cosh \alpha_n z + \frac{\sqrt{s+\alpha_n^2}}{\alpha_n} \left(C_n \sinh z\sqrt{s+\alpha_n^2} + D_n \cosh z\sqrt{s+\alpha_n^2} \right) \right].$$

The arbitrary constants A_n, B_n, C_n and D_n are determined from the Laplace-transformed boundary conditions at $z = \pm h$ and can be shown to be

$$A_n = \frac{J_1(\alpha_n)}{s^2 a^2 \left[J_1(\alpha_n a) \right]^2 \sinh \alpha_n h}, \qquad B_n = -A_n \tanh \alpha_n h,$$

$$C_n = \frac{-\alpha_n J_1(\alpha_n)}{s^2 a^2 \sqrt{s+\alpha_n^2} \left[J_1(\alpha_n a) \right]^2 \sinh h\sqrt{s+\alpha_n^2}}, \qquad D_n = -C_n \tanh h\sqrt{s+\alpha_n^2}.$$

This completes the determination of the transformed dependent variables of the problem, and it remains now to invert these quantities. The inversion is accomplished by use of the complex inversion integral formula of Laplace transform theory and makes use of the calculus of

residues (see, e.g., (6)), In the interest of brevity we omit the tedious details of this procedure and give the following results of the inversion process:

$$p = \frac{2}{a^2} \sum_{m=1}^{\infty} \frac{J_1(\alpha_m) J_0(\alpha_m r)}{\alpha_m \left[J_1(\alpha_m a)\right]^2} \frac{\sinh(h-z)\alpha_m}{\sinh 2\alpha_m h},$$

$$w = \frac{1}{a^2} \sum_{m=1}^{\infty} \frac{J_1(\alpha_m) J_0(\alpha_m r)}{\left[J_1(\alpha_m a)\right]^2} \left[\frac{\cosh(z-h)\alpha_m}{\alpha_m^2 \sinh 2\alpha_m h} + \frac{2h \cosh(z-h)\alpha_m \cosh 2h\alpha_m}{\alpha_m \sinh^2 2\alpha_m h} \right.$$

$$- \frac{(z-h)\sinh(z-h)\alpha_m}{\alpha_m \sinh 2\alpha_m h} - \frac{e^{-\alpha_m^2 t}}{h\alpha_m^3}$$

$$\left. + \frac{2}{h} \sum_{n=1}^{\infty} \frac{\alpha_m (-1)^{n+1}}{\left(\alpha_m^2 + \frac{n^2\pi^2}{4h^2}\right)^2} \cos(z-h)\frac{n\pi}{2h} \; e^{-t\left(\alpha_m^2 + \frac{n^2\pi^2}{4h^2}\right)} \right],$$

$$u = \frac{-2}{a^2} \sum_{m=1}^{\infty} \frac{J_1(\alpha_m) J_1(\alpha_m r)}{\left[J_1(\alpha_m a)\right]^2} \left[\frac{(h-z)\cosh(h-z)\alpha_m}{2\alpha_m \sinh 2h\alpha_m} \right.$$

$$- \frac{h \cosh(h-z)\alpha_m \cosh 2h\alpha_m}{\alpha_m \sinh^2 2h\alpha_m}$$

$$\left. + \frac{\pi}{2h^2} \sum_{n=1}^{\infty} \frac{n(-1)^{n+1}}{\left(\alpha_m^2 + \frac{n^2\pi^2}{4h^2}\right)^2} \sin\frac{n\pi}{2h}(h-z) \; e^{-t\left(\alpha_m^2 + \frac{n^2\pi^2}{4h^2}\right)} \right].$$

NUMERICAL RESULTS

As is typical of Fourier series the convergence of the foregoing expressions is extremely slow. Both the partial sums and the individual terms, when plotted against the summation index m, display a periodic behavior with slowly decreasing amplitude about an apparent final result. This fact was utilized in the criterion which was set up for ending the summation and determining the final result.**** Numerical results were calculated for a cylindrical particle of unit radius striking a plate whose thickness is equal to one particle radius ($2h/r_p = 1$) and whose outer radius is equal to ten particle radii ($a/r_p = 10$). The results for a unit impact pressure ($P_o = 1$) are plotted in Figures 1, 2, and 3 which depict the pressure and velocity as a function of position and time (all plotted quantities are dimensionless). It is evident from these figures that significant variations in the dependent variables occur only within two particle radii of the center of the plate and that their values decay rapidly at larger distances from the center. The variation with axial position is not too great in most instances except for the case of the pressure distribution,

****The author is indebted to S. Auslender for conceiving the criterion.

whose boundary values were prescribed. As could be expected the velocities increase with time and reach a steady value (not shown) which can be determined by letting t grow without bound in the velocity expressions, leaving quantities dependent only on position. Comparison of Figures 2 and 3 shows that except near the edge of the impact zone ($r/r_p = 1$) the radial velocities are about one order of magnitude smaller than are the axial velocities.

SEPARATION CRITERION

Separation was defined by Chou (1), (2) to occur when the viscous material could no longer transmit shear. He postulated that this occurred when the strain rate and the strain simultaneously reached critical values. Since the present analysis is not one-dimensional we generalize the above criteria by specifying that for separation the product of viscosity and the strain rate invariant be equal to the shear yield of the material and that the so-called effective strain (8) be equal to 2%. Mathematically, these criteria are stated as follows:

$$\mu I = k,$$

$$\bar{\epsilon} = \frac{\sqrt{2}}{3}\sqrt{(\epsilon_r - \epsilon_\theta)^2 + (\epsilon_\theta - \epsilon_z)^2 + (\epsilon_z - \epsilon_r)^2 + 6\gamma_{rz}^2},$$

with

$$\epsilon_r = \frac{\partial \zeta}{\partial r}, \quad \epsilon_\theta = \frac{\zeta}{r}, \quad \epsilon_z = \frac{\partial \xi}{\partial z}, \quad \gamma_{rz} = \frac{1}{2}\left(\frac{\partial \zeta}{\partial z} + \frac{\partial \xi}{\partial r}\right),$$

where ζ and ξ are, respectively, the radial and axial displacements. These are obtained by integrating the velocities with respect to time. The second condition can be simplified by expanding the quadratic terms and using the fact that for an incompressible material the sum of the normal strains is zero. In terms of the present dimensionless variables the criteria then become:

$$\sqrt{2\left[\left(\frac{\partial u}{\partial r}\right)^2+\left(\frac{u}{r}\right)^2+\left(\frac{\partial w}{\partial z}\right)^2\right]+\left(\frac{\partial u}{\partial z}+\frac{\partial w}{\partial r}\right)^2} = k/P_0$$

$$\sqrt{2\left[\left(\frac{\partial \zeta}{\partial r}\right)^2+\left(\frac{\zeta}{r}\right)^2+\left(\frac{\partial \xi}{\partial z}\right)^2\right]+\left(\frac{\partial \zeta}{\partial z}+\frac{\partial \xi}{\partial r}\right)^2} = \sqrt{3}\,\bar{\epsilon}\mu^2/P_0 r_p^2\rho$$

The point and time of separation are determined by a graphical procedure which is identical to that followed by Chou (1), (2) with the exception that in our case the process is a function of axial position and our criteria are, as noted previously, generalizations of the former ones. The procedure is illustrated in Figures 4, 5 and 6 and is explained as follows: In Figure 4 we have plotted the quantity

$$\sqrt{2\left[\left(\frac{\partial \zeta}{\partial r}\right)^2+\left(\frac{\zeta}{r}\right)^2+\left(\frac{\partial \xi}{\partial z}\right)^2\right]+\left(\frac{\partial \zeta}{\partial z}+\frac{\partial \xi}{\partial r}\right)^2}$$

against r/r_p for four values of the dimensionless time $t\mu/\rho\, r_p^2$. The horizontal lines correspond to critical values of the ordinate for the three sample velocities given in Table I. In Figure 5 we have done the same for

the quantity $\sqrt{2\left[\left(\frac{\partial u}{\partial r}\right)^2+\left(\frac{u}{r}\right)^2+\left(\frac{\partial w}{\partial z}\right)^2\right]+\left(\frac{\partial u}{\partial z}+\frac{\partial w}{\partial r}\right)^2}$ and its critical values for the velocities under consideration. Then, in Figure 6 we have plotted, for each velocity, the critical strain and critical strain rate curves. These are simply plots of the time versus radial position as obtained from the intercepts of each of the three horizontal lines in Figures 4 and 5. The intersections of the curves in each set in Figure 6 represent the time and radius at which the critical values of both the effective strain and the strain rate invariant are achieved and thereby define the instant and radius of perforation for each of the three sample velocities. The results are summarized and compared to Chou's results in Table I. Note that the material under consideration is aluminum and that the physical properties are those used by Chou. The quantities r_c and t_c refer to the "critical" time and radius at which the separation criteria are met. Results are presented for $z/r_p = +0.5$ only since the maximum critical radii were calculated at that axial position. The results are discussed in the next section.

DISCUSSION

In an attempt to determine the magnitude and the effect of any radial velocities that are induced in a thin target plate by an impacting

TABLE I

SUMMARY AND COMPARISON OF SEPARATION CALCULATIONS FOR AN ALUMINUM PLATE

r_p = 0.0469 in. $\quad \rho$ = 5.2 slugs/ft.^{3}

2h = 0.0469 in. $\quad \mu$ = 100 lb. sec./ft.^{2}

z/r_p = + 0.50 $\quad$ k = 10^5 lb./in.^{2}

V_o (ft./sec.)	7130	12,000	20,000
P_o (lb./ft.^{2})	1.32 (10^8)	3.74(10^8)	1.04 (10^9)
k/P_o	0.109	0.0385	0.0139
$\sqrt{3}\,\bar{\epsilon}\,\mu^2/P_o\,r_p^2\rho$	0.0331	0.0117	0.0042
r_c/r_p	1.89	2.53	3.32
r_c/r_p (2)	2.77	3.25	3.63
t_c (sec.)	4.48 (10^{-7})	5.95(10^{-7})	7.94(10^{-7})
t_c (2)	4.93 (10^{-7})	5.72(10^{-7})	6.84(10^{-7})

particle we have presented the results of a "first approximation" to the solution of the problem of a viscoplastic plate under hypervelocity impact.

We have shown (see Figures 2 and 3) that except at the edge of the impact zone the radial velocities are about one order of magnitude smaller than are the axial velocities. Our separation calculations have led to results that are different from those obtained in Chou's one-dimensional analysis (see Table I) in spite of these small radial velocities (which are ignored altogether in the one-dimensional case) because of differences in the manner of initiation of the impact process in the two analyses. We have assumed that the kinetic energy of the impacting particle is deposited on a small area on the forward surface of the plate, whereas the former analysis assumed a momentum exchange between the mass of the particle and the combined mass of the particle and a cylindrical slug of the target plate which is set into motion upon impact. Thus, the former analysis has assumed that at $t = 0$ the material is already moving whereas the present analysis has assumed that at $t = 0$ the material is at rest and the pressure load is first applied. On these grounds it is felt to be reasonable that our separation radii turned out to be less than those of the one-dimensional analysis.

Before closing this discussion we mention some of the short comings of the present analysis:

We have only considered the solution of the linearized set of equations (C), thus making the solution a first approximation. The results are thus expected to be valid for very small values of the perturbation parameter η which was shown to be equal to one half of the square of Reynolds' number for the process. Since not very much is known about dynamic viscosities of flowing solids the question of the accuracy of a one term approximation cannot be resolved as yet. Efforts will be made, however, to solve for the next term in each perturbed solution by solving the set of equations (B).

Our neglect of k in comparison to μI has removed the effect of strength from the calculations (except in the separation criterion). However, Chou (9) has found that retention of k in his solution did not change the results of his previous analysis significantly. It is reasonable to expect that the same would be true here.

In regard to the boundary conditions it must be pointed out that we have only been able to impose conditions on the normal stress and the pressure at the surfaces of the plate. Because of a lack of additional arbitrariness in the general solution conditions could not be prescribed

for the shear stress on the surfaces of the plate. This is not felt to be overly serious since our condition that the axial derivative of the axial velocity vanish on the plate surfaces implies (footnote***) that the radial velocity and its radial derivative vanish on the surfaces of the plate as well. This simply represents the plausible fact that there is a thin "crust" of material on the surfaces of the flowing material which can resist radial deformation. Hence, a shear stress can be tolerated between this crust and the flowing material underneath.

Our assumption that the entire material is flowing is extreme since in the actual situation there is constrained flow with a boundary between the flowing and the stationary portions of the material. The exact solution of the problem with a moving, unknown boundary of this type would be extremely difficult, especially in two-dimensions.

In common with the one-dimensional analysis we have ignored the compressibility of the material, and, therefore, no shock discontinuities arise in the solution. The validity of this neglect has yet to be demonstrated.

The resolution of these questions will undoubtedly involve an extremely complex numerical solution such as set up for the cratering problem

of a visco-plastic body in a recent report by Riney (7). The numerical solution of the perforation problem will be even more complex since one will be concerned with an additional free surface.

Finally, we have utilized estimated values for the viscosity and shear yield of the material in our sample problem. Experimental data on dynamic viscosities and yield strengths of materials will be required for use in the ultimate solution of the problem, be it a numerical or an analytical one.

ACKNOWLEDGEMENTS

The author is indebted to Dr. P. C. Chou for suggesting the subject of this investigation and for many valuable discussions during the progress of the solution. He is grateful to Mr. T. Osetek for writing the computer program which was used in obtaining the numerical results, and to his colleagues on the Scientific Staff of Pratt & Whitney Aircraft for many valuable suggestions.

REFERENCES:

1. P. C. Chou, "Perforation of Plates by High Speed Projectiles," Proceedings of the Seventh Midwestern Mechanics Conference, J. E. Lay and L. E. Malvern, eds., Plenum Press, New York (1961). pp 286 - 295.

2. P. C. Chou, "Visco-Plastic Flow Theory in Hypervelocity Perforation of Plates," Proceedings of the Fifth Hypervelocity Impact Symposium, Denver, Colorado, (1961).

3. T. D. Riney and F. R. Chernoff, "Inertia, Viscous and Plastic Effects in High Speed Impact," Proceedings of the Fifth Hypervelocity Impact Symposium, Denver, Colorado, (1961).

4. W. Prager, "On Slow Visco-Plastic Flow," Studies in Mathematics and Mechanics Presented to R. von Mises, Academic Press, New York (1954), pp. 208 - 216.

5. N. A. Haskell, "The Motion of a Viscous Fluid Under a Surface Load," Physics, 6, 265-269, (1935).

6. R. V. Churchill, Operational Mathematics, second ed., McGraw Hill, New York, (1958).

7. T. D. Riney, "PIC Formulation of Visco-Plastic Model of Hypervelocity Impact," APGC-TDR-62-24, (1962).

8. O. Hoffman and G. Sachs, Introduction to the Theory of Plasticity, McGraw-Hill, New York (1953).

9. P. C. Chou, personal communication.

FIGURE 1

PRESSURE DISTRIBUTION AS A FUNCTION OF AXIAL AND RADIAL POSITION

($a/r_p=10$, $2h/r_p=1$, all t)

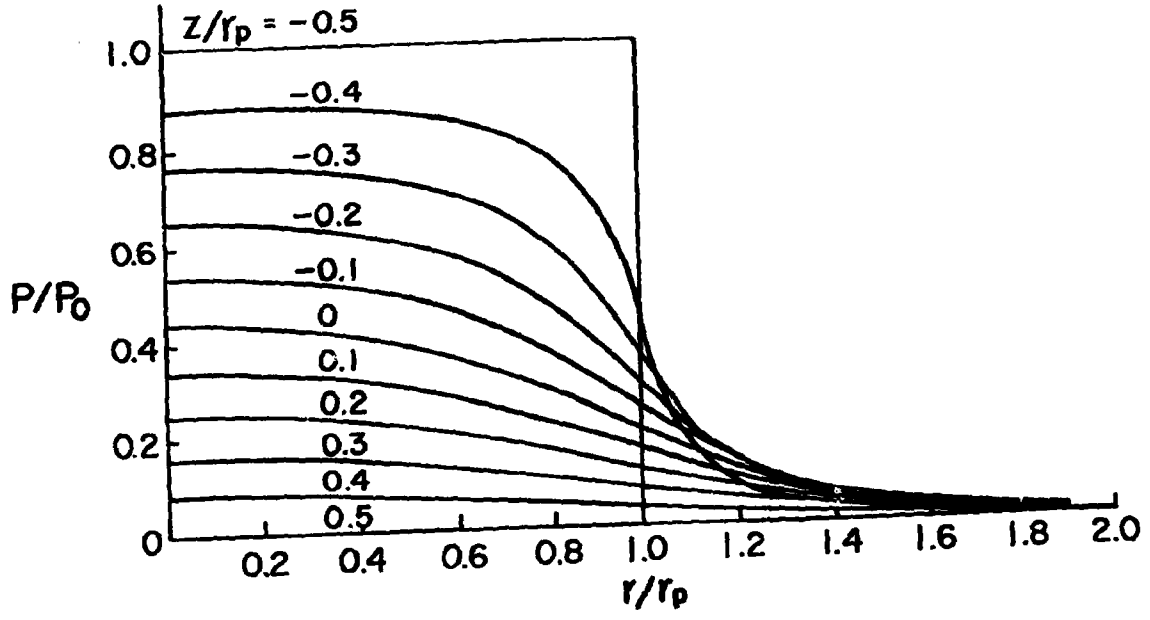

FIGURE 2

AXIAL VELOCITY AS A FUNCTION OF AXIAL POSITION RADIAL POSITION AND TIME

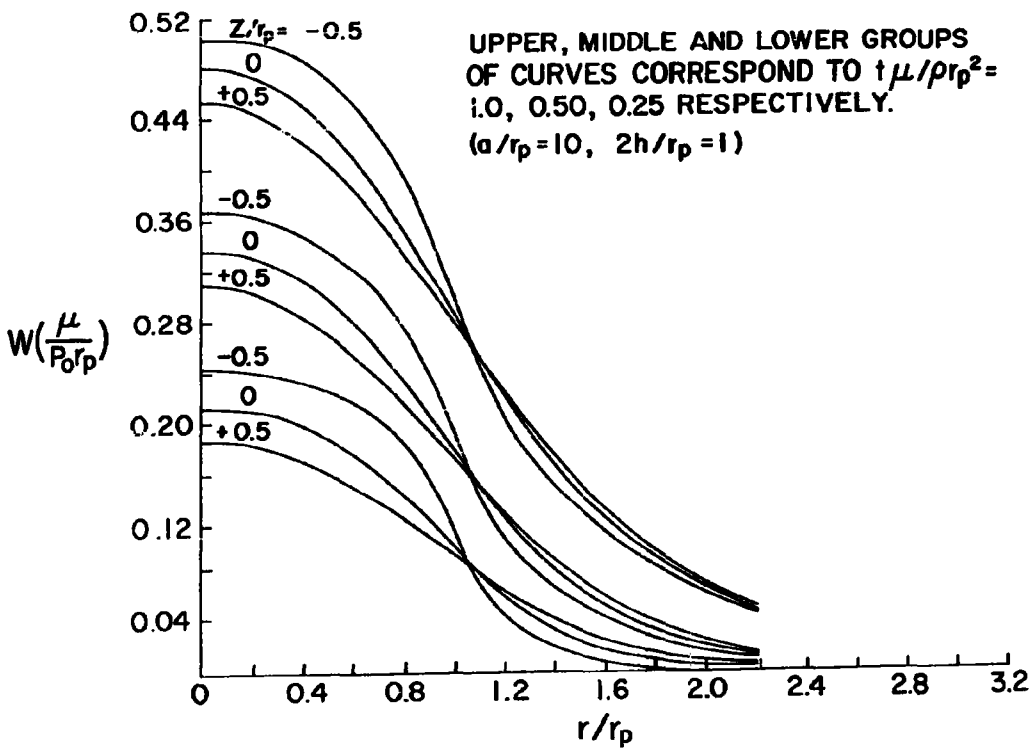

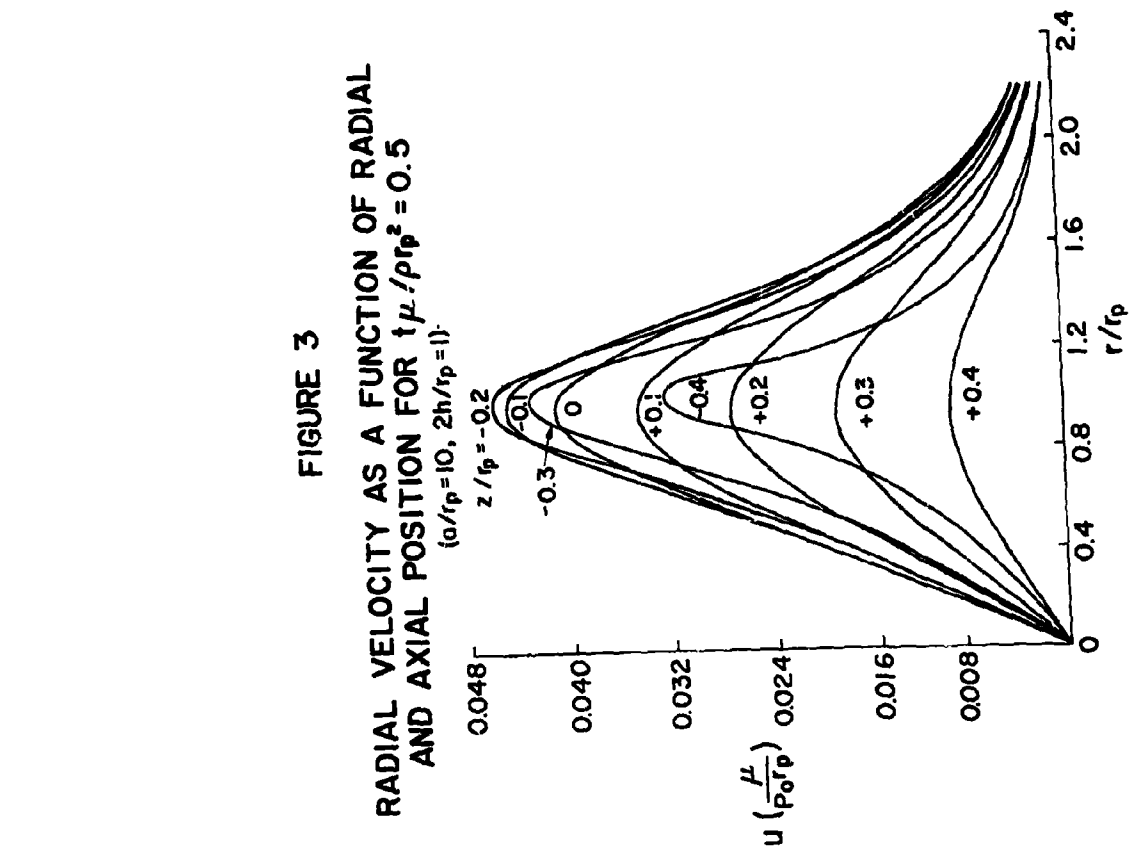
RADIAL VELOCITY AS A FUNCTION OF RADIAL AND AXIAL POSITION FOR $t\mu/\rho r_p^2 = 0.5$
$(a/r_p = 10,\ 2h/r_p = 1)$
$z/r_p = -0.2$
-0.1
0
-0.3
+0.1
-0.4
+0.2
+0.3
+0.4
$u\left(\frac{\mu}{P_o r_p}\right)$
0.048
0.040
0.032
0.024
0.016
0.008
0
0.4
0.8
1.2
1.6
2.0
2.4
r/r_p

FIGURE 3

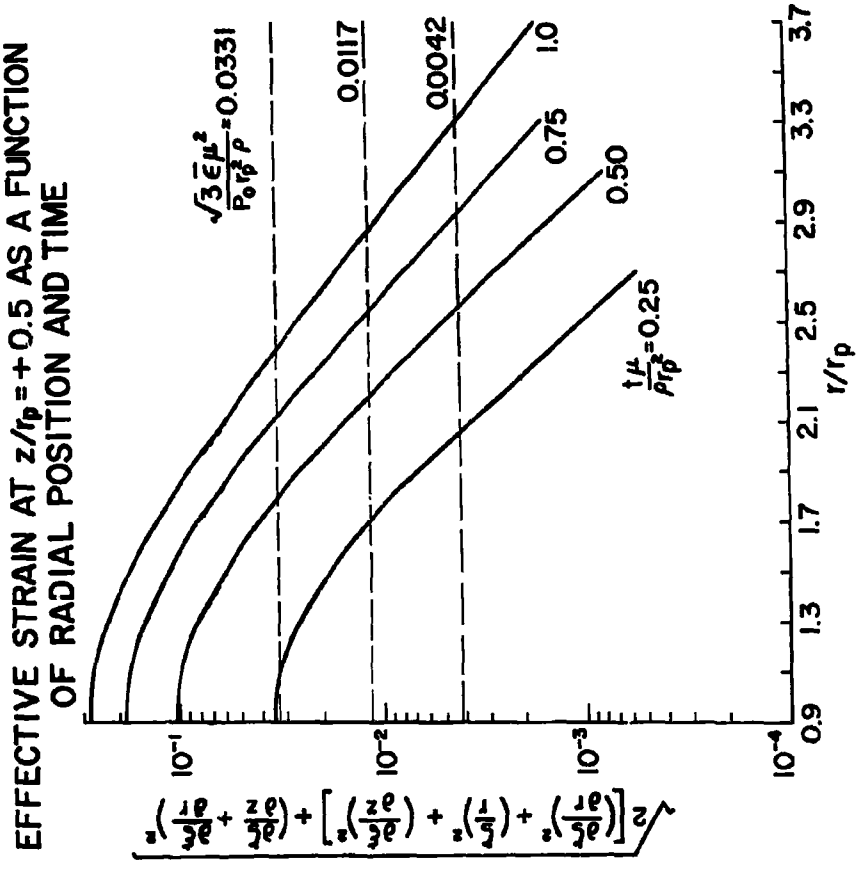

FIGURE 4
EFFECTIVE STRAIN AT $z/r_p = +0.5$ AS A FUNCTION OF RADIAL POSITION AND TIME

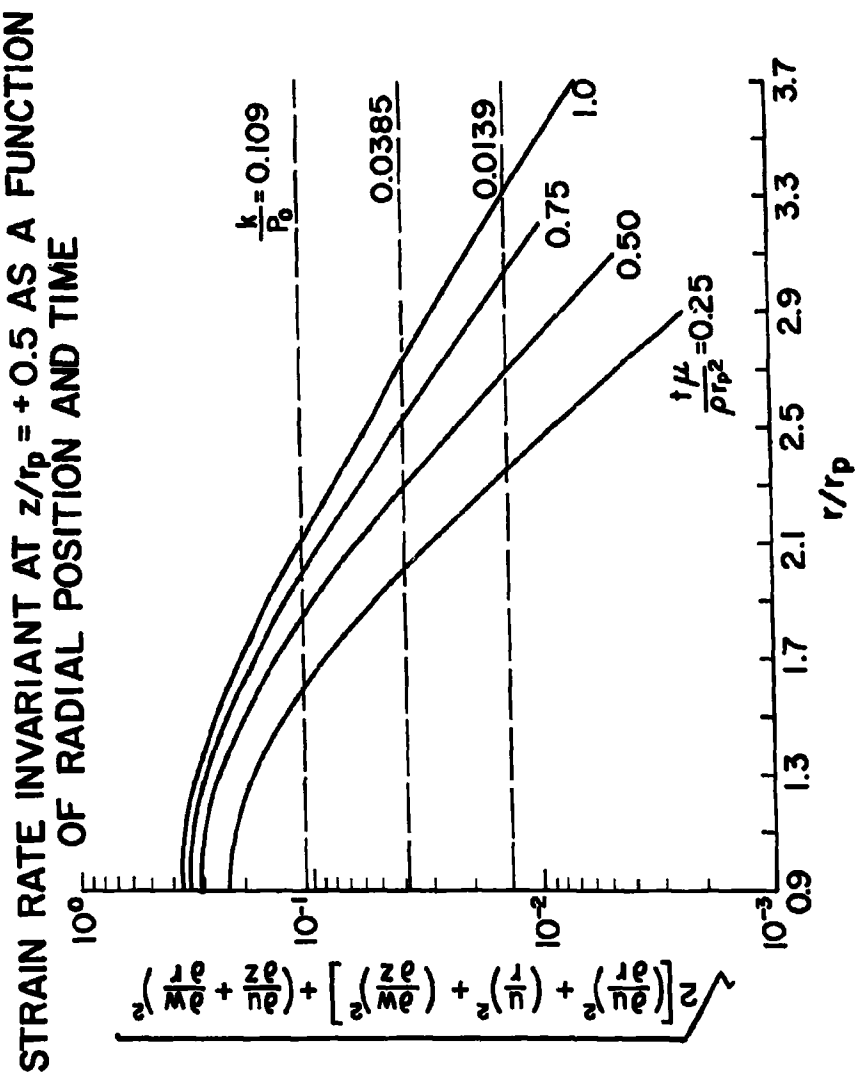

FIGURE 5
STRAIN RATE INVARIANT AT $z/r_p = +0.5$ AS A FUNCTION OF RADIAL POSITION AND TIME

FIGURE 6
DETERMINATION OF SEPARATION TIME AND RADIUS FOR $z/r_p = +0.5$

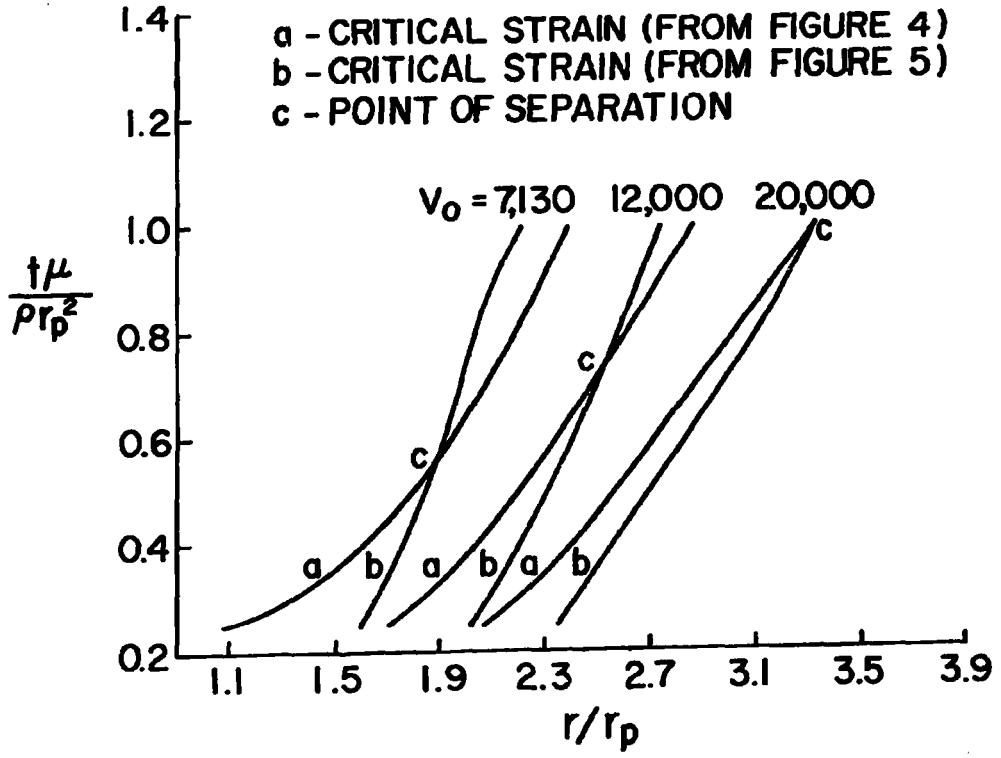

A Meteoroid Bumper Design Criterion

P. E Sandorff

Lockheed Missiles & Space Company, Palo Alto, California

METEOROID BUMPER DESIGN

INTRODUCTION

The design concept and the principles of operation of a Whipple "meteor bumper" for protection against hypervelocity impact are well known (1). An efficient bumper plate will be just thick enough to produce complete pulverization of the incident hypervelocity particle. Furthermore, it will result in extremely fine fragmentation and a uniformly expanding spray of debris, in order that full advantage can be taken of bumper spacing to minimize damage to the structure underneath. An approximation to the first requirement may be obtained by the application of one-dimensional shock wave mechanics. This approach also provides a qualitative appreciation of more complicated aspects of the bumper design problem.

THE PHYSICAL PROCESS

When hypervelocity impact occurs, a shock front proceeds from the interface of the two materials forward into the bumper plate, and similarly another shock front proceeds rearward into the projectile material. Considering only one-dimensional effects, that is, normal impact and conditions along the axis of impact, the speeds at which the shock fronts move, as well as the pressure level and densification of the materials between them, can be determined by the Hugoniot conservation relations and the adiabatic equations of state of the materials. When the shock front in the bumper reaches the rear face, an expansion process is initiated, which moves back into the bumper and then into the projectile, causing disruption and comminution. The head of this rarefaction wave propagates at the speed of sound for the densified material, and this speed is always greater than the relative speed at which the shock front propagates. Therefore, if the projectile dimension is large compared to the bumper thickness, it is possible for the rarefaction wave to overtake the slower moving shock front in the projectile. The nature of these processes is indicated schematically in Fig. 1.

The rarefaction wave is a mechanism which converts the energy of pressure-volume change in the densified zone back into energy of motion; it accelerates the material up to a velocity tending to move it out of the way of the impinging projectile.

When it overtakes the shock front, it consequently reduces the impact speed relative to the densified material and both the shock front velocity and the impact pressure are diminished accordingly. Mis-match between this impact pressure and the pressure established by the rarefaction wave, both of which continue to diminish as the overtaking process continues, gives rise to additional pressure wave phenomena which in general are of second order compared to the primary shock and rarefaction waves.

The nature of the rarefaction wave, however, is such that complete cancellation of the impact pressure is not possible. Indeed, it can be appreciated from elementary considerations, that if the momentum of any forward portion of the projectile is distributed between projectile mass and an incremental (bumper) mass, a reduction in velocity of the projectile mass involved must occur, and this could only impede the motion of the remaining portion of the projectile. Thus any bumper, however small, will produce effects that are felt by the entire projectile mass.

However, in the extreme case of a very long projectile such as a rod end-on the advanced overtaking process may be expected to degrade into a normal compression shock of diminishing severity, depending on the initial conditions and on the lateral boundaries, which drain off energy first in extensive lateral spall and then in plastic processes. Upon reaching the rear end of the projectile the traveling shock may still be strong enough to cause rear-face spall, but this process will dissipate all energy above the damage threshold. It is therefore possible for some portion of a rod-shaped projectile to pass through a "too-thin" bumper virtually undamaged and with only slight reduction in velocity. For a chunky projectile, essentially the same considerations apply, but the lateral rarefaction processes would be more important in reducing the projectile to fragments.

As far as bumper effectiveness in destroying the projectile is concerned, the critical point in the process is the instant at which the head of the rarefaction wave overtakes the rearward-moving shock front in the projectile material. As has been indicated, the disruption process is not complete at that point, but it will rapidly diminish in effectiveness thereafter. As a design criterion, therefore, the critical bumper thickness is defined as that which would delay

the rarefaction process long enough so that it overtakes the shock front at the rear surface of the projectile. If the bumper thickness to projectile dimension is greater than critical, the entire projectile is subjected to the full impact pressure.

ANALYSIS

The Hugoniot equations for the conditions behind normal shock as established by conservation of mass and momentum are, respectively:

$$\rho = \rho_0 u_s / (u_s - u_p) \qquad (1)$$

$$p = \rho_0 u_s u_p \qquad (2)$$

The shock-Hugoniot properties of materials are represented by the two-parameter analytical approximation used in Ref. 2, 3 and 4:

$$u_s = c_0 + S u_p \qquad (3)$$

$$p = \rho_0 u_p (c_0 + S u_p) \qquad (4)$$

where c_0 and S are material properties expressing the stiffness under impact. Although in many cases c_0 approximates the acoustic velocity of the material at zero pressure, in others the Hugoniot departs perceptibly from the quadratic (4) over the pressure range of interest. For the present purposes, the parameters c_0 and S correspond to behavior under the highest experimental impact pressures reported in the literature. By combining (3) and (4) the impact pressure can be expressed somewhat as in Ref. 4 in a form which will later be useful:

$$\frac{p}{\rho_0 c_0^2} = \frac{\sigma(\sigma-1)}{[\sigma-(\sigma-1)S]^2} \qquad (5)$$

where σ is the "densification" factor,

$$\sigma = \rho/\rho_0 = v_0/v \qquad (6)$$

When the shock condition arises as a result of impact of a projectile on a target, the different shock front and particle velocities may be established relative to each other after the manner of Ref. 5 as illustrated in Fig. 2. The relative particle velocities add up to the impact velocity,

$$u_{pp} + u_{pt} = V \qquad (7)$$

The impact pressure in projectile and target is assumed uniform in accordance with one dimensional consideration,

$$p_p = p_t \qquad (8)$$

Substituting (4) and (7) leaves only one unknown identified in terms of V. Application of (1) through (4) then identifies other pertinent quantities.

The rarefaction wave propagates at the acoustic velocity of the densified material, given by the slope of the pressure-volume relation in an isentropic process:

$$c^2 = \left(\frac{\partial p}{\partial \rho}\right)_s = -v^2\left(\frac{\partial p}{\partial v}\right)_s \qquad (9)$$

In the p-v diagram the Hugoniot curve, established by the dissipative shock process, is an irreversible adiabat; isentropic expansion from a given point establishes a reversible adiabat which lies above the Hugoniot (Fig. 3). For crystalline metals the relation between the two has been approximately expressed (Ref. 2, 3, 5) using the Mie-Gruneisen equation of state to obtain

$$(p_s - p_H) = \frac{\gamma}{v}(E_s - E_H) \qquad (10)$$

where the Grueisen ratio $\gamma = \gamma(v)$, a property of the material, and all values apply at the specific volume v. At a point p_1, v_1, where the two curves are coincident, (10) leads to the differential expression

$$\left(\frac{\partial p}{\partial v}\right)_H - \left(\frac{\partial p}{\partial v}\right)_S = \frac{\gamma}{v}\left[\left(\frac{\partial E}{\partial v}\right)_H - \left(\frac{\partial E}{\partial v}\right)_S\right] \quad (11)$$

The right hand is identifiable from the Hugoniot equation for conservation of energy

$$(E - E_0)_H = \frac{1}{2} p (v_0 - v) \quad (12)$$

which leads to

$$\left(\frac{\partial E}{\partial v}\right)_H = \frac{1}{2}\left[\left(\frac{\partial p}{\partial v}\right)_H (v_0 - v) - p\right] \quad (13)$$

and the thermodynamic relation which applies on an isentrope,

$$\left(\frac{\partial E}{\partial v}\right)_S = -p \quad (14)$$

Substitution of (13) and (14) in (11) gives the desired acoustic velocity in terms of the slope of the Hugoniot at that point

$$c^2 = -v^2\left(\frac{\partial p}{\partial v}\right)_H\left[1 - \frac{\sigma - 1}{2}\gamma\right] + \frac{pv}{2}\gamma \quad (15)$$

By application to (5) the following convenient forms are derived:

$$\frac{(\partial p/\partial \rho)_H}{c_0^2} = \frac{\sigma + (\sigma-1)S}{[\sigma - (\sigma-1)S]^3} \quad (16)$$

$$\frac{(\partial p/\partial \rho)_S}{(\partial p/\partial \rho)_H} = 1 - \frac{(\sigma-1)^2 S \gamma}{\sigma + (\sigma-1)S} \quad (17)$$

$$\left(\frac{c}{c_0}\right)^2 = \frac{\sigma + (\sigma-1)S - (\sigma-1)^2 S\gamma}{[\sigma - (\sigma-1)S]^3} \quad (18)$$

The structure of the rarefaction wave can be approximately determined by assuming an equation of state for the isentropically expanding material of the form

$$p \doteq A\rho^k \quad (19)$$

For such a material, typical of a polytropic gas, the acoustic velocity is

$$c^2 = (\partial p/\partial \rho)_S = k\,p/\rho \qquad (20)$$

Applying (20) to (18) permits evaluation of the appropriate value of the exponent k at the point where expansion is initiated:

$$k = \frac{\sigma + (\sigma-1)S - (\sigma-1)^2 S\gamma}{(\sigma-1)\left[\sigma - (\sigma-1)S\right]} \qquad (21)$$

The rarefaction process, or at least the high pressure portion of it, initiating at the back face of the bumper can in this way be approximately described by solutions which are available, for example, for the expansion of gas into an evacuated shock tube when the diaphragm is ruptured. From Ref. 6, the pressure, particle velocity, and acoustic velocity in the expanding medium, scale uniformly with time τ, and can be expressed in terms of distance x from the original free surface as follows:

$$\frac{p_r}{p_1} = \left[\frac{2}{k+1} - \frac{k-1}{k+1}\frac{x}{c_1\tau}\right]^{\frac{2k}{k-1}} \quad ; \quad p_1 \geq p_r \geq 0 \qquad (22)$$

$$\frac{u_r}{c_1} = \frac{2}{k+1}\left[1 + \frac{x}{c_1\tau}\right] \quad ; \quad \frac{2c_1}{k-1} \geq u_r \geq 0 \qquad (23)$$

$$\frac{c}{c_1} = \frac{1}{k+1}\left[2 - (k-1)\frac{x}{c_1\tau}\right] \quad ; \quad c_1 \geq c \geq 0 \qquad (24)$$

These relations are illustrated graphically in Fig. 4.

There remains the question of secondary wave generation at the interface between bumper and projectile material, and when the rarefaction wave overtakes the impact shock front. Effects at the interface are governed by the relative acoustic impedance of the two materials (Ref. 10). If the acoustic impedance (ρc)

of the bumper is less than that of the projectile, the rarefaction is reflected in positive fashion, and the rarefaction front advancing into the projectile is strengthened and steepened. This hastens cancellation of the impact pressure and favors projectile penetration. On the other hand, if ρc of the bumper exceeds ρc of the projectile, reflection will be negative and the wave transmitted into the projectile will be weaker. The fraction of incident stress transmitted from material 1 to material 2 is given by the ratio $2(\rho c)_2 / [(\rho c)_1 + (\rho c)_2]$. An example of these effects is given in Fig. 4c. Clearly, if projectile disruption is associated with some critical pressure less than that produced by the impact, bumper materials which have large ρc (generally the denser materials) have a strong advantage.

The extent of mis-match in the calculated pressures when the rarefaction wave overtakes the impact shock front can be explored by comparing the rarefaction wave pressure with the Hugoniot pressure which applies as the relative particle velocity is reduced according to $(u_p - u_r)$. Representative examples are presented in Fig. 4a and b. Differences at the high pressures are strictly secondary, and use of the simple exponential equation of state (19) to predict the initial portion of the rarefaction wave is justified.

The "critical" bumper thickness, established by the requirement that overtaking not begin within the projectile length, is derived by relating the time intervals

$$\tau_{sp} = \tau_{st} + \tau_{rt} + \tau_{rp} \qquad (25)$$

where, with reference to Fig. 3 for relative velocities, the time intervals are

$$\tau_{sp} = L / u_{sp} \; ; \qquad \tau_{rp} = L / \sigma_p c_{1p}$$

$$\tau_{st} = t / u_{st} \; ; \qquad \tau_{rt} = t / \sigma_t c_{1t} \qquad (26)$$

Critical bumper thickness to projectile length is therefore given by

$$\frac{t}{L} = \frac{1/u_{sp} - 1/\sigma_p c_{1p}}{1/u_{st} + 1/\sigma_t c_{1t}} \qquad (27)$$

RESULTS

Calculations have been made to explore the conditions of impact which arise at 20,000 fps (6.1 km/sec) and at 100,000 fps (30.5 km/sec) with a number of combinations of target and projectile materials. A comparison is thus established between typical experimental conditions and typical meteoritic impact conditions. Material properties used in these calculations are summarized in Table 1 and Fig. (5). The results, together with calculated critical bumper thickness values, are presented in Table 2 and 3. To aid in appreciation of the variation in properties of different materials, computations of the acoustic velocity of the densified material have been displayed in graphical form against densification σ in Fig. (6). Figs. (7) and (8) present the calculated critical thickness ratiosfor various combinations with the density of bumper material as an argument.

DISCUSSION

Nature of Results: The display of critical t/L ratios in Figs. (7) and (8) provides a qualitative estimate of bumper performance in disrupting the incident projectile. That the plots of t/L against target density are roughly linear in character indicates that other properties of the target material are of secondary importance. For the projectile, however, two anomalies are noted; both magnesium and tuff (which may be more representative of meteoritic matter than the metals) are indicated as being disproportionately effective in penetrating thin bumpers.

Comparison of the two displays for different impact velocities indicates that velocity interacts with material properties in such a way as to preclude a simple scaling law and to make it extremely difficult to study meteoritic impact effects by means of ordinary hypervelocity tests.

Comparison with Experimental Work of Maiden: Maiden in Ref. (8) presents results of a correlated series of tests of various bumper materials.* While the general trends indicated by the present analysis are in agreement with Maiden's experimental results, the latter indicate much greater effectiveness for high-density bumper materials in reducing witness plate damage than do the calculated critical t/L ratios.

The quantitative differences appear to be due primarily to oversimplification of the analytical model. Projectile break-up, for example, will continue after the head of the rarefaction wave overtakes the shock front. An obvious refinement of the criterion proposed here would be to relate it to a maximum-pressure value which would be cited as a projectile material property or "allowable stress." Secondary wave generation at the projectile-bumper interface would be important in applying this criterion and would favor the denser materials. However, it is also of significance that the experimental results of Ref. (8) are recorded as damage to the witness plate, which involves many other aspects not considered in the analysis, such as damage caused by bumper material, three-dimensional effects, bumper-witness plate spacing, and modifications introduced by mechanical properties, spall effects, and melting. It is therefore difficult to recommend refinement of analytical methods without recognizing an urgent need for experimental effort to determine which aspects of the theory need attention most. It may be necessary to utilize a 3-dimensional hydrodynamic solution of the Bjork variety to achieve acceptable analytical accuracy.

Equation of State: The simplified equation of state with $(\partial E/\partial p)_v$ assumed constant in extrapolating the Gruneisen ratio γ to very high pressures is utilized here as the most suitable of several which were applied. Recent Soviet publications (Ref. 7, 9) indicate that the extrapolation should involve decreasing values of S (a condition which is also obvious from the form of Eq. 5) with γ tending toward a constant value; additional provision is made for thermal pressure. This treatment is in accord with a more gas-like behavior of the highly compressed metals;

*At the time of writing the author was acquainted with Maiden's experimental results, but not with his theoretical treatment.

however, it produces inconsistencies in the current application, in some cases leading to a reversal in slope of the isentrope and a negative value for the calculated acoustic velocity.

Three-Dimensional Effects: The effects which occur off the axis of penetration are of major importance to bumper performance, and the present analysis provides little help here. In a thin bumper the shock front which expands laterally from the penetration axis will be nearly cylindrically symmetric; in a thick bumper, the expanding front will approach spherical symmetry. In either case the intensity of the shock will be degraded with distance, and in peripheral regions the bumper material will be subjected to diminishing severity of pressure. The spray coming off the rear surface of the bumper under a high velocity strike may therefore be expected to be comprised of a central cone of finely divided particles, surrounded by a zone of more chunky bumper debris or spall moving at slower speeds. Striking evidence of such an effect is found in the work of Maiden (Ref. 8).

Increase in the impact velocity is not expected to eliminate the zone of spall but merely increase the angle of divergence; the size and velocity of the spall particles are controlled primarily by physical properties of the bumper material.

This three-dimensional model can be generalized to explain with some success the mixture of spray and debris observed under oblique impact. In this case large particles of bumper spall should be expected at directions approaching the normal to the plane of the bumper.

Bumper Design Considerations: Bumper design must be directed not only at efficiency in breaking up the projectile but at the minimization of bumper spall. These larger fragments, although possibly low in energy, are potentially much more dangerous than the finely divided spray.

Especially objectionable spall fragments are to be expected when the bumper is "too thick" for the size of the incident projectile and is penetrated by the expanding, cratering shock process. However, it does not seem possible to avoid the "too thick" meteoroid bumper by design, because the distribution of meteoroid size is such that whatever mass is selected as the "design meteoroid," many more must be expected at somewhat smaller size. Furthermore, as has been mentioned, peripheral spalling of the bumper material may be an unavoidable part of the bumper process, and spalling may be aggravated by the fact that in service, exposure to oblique impact is in general always greater than normal exposure. These conditions make bumper spall a necessary consideration in design. In many cases, therefore, the simple Whipple bumper plate may need to be augmented with auxiliary spall shielding.

In a multiple plate shield design, the second plate performs a dual function in stopping not only the broadly distributed impulsive loading of the high velocity finely divided spray, but the localized impact of lower velocity spall particles as well. This leads to an optimization problem in spacing and thickness. At present there is a dearth of experimental information on these interaction effects.

CONCLUSIONS

One-dimensional shock mechanics permits estimating the effectiveness of a Whipple bumper in breaking up an incident projectile or meteoroid; and leads to a qualitative design criterion for required bumper thickness. The density of both projectile and target are unquestionably the most important material properties affecting bumper performance. Other properties at extreme pressures, however, influence the performance to a noticeable degree.

The bumper thickness required to effectively destroy an incident projectile of a given size is approximately doubled when the impact velocity is increased from the current experimental range to the meteoritic range. In addition, denser materials appear to have a greater advantage at the meteoritic velocities.

Comparison with experimental results reported in the literature indicates that other aspects of the projectile-bumper-target interaction must be included in the theoretical model before quantitative prediction of performance can be realized.

METEOROID BUMPER DESIGN

Problems involving impact at meteoritic velocity, being beyond the reach of direct experiment, require an advance in analytical capabilities. Experimental effort is needed to develop theoretical tools rather than accumulate empirical data.

Symbols

c	acoustic velocity, cm/μ sec
E	specific internal energy
k	exponent in gaseous equation of state
L	projectile or meteoroid length, cm
p	pressure, megabars
S	material stiffness parameter in Hugoniot eq. of state
t	bumper thickness, cm
u	particle or shock velocity, cm/μ sec
v	specific volume
V	impact velocity, cm/μ sec
x	distance, cm
γ	Gruneisen ratio
ρ	density, grams/cc
σ	relative density = ρ/ρ_o
τ	time, μ seconds

Subscripts

o	initial, at zero pressure
1	end point in shock compression
H	Hugoniot
p	particle, or projectile
r	rarefaction
S	isentropic
s	shock front
t	target or bumper

REFERENCES

1. Humes, D.; Hopko, R.N., and Kinard, W.H., "An Experimental Investigation of Single Aluminum Meteor Bumpers," Proceedings, Fifth Hypervelocity Impact Symposium (1962)

2. Walsh, J.M.; Rice, M.H.; McQueen, R.G., and Yarger, F.L., "Shock Wave Compressions of Twenty Seven Metals. Equations of State of Metals," Phys Review, 108, 196-216 (Oct. 15, 1957)

3. McQueen, R.G., and Marsh, S.P., "Equation of State for Nineteen Metallic Elements from Shock-Wave Measurements to Two Megabars," Jr. App. Physics, 31, 7, 1253-1269 (July 1960)

4. Al'tshuler, L.V.; Krupnikov, K.K.; Ledener, B.N.; Zhuchikhin, V.I., and Brazhnik, N.I., "Dynamic Compressibility and Equation of State of Iron under High Pressure," J. Exptl. Theoret. Phys. (USSR) 34, 874-885 (April 1958), Soviet Phys. JETP 7, 606-614

5. Olshaker, A.E., and Bjork, R.L., "Hydrodynamics Applied to Hypervelocity Impact, I, Scaling Laws," Proceedings, Fifth Symposium on Hypervelocity Impact, 1962

6. Stanyukovich, K.P., Unsteady Motion of Continuous Media, Pergamon Press, 1960

7. Al'tschuler, L.V.; Bakanova, A.A.; and Trunin, R.F., "Shock Adiabats and Zero Isotherms of Seven Metals at High Pressures," J. Exptl. Theoret. Phys. (USSR) 42, 91-104 (Jan. 1962); Soviet Phys. JETP 15, 65-73

8. Maiden, D.J., "Experimental and Theoretical Results Concerning the Protective Ability of a Thin Shield Against Hypervelocity Projectiles," Sixth Hypervelocity Impact Symposium, Session IV, May 1, 1963

9. Al'tschuler, L.V.; Kormer, S.B.; Bakanova, A.A.; and Trunin, R.F., "Equation of State for Aluminum, Copper and Lead in the High Pressure Region," J. Exptl. Theoret. Phys. (USSR) 38, 790-798 (March 1960); Soviet Phys. JETP 11, 573-579.

10. Rinehart, J. S., "Practical Countermeasures for the Prevention of Spalling," AFSWC-TR-60-7, Feb. 1960, (Astia Doc. No. 236719).

TABLE 1 MATERIAL PROPERTIES USED IN ANALYSIS

MATERIAL	DENSITY g/cm^3	REFERENCE ACOUSTIC VEL cm / μ sec	COMPRESSIBILITY FACTOR S	DATA SOURCE
Magnesium	1.735	0.470	1.145	Reduced from Ref (2)
Aluminum	2.785	0.62	1.17	Reduced from (5)
Titanium	4.51	0.478	1.09	Ref (3)
Iron	7.85	0.50	1.33	Reduced from (5) and (7)
Copper	8.90	0.396	1.50	Ref (3)
Lead	11.34	0.203	1.52	Ref (3)
Tungsten	19.17	0.401	1.27	Ref (3)
Gold	19.24	0.306	1.56	Ref (3)
Tuff (compacted volcanic dust)	1.70	0.20	1.19	Reduced from (5)

TABLE 2 IMPACT AT 20000 FPS (6.10 KM/SEC)

MATERIAL		Imp. Pressure P	DENSIFICATION σ'		Crit. Bumper Thick. Ratio
Projectile	Bumper	Megabars	Projectile	Bumper	t/L
Magnesium	Magnesium	0.43	1.59	1.59	0.18
	Aluminum	0.59	1.72	1.35	0.19
	Titanium	0.65	1.77	1.40	0.15
	Iron	0.80	1.88	1.27	0.15
	Copper	0.81	1.86	1.31	0.13
	Lead	0.78	1.84	1.55	0.10
	Tungsten	0.95	1.94	1.22	0.10
	Gold	0.93	1.93	1.28	0.09
Aluminum	Magnesium	0.59	1.35	1.71	0.13
	Aluminum	0.83	1.45	1.45	0.14
	Titanium	0.95	1.50	1.54	0.12
	Iron	1.24	1.59	1.36	0.11
	Copper	1.25	1.59	1.41	0.10
	Lead	1.22	1.59	1.67	0.08
	Tungsten	1.53	1.68	1.31	0.08
	Gold	1.50	1.67	1.39	0.08
Iron	Magnesium	0.81	1.27	1.88	0.20
	Aluminum	1.24	1.36	1.59	0.21
	Titanium	1.50	1.41	1.73	0.19
	Iron	2.17	1.51	1.51	0.19
	Copper	2.37	1.53	1.44	0.18
	Lead	2.24	1.52	1.83	0.15
	Tungsten	3.02	1.61	1.49	0.14
	Gold	2.95	1.61	1.53	0.14
Tungsten	Magnesium	0.95	1.22	1.94	0.25
	Aluminum	1.53	1.31	1.68	0.27
	Titanium	1.93	1.37	1.86	0.25
	Iron	3.02	1.49	1.61	0.25
	Copper	3.17	1.51	1.64	0.25
	Lead	3.20	1.52	1.95	0.21
	Tungsten	4.13	1.63	1.63	0.20
	Gold	4.60	1.63	1.64	0.19

TABLE 3 IMPACT AT 100,000 FPS (30.5 KM/SEC)

Material		Imp. Pressure P	Densification σ		Crit. Bumper Thick. Ratio
Projectile	Bumper	Megabars	Projectile	Bumper	t/L
Tuff	Magnesium	5.55	4.17	3.15	0.51
	Aluminum	7.22	4.35	2.49	0.38
	Titanium	8.33	4.42	2.90	0.30
	Iron	10.7	4.57	2.08	0.26
	Tungsten	13.1	4.65	2.07	0.16
Magnesium	Magnesium	5.57	3.21	3.21	0.37
	Aluminum	7.63	3.43	2.53	0.29
	Titanium	8.85	3.46	2.96	0.23
	Iron	11.3	3.73	2.10	0.21
	Tungsten	13.8	3.94	2.08	0.14
Aluminum	Magnesium	7.63	2.53	3.43	0.32
	Aluminum	10.2	2.73	2.73	0.26
	Titanium	12.1	2.85	3.30	0.21
	Iron	16.2	3.06	2.26	0.19
	Tungsten	20.9	3.20	2.28	0.11
Iron	Magnesium	11.3	2.10	3.73	0.60
	Aluminum	16.2	2.26	3.06	0.51
	Titanium	20.4	2.36	3.82	0.43
	Iron	30.3	2.53	2.53	0.40
	Tungsten	43.4	2.68	2.65	0.26

τ_1 PROJECTILE CONTACTS BUMPER

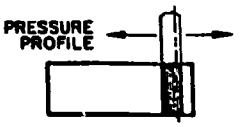

τ_2 SHOCK FRONTS PROGRESS BOTH DIRECTIONS AS PROJECTILE FEEDS IN

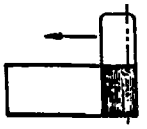

τ_3 SHOCK IN BUMPER REACHES REAR FACE; RAREFACTION INITIATED

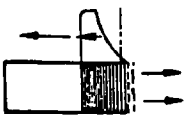

τ_4 RAREFACTION SHATTERS BUMPER MATERIAL; RAREFACTION WAVE ADVANCES INTO PROJECTILE

τ_5 RAREFACTION WAVE OVERTAKES SHOCK WAVE IN PROJECTILE, REDUCES IMPACT PRESSURE

τ_6 IMPACT EFFECT GREATLY DIMINISHED; BUMPER AND SOME OF PROJECTILE SHATTERED

τ_7 SHOCK AND RAREFACTION EFFECTS DEGENERATE TO NORMAL COMPRESSION SHOCK WAVE

τ_8 SHOCK REACHES PROJECTILE REAR FACE, DISSIPATES IN SPALL. CENTRAL PORTION OF PROJECTILE CONTINUES UNHINDERED

FIG 1 PROJECTILE-BUMPER INTERACTION-SCHEMATIC

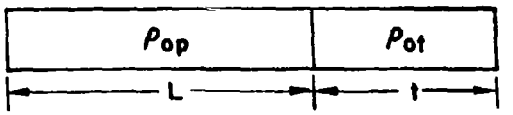

a PROJECTILE AND BUMPER AT INSTANT OF CONTACT

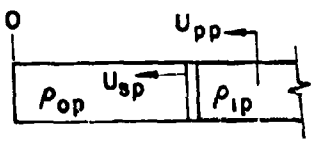

b SHOCK IN PROJECTILE

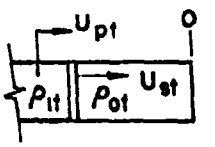

c SHOCK IN BUMPER

d PARTICLE AND SHOCK FRONT VELOCITIES REFERRED TO ZONE OF Ddensified MATERIAL

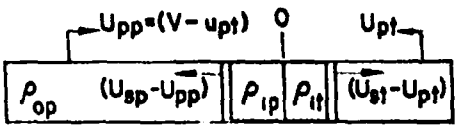

e SHOCK FRONT IN BUMPER REACHES BUMPER REAR FACE

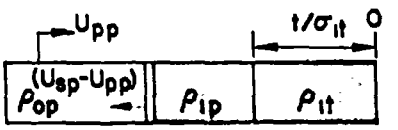

f RAREFACTION WAVE REFERRED TO ZONE OF DENSIFIED MATERIAL

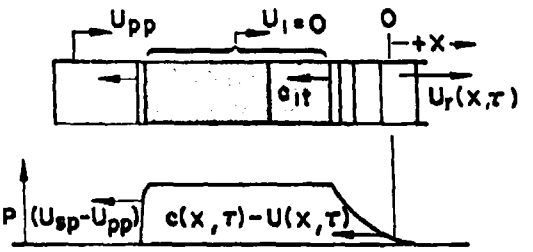

FIG. 2 PARTICLE AND WAVE FRONT VELOCITIES

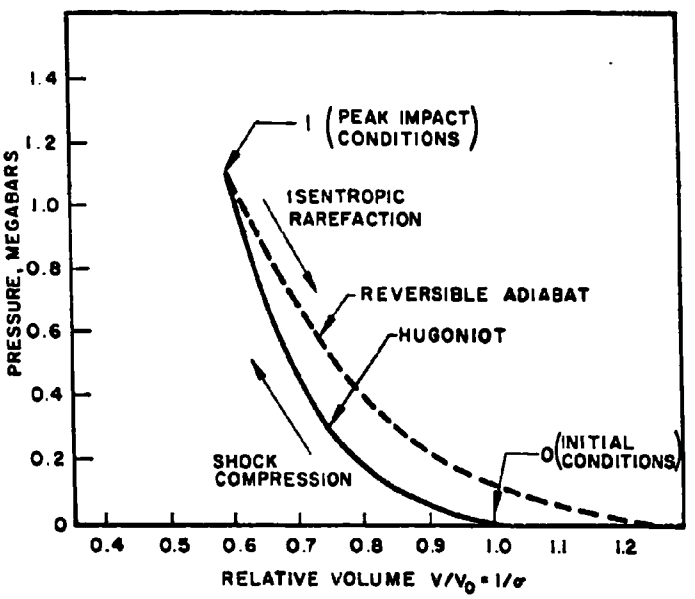

FIG 3 TYPICAL ADIABATIC PROCESSES
(SHOWN FOR LEAD, FROM REF. 2)

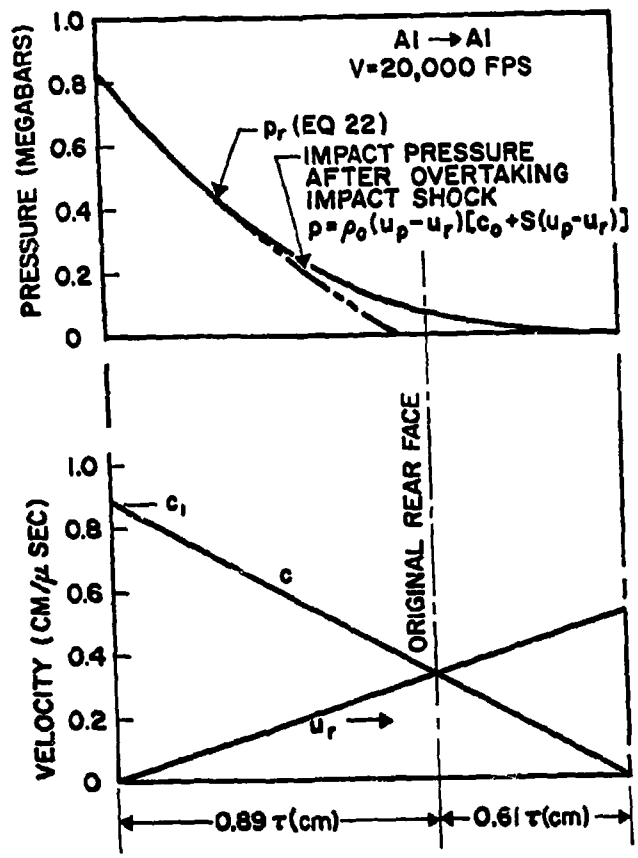

FIG 4 RAREFACTION WAVE IN ALUMINUM AFTER IMPACT BY ALUMINUM, APPROXIMATED USING $p_r = A\rho^k$

a. IMPACT VELOCITY V = 20,000 FPS, k = 3.9

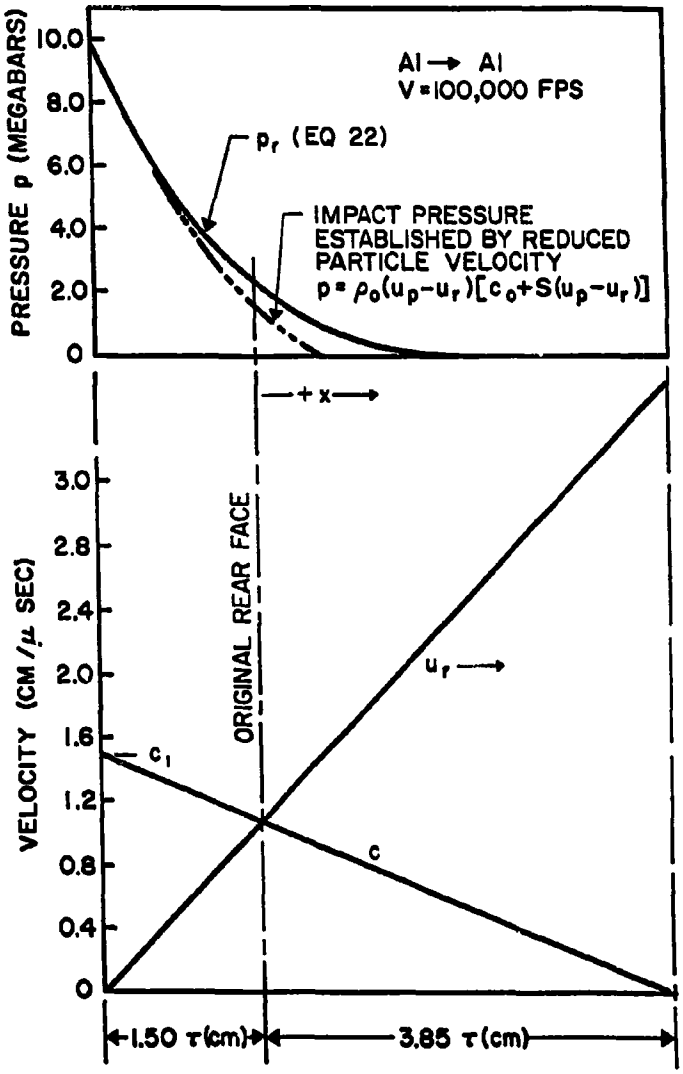

FIG 4 RAREFACTION WAVE IN ALUMINUM AFTER IMPACT BY ALUMINUM, APPROXIMATED USING $p_r = A\rho^k$

b. IMPACT VELOCITY V = 100,000 FPS, k = 1.8

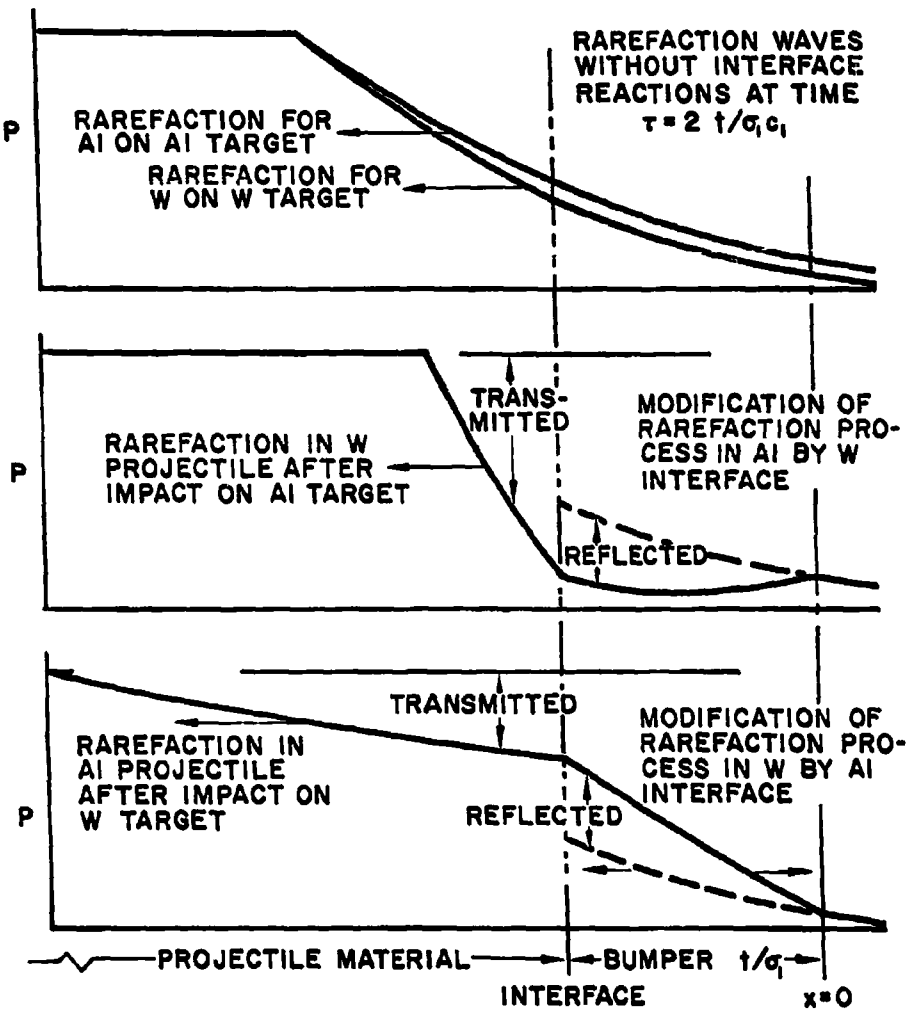

FIG. 4C EFFECT OF DISSIMILAR MATERIALS ON RAREFACTION WAVES TRANSMITTED ACROSS INTERFACE (ANALYSIS BY METHODS OF REF. 10, FOR V=20,000 FPS)

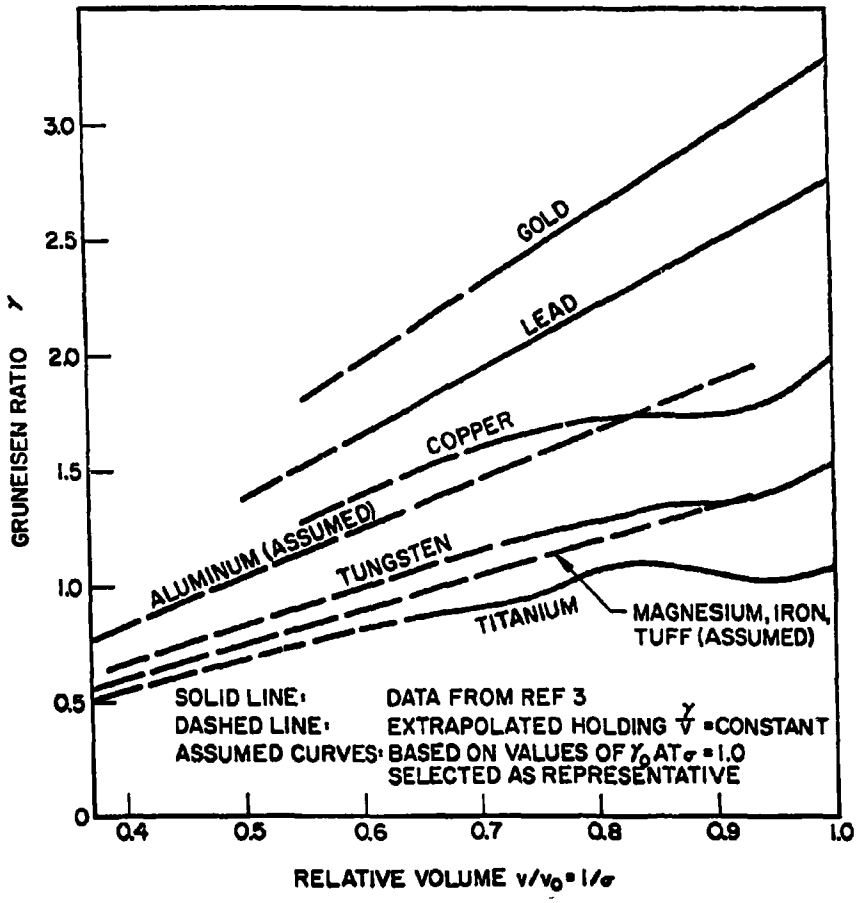

FIG 5 VALUES OF THE GRUNEISEN RATIO γ USED IN THE CALCULATIONS

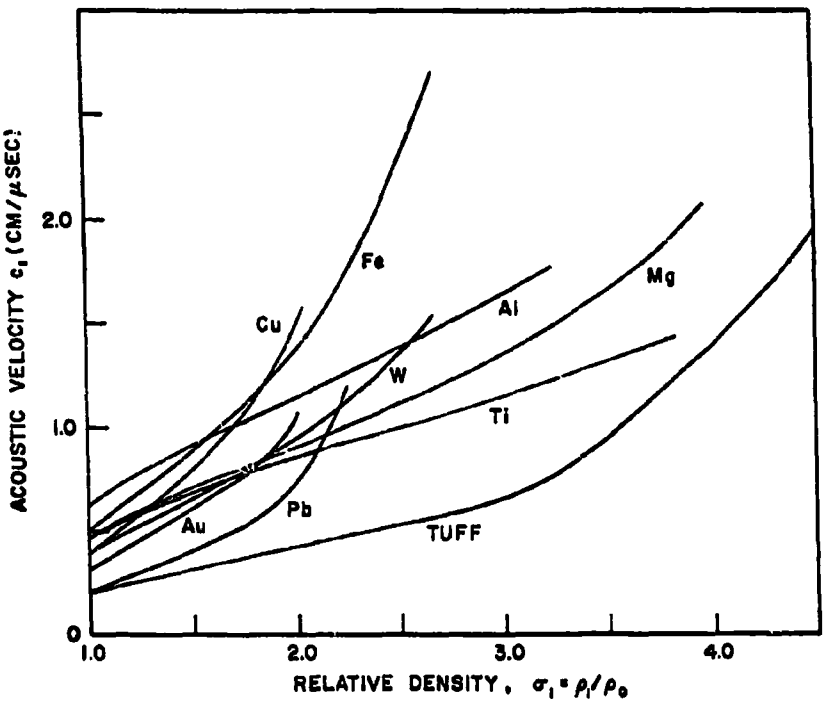

FIG. 6 CALCULATED SPEED OF THE HEAD OF THE RAREFACTION WAVE IN VARIOUS MATERIALS

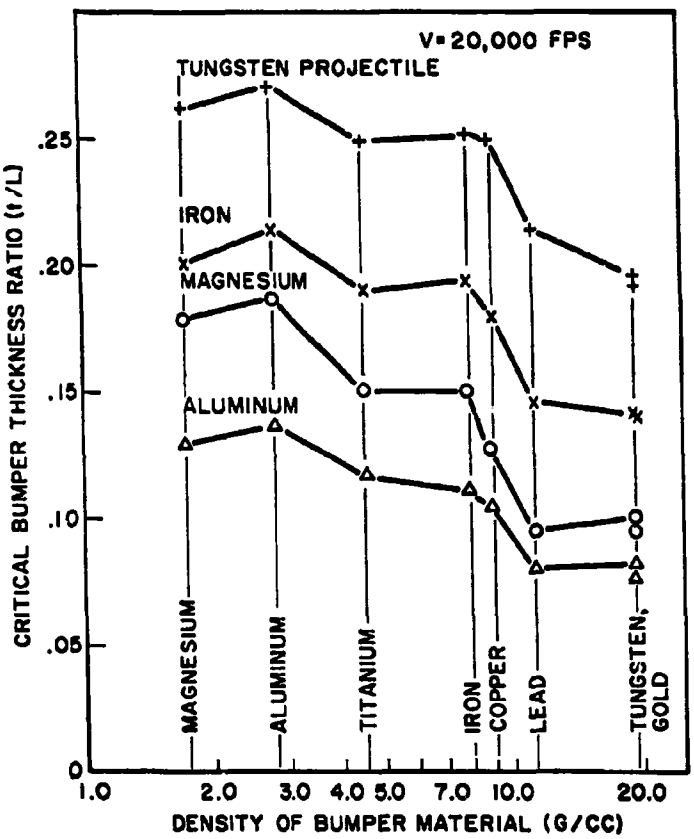

FIG. 7 CALCULATED CRITICAL BUMPER THICKNESS RATIO FOR PROJECTILES IMPACTING VARIOUS MATERIALS AT V= 20,000 FPS (6.10 KM/SEC)

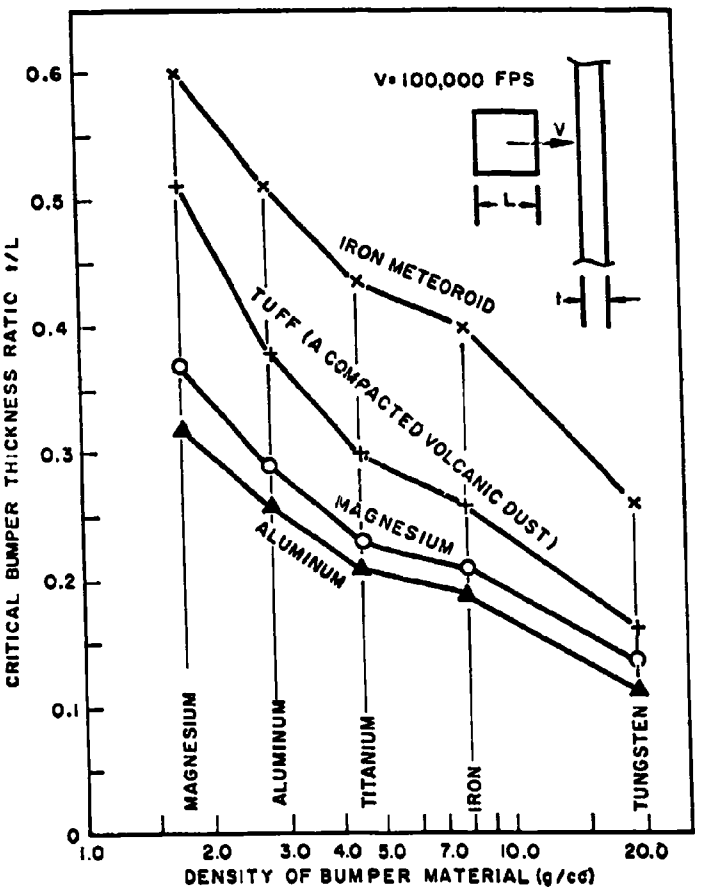

FIG 8 CALCULATED CRITICAL BUMPER THICKNESS RATIO FOR PROJECTILES IMPACTING VARIOUS MATERIALS AT V=100,000 FPS (30.5 KM/SEC.)

EXPERIMENTAL AND THEORETICAL RESULTS CONCERNING THE PROTECTIVE ABILITY OF A THIN SHIELD AGAINST HYPERVELOCITY PROJECTILES

by C. J. Maiden

Technical Specialist

GM Defense Research Laboratories

General Motors Corporation

Santa Barbara, California

PROTECTIVE ABILITY OF THIN SHIELD

1. INTRODUCTION

Several years ago Whipple[1] proposed that a spacecraft could be protected against meteoroids by a thin shield spaced at a distance from the main hull of the vehicle. The present paper presents some results from a theoretical and experimental program to investigate the protective value of such a shield against hypervelocity projectiles. This work is sponsored by ARPA's Project Defender under contract number Nonr 3891 (OO) (X).

The sequence chosen for the present paper is to describe the experimental and theoretical results separately, and then to compare theory and experiment.

2. EXPERIMENTAL TECHNIQUES

All experiments were conducted using the Ballistic Range facility[2] of the GM Defense Research Laboratories, General Motors Corporation. This facility consists of a 5.6 mm caliber light-gas gun, a 6.1 meter long flight range and an impact chamber. The performance of the gun is such that 10 km/sec has been achieved

with a 0.07 gm plastic cylinder, 8.7 km/sec with a saboted 3.2 mm diameter aluminum sphere, and 7.3 km/sec with a 4.8 mm aluminum sphere. The range can be evacuated, and the velocity and condition of the model obtained from spark shadowgraph stations. The model flight is terminated in the impact chamber where the shield and target can be held a fixed distance apart. The impacts can be observed with a three channel flash X-ray unit (flash duration of 0.07 μ secs), and with a Beckman-Whitley framing camera (1.4 million frames per second).

3. EXPERIMENTAL RESULTS

3.1 Impacts in Unprotected Targets

The protection afforded by a shield against a hypervelocity projectile can be measured by comparing the damage produced in protected and unprotected targets. Thus, in order to make this comparison, tests were conducted using 3.2 mm aluminum spheres and unprotected targets of 2024-T3 and 1100 F aluminum. The results of the experiments, plus several popular damage relationships[3][4][5][6], are shown in Figures 1, 2, and 3. Figure 1 shows results corresponding

to targets of 2024-T3 aluminum. Figure 2 presents results for targets of 1100 F aluminum and Fig. 3 compares the two sets of experimental data. It should be noted that the results for 1100 F aluminum include data obtained by Atkins[7].

Although it is digressing somewhat from the main theme of this paper, it is informative to discuss a number of interesting features of the above figures. Firstly, the empirical relationships of Charters and Summers, Eichelberger and Gehring, and Herrmann and Jones, all agree with the experimental data to within a factor of two. This is not too surprising as these empirical equations were derived by curve fitting to experimental measurements. Also, of the empirical relationships, that of Herrmann and Jones shows the best agreement with Bjork's theoretical points. Herrmann and Jones consider that this agreement is encouraging, but rather fortuitous. Unfortunately, the experimental data are limited to velocities less than 10 km/sec, so no firm statement can be made concerning the validity of any of the damage formula at higher velocities than this. Another interesting point is that, even though the experimental data for the two aluminum alloys are substantially different, there is an indication that the spread between the two sets of data becomes less as the velocity

increases. This question of the importance of target strength as the impact velocity increases, has caused a great deal of controversy and is, as yet, unresolved. However, it is obvious that strength effects still exert a considerable influence on the cratering process at 10 km/sec.

3.2 Impacts in Protected Targets

Several sets of diagnostic experiments were conducted in which only one parameter was varied at a time. The results of these experiments are now described.

3.2.1 The Effects of Shield Thickness

Figures 4(a) and (b) show the damage suffered by targets placed behind aluminum (2024-T3) shields of various thicknesses. The projectiles were 4.8 mm aluminum spheres at 6.1 km/sec, and the targets were 6.4 mm thick aluminum (2024-T3) plates spaced at 5.48 cms. from the shields. It is seen that with the two thinnest shields (0.076 and 0.204 mms) the backup target is completely penetrated. With the medium-thickness shields (0.408 and 0.816 mms) a spall is detached, and with the thickest shields (1.632 and 3.17 mms)

the only damage is to the front of the targets. From these tests the total depth of penetration, including shield thickness but excluding spall effects, has been determined and is shown as Curve A in Figure 5(a). This figure shows that there is an optimum shield thickness for minimum damage. For the impact conditions relevant to the above tests, this optimum is such that the ratio of shield weight per unit area to projectile weight per unit area (hereafter called shield to projectile weight per unit area) is approximately 0.25 to 0.5. Note that in Fig. 5(a), Curve B refers to the thickness of shield penetrated and Curve C refers to the depth of penetration in the main target only. Thus Curve A is the sum of Curves B and C.

Figure 5(b) presents spray angles Θ for the present tests. The spray angle Θ is defined here as $\Theta = \tan^{-1} \frac{D_t}{2S}$, where D_t is the relevant diameter of damage on the backup target and S is the spacing between shield and target. However, Fig. 4(a) shows that it is very difficult to define one meaningful diameter of damage on the targets. For this reason two curves are presented in Figure 5(b). Curve A is an estimate of the spray angle in which all the fragments are confined; and Curve B represents spray angles calculated using the diameter of the area in which no undamaged portion of the original target surface can be observed between craters. The absolute accuracy of the above curves is questionable, however, there is an indication

that the two curves get closer as the shield thickness increases. This indicates that, as the shield becomes thicker, a more complete and uniform fragmentation of the projectile occurs.

A similar series of tests to the above were conducted using various thickness copper shields. The projectiles were again 4.8 mm aluminum spheres at 6.1 km/sec. In these tests the protective mechanism of the shields was studied using flash X-ray techniques. Some results are shown in Fig. 6 and it is seen that, if the shield is sufficiently thick, an expanding bubble of fragments merges from behind the shield. Not only are the fragments spread over a large area, but also, the velocity component normal to the shield of many of the fragments is significantly reduced below the velocity of the original projectile. Both these factors result in a protected target having less momentum and energy per unit area applied to it than would an unprotected target. Figure 6 also shows that as the shield becomes thinner the spread of fragments decreases slightly and there is less variation in velocity, normal to the shield, among the fragments. The shield thus becomes increasingly ineffective.

3.2.2 The Effects of Shield Material

Given a specific weight shield, is there any preference in the material from which the shield is to be manufactured? Experiments

were conducted to help answer this question. In these experiments the projectiles were 4.8 mm aluminum spheres at 6.1 km/sec, the main targets were 6.4 mm thick aluminum (2024-T3) sheets, and the spacing between shields and targets was 5.48 cms. Tests were conducted at shield weights per unit area (W) of 0.113, 0.226 and 0.452 gms/cm^2 using shields of magnesium (AZ31B-F), aluminum (2024-T3), titanium, copper (OFTP) and gold (24 carat). Unfortunately, it was not possible to obtain all the shield materials in the exact required thicknesses. However, the differences were felt to be sufficiently small not to influence the results significantly.

The front and rear of the impacted targets are shown in Figures 7(a) and (b). In each figure the bottom, middle, and upper rows of targets correspond to shield weights of 0.113, 0.226, and 0.452 gms/cm^2, the shields are almost equally effective. However, for the two other shield weights the effectiveness of the shields increases from magnesium to gold. From damage graphs (not shown) similar to that shown for aluminum in Fig. 5 it is found that the optimum shield (excluding spall effects) of those tested is the 0.15 mm thick gold shield. This shield corresponds to a shield to projectile weight per unit area of 0.35.

The diameter of holes produced in the various shields are shown in Figure 8. It is seen that, for a specific shield material, the hole

diameter increases with shield thickness. Also, for a specific weight shield, the hole diameter decreases as the shield material is changed from magnesium to titanium, and then remains fairly constant for higher density shield materials.

3.2.3 The Effect of Shield Strength

Three further tests were conducted using 4.8 mm aluminum spheres at 6.1 km/sec, 6.4 mm thick aluminum (2024-T3) target plates, and a spacing of 5.48 cms between the shields and targets. The shields were all 0.81 mm thick and made of 2S-O, 2024-T3 and 7075-T6 aluminum alloys. The handbook strength properties of these alloys are as follows:

Alloy	2S-O	2024-T3	7075-T6
Tensile Strength (dynes/cm^2)	9×10^8	48×10^8	57×10^8
Yield Stress (dynes/cm^2)	3.5×10^8	35×10^8	50×10^8
Elongation (%)	45	18	11
Hardness (Brinell)	23	120	150
Shear Stress	6.5×10^8	28×10^8	33×10^8

It is seen that, 2S-O aluminum is much weaker than 2024-T3 and 7075-T6 aluminum alloys which are fairly similar in strength properties.

The impacted targets are shown in Figs. 9 (a) and (b) and it is seen that the gross features of target damage are not very dependent upon shield strength. The major difference in the results is that the individual craters on the targets are largest with the least brittle aluminum shield (2S-O), and smallest with the most brittle shield material (7075-T6).

3.2.4. The Effect of Impact Velocity

How does the effectiveness of a shield vary with velocity? In an endeavor to help answer this question the results of Fig. 10 were obtained. Figure 10 (a) shows the total penetration as a function of impact velocity for aluminum spheres impacting protected and unprotected aluminum (2024-T3) targets. The curve for the unprotected target was taken from Figure 1. The protected target results were obtained using 0.81 mm thick aluminum (2024-T3) shields and a ratio of shield to projectile weight per unit area of 0.375. It is seen that, up to about 2.5 km/sec, the total depth of penetration with the shield is slightly more than the penetration in the unprotected target. Apparently, at these velocities it is easier to perforate the shield than to penetrate an equal distance into the main target. However,

as the velocity is increased above 2.5 km/sec the shield becomes more and more effective. Some understanding of what is happening as the impact velocity increases can be obtained from the results of Figures 10 (b) and (c). Figure 10 (b) shows some of the backup targets and Fig. 10 (c) presents the spray angles Θ defined in the same manner as in Section 3.2.1. These figures show that very incomplete fragmentation of the projectile occurs until a velocity of 2.5 to 4.5 km/sec is reached. As the impact velocity is increased above this value, more uniform and complete fragmentation of the projectile occurs. This is reflected in the fact that Curves A and B in Fig. 10 (c) get closer as the impact velocity is increased; also, the total depth of penetration in Fig. 10 (a) becomes less.

The ratio of shield to projectile weight per unit area of 0.375 used in the present tests was chosen on the basis that it was near the optimum ratio for minimum total damage in Figure 5 (a). It is of interest to consider what the curve of total penetration will look like for other shield thicknesses. With regard to this, the curve representing penetration in a semi-infinite target in Fig. 10 can be looked upon as being the result for a very thick or negligibly thin shield. In the former case, the projectile will not penetrate the shield, and in the latter case, the shield will be completely ineffective. The

optimum shield thickness for minimum total damage will be somewhere in between these extremes, and may vary with velocity. Thus, although the 0.81 mm shield used in the investigation is near optimum at 6.1 km/sec, it may not be the best shield at other velocities. This point is discussed later in light of the theoretical results.

4. THEORETICAL CONSIDERATIONS

4.1 Theoretical Model

Consider a right-circular cylinder impacting a thin shield. The estimated wave pattern shortly after impact is shown schematically in Figure 11 (a). Two shock waves S_1 and S_2 have propagated away from the interface (I). The fact that the projectile is finite in diameter is transmitted towards the axis of symmetry as rarefaction waves R_1 and R_2. Also the formation of these rarefactions has resulted in the ejection of both projectile and shield material in a rearward direction (see Figure 6). Now consider the situation shortly after the shock S_2 has reflected from the back face of the shield (Figure 11 (b)). To satisfy the boundary condition of zero pressure, the shock is reflected as a rarefaction wave R_3. The resultant particle

velocities behind R_3 are such that the profile of the back face of the shield will be as shown in the figure. As the process continues the bubble grows due to the addition of material from both the shield and projectile. From a physical viewpoint the rarefaction R_1, R_2 and R_3, generated to satisfy boundary conditions, can be looked upon as tension waves. Hence, fracture will occur if at any point in the projectile or shield the net tensile stress exceeds the fracture strcss of the material. Also, rarefactions will be produced to satisfy boundary conditions at any new fracture surfaces, and these can lead to the occurrence of further fractures. Thus, the whole process of fracture of a projectile and shield can be interpreted as a multiple spalling phenomenon which starts at the free surfaces (see Figure 6).

Complete details of the flow fields illustrated in Figure 11 can, in principle, be determined if the process is assumed to be an unsteady, non-viscous, compressible fluid flow problem. Such an approach is somewhat limited, in that strength effects are ignored in the analysis. The present study considers several significant aspects of the problem. In this way, it is hoped to be able to obtain an understanding of the essential features of the phenomena

for a wide range of materials and impact conditions.

4.2 One-Dimensional Considerations

4.2.1 Maximum Impact Pressure

The flow between the shocks S_1 and S_2 is one-dimensional until reached by rarefactions R_1 and R_2. The situation in this one-dimensional region immediately after impact is shown in Figure 12. In this figure, and in the subsequent analysis, all velocities are measured with respect to a set of co-ordinates fixed in the shield. The following symbols are used:

v_o = impact velocity

v_1 = velocity of material between shocks

U_1 = velocity of shock S_1 in projectile

U_2 = velocity of shock S_2 in the shield

P_1 = pressure in region between the shocks

ρ_o = density of uncompressed projectile material

ρ_1 = density of projectile material at pressure P_1

q_o = density of uncompressed shield material

and q_1 = density of shield material at pressure P_1

Use of the normal shock relationships across each shock,[8] plus continuity considerations at the interface, produce the following equations:

$$P_1 = \frac{\rho_0 V_0^2}{1 - \frac{\rho_0}{\rho_1}} \left[1 + \left\{ \frac{\rho_0 \left(1 - \frac{\rho_0}{\rho_1}\right)}{\rho_0 \left(1 - \frac{\rho_0}{\rho_1}\right)} \right\}^{1/2} \right]^{-2} \quad (1)$$

$$V_1 = V_0 \left[1 + \left\{ \frac{\rho_0 \left(1 - \frac{\rho_0}{\rho_1}\right)}{\rho_0 \left(1 - \frac{\rho_0}{\rho_1}\right)} \right\} \right]^{-1} \quad (2)$$

$$U_1 = \frac{V_0 - \frac{\rho_1}{\rho_0} V_1}{\frac{\rho_1}{\rho_0} - 1} \quad (3)$$

and

$$U_2 = \frac{V_1}{\frac{\rho_1}{\rho_0} - 1} \quad (4)$$

To solve a specific example, two more equations are necessary. These are the Hugoniot equations for the projectile and shield materials.

From the above equations the parameters P_1, U_1, etc. have been calculated for the case of aluminum projectiles and shields of magnesium, aluminum, titanium, copper and gold. These materials correspond to those used in the experiments described in Section 3 of this paper. Velocities of 4.9, 6.1, 7.6, 9.2, and 15.2 km/sec have been used in the calculations. Higher velocities were not considered due to the lack

of Hugoniot relationships at the pressures concerned. Figure 13 shows the Hugoniot curves used in the present investigation. The curves for aluminum, copper and gold represent a combination of United States [9, 10] and Soviet data [11, 12] up to pressures of 2 to 5 megabars. The data for magnesium and titanium was obtained from reference 9 but is limited to pressures below 2 megabars. To permit calculations for impact velocities up to 15.2 km/sec, the latter curves were extrapolated linearly as shown in Figure 13. This extrapolation seems reasonable as the experimental curves are very nearly linear on a log-log plot. The results of the calculations are presented in Figures 14 (a) - (d). It is seen in Fig. 14 (a) that the impact pressure P_1, at a fixed impact velocity, increases as the shield material is varied in the order magnesium, aluminum, titanium, copper and gold. Also, Figure 14 (b) shows the shock velocity in the projectile and reveals how, in some cases, the shock wave never gets above the surface of the shield. This figure and Figs. 14 (c) and (d) indicate that the parameters U_1, V_1 and U_2 vary in an approximately linear manner with v_o.

Now consider the general case in which the projectile material and impact pressure P_1^* (and thus ρ_1) are fixed. Let the independent

variables be v_o, q_o and q_1. Equation (1) then indicates that the impact velocity v_o, necessary to generate the pressure P_1, becomes less as the parameter $\frac{q_o}{1 - \frac{q_o}{q_1}}$ increases. This parameter has been calculated from reference (10) for 28 metals at a pressure of 500 Kbars, and the values are listed in decreasing order in Table I. Unfortunately, no such extensive data is available at higher pressures; so, for purposes of discussion, it is assumed that the order of Table I applies at all pressures. With this assumption, some consideration shows that the following conclusion can be drawn. For a fixed projectile and velocity, the pressure P_1 decreases as the shield material is changed in the sequence of Table I. The results of Figure 14 (a) are consistent with this conclusion. Obviously, to obtain a high impact pressure, a shield material of high density and low compressibility is required. Also, it can be shown from Eqs. (1) - (3) that, for a fixed projectile and velocity, the velocity v_1, increases and the velocity U_1 decreases as the shield material is changed in the sequence of Table I.

4.2.2 The Effect of Shield Thickness

Figure 11 (b) shows the situation after the shock in the shield has reflected as a rarefaction wave R_3. The flow in the volume that has

not been reached by the rarefactions R_1 and R_2 is one-dimensional and is represented on an x-t diagram in Figure 15. The shock S_2 is assumed to reflect as a centered rarefaction R_3 from the back of the shield. The leading edge of this rarefaction travels at velocity c_{q_1} relative to the shield material (which is moving at velocity v_1), where c_{q_1} is the speed of sound in the shield material at pressure P_1. Also, when the rarefaction reaches the interface (I), a reflected and transmitted wave are produced. The transmitted wave is a rarefaction R_4 with the leading edge traveling at velocity c_{ρ_1}, relative to the projectile material moving at velocity v_1. Here again c_{ρ_1} represents the speed of sound in the projectile material at pressure P_1. Note that if the projectile and shield are made of the same material then no reflected wave is produced at the interface.

If the shield is sufficiently thin, the rarefaction R_4 can overtake and weaken the shock in the projectile. It can be shown that the leading edge of the rarefaction overtakes the shock at a point in the projectile given by

$$\ell = t_s \left(\frac{c_{q_1} + u_2 - v_1}{c_{\rho_1} - u_1 - v_1} \right) \left(\frac{c_{\rho_1}}{c_{q_1}} \right) \left(\frac{u_1 + v_0}{u_2} \right) \quad (5)$$

where ℓ is measured from the front face of the uncompressed projectile and t_s is the shield thickness. Thus the fraction of the original projectile length L_s on the axis of symmetry, that experiences the peak impact pressure P_1 is given by

$$\frac{\ell}{L} = w \frac{\rho_0}{\rho_0} \left(\frac{c_{q_1} + u_2 - v_1}{c_{\rho_1} - u_1 - v_1} \right) \left(\frac{c_{\rho_1}}{c_{q_1}} \right) \left(\frac{u_1 + v_0}{u_2} \right) \qquad (6)$$

where $w = \dfrac{\rho_0 t_s}{\rho_0 d} = \dfrac{\text{weight of shield/unit area}}{\text{weight of projectile/unit area}}$

In order to calculate $\frac{\ell}{L}$ from Eq. (6), it is necessary to know the relevant speeds of sound c_ρ and c_q for the materials concerned. If the equations of state of the materials are known then the speeds of sound can be found from the relationship

$$c^2 = \left(\frac{\partial P}{\partial \rho} \right)_S \qquad (7)$$

where S denotes differentiation at constant entropy. Unfortunately, even though the Hugoniots of many materials are known, their equations of state are not available. However, the Soviets[13] have measured values of c for several materials and indicate that, for metals up to about 5 megabars, a reasonable approximation for the speed of sound at pressure P behind a shock is given by

$$c_p = D \left[0.49 + \left(\frac{D - v}{D} \right)^2 \right]^{1/2} \qquad (8)$$

where D is the shock velocity relative to a pressure P, and v is the particle velocity behind the shock. In this equation, both these velocities must be measured relative to the undisturbed material considered at rest. Thus, in the coordinates of Fig. 12, $D = U_2$ and $v = v_1$ for the shield material, and $D = U_1 + v_o$ and $v = v_o - v_1$ for the projectile material. Hence, from Eq. (7) and the data of Fig. 14, the speeds of sound of magnesium, aluminum, titanium, copper, and gold have been calculated as a function of pressure (and thus density). The results are presented in Fig. 16, and have been used, with the data of Fig. 14, to calculate values of $\frac{\perp}{w}\frac{\ell}{L}$ from Equation (6). These results are shown in Fig. 17 and show that, for the same projectile, impact velocity, and value of w, the rarefaction R_4 overtakes the shock in the projectile more rapidly as the shield material is altered in the order magnesium, aluminum, titanium, copper, and gold. Also, for a fixed projectile and shield, the shock in the projectile is overtaken more rapidly as the impact velocity increases.

4.2.3 The "Slowest" and Fastest Fragment Velocities

PROTECTIVE ABILITY OF THIN SHIELD

Now consider in Fig. 11 the free surfaces of the projectile and shield at the ends of the axial stream tube. The fragments produced from these points represent extremes of fragment velocity towards the target. In order to assess the velocity of these fragments the assumption is made that, when a shock corresponding to a particle velocity v and pressure P reflects at a free surface, the surface is accelerated to a velocity 2v. This assumption is discussed in Reference 9 and is considered to be reasonable up to shock pressures of a few megabars. For higher pressures, Bull [14] has postulated that after shock reflection, the surface material will be gaseous and will move at escape velocity ($\frac{2}{\gamma-1}\, c_\ell$). However, the present theoretical discussion limits itself to spall velocities near those attained in the experimental part of the program, and the 2v reflection law is thought to be adequate. Certainly, Fig. 6 shows that in the present experiments the spray is fragmentary in nature rather than gaseous. Note that the 2v reflection law can be interpreted as being made up of a contribution v from the shock and a contribution v from the reflected rarefaction. This latter contribution implies that sudden release from a pressure P adds a velocity component v perpendicular to a free surface.

PROTECTIVE ABILITY OF THIN SHIELD

First, consider the fragment of projectile that does least damage to the target. This fragment originates from the center of the back surface of the projectile and will be referred to as the "slowest" fragment. If the shock S_1 reaches the rear of the projectile without being overtaken by rarefaction R_4 (or R) then, by the assumed reflection law, this slowest fragment will travel at a velocity $2v_1 - v_o$ towards the target. This velocity has been plotted in Fig. 18 for the previous example of aluminum projectiles and various shield materials. It is seen that, for a magnesium shield the slowest fragment moves towards the target, for an aluminum shield the fragment is brought to rest, and for titanium, copper, and gold the slowest fragment moves away from the main target. Note that the above calculation assumes that, at reflection, the segment of shock S_1 on the axis of symmetry is planar (this point is discussed more fully in the next section).

Figure 18 was plotted on the supposition that an unweakened shock S_1 reflects from the rear of the projectile. However, if the shield is thin enough, the rarefaction R_4 will overtake the shock S_1 at a point in the projectile given by Equation (6) (also Figure 17). As this rarefaction interacts with the shock, the pressure behind it is progressively decreased. Also, the particle velocity v_1' behind the shock

(measured in the co-ordinate system of Fig. 11) is progressively increased. Thus, upon reflection, the velocity of the slowest fragment, which is now given by $2v_1' - v_o$ (instead of $2v_1 - v_o$), increases as the shield is made thinner. As the shield thickness tends to zero, v_1' approaches v_o and the velocity of the fragment tends to the original projectile velocity. Note that, in the above discussion, it has been assumed that the velocity of the slowest fragment is not affected by the fracture process.

Now consider the velocity of the fastest fragment. This fragment originates from the bottom surface of the shield at a point on the axial steamtube. By the assumed reflection law this element of surface is accelerated to a velocity $2v_1$ when the shock S_2 reflects as rarefaction R_3. The variation in the velocity can be seen from Fig. 14 (d) for the case of aluminum projectiles and various shield materials. It must be remembered that this velocity only refers to the initial motion of the surface. The final velocity of this element of surface will be determined by the ensuing wave motion in the shield. Three cases can be qualitatively discussed. First, if the shield and projectile materials are alike, then the rarefaction R_3 does not interact with the interface, and the axial element of the shield is accelerated by the initial shock reflection to the initial projectile velocity. Secondly, as a rough guide,

if the shield material is less dense than the projectile material (say aluminum impacting magnesium) the rarefaction R_3 interacts with the interface to produce a reflected rarefaction wave in the shield. This rarefaction in turn reflects from the free surface as a compression wave and so the process of wave reflection between the back of the shield and interface continues. The net result of this process is to reduce the velocity of the surface to a value less than $2v_1$. The third and final situation roughly corresponds to the case where the shield material is more dense than the projectile material. In this case the rarefaction R_3 interacts with the interface to produce a reflected compression wave in the shield. Once again multiple wave reflection occurs between the back of the shield and the interface. This process increases the velocity of the axial surface element to a value greater than $2v_1$. Note that using the density ratio of the shield to projectile material in order to differentiate the above three cases is not strictly accurate, but suffices to indicate trends. Also, note that the above behavior only applies for the period of time before the rarefaction R_2 reaches the axis of symmetry. If this rarefaction reaches the axis before the shock S_2 reflects from the back of the shield then the initial velocity of the axial element of shield surface is no longer $2v_1$. The following section shows that this occurs when $t_s \geq 0.72\, d$. For this case the shock decays due to divergence, and the greater the decay, the more

the velocity of the fastest fragment will be reduced. In the limit, if the shield is thick enough, no spall will be produced.

4.3 Three-Dimensional Effects

4.3.1 Effects of the Finite Projectile Diameter

In previous sections of this paper, conditions on the axis of symmetry in Fig. 11 have been calculated using one-dimensional considerations. It is of interest to discuss the limitations of such calculations.

It was shown in Section 4.2.2 that the shock S_1 in the projectile can be weakened by interaction with the rarefaction R_4 from the back of the shield. Figure 11 shows that the shock in the projectile is also weakened by interaction with the axially symmetric rarefaction R_1. This rarefaction originates at the circumference of the initial area of impact. In the case where this rarefaction overtakes the shock S_1 on the axis of symmetry before rarefaction R_4, it will travel at the speed of sound c_{ρ_1} relative to the one-dimensional region. In this case it can be shown that the rarefaction R_1 just meets the shock S_1 on the axis of symmetry at a point in the projectile given by

$$\ell_1 = \frac{d}{2} \frac{u_1 + v_0}{\left[c_{\rho_1}^2 - (u_1 - v_1)^2\right]^{1/2}} \qquad (9)$$

where ℓ_1 is measured from the front face of the initially uncompressed projectile. Substitution in Eq. (9) of c_{ρ_1} from Eq. (8) (with $D = U_1 + v_o$ and $v = v_o - v_1$) yields

$$\ell_1 = 0.72\, d \tag{10}$$

This relationship is seen to be independent of material and impact velocity, and defines the maximum length of projectile, on the axis of symmetry, which can feel the full impact pressure P_1. Similarly, it can be shown that the rarefaction R_2 in the shield just meets the shock S_2 on the axis of symmetry at a point in the shield given by

$$\ell_2 = 0.72\, d \tag{11}$$

where ℓ_2 is measured from the upper surface of the undisturbed shield. Thus, this equation defines the maximum thickness of shield, on the axis of symmetry, which can feel the full impact pressure P_1. Also if $t_s < \ell_2$ the side rarefaction never meets the axial segment of the shock S_2 before it reflects from the back of the shield.

Now consider the one-dimensional calculation of Section 4.2.2 which determines the point where the rarefaction R_4, from the back of the shield, overtakes the shock S_1 in the projectile. The results apply to the axial streamtube, and are correct provided the axial segment of

the leading edge of rarefaction R_3 is not interfered with by rarefactions R_1 and R_2 before reaching the shock S_1. The side rarefactions R_1 and R_2 first reach the axis of symmetry on the interface I; hence, a reasonable criterion for the validity of the results of Section 4.2.2, is thought to be that the axial segment of R_3 must reach the interface I before the side rarefactions reach the axis of symmetry. It can be shown that this occurs provided

$$\frac{t_s}{d} \ll \frac{u_2}{2(c_{\ell,} + u_2 - v_1)} \left[\frac{c_{\ell,}}{c_{\rho,} \text{ or } c_{\ell,}}\right] \qquad (12)$$

where the term to be chosen in the square brackets must be the larger of the two speeds of sound. The maximum permissable value of $\frac{t_s}{d}$ (called $\left(\frac{t_s}{d}\right)_{max}$), determined by the value of the R.H.S. of Eq. (12), has been plotted in Fig. 19 for the case of aluminum projectiles and various shield materials. These results will be referred to later. For the moment consider two extreme situations.

The first situation is where $\frac{t_s}{d} \gg \left(\frac{t_s}{d}\right)_{max}$. In this case the rarefactions R_1 and R_2 reach the axis of symmetry well before the rarefaction R_4 from the back of the shield gets near the projectile. Hence, the motion (and fragmentation) of the projectile is completely determined by the interaction of rarefaction R_1 and shock S_1. One

example of this situation is the case of impact into an effectively semi-infinite target, where $\frac{t_s}{d} \gg \left(\frac{t_s}{d}\right)_{max}$ because t_s is large. Another example is the case of a very small diameter projectile impacting a shield. In this case $\frac{t_s}{d} \gg \left(\frac{t_s}{d}\right)_{max}$ because d is small. Also, if in this latter situation the projectile length L is much greater than the shield thickness, the rarefaction R_1 may completely destroy the shock S_1 leaving an undisturbed portion of the projectile (long rod) to pass through the shield.

The second extreme situation is when $\frac{t_s}{d} \ll \left(\frac{t_s}{d}\right)_{max}$. In this case the rarefaction R_4 exerts a very strong effect on the motion of the projectile. For instance, the results of Section 4.2.2 are correct, and the shock in the projectile can be completely nullified by rarefaction R_4. An example of such a situation has often been shown in free-flight ranges when a hypersonic projectile has penetrated a thin mylar diaphragm without damage. In this case the initial impact pressure P_1 can be very high, however, because $\frac{t_s}{d} \ll \left(\frac{t_s}{d}\right)_{max}$, the release rarefaction R_4 destroys the shock in the projectile almost immediately.

Between the above two extreme situations, the projectile motion is determined by a combination of effects due to the interaction of shock S_1 and rarefactions R_1 and R_4.

PROTECTIVE ABILITY OF THIN SHIELD

4.3.2 Estimation of Spray Angles

The fragments coming through the shield in Fig. 11 are confined to a conical volume of space. The author feels that the following method for estimating the vertex angle of this cone is illustrative. The method was first used by Bull[14], however, only for the case where the projectile and shield were assumed to be in a gaseous state.

It is assumed that the complete front portion of the projectile is uniformly compressed to the one-dimensional pressure P_1 and particle velocity v_1 by the shock S_i. It is then assumed that the projectile is suddenly released to atmospheric pressure. One can crudely visualize the instantaneous release of constraint being caused by the flow and fragmentation of the shield material adjacent to the projectile. The assumed flow in the projectile shortly after this release is shown in Figure 20 (a). An axially symmetric rarefaction R_c has been generated at the cylindrical boundaries and starts to accelerate the projectile radially. This rarefaction grows in strength as it proceeds toward the axis and will cause fracture. Another axially symmetric rarefaction will subsequently proceed

inward from the new boundary and the process will be repeated. In accordance with the previous discussion (Section 4. 2. 3), it is assumed that sudden release from pressure P_1 corresponds to a radial velocity component $v_o - v_1$ for the outermost fragments. Also, since the initial flow is translating with a velocity v_1 the envelope of the expansion products will be a cone of semi-vertex angle given by

$$\theta_p = \tan^{-1} \frac{v_o - v_1}{v_1} \qquad (13)$$

In addition, if a plug of shield of the same diameter as the projectile is assumed to be compressed to a pressure P_1 by the impact and then suddenly released, the vertex angle of the spray of shield fragments will be given by

$$\theta_s = \tan^{-1} \frac{v_1}{v_1} = 45^o \qquad (14)$$

The spray angles calculated from Eq. (13) for the case of an aluminum projectile and various shields are presented in Figure 20(b).

This completes the present theoretical description of thin shield impact. Some consideration is now given to the well-known theory of Lull[5]. In a later section of this paper (Section 6) the present theory and that of Lull will be compared critically with the previously presented experimental results.

PROTECTIVE ABILITY OF THIN SHIELD

5. THE THIN TARGET THEORY OF LULL[15]

As opposed to the previous theoretical discussion, Lull's theory does not consider the details of wave motion in the projectile and shield immediately after impact. His theory treats the gross process and uses simple arguments of conservation of momentum and energy. The theory is as follows.

The assumed sequence of events after impact is illustrated in Figures 21(a) to (c). The projectile is first assumed to punch out a section of the shield of area equal to the presented area of the projectile. Shortly after impact, the projectile and punched-out section of the shield are assumed to have moved out of contact with the remainder of the shield. A momentum balance then gives

$$m_1 v_o = (m_1 + m_2)\ v_2 \qquad (15)$$

where m_1 is the projectile mass, m_2 is the mass of the segment of shield, v_o is the impact velocity, and v_2 is the velocity of the projectile-shield segment combination. The energy balance gives

$$\frac{1}{2} m_1 v_o^2 = \frac{1}{2} (m_1 + m_2) v_2^2 + \Delta E$$

where ΔE is the increase in internal energy of the projectile and shield segment. This is given by

$$\Delta E = \frac{1}{2} \frac{m_1 m_2}{m_1 + m_2} v_2^2 \qquad (16)$$

Lull then assumes that the projectile and shield segment shatter, and all of the increase in internal energy goes into accelerating the material in a radial direction. The projectile and shield material are then assumed to be distributed uniformly throughout an expanding sphere, the center of gravity of which is moving at velocity v_2. This situation is shown in Fig. 21 (c) which defines the parameters v_3, θ_1 and θ_2. From the above assumptions it can easily be shown that

$$\frac{v_3}{v_0} = \left(\frac{5}{3}\right)^{1/2} \frac{(m_1 m_2)^{1/2}}{m_1 + m_2} \qquad (17)$$

$$\theta_2 = \tan^{-1} \left(\frac{5}{3} \frac{m_2}{m_1}\right)^{1/2} \qquad (18)$$

and

$$\theta_1 = \sin^{-1} \left(\frac{5}{3} \frac{m_2}{m_1}\right)^{1/2} \qquad (19)$$

Note that Θ_2 is the spray angle of the leading hemisphere of debris, and Θ_1 is the spray angle of the trailing hemisphere. Note also that the velocity v_f of the fastest fragment is given by

$$v_f = v_2 + v_3 = v_o \left[\frac{m_1}{m_1+m_2} + \left(\frac{5}{3}\right)^{1/2} \frac{(m_1 m_2)^{1/2}}{m_1+m_2} \right] \quad (20)$$

and the velocity of the "slowest" fragment is given by

$$v_s = v_2 - v_3 = v_o \left[\frac{m_1}{m_1+m_2} - \left(\frac{5}{3}\right)^{1/2} \frac{(m_1 m_2)^{1/2}}{m_1+m_2} \right] \quad (21)$$

Equations (18), (19), (20), and (21) are plotted in Figures 22 (a) and (b). The results of these figures are discussed more fully in the next section of this paper.

6. COMPARISON OF THEORY AND EXPERIMENT

In this section the experimental results of Section 3 will be discussed in terms of the theoretical considerations of Sections 4 and 5. Although the experiments were performed using spherical projectiles (whereas the theories refer to cylindrical projectiles) it is felt that this comparison is reasonable provided, in both cases, equal weight projectiles of approximately the same basic dimensions are considered.

PROTECTIVE ABILITY OF THIN SHIELD

6.1 The Effect of Shield Thickness

The series of experiments described in Section 3.2.1 were such that only the shield thickness was varied. Theoretical considerations (Section 4.2.1) indicate that in all such impacts the initial impact pressure P_1 and particle velocity v_1 will be the same. However, Sections 4.2.2 shows that the rarefaction R_4 will overtake the shock S_1 in the projectile much more quickly as the shield is made thinner. As a result of this, Section 4.2.3 points out that the deceleration of the back of the projectile, and hence the spread between the fastest and slowest fragments, becomes less as the shield is made thinner. The X-ray results of Figure 6 confirm this conclusion.

Consider in particular the results for an aluminum projectile and shield. It is fairly obvious that the thicker the shield the greater will be the deceleration and fragmentation of the projectile. However, Curve C in Fig. 5 (a) indicates that the damage to the back-up target decreases very little for values of $\frac{t_s}{d}$ greater than about 0.3. The reason for this has been determined from X-rays which indicate that, for values of $\frac{t_s}{d}$ less than about 0.3, the fragments are not uniformly

distributed in space. In light of these facts it is interesting to note that, for an aluminum projectile and shield at 6.1 km/sec, $\frac{t_s}{d} \doteq 0.3$ corresponds to the situation where the rarefaction R_1 reaches the axis of symmetry before the rarefaction R_3 reaches the projectile (see Fig. 19). Thus, it would appear that, when this happens, the effect of the rarefaction R_4 on the subsequent projectile motion and fragmentation is small. Physically one can envisage that shortly after R_1 has reached the axis of symmetry, it has effected almost complete fragmentation of the projectile and there is little continuous portion of the projectile remaining for R_4 to effect.

Now consider the spray angle Θ in which the debris is confined. Equations (12) and (13) show that, for an aluminum projectile and shield, the spray angle Θ is 45° irrespective of shield thickness. The results of Fig. 5 (a) (Curve A) from Section 3.2.1 agree with this value fairly well. However, the majority of the debris (Curve B) is confined in a cone of semi-vertex angle less than half that estimated theoretically.

It is of interest to consider Lull's theory in light of the experimental results of Section 3.2.1. Figure 22 (a) shows that the

estimates of spray angle from this theory are also much greater than the actual spray angle in which most of the debris is concentrated. Also, Fig. 22 (b) shows that the spread between the velocity of the fastest and slowest fragment becomes less as the shield is made thinner. This is consistent with the experimental results. However, this figure shows that the velocity of the fastest fragment is always faster than the original projectile velocity. The theory of Section 4.2.3 suggests that this can only be true for very thin shields of lower density than the projectile. Another comment concerning Lull's theory is that, even for very thin shields, it assumes the fragments are uniformly distributed in space (Fig. 22 (c)). X-ray results, similar to those shown in Fig. 6, indicate that this does not occur until the ratio of shield to projectile weight per unit area is about 0.3.

5.2 The Effect of Shield Material

Consider the series of experiments described in Section 3.2.2 in which the shield weight was held constant and the shield material varied. Theoretical considerations (Section 4.2.1) indicate that as

the shield material is altered in the order magnesium, aluminum, titanium, copper and gold, the initial impact pressure P_1 increases, and the particle velocity v_1 decreases. Also, Section 4.3.2 predicts that the spray angle increases as the shield material is altered in the above sequence. Both the above effects suggest that as the shields are altered in this sequence they will become increasingly more effective due to increased fragmentation, deceleration and spread of the debris. However, there is another effect, discussed in Sections 4.2.2 and 4.3.1, to take into account. This factor, illustrated in Figs. 17 and 19. refers to the fact that, as one progresses from equal weight shields of magnesium to gold, the rarefaction R_4 starts to exert a greater influence on the fracture mechanism by overtaking the shock S_1 in the projectile more quickly. Thus, as the shields are altered in the above sequence from magnesium to gold, the shock in the projectile is much sooner reduced in intensity. This trend tends to continually reduce the fragmentation, deceleration and spread of the projectile material, as the progressively decaying shock travels back into the projectile. It can be expected that the best shield material, on a fixed weight basis, will depend on which of the above effects predominate. In this regard, the experimental results indicate that, at 6.1 km/sec, the two effects are compensating for a shield weight of 0.113 gms/cm^2. However, for greater ratios of

shield to projectile weight per unit area, the effectiveness of the shields increase from magnesium to gold, i. e. as P_1 increases. In contrast to this, it is expected that for shield weights less than 0.113 gms/cm^2, the role will be reversed and the effectiveness of the shields will increase as P_1 decreases.

A few further comments concerning spray angles in the present tests are pertinent. The theory of Section 4.3.2 suggests that the projectile spray angle will increase as the shields are altered in the order magnesium, aluminum, titanium, copper, and gold. While there is some evidence of this occurring, the experimental spray angles are all found to be fairly similar with most of the debris (Curve B) confined in a cone of semi-vertex angle less than half that predicted in Figure 20 (b). Another point of interest is that with a magnesium shield the debris from the shield is predicted to lie completely within the cone of debris from the projectile. The results in Figure 7 (a) for magnesium shields show two distinct damage regions and seem to indicate that this does occur. Note that for all the other shield materials, the debris from the projectile is predicted to be within the cone of fragments from the shield.

PROTECTIVE ABILITY OF THIN SHIELD

Again it is of interest to compare Lull's theory with the experimental results. This theory predicts that, provided the weight of shield per unit area is held constant, the shields should be equally effective irrespective of shield material. The experimental results of Section 4.3.2 indicate that at 6.1 km/sec this is not so, however, it is a fairly good first approximation.

5.3 The Effect of Impact Velocity.

Consider the series of experiments described in Section 3.2.4 in which only the projectile velocity is altered. As the impact velocity increases, Sections 4.2.1 and 4.2.3 indicate that the velocity v_1, and hence the velocity of the debris coming through the shield, will increase. Also, Sections 4.2.2 and 4.3.1 show that the rarefaction R_4 starts to exert a greater influence on the fracture process by overtaking the shock S_1 in the projectile more quickly with increasing velocity. The above effects, coupled with the fact that the spray angle is predicted to be fairly independent of impact velocity, suggest that a given shield may become less effective against a specific projectile as the impact velocity increases. However, there is another factor to consider, based on the size of fragments produced by the impact.

PROTECTIVE ABILITY OF THIN SHIELD

Obviously the size of fragment tends to decrease as the impact velocity, and hence P_1, increases. Thus, how the effectiveness of a specific shield varies with impact velocity depends upon the relative importance of the above effects.

Consider the results of Figure 10 (a). The total depth of penetration for a 0.81 mm shield, as the velocity increases, is seen to increase, reach a maximum, and then decrease. This behavior appears to be dominated by the size of projectile fragment produced upon impact. Figure 10 (b) shows that, up to a velocity of between 2.5 to 4.5 km/sec (P_1 of $2 - 6 \times 10^{10}$ dynes/cm^2), very incomplete fracture of the projectile occurs. Hence, in this region, the projectile is effected very little by the shield, and the total depth of penetration approximates that in a semi-infinite target. As the velocity is increased further, the fragments of projectile becomes smaller and more uniformly distributed. Apparently, this effect more than neutralizes the fact that the velocity of the debris increases with increasing impact velocity, for the depth of penetration in Fig. 10 (b) decreases as v_o increases. It should be noted that this type of behavior might not always occur. For instance, if the shield is too thin, rarefaction

R_4 can predominate and rapidly reduce the pressure pulse in the projectile at all impact velocities. In this case, the essentially complete rear portion of the projectile penetrates the shield, and the damage curve tends to follow the curve for an unprotected semi-infinite target (zero shield thickness). Also, as the shield becomes very thick, the curve for total depth of penetration again tends to follow the curve for an unprotected semi-infinite target. In this case the damage due to the projectile fragments may be very small, with the majority of the depth of penetration occurring in the shield itself.

PROTECTIVE ABILITY OF THIN SHIELD

CONCLUSIONS

The present study of thin shield impact is not yet complete; however, the results obtained to date lead to certain conclusions. Some of these conclusions are now presented.

1. The present experimental and theoretical results have indicated that a shield is effective because it fragments the projectile, spreads the fragments, and reduces the velocities of the fragments normal to the target. As a shield is made thinner the spread of fragments decreases and the velocities of the fragments tend to the original projectile velocity. Conversely, as the thickness of a shield increases, its effectiveness increases. However, there does exist an optimum shield thickness for which the total depth of penetration, including shield thickness, is a minimum. For aluminum projectiles at 6.1 km/sec and aluminum shields this optimum shield thickness is such that $\frac{t}{s} \doteq .03$. This value corresponds to the situation where the release rarefaction R_3 from the back of the shield just enters the projectile as the side rarefaction R_1 converges upon the axis of symmetry. Physically, one can envisage that when R_1 has reached the axis of symmetry it has almost effected complete fragmentation of the projectile, and there is little continuous portion of

the projectile remaining to be influenced by rarefaction R_3. Thus, there is no point in making a shield any thicker than the thickness corresponding to the above situation.

2. A comparison has been made of the effectiveness of various shield materials keeping the weight of the shield constant. It is found that for a shield to projectile weight per unit area of almost 0.13 the shields are equally effective. However, for ratios of shield to projectile weight per unit area greater than this value, the shields become slightly more effective as the initial impact pressure P_1 increases. (see Table I). This result has been discussed in terms of the theoretical considerations.

3. Tests were conducted to investigate the effect of projectile velocity on the effectiveness of a specific shield. It is found that, up to an impact pressure P_1 of $2 - 6 \times 10^{10}$ dynes/cm^2 (v_o = 2.5 - 4.5 km/sec), incomplete fragmentation of the projectile occurs and the total depth of penetration, including shield thickness, is no less than with an unprotected target. Above this point, the total depth of penetration is found to increase or decrease with increasing impact velocity, depending upon the shield thickness. If the shield is too thin or too thick, the total depth of penetration will increase

as the impact velocity increases. The most effective shields are in between these limits, and the damage with these shields is found to decrease with increasing impact velocity. The reason for the above behavior has been explained by the theoretical considerations.

4. In light of the above conclusions, the author presents the following procedure to determine an adequate shield to give near minimum total depth of penetration with a specific projectile ($\frac{l}{d} \doteq 1$) . Because the present study of thin shield impact is not yet complete, this design procedure must be regarded as very preliminary.

The first step in the method is to determine the thickness of shield, of same material as the projectile, such that rarefaction R_3 just enters the projectile as rarefaction R_1 reaches the axis of symmetry (see Section 4.3.1, Eq. 12). Then choose an equal weight shield made of a material as high in Table I as is consistent with other requirements (cost, structural, radiation shielding etc.). The above calculation is made at a specific impact velocity, however, Fig. 19 indicates that the calculated shield thickness will be fairly independent of impact velocity. It can thus be assumed that the

shield will be reasonably effective at all impact velocities. Finally the results of Section 3 indicate that there is some advantage in using a strong alloy of the chosen shield material.

ACKNOWLEDGEMENTS

The author is grateful to Dr. A. C. Charters and Mr. J. W. Gehring for their helpful comments during the course of this investigation. Also, thanks are due to D. Sieck, J. S. Curtis, and A. R. McMillan for conducting the experimental program.

REFERENCES

1. Whipple, F.L: The Meteoritic Risk to Space Vehicles, in "Vistas in Astronautics", Vol. 2, pp. 115-124, Permagon Press, New York, 1958.

2. Charters, A. C., and Curtis, J. S: High Velocity Guns for Free-Flight Ranges, presented at AGARD Specialists' Meeting on "High Temperature Aspects of Hypersonic Flow", Belgium, 1962.

3. Charters, A.C., and Summers, J. L: High Speed Impact of Metal Projectiles in Targets of Various Materials, Proc. of Third Hypervelocity Impact Symposium, 1958.

4. Eichelberger, R. J., and Gehring, J. W: Effects of Meteoroid Impacts on Space Vehicles, ARS Jour., Vol. 32, No. 10, 1962.

5. Herrmann, W., and Jones, A. H: Correlation of Hypervelocity Impact Data, Proc. of Fifth Hypervelocity Impact Symposium, 1961.

6. Bjork, R.L: Effect of Meteoroid Impact on Aluminum and Steel, Rand Paper No. P-1662, 1959.

7. Atkins, W. W., and H. F. Swift: Hypervelocity Capability and Impact Research, ARPA Order 70-59, NRL Memo, Rept. 1115, 1960.

8. Courant, R., and Friedrichs, K. O: "Supersonic Flow and Shock Waves," Interscience Publishers Inc., New York, 1948.

9. Walsh, J. M., Rice, M. H., McQueen, R. G., and Yarger, F. L: Shock Wave Compressions of Twenty-Seven Metals. Equations of State of Metals, Phys. Rev., Vol. 108, No. 2, 1957.

10. McQueen, R. G., and March, S. P: Equation of State for Nineteen Metallic Elements from Shock Wave Measurements to Two Magabars, Jour. App. Phys, Vol. 31, No. 7, 1960.

11. Al'Tshuler, L. V., Krupnikov, K. K., and Brazhnik, M. I: Dynamic Compressibility of Metals Under Pressures from 400,000 to 4,000,000 Atmospheres, Soviet Physics JETP, Vol. 34, No. 7, 1958.

12. Al'Tshuler, L. V., Kormer, S. B., Bakanova, A. A., and Trunin, R. F: Equation of State for Aluminum, Copper, and Lead in the High Pressure Region, Soviet Physics, JETP, Vol. 11, No. 3, 1960.

13. Al'Tshuler, L. V., Kormer, S. B., Brahznik, M. I., Vladimirov, L. A., Speranskaya, M. P., and Funtikov, A. I: The Isentropic Compressibility of Aluminum, Copper, Lead and Iron at High Pressures, Soviet Physics JETP, Vol. 11, No. 4, 1960.

14. Bull, G. V: On the Impact of Pellets with thin Plates. Theoretical Considerations - Part I, A. D. Little, Inc., Rept. No. 63270-03-01, 1962.

PROTECTIVE ABILITY OF THIN SHIELD

TABLE I

Material	Density ρ_0 gms/cc	$(1-\frac{\rho}{\rho_0})\times 10$ at 500 Kbars		$\frac{\rho_0}{(1-\frac{\rho_0}{\rho})\times 10}$
Platinum	21.37	1.3		16.4
Gold	19.24	1.7		11.3
Uranium	18.70	1.7		11.0
Rhodium	12.42	1.35		9.2
Tantalum	16.46	1.9		8.7
Palladium	11.94	1.7		7.0
Molybdenum	10.2	1.45		7.0
Nickel	8.86	1.8		4.9
Cobalt	8.82	1.8		4.9
Niobium	8.6	1.8		4.8
Silver	10.49	2.2		4.8
Chromium	7.13	1.55		4.6
Copper	8.9	2.1		4.2
Iron	7.84	1.9	Increasing U_1 Decreasing v_1 Increasing P_1	4.1
Brass	8.4	2.2		3.8
Thallium	11.84	3.2		3.7
Thorium	11.68	3.3		3.5
Lead	11.34	3.3		3.5
Cadmium	8.64	2.7		3.2
Zinc	7.14	2.6		2.8
Tin	7.28	3		2.4
Zirconium	6.49	2.9		2.2
Indium	7.27	3.3		2.2
Titanium	4.51	2.5		1.8
Aluminum	2.78	2.7		1.0
Beryllium	1.85	2.4		0.8
Magnesium	1.74	4.1		0.4
Bismuth	0.79	3.4		0.2

PROTECTIVE ABILITY OF THIN SHIELD

CAPTIONS TO FIGURES

Fig. 1. Depth of Penetration in Effectively Semi-Infinite Targets of Aluminum (2024-T3)

Fig. 2. Depth of Penetration in Effectively Semi-Infinite Targets of Aluminum (1100 F)

Fig. 3. Comparison of Experimental Depth of Penetration in 2024-T3 and 1100 F Aluminum.

Fig. 4 (a) Effect of Shield Thickness - Aluminum Shields, 4.8 mm Aluminum Projectiles at 6.1 km/sec, 5.48 cms Spacing Between Shields and Targets. Front of Targets Shown.

Fig. 4 (b) Effect of Shield Thickness- Aluminum Shields, 4.8 mm Aluminum Projectiles at 6.1 km/sec, 5.48 cms Spacing Between Shields and 6.4 mm Thick Aluminum (2024-T3) Targets. Rear of Targets Shown.

Fig. 5 (a) Equivalent Depth of Penetration for Aluminum Shields of Various Thicknesses. 4.8 mm Aluminum Projectiles at 6.1 km/sec, 5.48 cms Spacing Between Shields and 6.4 mm Thick Aluminim (2024-T3) Targets.

Fig. 5 (b) Spray Angle for Aluminum Shields of Various Thicknesses. 4.8 mm Aluminum Projectiles at 6.1 km/sec, 5.48 cms Spacing Between Shields and Targets.

Fig. 6. X-Rays of Impacts of 4.8 mm Aluminum Projectiles at 6.1 km/sec Against Various Thickness Copper Targets.

Fig. 7 (a) Effect of Shield Material - 4.8 mm Aluminum Projectiles at 6.1 km/sec, 5.48 cms. Spacing Between Shields and 6.4 mm Thick Aluminum (2024-T3) Targets. Front of Targets Shown.

Fig. 7 (b) Effect of Shield Material - 4.8 mm Aluminum Projectiles at 6.1 km/sec, 5.48 cms Spacing Between Shields and 6.4 mm Thick Aluminum (2024-T3) Targets. Rear of Targets Shown.

Fig. 8 Diameter of Holes in Shields of Various Materials. 4.8 mm Aluminum Projectiles at 6.1 km/sec.

Fig. 9 (a) Effect of Shield Strength - 0.81 mm Aluminum Alloy Shields. 4.8 mm Aluminum Projectiles at 6.1 km/sec. 5.48 cms Spacing Between Shields and 6.4 mm Thick Aluminum (2024-T3) Targets. Fron of Targets Shown.

Fig. 9 (b) Effect of Shield Strength - 0.81 mm Aluminum Alloy Shields. 4.8 mm Aluminum Projectiles at 6.1 km/sec. 5.48 cms Spacing Between Shields and 6.4 mm Thick Aluminum (2024-T3) Targets. Front of Targets Shown.

Fig. 10 (a) Penetration Depth as a Function of Impact Velocity for Protected and Unprotected Aluminum (2024-T3) Targets.

Fig. 10 (b) Effect of Impact Velocity - 0.81 mm Aluminum (2024-T3) Shields. 3.2 mm Aluminum Projectiles. 5.48 cms Spacing Between Shields and Thick 2024-T3 Aluminum Targets. Front of Targets Shown.

Fig. 10 (c) Spray Angle for a 0.81 mm Aluminum (2024-T3) Shield as a Function of Impact Velocity.

Fig. 11 (a) Estimated Wave pattern in a projectile and shield soon after impact.

Fig. 11 (b) Estimated Wave Pattern after the shock in the shield has reflected from the bottom face of the shield.

Fig. 12 One-dimensional situation immediately after impact of a projectile and shield.

Fig. 13 Hugoniot curves used in the Analysis.

Fig. 14 (a) One-dimensional Pressure P_1 generated by impact of an Aluminum Projectile with various Shield Materials.

Fig. 14 (b) One-dimensional Shock Velocity U_1 in an Aluminum Projectile after Impacting Various Shield Materials.

Fig. 14 (c) One-dimensional Particle Velocity v_1 for an Aluminum Projectile and Various Shield Materials.

Fig. 14 (d) One-dimensional Shock Velocity U_2 in Shields of Various Materials after Impact with an Aluminum Projectile.

Fig. 15 x-t Diagram illustrating how the rarefaction from the back of a Shield can overtake the Shock S_1 in a Projectile.

Fig. 16 Speeds of Sound of Various Materials as a Function of Density Ratio.

Fig. 17 Calculation of Point where the Rarefaction from the back of Shields of Various Materials overtakes the Shock S_1 in an Aluminum Projectile.

Fig. 18 Velocity of "Slowest" fragment if unreduced Shock S_1 reflects from the back of an Aluminum Shield.

Fig. 19 Parameter $(\frac{ts}{d})_{max}$ as a Function of Shield Material and Velocity.

Fig. 20 (a) Simplified Physical Model for Estimating Spray Angles.

Fig. 20 (b) Estimated Spray Angles for Aluminum Projectiles and Various Shield Materials.

Fig. 21 Physical Model of Thin Sheet Impact by Lull.

Fig. 22 (a) Spray Angles Calculated from Lull's Theory.

Fig. 22 (b) Velocity of "Slowest" and Fastest Fragments from Lull's Theory.

PROTECTIVE ABILITY OF THIN SHIELD

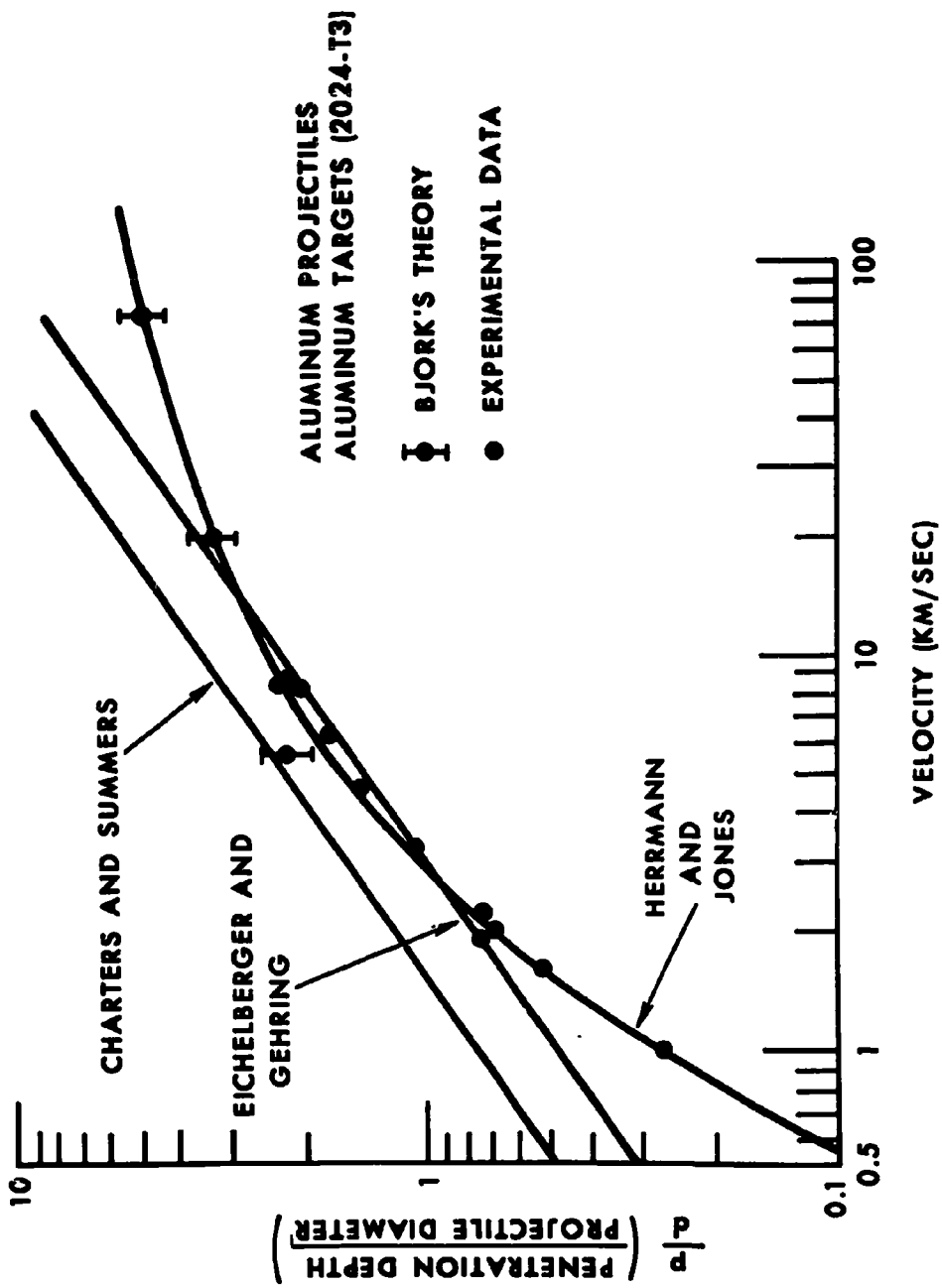

PROTECTIVE ABILITY OF THIN SHIELD

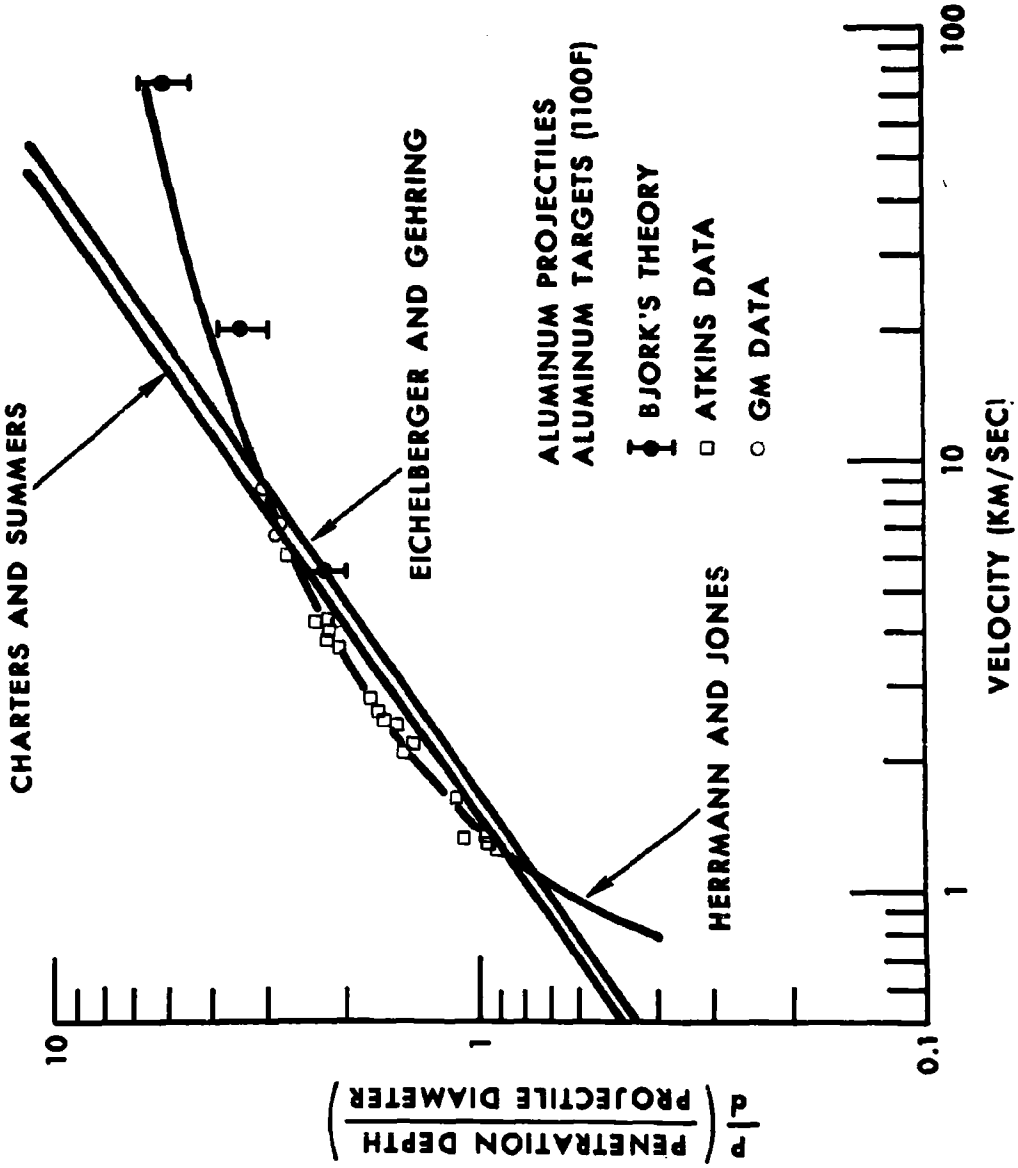

PROTECTIVE ABILITY OF THIN SHIELD

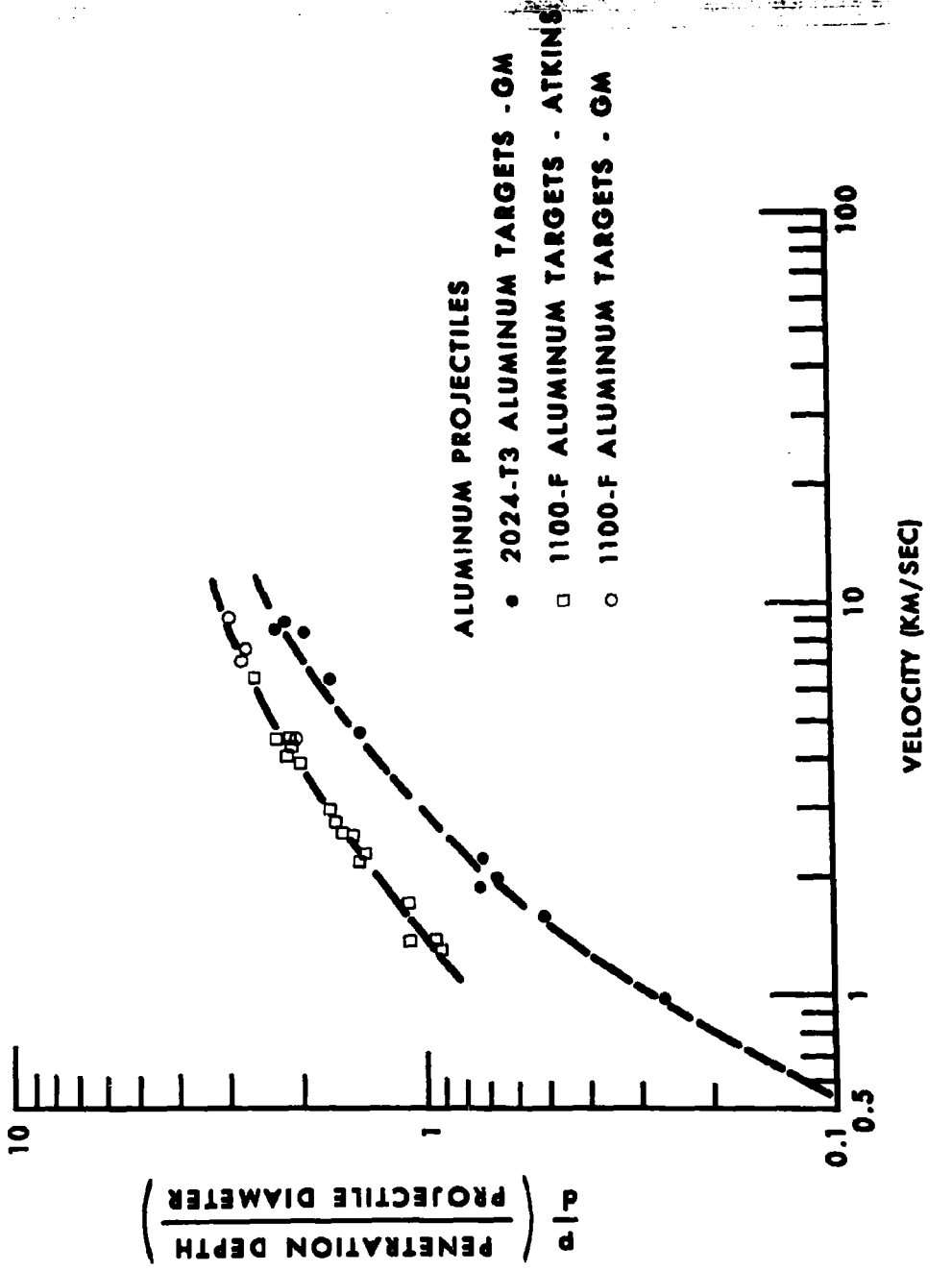

PROTECTIVE ABILITY OF THIN SHIELD

FRONT OF TARGETS - 6.4mm THICK ALUMINUM (2024-T3)

SHIELD THICKNESS: 0.08

0.20

0.41 mms

SHIELD THICKNESS: 0.82

1.64

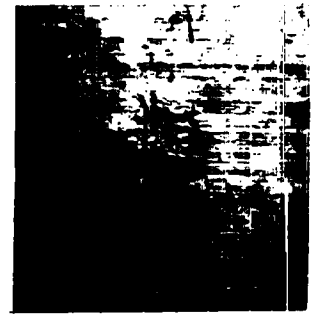

3.17 mms

PROTECTIVE ABILITY OF THIN SHIELD

REAR OF TARGETS - 6.4mm THICK ALUMINUM (2024-T3)

PROTECTIVE ABILITY OF THIN SHIELD

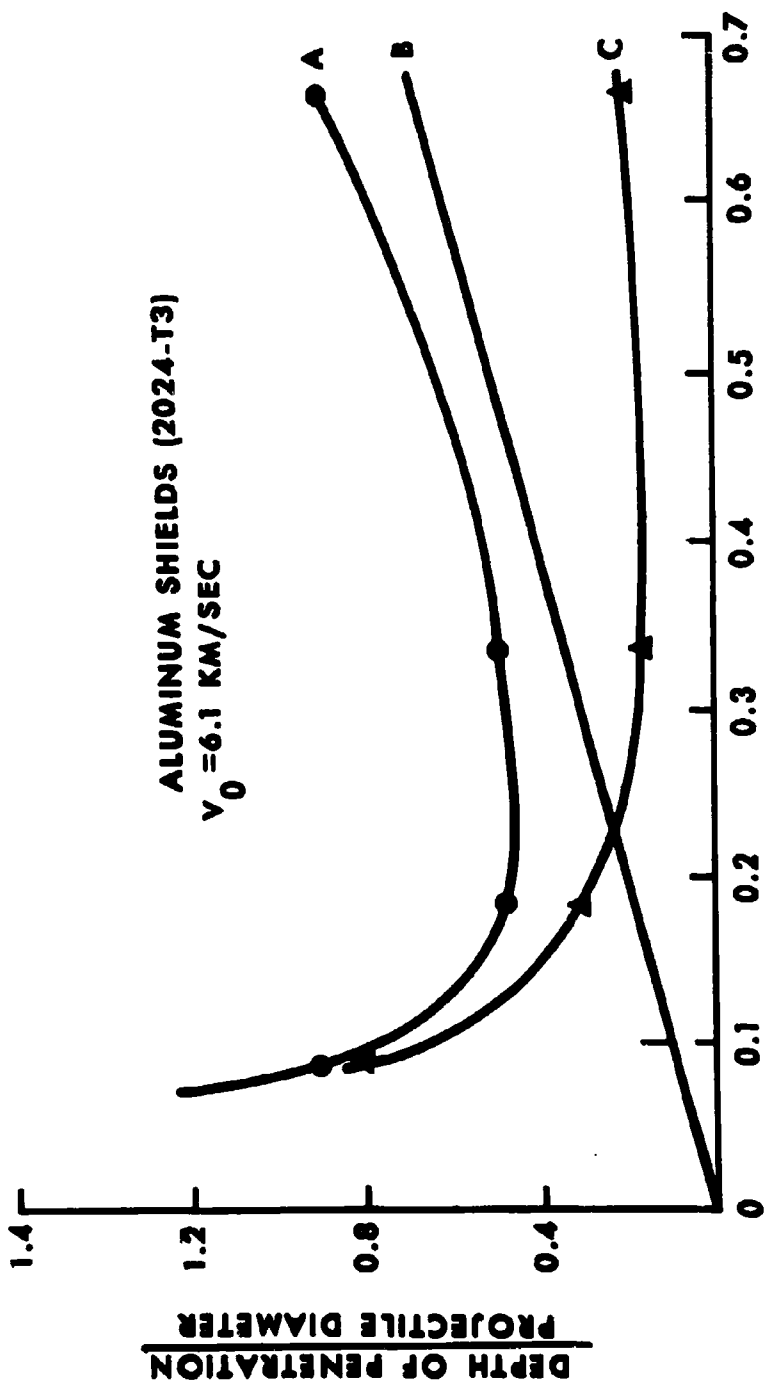

DEPTHS OF DAMAGE FOR ALUMINUM SHIELDS OF VARIOUS THICKNESSES

PROTECTIVE ABILITY OF THIN SHIELD

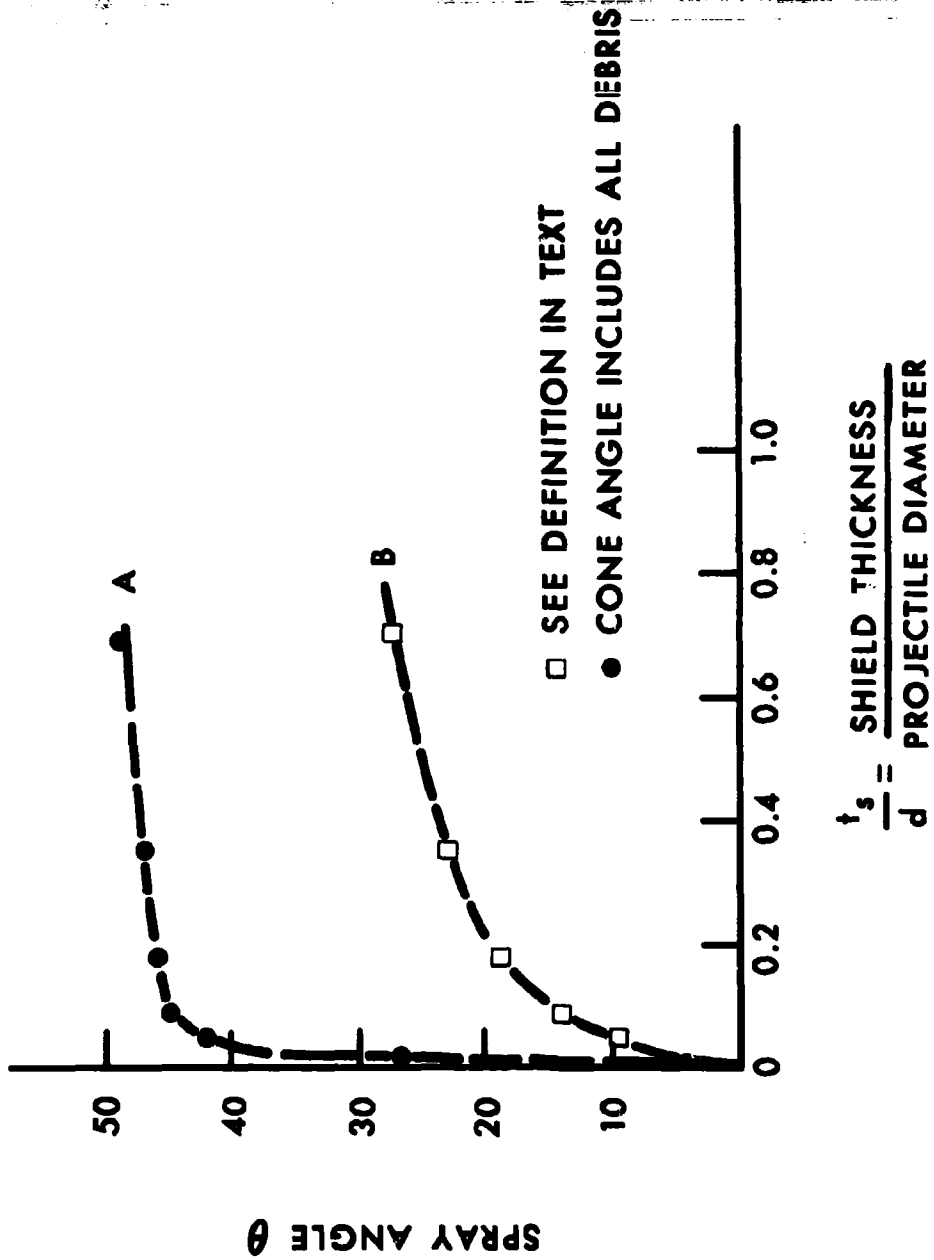

PROTECTIVE ABILITY OF THIN SHIELD

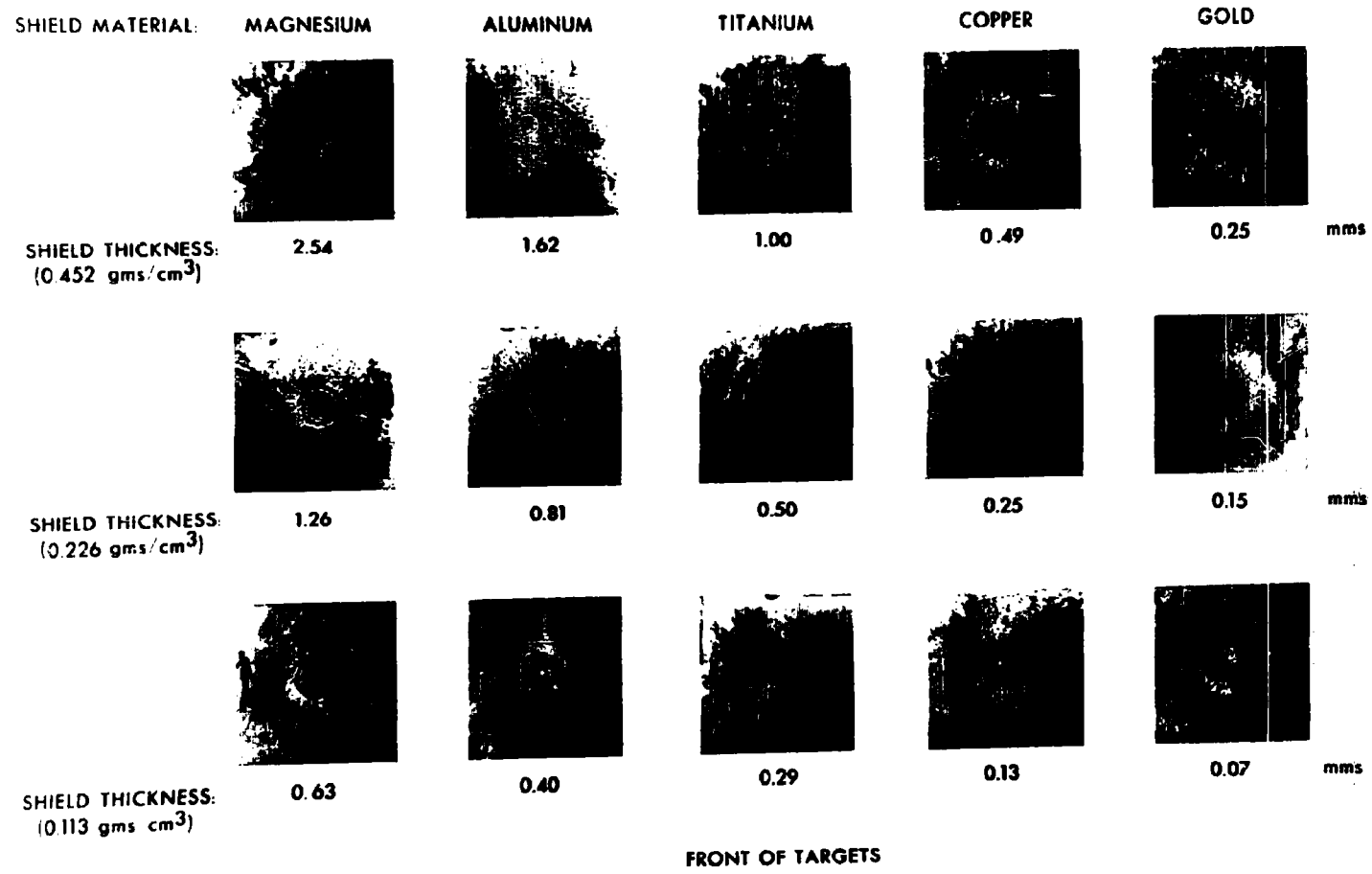
SHIELD MATERIAL:
MAGNESIUM
ALUMINUM
TITANIUM
COPPER
GOLD
SHIELD THICKNESS: (0.452 gms/cm3)
2.54
1.62
1.00
0.49
0.25
mms
SHIELD THICKNESS: (0.226 gms/cm3)
1.26
0.81
0.50
0.25
0.15
mms
SHIELD THICKNESS: (0.113 gms cm3)
0.63
0.40
0.29
0.13
0.07
mms
FRONT OF TARGETS
PROTECTIVE ABILITY OF THIN SHIELD

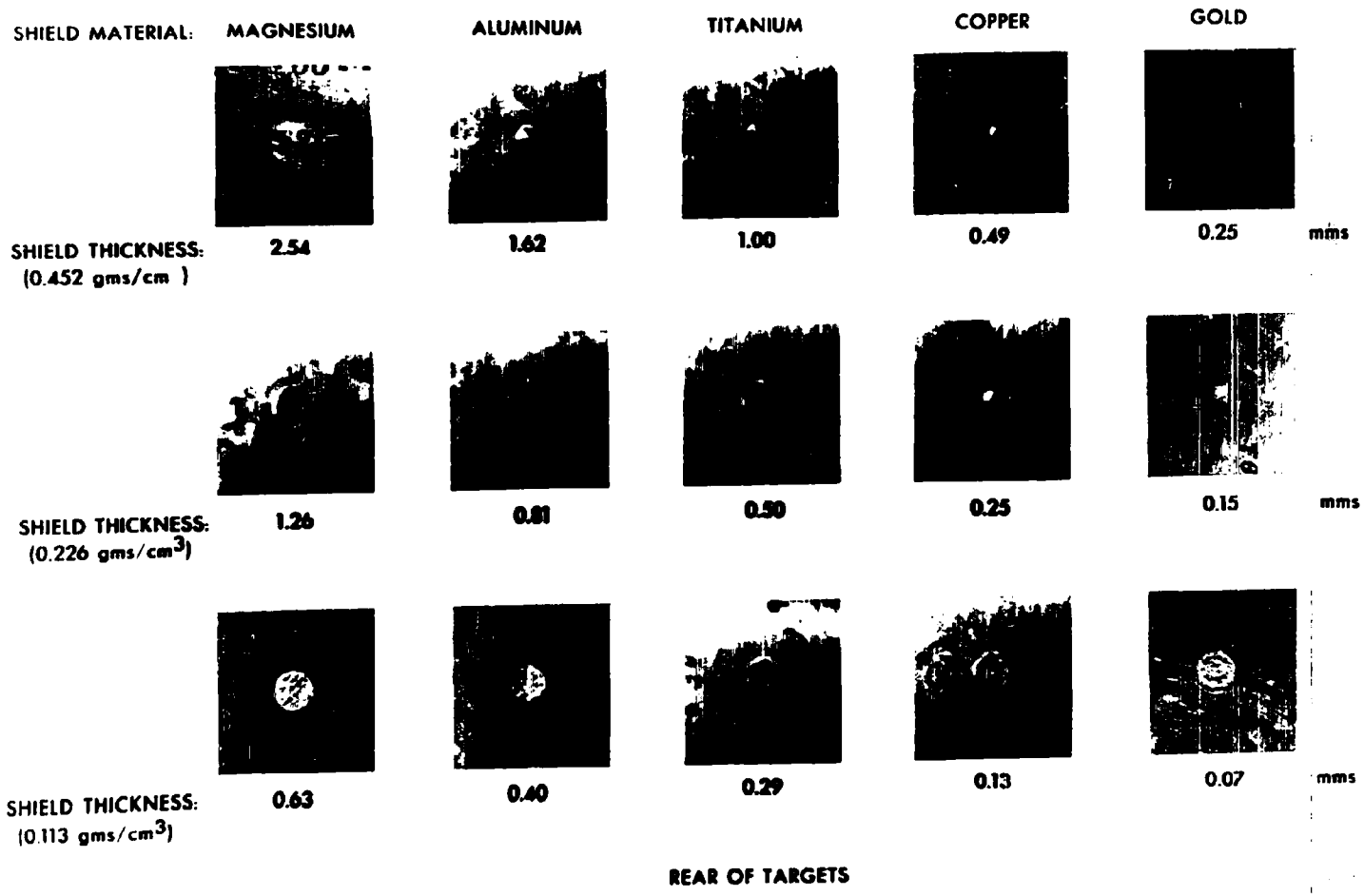

PROTECTIVE ABILITY OF THIN SHIELD

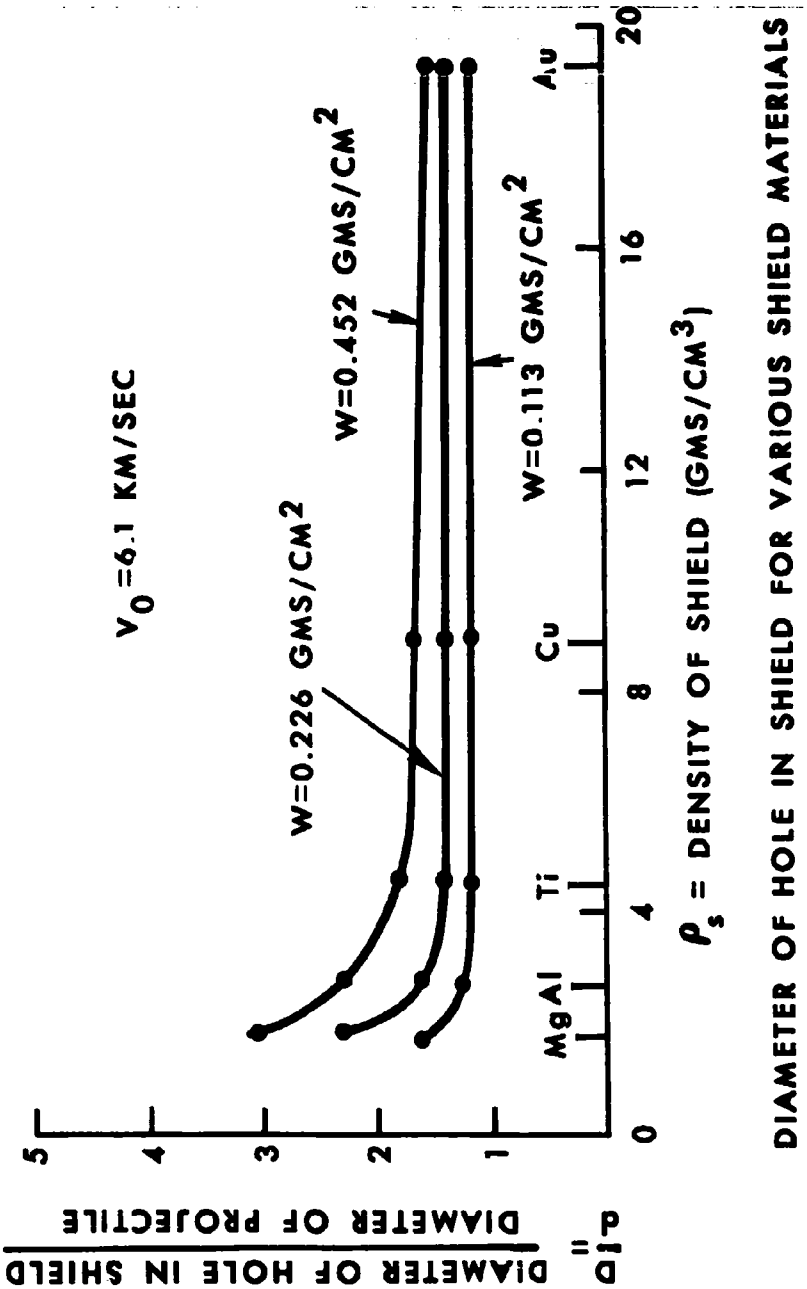

DIAMETER OF HOLE IN SHIELD FOR VARIOUS SHIELD MATERIALS

PROTECTIVE ABILITY OF THIN SHIELD

PROTECTIVE ABILITY OF THIN SHIELD

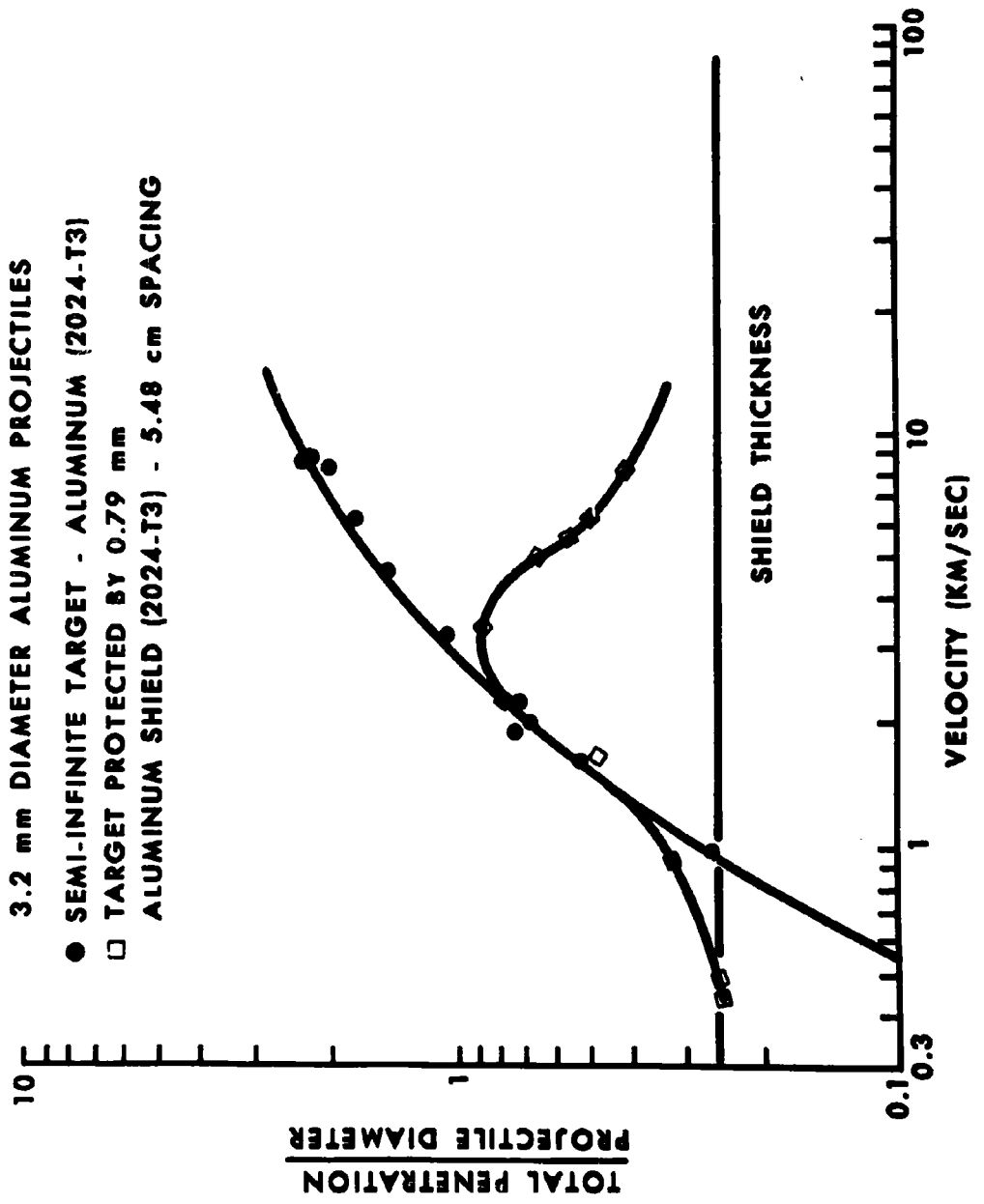
3.2 mm DIAMETER ALUMINUM PROJECTILES
● SEMI-INFINITE TARGET - ALUMINUM (2024-T3)
□ TARGET PROTECTED BY 0.79 mm
ALUMINUM SHIELD (2024-T3) - 5.48 cm SPACING
SHIELD THICKNESS
TOTAL PENETRATION / PROJECTILE DIAMETER
VELOCITY (KM/SEC)
10
1
0.1
0.3
1
10
100

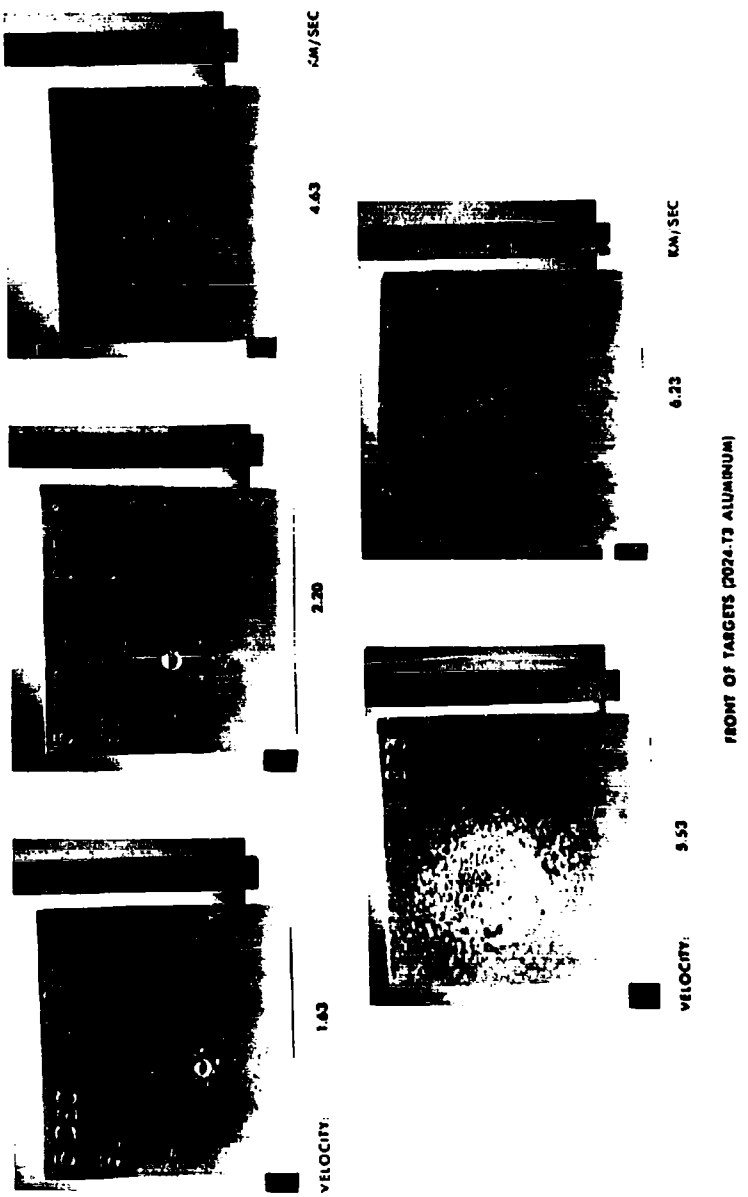
KM/SEC
4.43
2.20
1.43
VELOCITY:
KM/SEC
6.23
5.53
VELOCITY:
FRONT OF TARGETS (2024-T3 ALUMINUM)

PROTECTIVE ABILITY OF THIN SHIELD

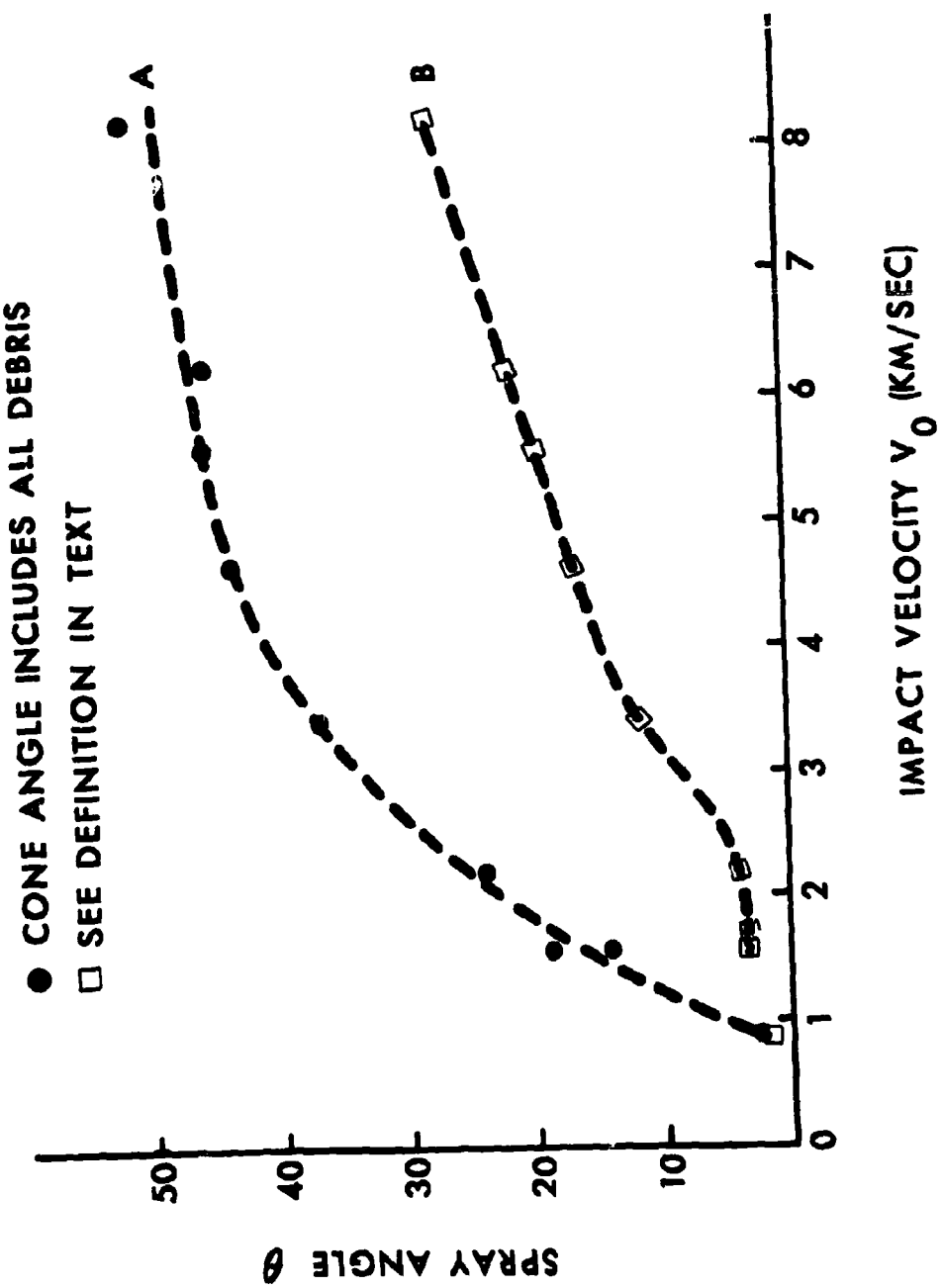

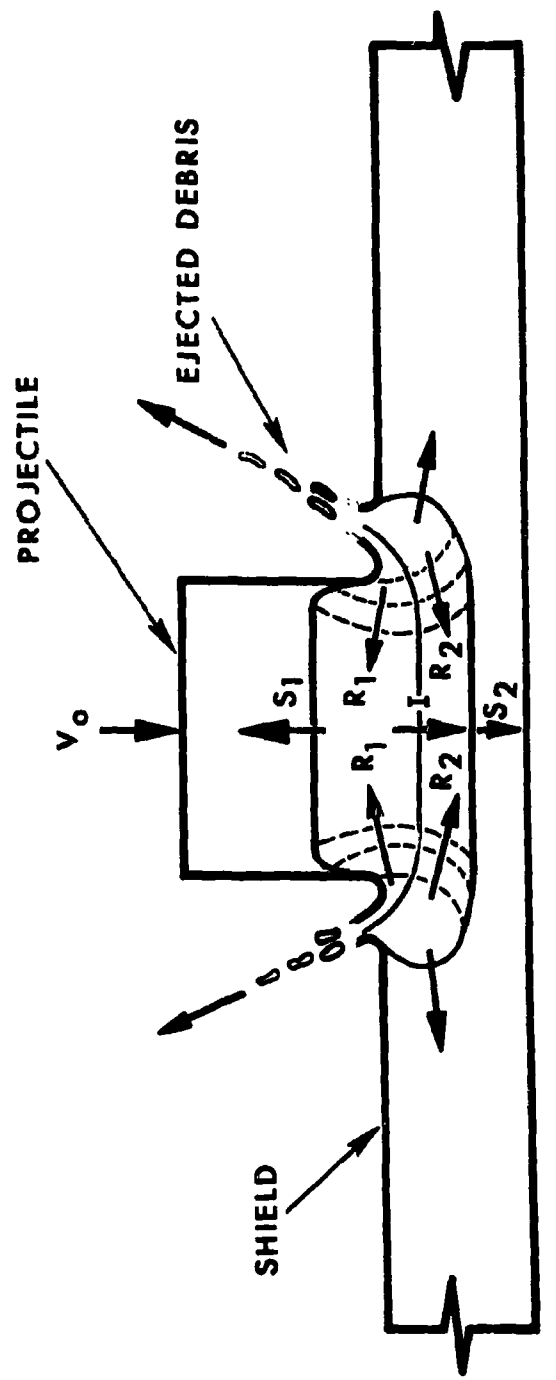
EJECTED DEBRIS
PROJECTILE
V_o
S_1
R_1
R_2
I
R_1
R_2
S_2
SHIELD

PROTECTIVE ABILITY OF THIN SHIELD

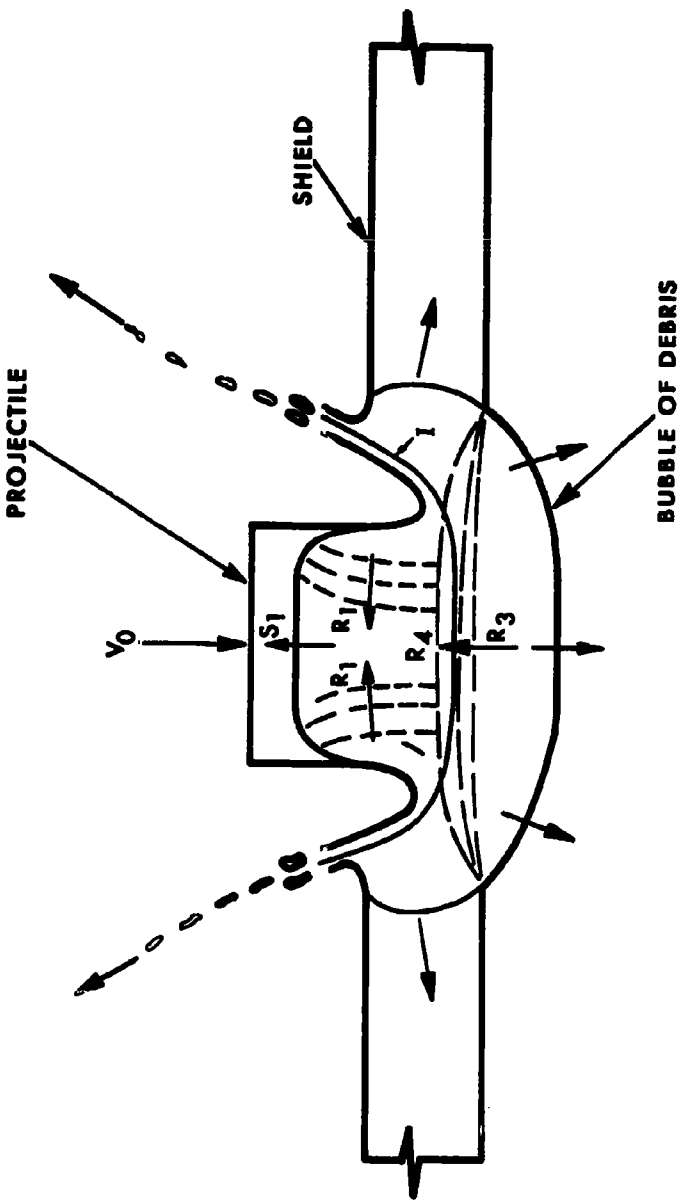

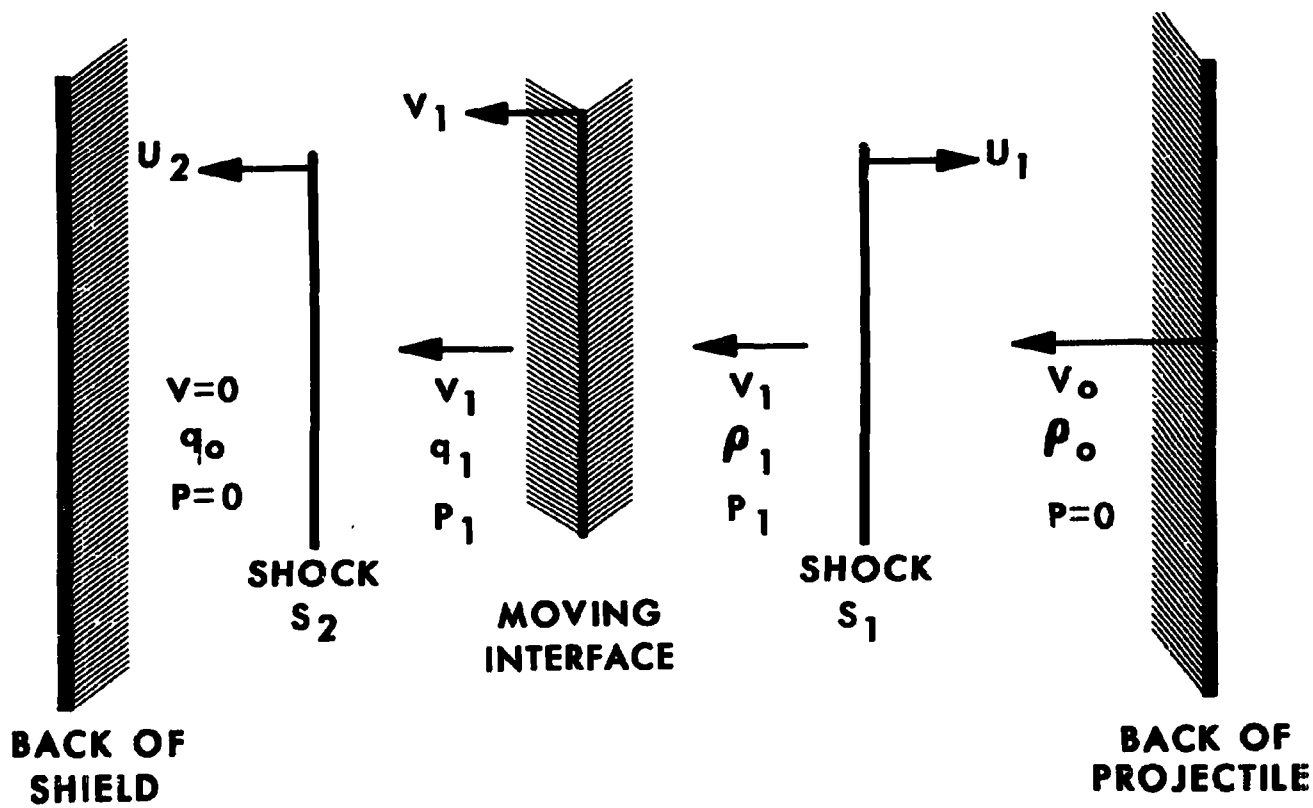

ONE-DIMENSIONAL IMPACT

PROTECTIVE ABILITY OF THIN SHIELD

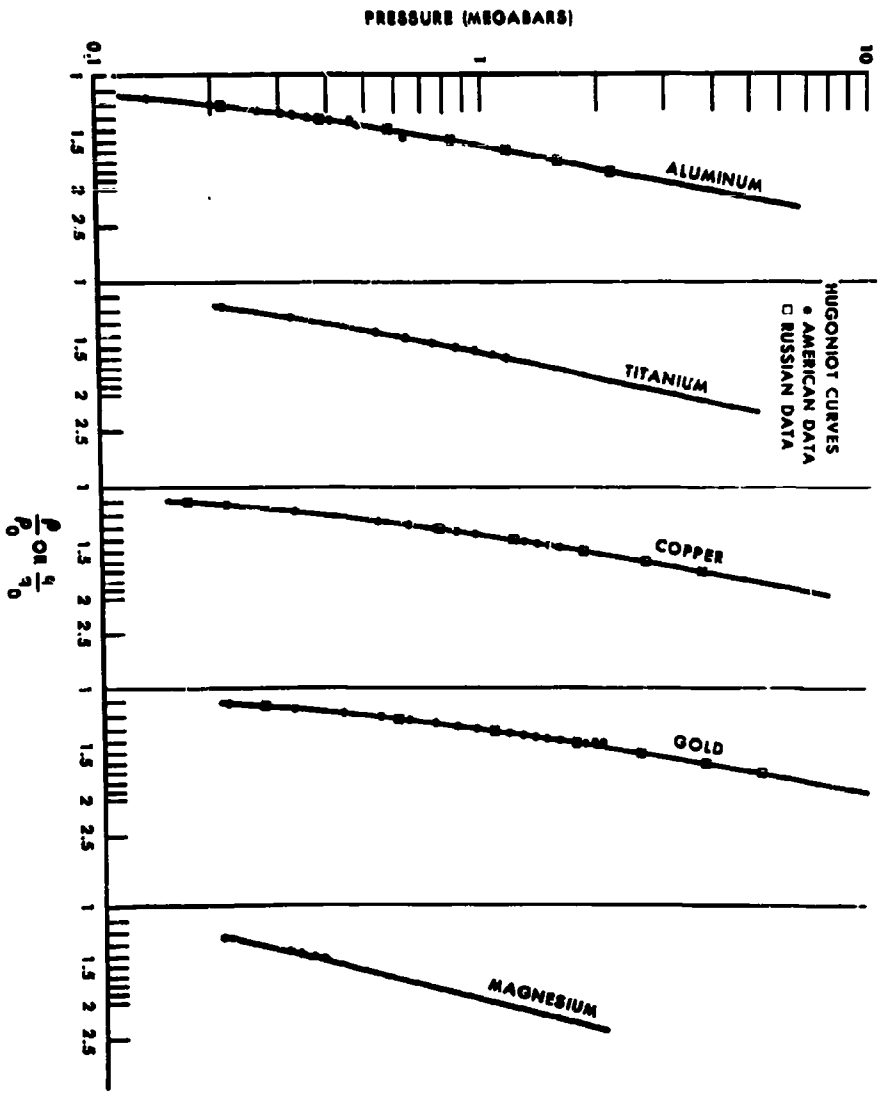

PROTECTIVE ABILITY OF THIN SHIELD

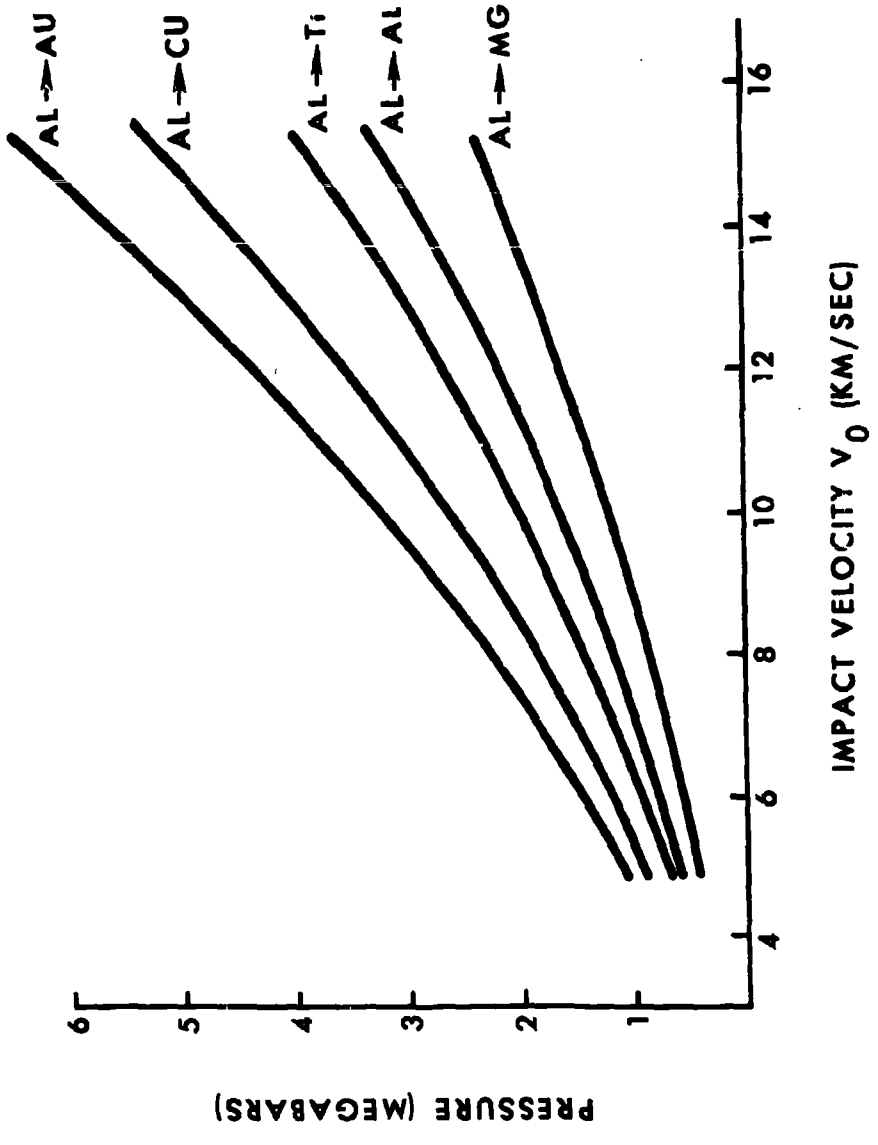

PROTECTIVE ABILITY OF THIN SHIELD

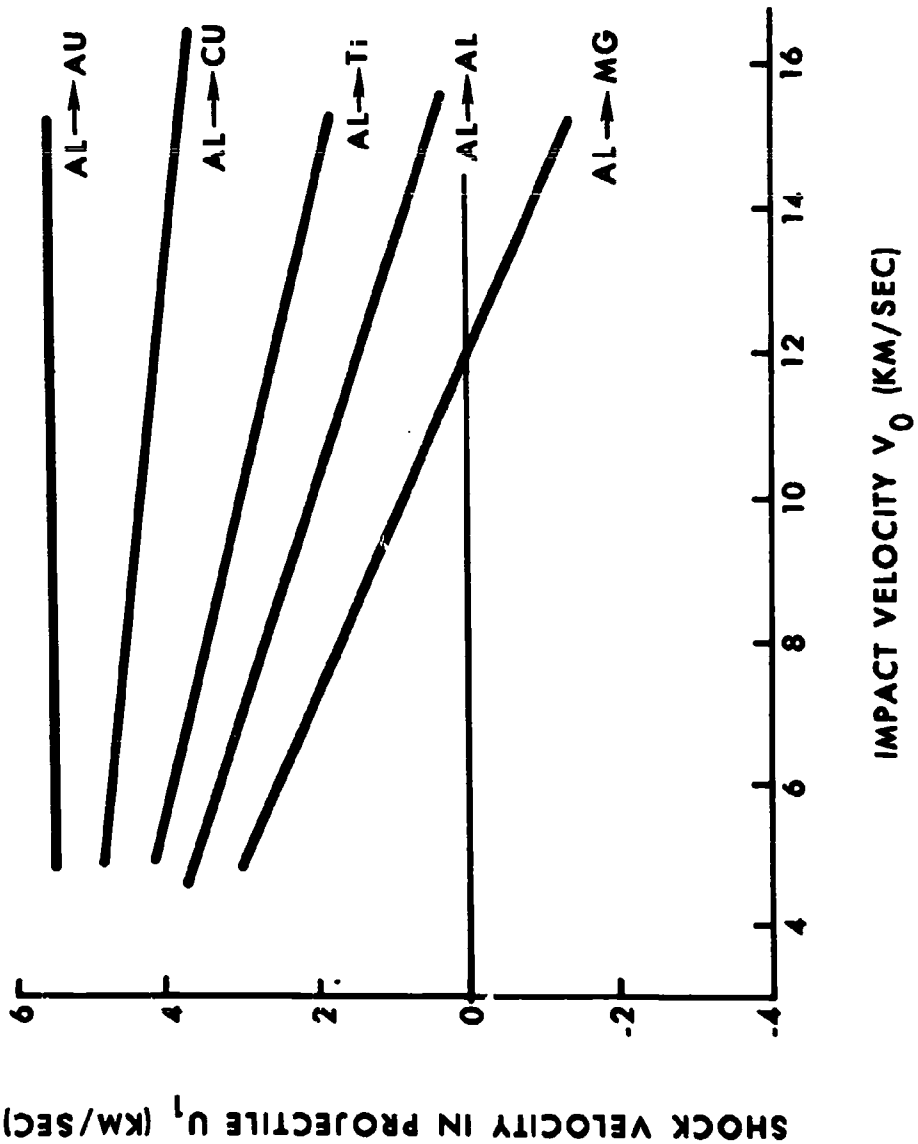

PROTECTIVE ABILITY OF THIN SHIELD

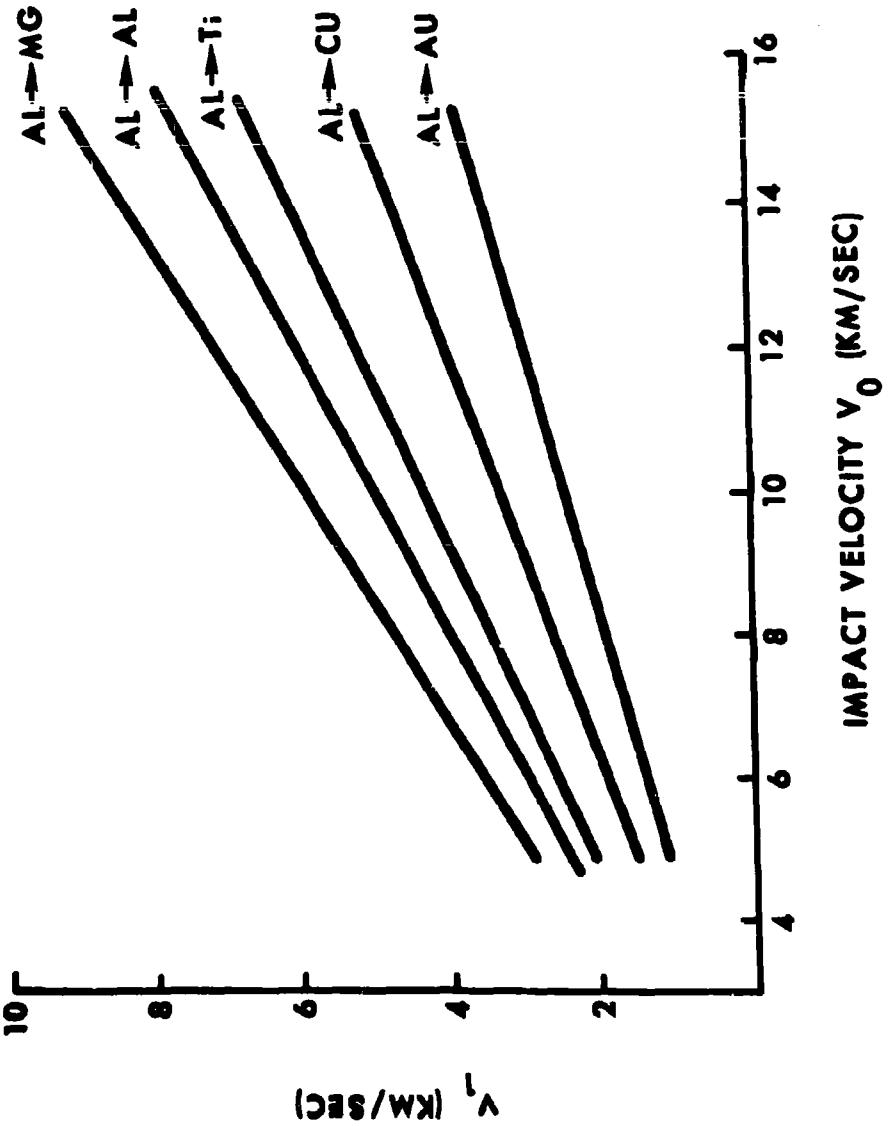

PROTECTIVE ABILITY OF THIN SHIELD

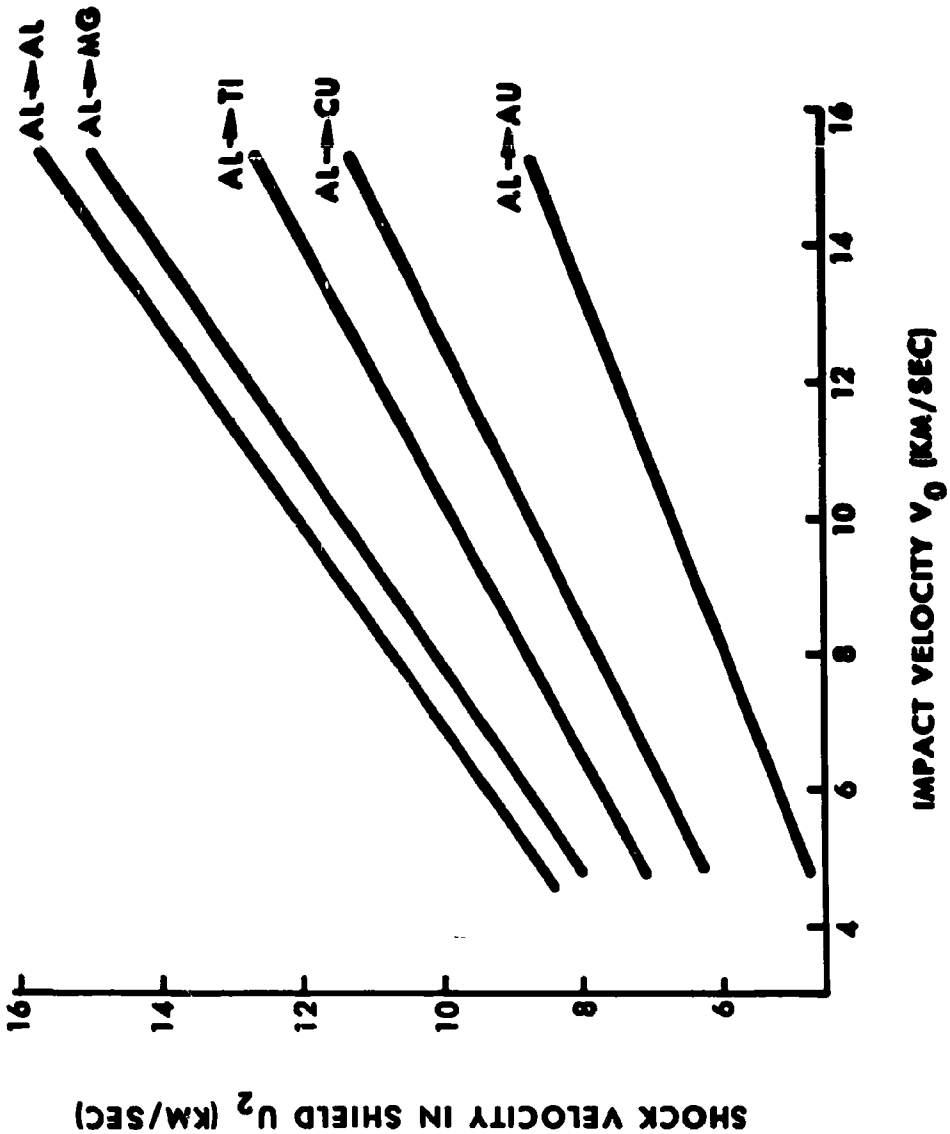

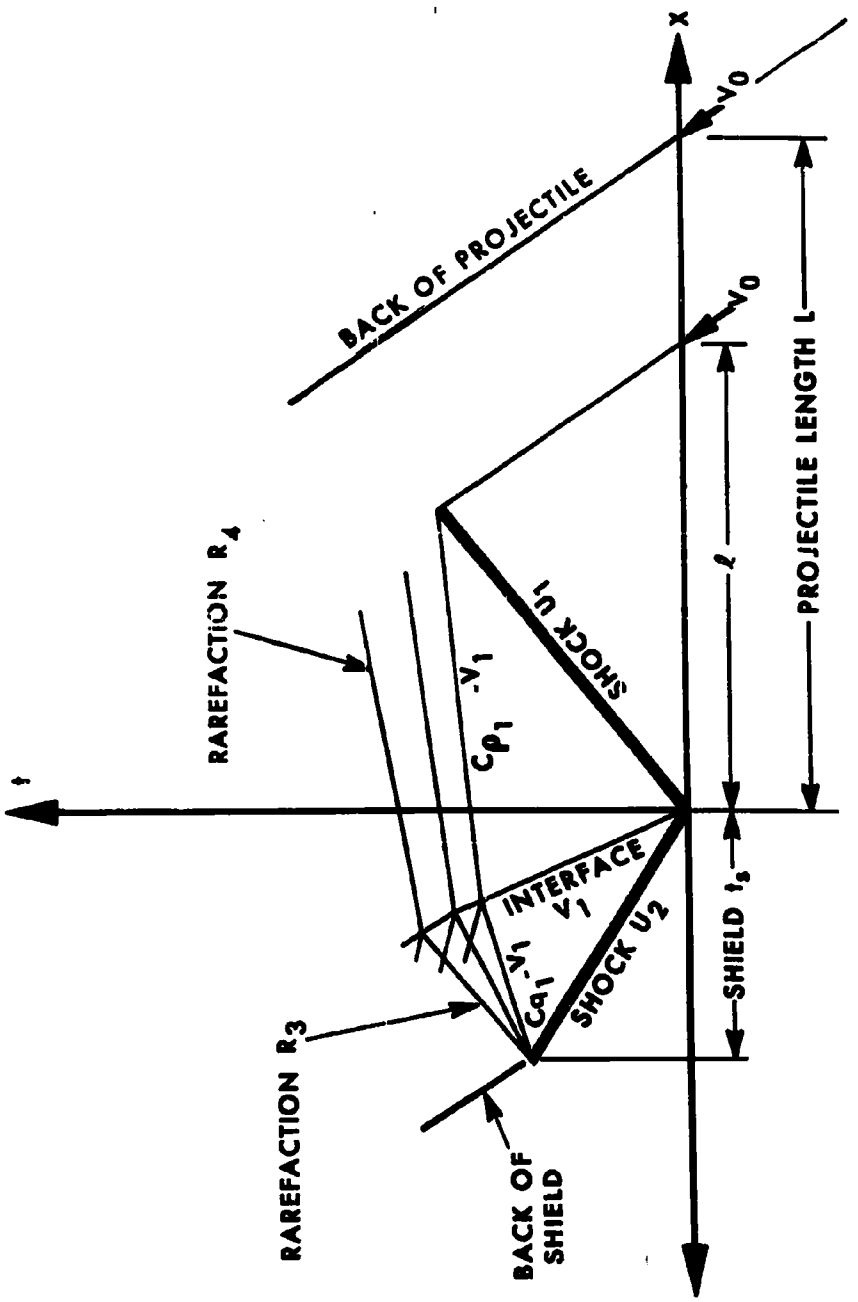
x
t
V_0
V_0
BACK OF PROJECTILE
PROJECTILE LENGTH L
ℓ
RAREFACTION R_4
$C\rho_1 - V_1$
SHOCK U_1
INTERFACE V_1
$C\rho_1 - V_1$
SHOCK U_2
SHIELD t_s
RAREFACTION R_3
BACK OF SHIELD

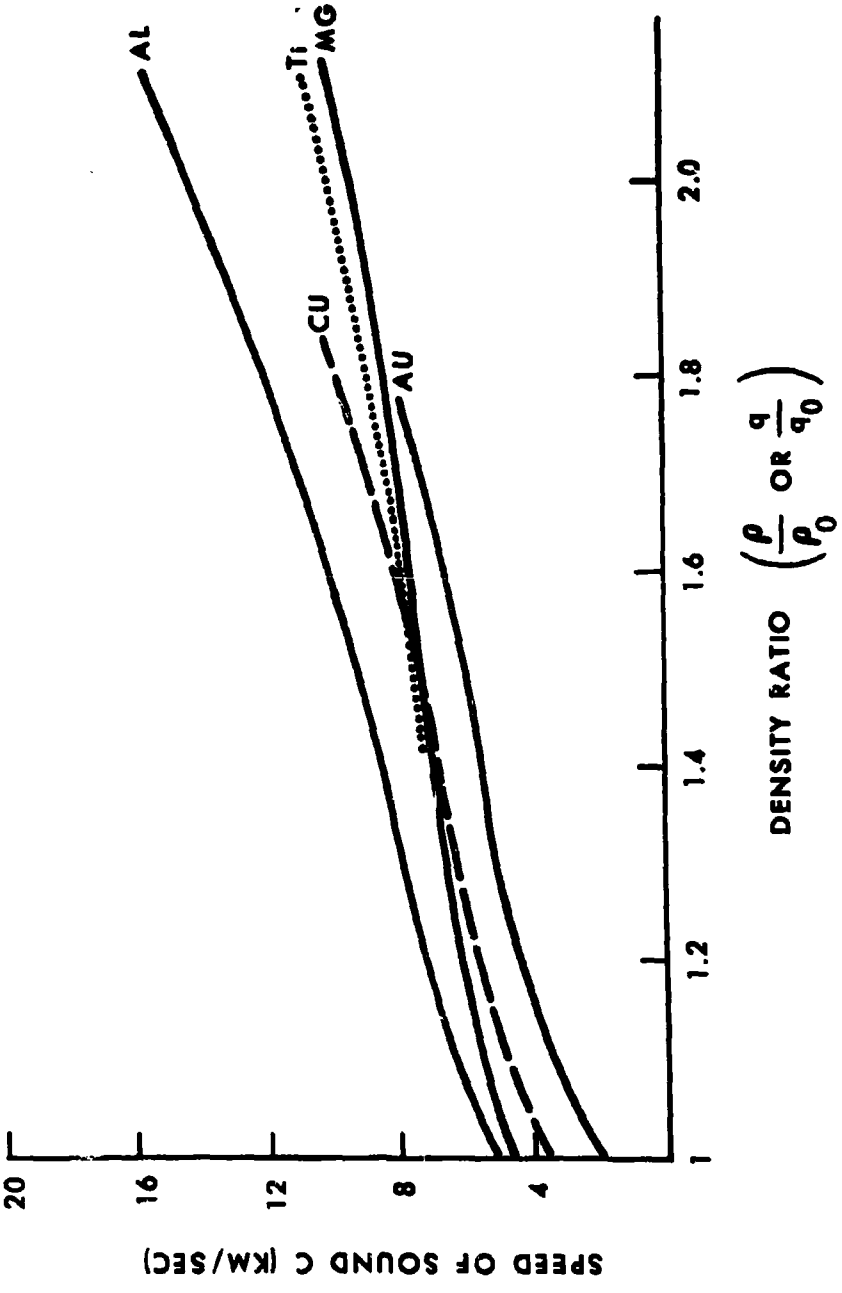
AL
Ti
MG
CU
AU
20
16
12
8
4
1
1.2
1.4
1.6
1.8
2.0
SPEED OF SOUND C (KM/SEC)
DENSITY RATIO $\left(\frac{\rho}{\rho_0} \text{ OR } \frac{q}{q_0}\right)$

PROTECTIVE ABILITY OF THIN SHIELD

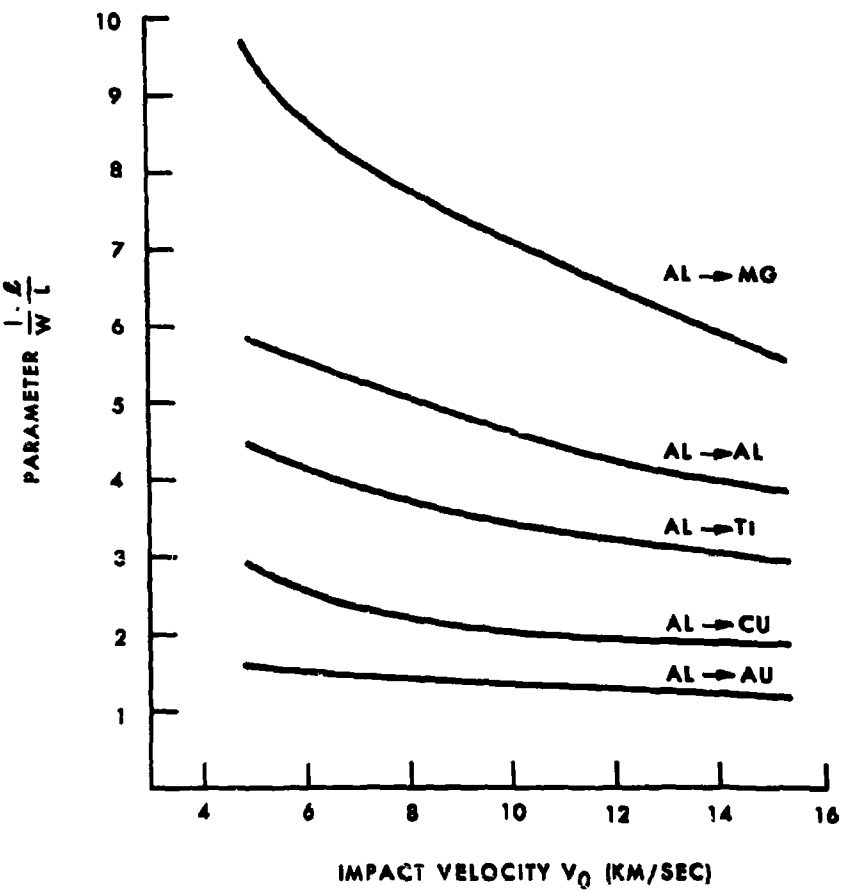

PROTECTIVE ABILITY OF THIN SHIELD

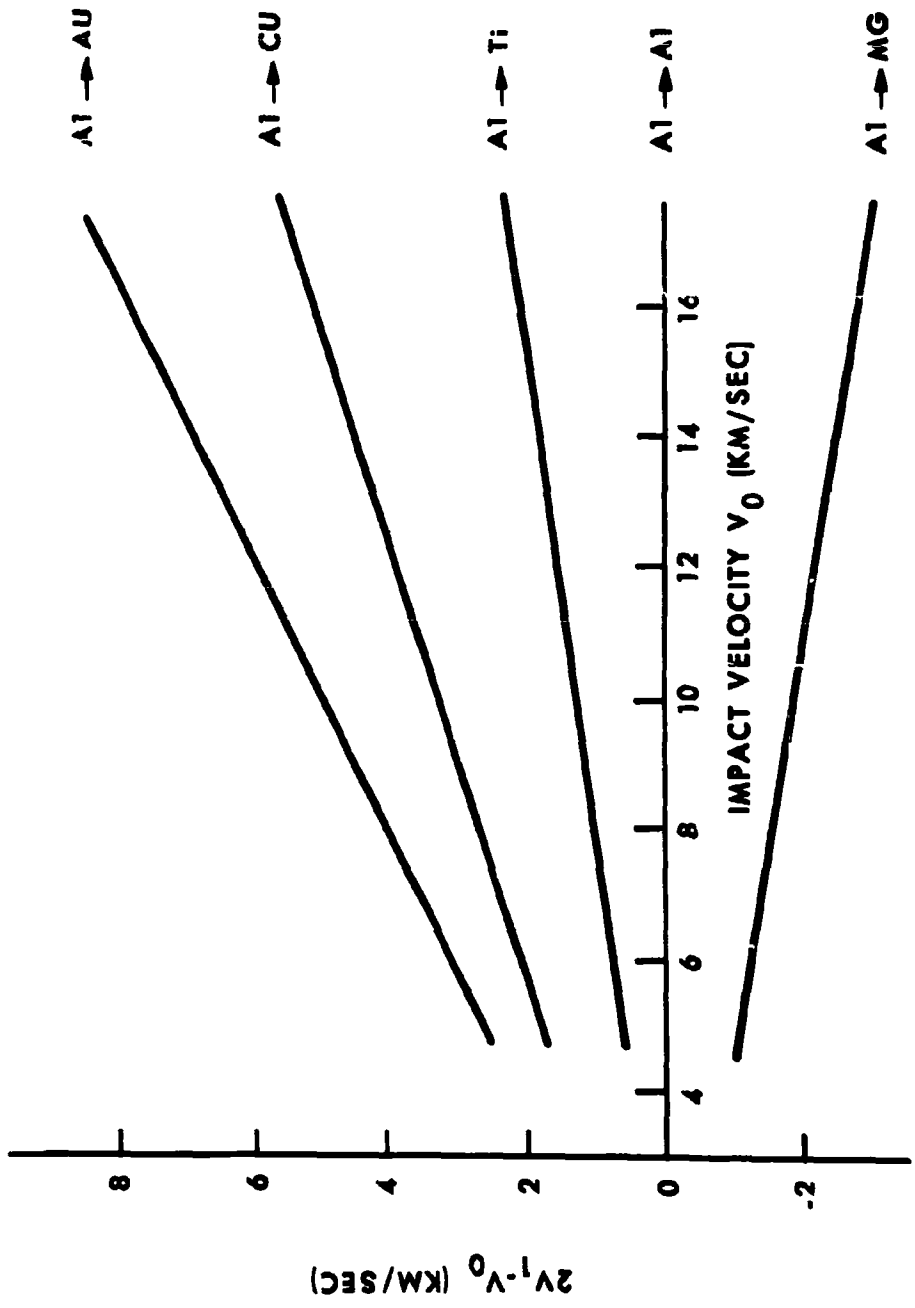

PROTECTIVE ABILITY OF THIN SHIELD

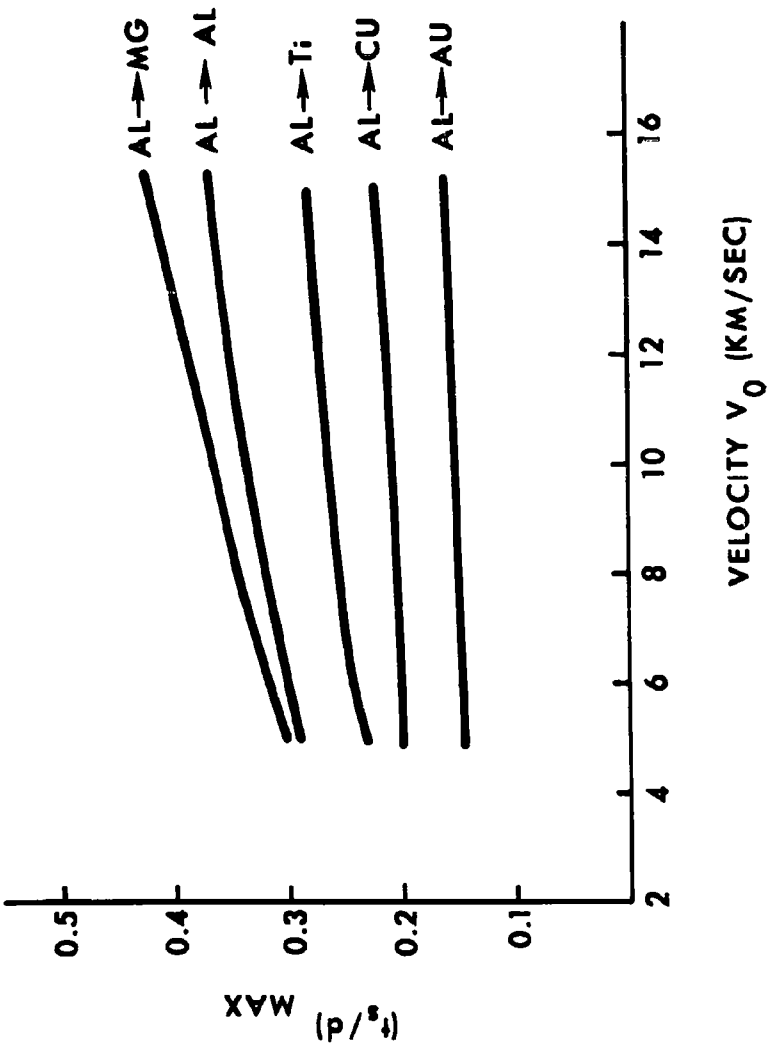

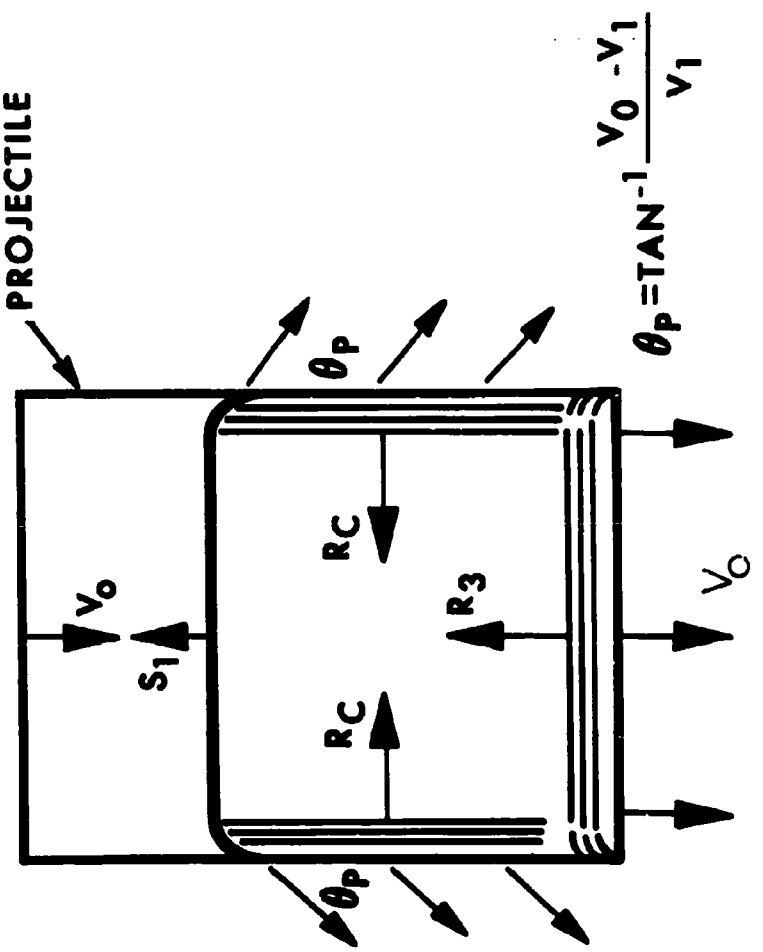

IDEALISED MODEL OF PROJECTILE FRAGMENTATION

PROTECTIVE ABILITY OF THIN SHIELD

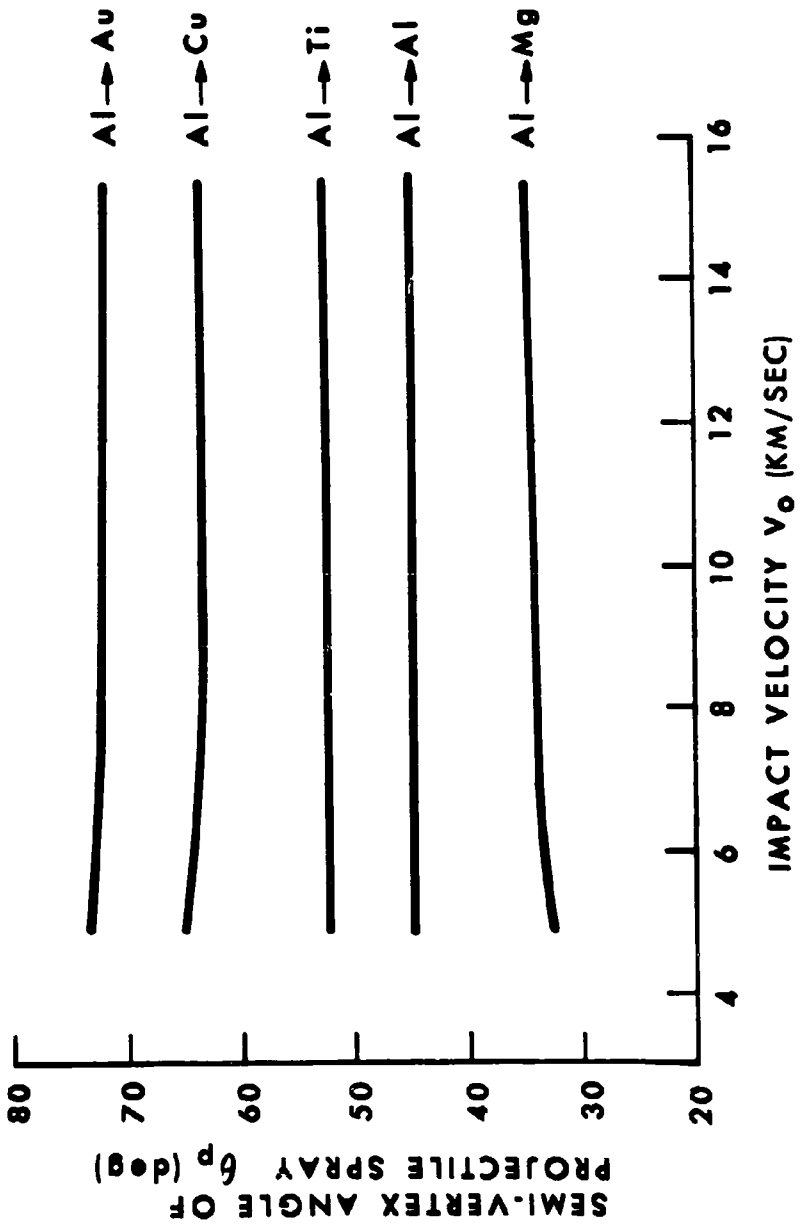

PROTECTIVE ABILITY OF THIN SHIELD

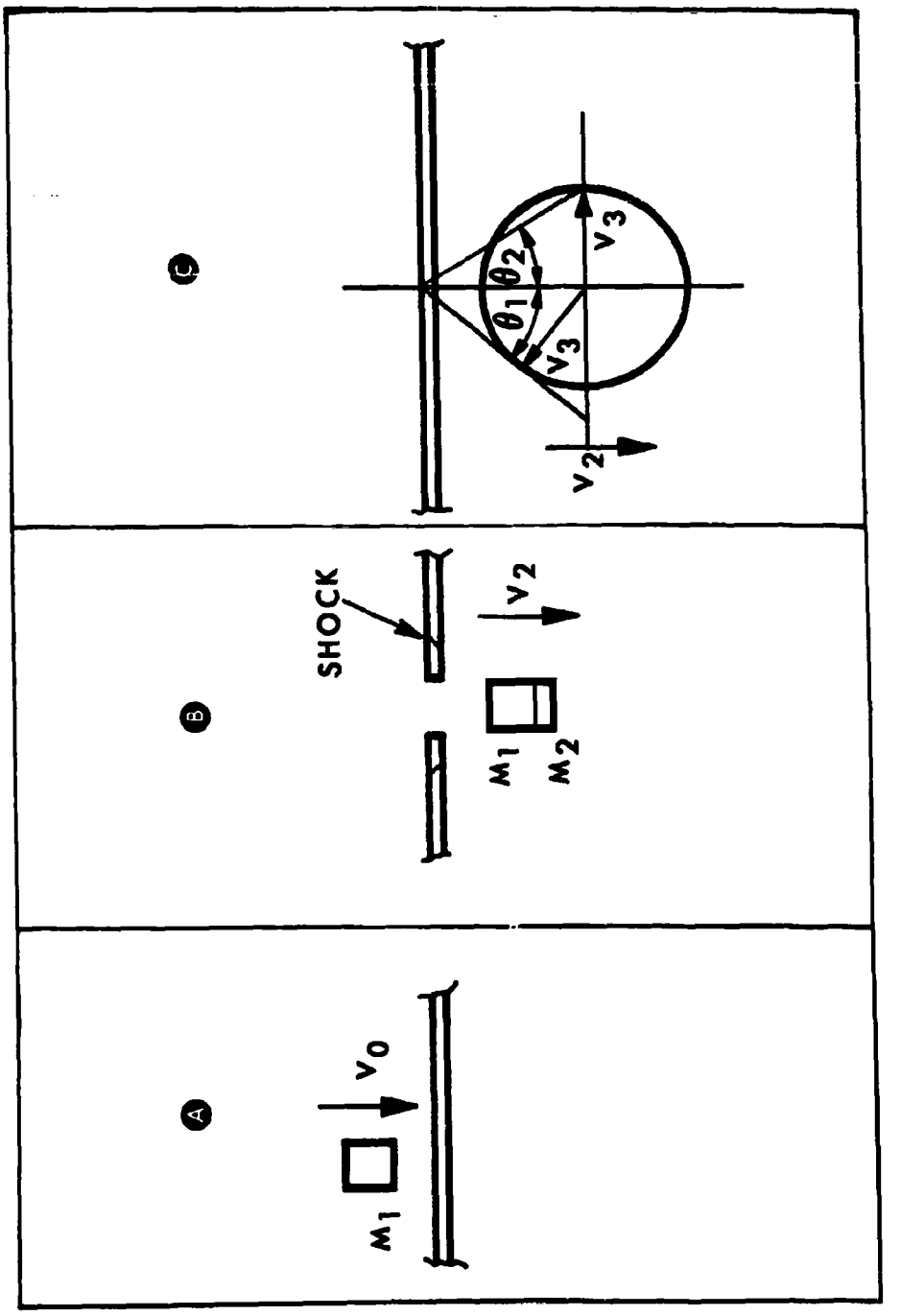

PROTECTIVE ABILITY OF THIN SHIELD

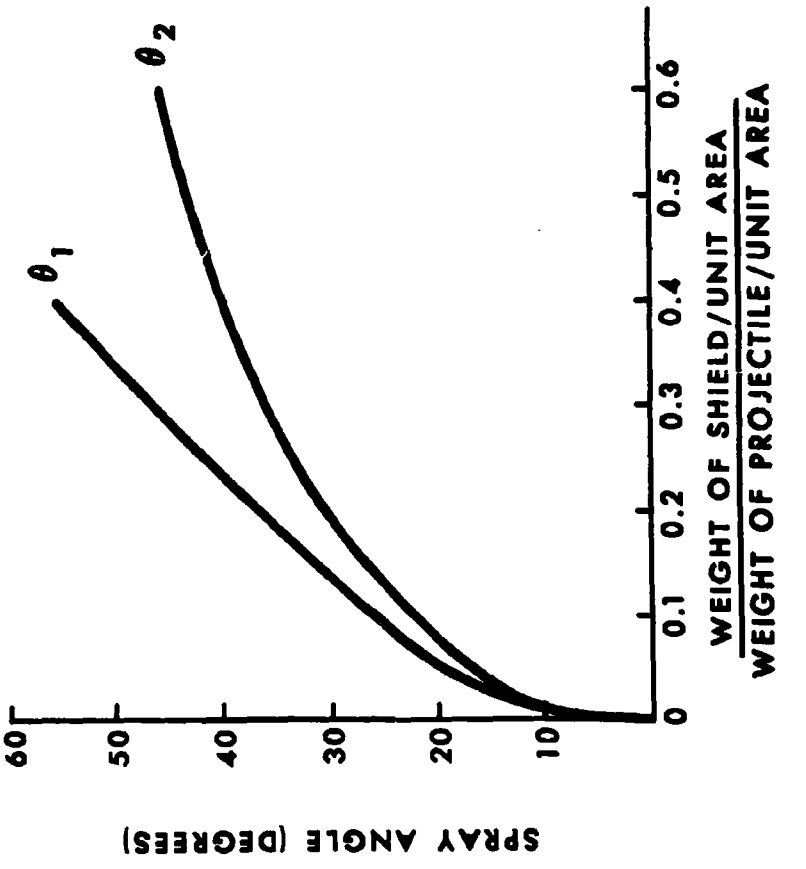

PROTECTIVE ABILITY OF THIN SHIELD

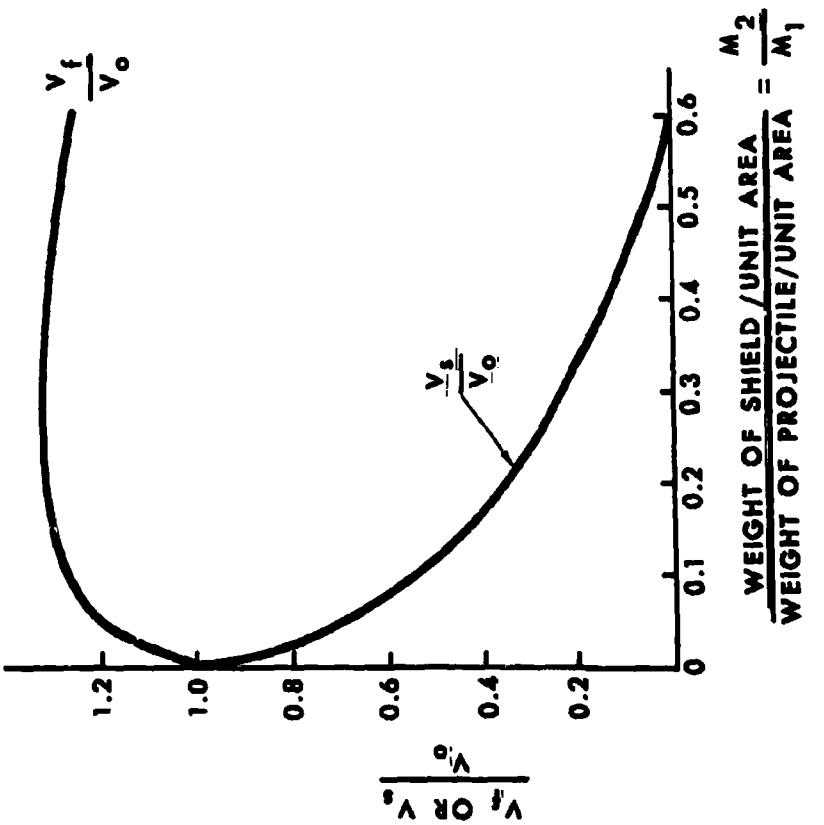

EFFECTS OF 3 TO 12 KM/SEC IMPACTS ON FINITE TARGETS

R. B. Mortensen
J. E. Ferguson
J. P. Joyce
K. N. Kreyenhagen

AEROJET-GENERAL CORPORATION
Ordnance Division
11711 Woodruff Avenue
Downey, California

3 TO 12 KM/SEC IMPACTS

ABSTRACT

This paper summarizes a series of experimental programs conducted to study hypervelocity impact and penetration phenomena for finite metal targets. Aluminum and titanium projectiles have been projected against 0.032 to 4.00-in. thick aluminum targets at velocities from 3 to 12 km/sec. Photographs and curves show the observed relations between target hole sizes, crater shapes, etc. and the projectile variables. Effect of special projectiles such as long rods and thin foils is presented.

3 TO 12 KM/SEC IMPACTS

CONTENTS

		Page No.
I.	INTRODUCTION	162
II.	ACCELERATORS	162
	A. Shaped-Charge Hypervelocity Projectile Accelerator	162
	B. Explosive Cavity Charge Projector	163
	C. Explosive Plate Projector	163
	D. Light Gas Gun	163
III.	PERFORATION OF ALUMINUM BY TITANIUM AND ALUMINUM AT 3.5 - 8.1 KM/SEC	164
	A. Titanium on Aluminum	164
	B. Aluminum on Aluminum	167
IV.	PERFORATION OF ALUMINUM BY ALUMINUM AT 9-12 KM/SEC	172
	A. Hole Size vs Projectile Area	172
	B. Penetration of Thicker Targets	176
	C. Perforation Limit	182
	D. Oblique Impacts	186
V.	SPECIAL PROJECTILE SHAPES	192
	A. Rod Projectiles	192
	B. Foils and Washers	200
	C. Hollow Spheres	202

3 TO 12 KM/SEC IMPACTS

ILLUSTRATIONS

Figure		Page No.
1.	Target Hole Area to Projectile Impact Area Ratio vs Velocity. Titanium vs Aluminum, 0.100-in. Target, 90° Obliquity, 3.7-8.1 km/sec.	165
2.	Residual Fragments from 8.2 gm Titanium Projectile Against 0.100-in. Aluminum Target, 90° Obliquity, 3.5 km/sec.	166
3.	Effect of Projectile Mass on Second Plate Damage.	168
4.	Effect of Impact Velocity on Second Plate Damage.	169
5.	Effect of Target Thickness on Thin Plate Damage. 1.0 gm Aluminum Projectile Against Aluminum Targets, 90° Obliquity, 3.7 km/sec.	171
6.	7.4 gr Aluminum Projectile after Penetration of 0.100-in. Aluminum Target. Impact and Residual Velocities 8.65 and 4.65 km/sec.	173
7.	Target Hole Area vs Projectile Area, 0.100-in. Target at 90° Obliquity, 8.1-10.3 km/sec.	174
8.	Target Hole Area vs Projectile Area, 0.100-in. Target at 90° Obliquity, 10.7-11.9 km/sec.	175
9.	Target Hole Area vs Projectile Mass, 0.100-in. Target at 90° Obliquity, 8.1-10.3 km/sec.	177
10.	Target Hole Area vs Projectile Mass, 0.375-in. Target at 90° Obliquity, 9.4-10.3 km/sec.	178
11.	Target Hole Area vs Projectile Mass, 0.500-in. Target at 90° Obliquity, 9.5-10.4 km/sec.	179
12.	Target Hole Area vs Projectile Mass, 1.000-in. Target at 90° Obliquity, 8.2-9.8 km/sec.	180
13.	Target Hole Area vs Projectile Mass for Four Target Thicknesses at 90° Obliquity, 8.2-10.4 km/sec.	181

Figure		Page No.
14.	Sectioned 1.0-in. Aluminum Target Impacted at 9-10 km/sec Showing Spalling.	183
15.	Front and Rear Spall Area, Aluminum Target at 90° Obliquity 9.8 km/sec.	184
16.	Front Spall Formation in 0.375 and 0.500-in. Aluminum Targets.	185
17.	Target Penetration vs Projectile Mass, 4.0-in. Aluminum Targets at 90° Obliquity, 8.2-10.4 km/sec.	187
18.	Target Hole Area vs Projectile Area, 0.100-in. Target at 50° Obliquity, 9.6-10.2 km/sec.	188
19.	Target Hole Area vs Projectile Area, 0.100-in. Target at 20° Obliquity, 9.6-10.1 km/sec.	189
20.	Target Hole Area vs Projectile Mass, 0.100-in. Target at 50° Obliquity, 9.6-10.2 km/sec.	190
21.	Target Hole Area vs Projectile Mass, 0.100-in. Target at 20° Obliquity, 9.6-10.1 km/sec.	191
22.	Penetration of 0.375-in. Aluminum Target at 20° Obliquity, 9.1 km/sec.	193
23.	End-on Impact, Titanium Rod Against Multiplate Aluminum Target, 3.1 km/sec.	194
24.	Side-on Impact, Titanium Rod Against Multiplate Aluminum Target, 4.1 km/sec.	195
25.	Effect of Projectile Diameter on A_1/A_{01} Ratio, Aluminum vs Aluminum at 3.5 km/sec.	197
26.	Rod Deformation During Target Penetration, Aluminum vs Aluminum, 3.5 km/sec.	199
27.	Flash Radiographs of Stainless Steel Foils Penetrating Aluminum Plate Target, 3.5 km/sec.	203

EFFECTS OF 3 TO 12 KM/SEC IMPACTS ON FINITE TARGETS

R. B. Mortensen
J. E. Ferguson
J. P. Joyce
K. N. Kreyenhagen

Aerojet-General Corporation
Downey, California

I. INTRODUCTION

This paper discusses the effects of hypervelocity impact by 0.1 to 10.0-gm aluminum and titanium projectiles from 3 to 12 km/sec against finite aluminum targets, varying in thickness from .032 to 1.000-inches. As a result of the target thickness selection, nearly all firings resulted in complete penetration. The data gathered show the effect of projectile mass and velocity on damage area in the relatively thin plate targets. Projectile breakup and secondary damage capability is described. Also discussed is the effect of target thickness upon damage area and special damage effects from such extreme projectile shapes as rods, flat thin sheets, and hollow shapes.

The work reported was performed under Contract AF 08(635)-1382 with the Weapons Laboratory, Det. 4, ASD, Eglin Air Force Base, and under Contracts AF 08(635)-975 and AF 08(635)-2552 with the Ballistics Branch, Directorate of Aerospace, Eglin Air Force Base.

II. ACCELERATORS

Four acceleration techniques were employed to obtain flexibility in the several hundred impact experiments which form the basis for these studies. Since special projectors are the subject of another paper (Reference 1) at this symposium, no detailed description will be given here. The projectors are:

A. The Shaped-Charge Hypervelocity Projectile Accelerator

This is a specially adapted shaped charge that, through special initiation, projects discrete aluminum fragments in the 0.1 to 1.0-gm range at

velocities up to 12 km/sec. The majority of data have been in the 8 to 10-km/sec range, obtained with a 42° cone liner. Higher velocities are obtained from a 25° cone liner.

B. Explosive Cavity Charge Projector

This projector, which has been described in detail at earlier symposia, basically consists of a 2-in.-dia x 6-in.-long explosive cylinder that is initiated from one end through a tetryl booster. The projectile is mounted in a cavity in the opposite end of the cylinder. Through use of various explosives (TNT, Composition C-4, Composition B, and Octol) and by changing the diameter and depth of the cavity, 0.1 to 10.0-gm titanium discs have been projected at velocities from 3 to 6.5 km/sec. Actual recovery of projectiles form the basis for determination of the shape and mass of the projectiles at the time of impact. This projection technique has been used for the majority of firings with compact projectiles. It has also been used for firing with square cross-section rod projectiles (L/D of 3 and 10), either for side-on impact or, through controlled tumbling, for end-on impact.

C. Explosive Plate Projector

This projector is used for all projectiles that, due to material or shape, are unsuited for acceleration in light gas guns or explosive projectors. The explosive plate projector can be used at velocities as high as 3.5 km/sec with a 5 x 5 in., 0.100-in.-thick aluminum plate. This target plate has been standard for a majority of test firings with explosive projectiles, thin foils, very thin rods, and hollow, thin-wall spheres. In special cases, a 6 x 6-in. plate has been used. Target damage is ascertained from orthogonal flash radiograph pictures obtained at various times during and after penetration. The damage area measurements obtained through this method are believed accurate within 1%.

D. Light Gas Gun

A 20mm, 0.30 Cal light gas gun of the NRL type has been used for a number of firings with aluminum and titanium compact and rod-shaped projectiles. Most of these firings have been in the 3 to 4-km/sec range.

III. PERFORATION OF ALUMINUM BY TITANIUM AND ALUMINUM AT 3.5-8.1 KM/SEC

A. Titanium on Aluminum

Titanium discs, L/D 1/3, and ranging in mass from .083 to 8.2 grams, have been impacted against 0.100-in.-thick 2014-T6 aluminum target plates in order to study the hole formation, the projectile breakup, and the damage to second target plates behind the initial plate. Most of these tests used the cavity charge to accelerate the discs against a stationary target plate. The higher velocities, however, required an arrangement wherein cavity charges and explosive plate projectors were counterfired towards each other.

1. Hole Area vs Impact Velocity

Figure 1 summarizes the effect of impact velocity upon the area of the hole produced in the initial target plate. Hole size data have been normalized by dividing by the area of the impacting projectiles (in this case, by the average presented area of a tumbling projectile, since orientation at impact was not determined). The ratio of hole area to projectile area is seen to increase with higher velocities, but at a decreasing rate. It was interesting to observe in the several hundred firings which are summarized by Figure 1 that the target holes were always circular or nearly so, despite the fact that many of the tumbling projectiles impacted on edge.

2. Projectile Breakup

When projectiles impact thin plates, the interactions of the strong shock wave with the sides and back of the projectile and with the free front and rear surfaces of the target produce several distinct phenomena which are nearly always observable. These are: a. "Spraying" of high velocity particles from the front surface of the target adjacent to the impact zone, b. Ejection of an envelope of spall particles from the rear surface of the target. These are mentioned in a subsequent section of this paper. c. Extensive fragmentation of the projectile, such that compact projectiles will emerge from targets of reasonable thicknesses in several or many small pieces.

The magnitude of this fragmentation is illustrated by the size distribution given in Figure 2 for the residual fragments recovered after penetration

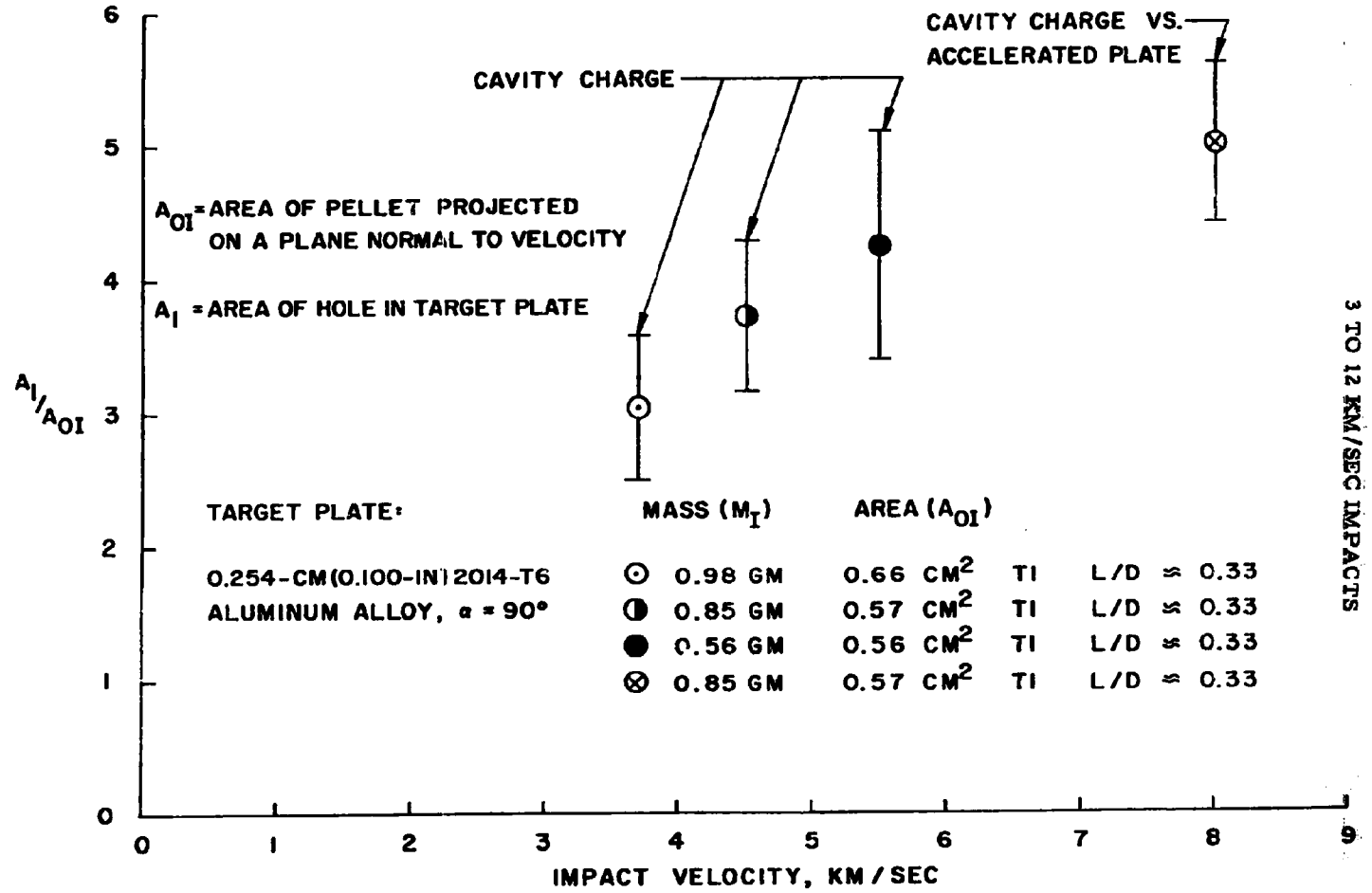
CAVITY CHARGE VS. ACCELERATED PLATE
CAVITY CHARGE
A_{OI} = AREA OF PELLET PROJECTED ON A PLANE NORMAL TO VELOCITY
A_I = AREA OF HOLE IN TARGET PLATE
A_I/A_{OI}
TARGET PLATE:
0.254-CM (0.100-IN) 2014-T6 ALUMINUM ALLOY, α = 90°
MASS (M_T)
AREA (A_{OI})
⊙ 0.98 GM 0.66 CM^2 TI L/D ≤ 0.33
◑ 0.85 GM 0.57 CM^2 TI L/D ≤ 0.33
● 0.56 GM 0.56 CM^2 TI L/D ≤ 0.33
⊗ 0.85 GM 0.57 CM^2 TI L/D ≤ 0.33
3 TO 12 KM/SEC IMPACTS
IMPACT VELOCITY, KM/SEC
0 1 2 3 4 5 6 7 8 9
0 1 2 3 4 5 6

3 TO 12 KM/SEC IMPACTS

of a 0.100-in. aluminum plate by a 8.2-gram titanium disc impacting at 3.7 km/sec. The pressure generated by impact under these conditions can be calculated from Hugoniot data to be 478 kilobars. Target spall particles and projectile fragments were separated by flotation. The projectile was broken into more than 3,500 fragments.

3. Second Plate Perforation

Perforation of a second target plate will occur either (1) if the energy or momentum density of the dispersing pattern of residual fragments and spall particles is adequate, or (2) if any individual fragment is large enough and fast enough to penetrate through. With increased spacing between the target plates, the density of the fragment pattern will drop rapidly, and there will be a corresponding drop in the effectiveness of the initial criteria. The second criteria, on the other hand, is independent of spacing (neglecting possible atmospheric conditions). The existence of individual fragments capable of penetrating the second target, however, either means that the projectile was large relative to the initial target, or else that the impact velocity was relatively low so that fragmentation was not excessive.

Figure 3 illustrates the efficiency of larger projectile masses upon damage to a second target plate. Here damage is characterized as the total area of perforations in the second plate, A_2, normalized by dividing by the area of the projectile which impacted the initial target, A_{0I}. Impact velocity and plate spacing were held constant at 3.7 km/sec and 12-inches. An increase in the second plate damage efficiency is seen with increasing projectile masses, due to the fact that these larger projectiles are less completely fragmented as a result of impact with the initial target.

The effect of impact velocity upon second plate damage is shown in Figure 4. (Unfortunately, it was impossible to hold projectile mass constant, and it varied in a narrow range in this experiment. However, the use of the ratio of total perforation area to initial impact area, A_2/A_{0I} to express second plate damage effectively minimizes the small mass effect of this variation.) At the two impact velocities of 3.7 and 4.6 km/sec the impact pressures are 478 and 630 kilobars. The increased projectile breakup caused by the higher shock strengths results in the reduced second plate damage efficiency seen in Figure 4.

B. Aluminum on Aluminum

A light gas gun was used to study the effect of target plate thickness upon the hole diameter produced by impacts at 3.7 km/sec.

3 TO 12 KM/SEC IMPACTS

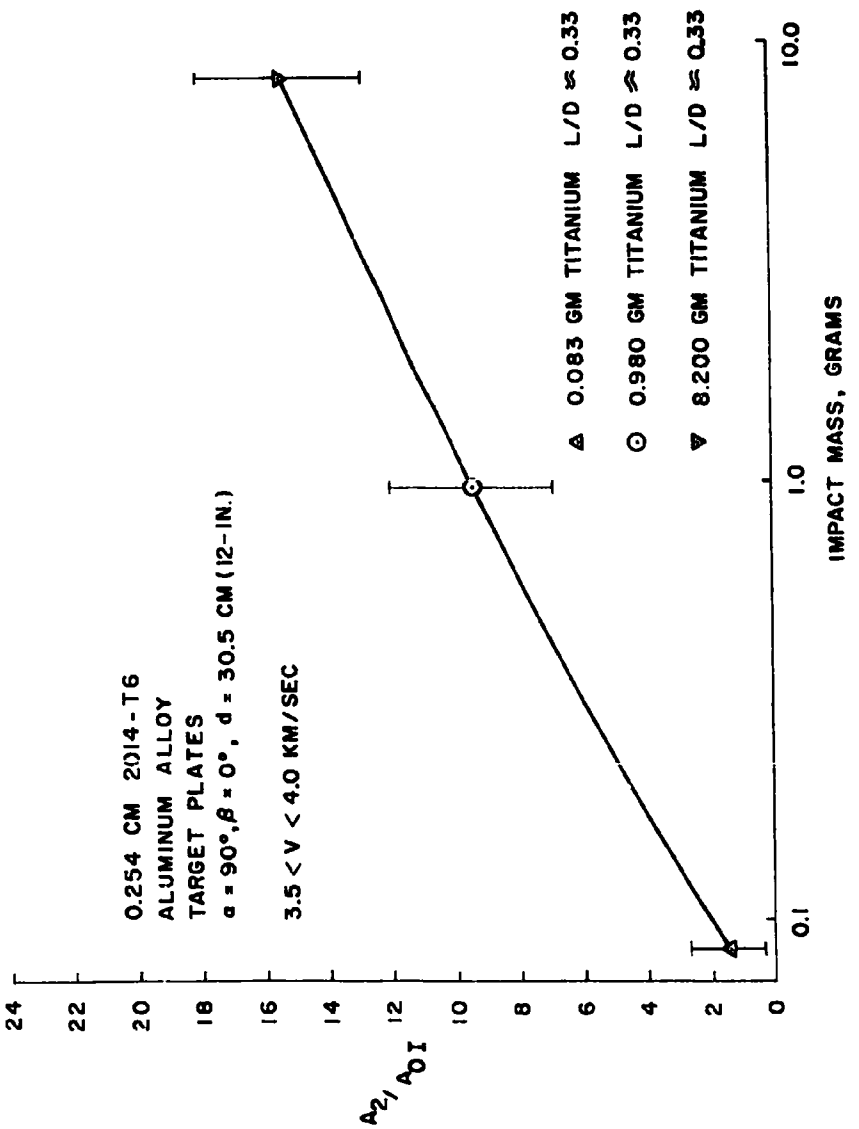

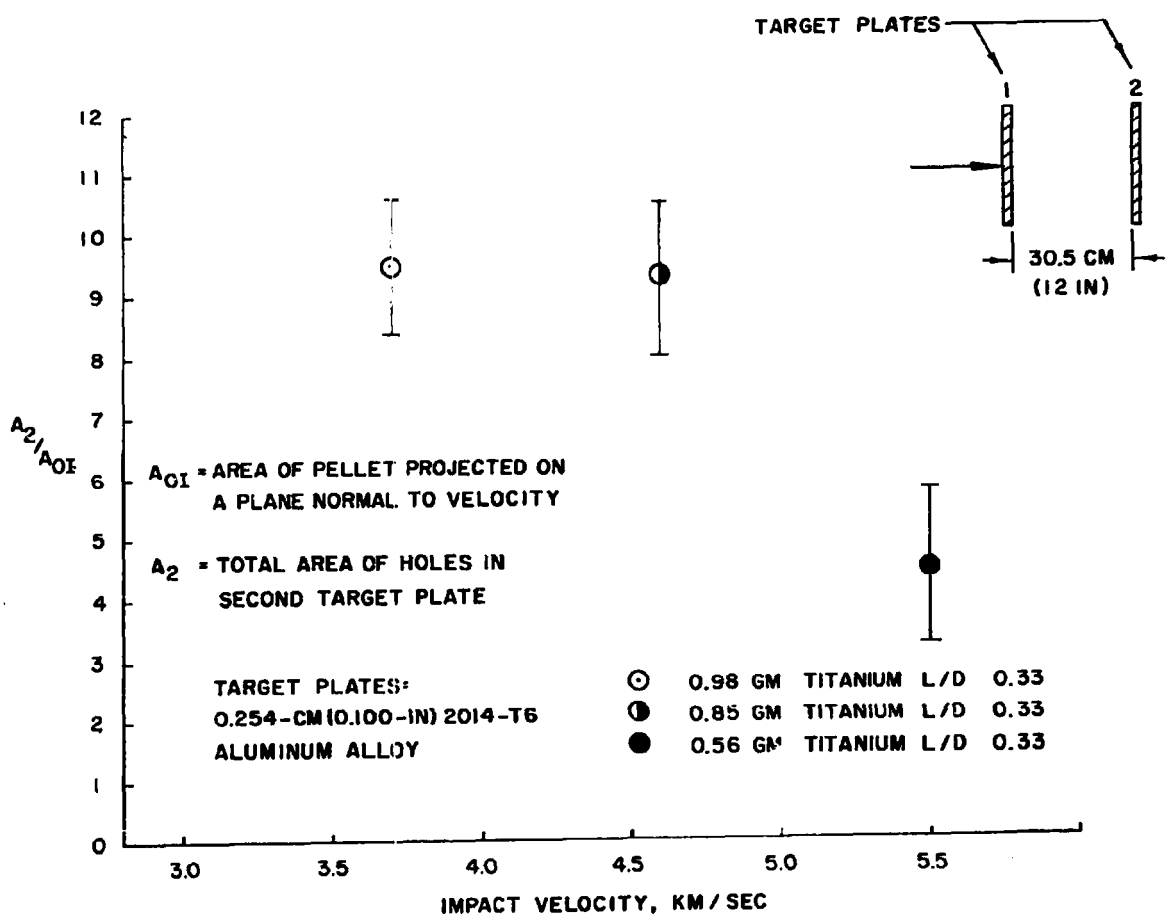

3 TO 12 KM/SEC IMPACTS

3 TO 12 KM/SEC IMPACTS

1. Hole Size and Residual Velocity vs Thickness - 3.7 km/sec

Table I summarizes results of firings of 0.3-in. dia x 0.3-in. long 1-gram aluminum cylinders at 3.7 km/sec on aluminum alloy target plates of various thicknesses. For these experiments, the velocity of the fastest particles flying off the rear surface of the target plate were also measured. One expects that as the target thickness approaches zero, the hole diameter will approach the diameter of the projectile, and in addition, as the target thickness goes to infinity, the crater diameter will become the diameter of a crater in a semi-infinite target. Figure 5 contains a plot of the hole size data for the four thicknesses given in Table I, and the data is seen to follow expectations. Three representative target plates are also shown; the formation of a more distinct lip around the hole for the thicker plates is noticeable.

Table I.

One-Gram Aluminum Cylinders (0.3-in. dia x 0.3-in. long) Impacting 2014-T6 Aluminum at 3.7 Km/sec.

Target Thickness (in.)	Hole Diameter (in.)	A_1/A_0	Maximum Residual Velocity (km/sec)
0.032	0.45	2.25	3.30
0.052	0.54	3.2	3.21
0.071	0.66	4.7	3.10
0.100	0.67	4.7	2.93

The maximum residual velocities shown in Table I drop with increasing plate thickness. Hydrodynamic considerations tell us that, assuming no attenuation and neglecting strength effects, the first spall layer will be ejected at a velocity equal to the impact velocity where the projectile and target are the same material. (Where the projectile is denser than the target, the spall velocity will be higher than the impact velocity, and where the projectile is less dense, the spall velocity will be lower.) For the case at hand, the fact that the observed spall velocity was less than the impact velocity even for the .032-in. target suggests the influence of

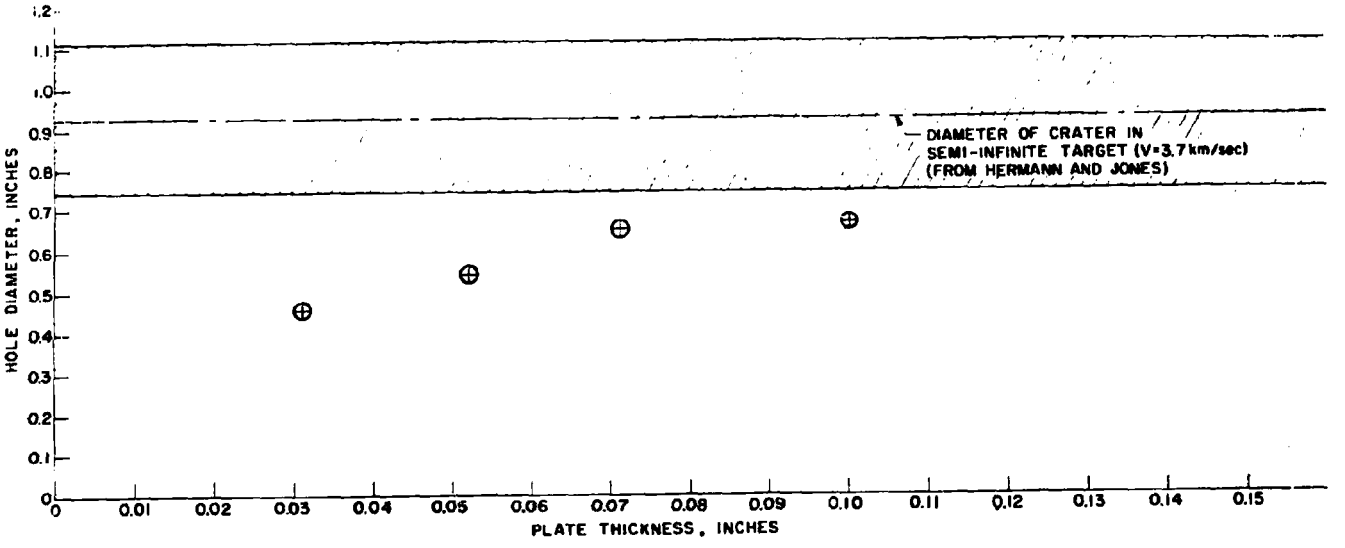

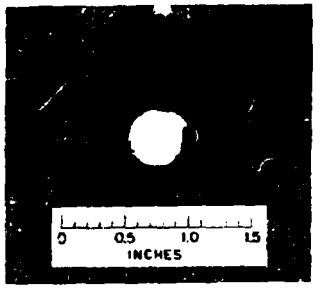

0.032 - INCH

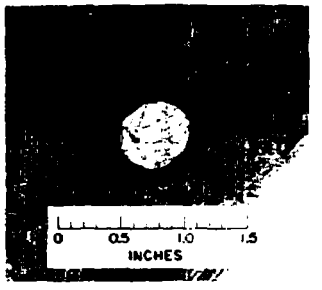

0.071 - INCH

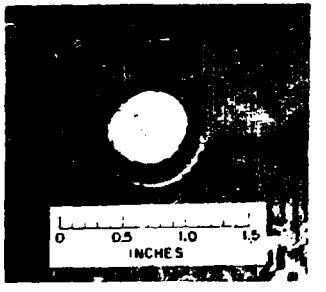

0.100 - INCH

strength effects at the rear surface of the target. The observed drop in spall velocity with increasing thickness is consistent with attenuation of the peak wave pressure as it traverses the targets.

IV. PERFORATION OF ALUMINUM BY ALUMINUM AT 9-12 KM/SEC

The perforation of thin plates by projectiles impacting at much higher velocities (9-12 km/sec) follow the same general mechanisms which have been observed in lower regimes. Impact produces strong shocks in both the target and projectile. Interactions of these shocks with the free surfaces of the system cause spallation of the target, formation of the hole boundaries, and extensive fragmentation of the projectile. Figure 6 is a radiograph of a typical perforation in this velocity range. This was taken shortly after impact of an aluminum projectile (7.4 grain) at approximately 8.6 km/sec on a 0.100-in. aluminum alloy target plate. The same splash of particles from the front surface and the envelope of spall particles from the rear surface as are observed at lower velocities are seen, except that the particles are so small as to be individually indistinguishable. The projectile fragments are apparently contained in the spall envelope. The maximum velocity of the leading fragments is 4.65 km/sec or 54% of the impact velocity.

A. Hole Size vs Projectile Area

For target plates up to about a thickness corresponding to the major dimension of the projectile, the major determinant of hole size appears to be the cross-sectional area of the projectile striking the target (the impact area). Figures 7 and 8 are plots of data for firings against 0.100-in. target plates in two velocity ranges, 8.1 to 10.3 km/sec and 10.7 to 11.9 km/sec. The scatter in these and in subsequent curves is due primarily to the inclusion of data covering both a range of impact velocities and a range of projectile shapes and impact orientations. Other factors contributing to the scatter are discussed in Reference 1.

The impact area is, of course, the origin of the pressure pulse which propagates into the target material. Interaction with the free surfaces of a thin plate target cause it to fracture, and also cause very rapid attenuation of the shock wave as it travels transversely. The peak pressure quickly drops to a critical level where fracture no longer occurs, thereby establishing the periphery of the hole. As a first order approximation, one expects that, for a given velocity and target thickness, this critical level would be reached at a constant distance from the edges of

3 TO 12 KM/SEC IMPACTS

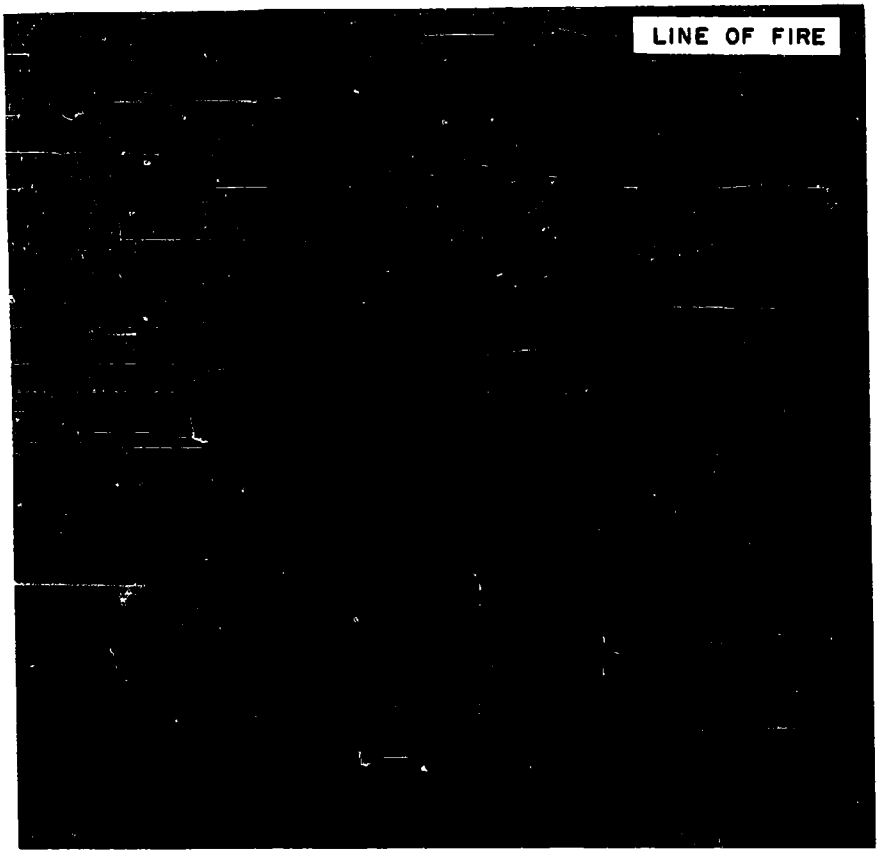

TARGET HOLE AREA VS PROJECTILE AREA*

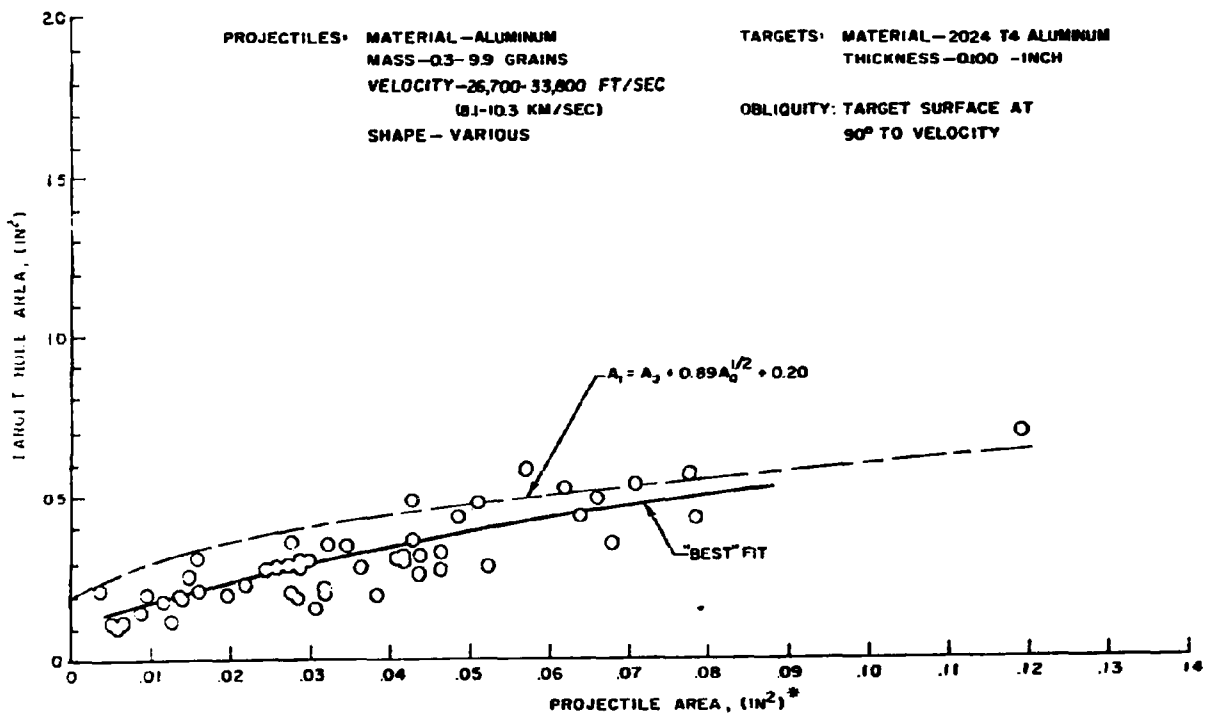

*ON PLANE NORMAL TO VELOCITY

3 TO 12 KM/SEC IMPACTS

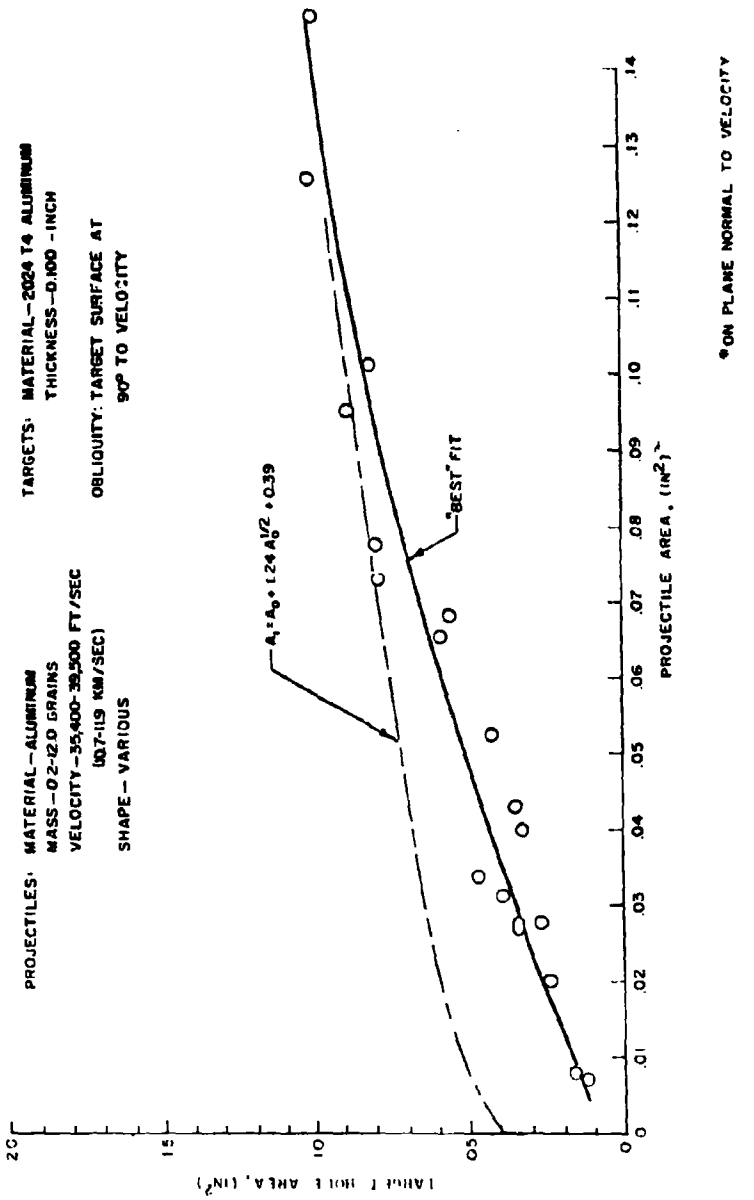
TARGET HOLE AREA VS PROJECTILE AREA*
PROJECTILES: MATERIAL—ALUMINUM
MASS—0.2-12.0 GRAINS
VELOCITY—35,400-39,500 FT/SEC
(10.7-11.9 KM/SEC)
SHAPE—VARIOUS
TARGETS: MATERIAL—2024 T4 ALUMINUM
THICKNESS—0.100 - INCH
OBLIQUITY: TARGET SURFACE AT
90° TO VELOCITY
$A_t = A_p + 1.24 A_p^{1/2} + 0.39$
"BEST" FIT
TARGET HOLE AREA, (IN^2)
PROJECTILE AREA, (IN^2)
0
.01
.02
.03
.04
.05
.06
.07
.08
.09
.10
.11
.12
.13
.14
0
.5
1.0
1.5
2.0
*ON PLANE NORMAL TO VELOCITY

the impact area, or, stated another way, that the hole radius will be larger than the radius of the impact area by a fixed increment, as shown in the following sketches by "a".

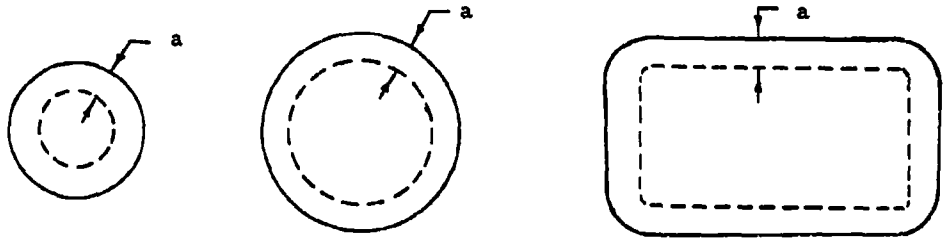

This approximation neglects, of course, the attenuation of the shock wave due to geometrical dispersion. This dispersion would have the effect of reducing "a" where the radius of curvature of the impacting area is smaller.

On Figures 7 and 8, the data points appear to converge with curves of a form based upon the above-described approximation. The value of "a" was found to be 0.25-inches, for the 8.1-10.3 km/sec data and 0.35-inches for the 10.7-11.9 km/sec data.

B. Penetration of Thicker Targets

A series of experiments were performed using the shaped charge projectile accelerator to impact aluminum upon aluminum alloy targets of 0.100-in., 0.375-in., 0.500-in., and 1.000-in. thicknesses. Data from these experiments are given in Figures 9, 10, 11, and 12. These are plots of the hole area vs projectile mass, since for targets which are thicker than roughly the major dimensions of the projectile, mass appears more important than impact area in determining the hole size. The 0.100-inch plot is included here only for crude comparison, since the scatter is excessive. Figure 13 is a summary of data in the form of best fit curves for the four target thicknesses. The results show that a given projectile will make an appreciably larger hole in either a 0.375, 0.500, or 1.000-in. thick target than in a 0.100-in. thick target, but the differences between the three thicker targets themselves are barely detectable. One expects that, for a given projectile and impact velocity, the diameters of the hole at the target surface will increase with increasing target thickness, becoming asymptotic to the crater diameter in a semi-infinite target.

TARGET HOLE AREA VS PROJECTILE MASS

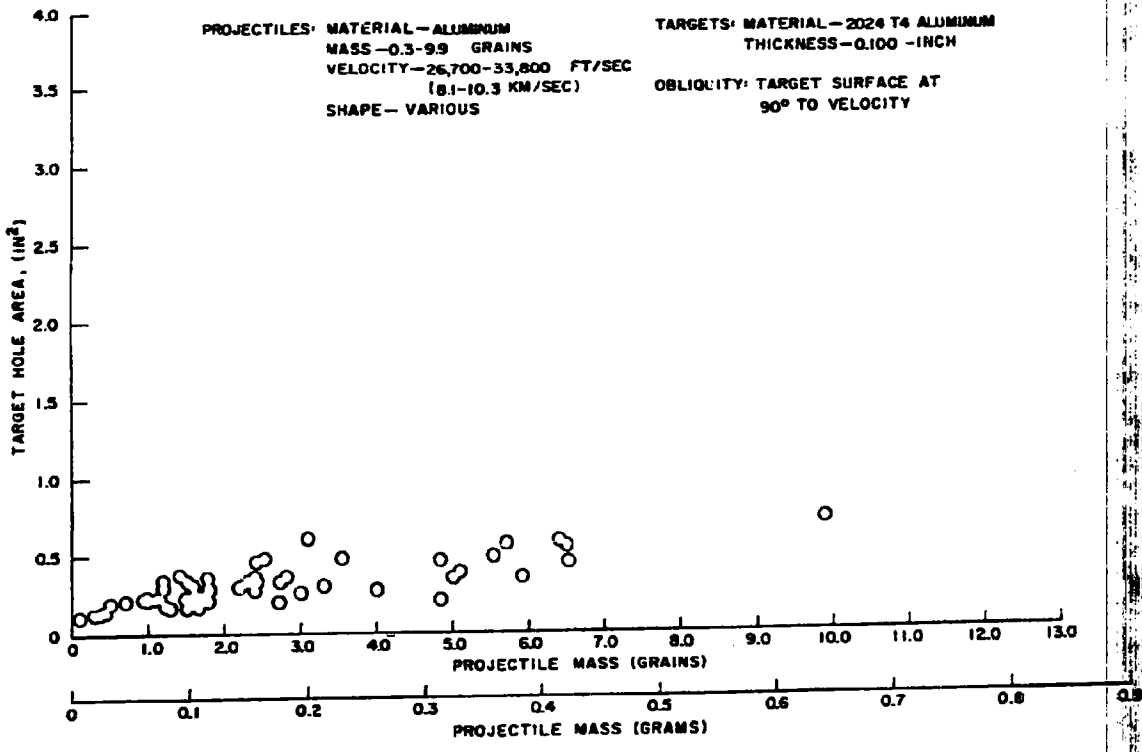

3 TO 12 KM/SEC IMPACTS

TARGET HOLE AREA VS PROJECTILE MASS

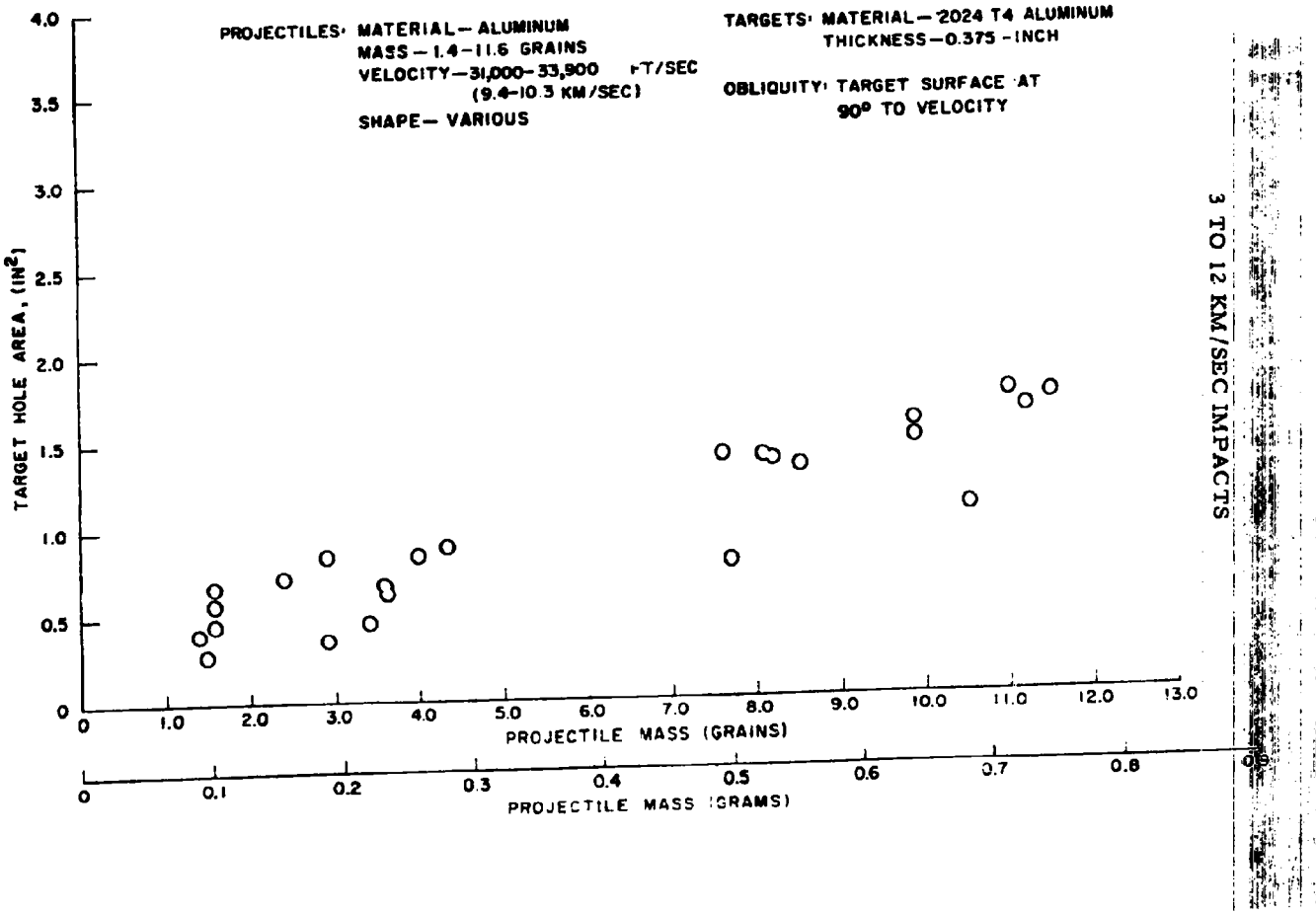

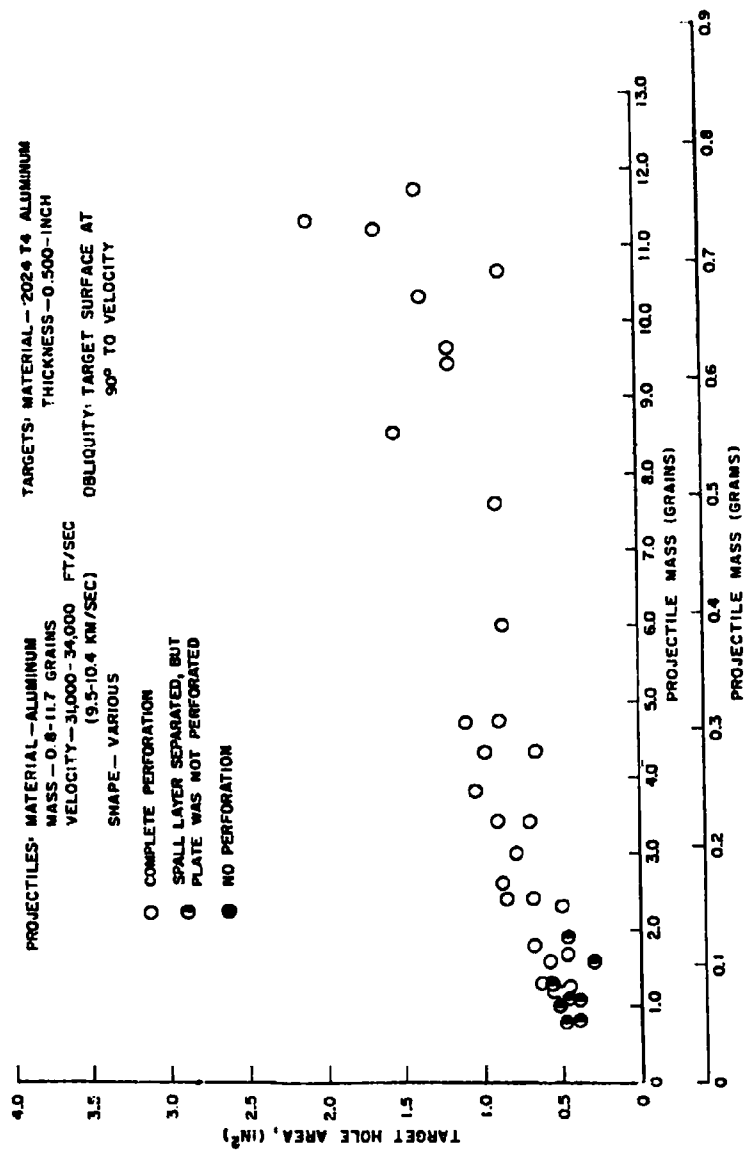
TARGET HOLE AREA VS PROJECTILE MASS
PROJECTILES: MATERIAL—ALUMINUM
MASS—0.8-11.7 GRAINS
VELOCITY—31,000-34,000 FT/SEC
(9.5-10.4 KM/SEC)
SHAPE—VARIOUS
TARGETS: MATERIAL—2024 T4 ALUMINUM
THICKNESS—0.500-INCH
OBLIQUITY: TARGET SURFACE AT
90° TO VELOCITY
○ COMPLETE PERFORATION
◐ SPALL LAYER SEPARATED, BUT PLATE WAS NOT PERFORATED
● NO PERFORATION
TARGET HOLE AREA, (IN²)
PROJECTILE MASS (GRAINS)
PROJECTILE MASS (GRAMS)

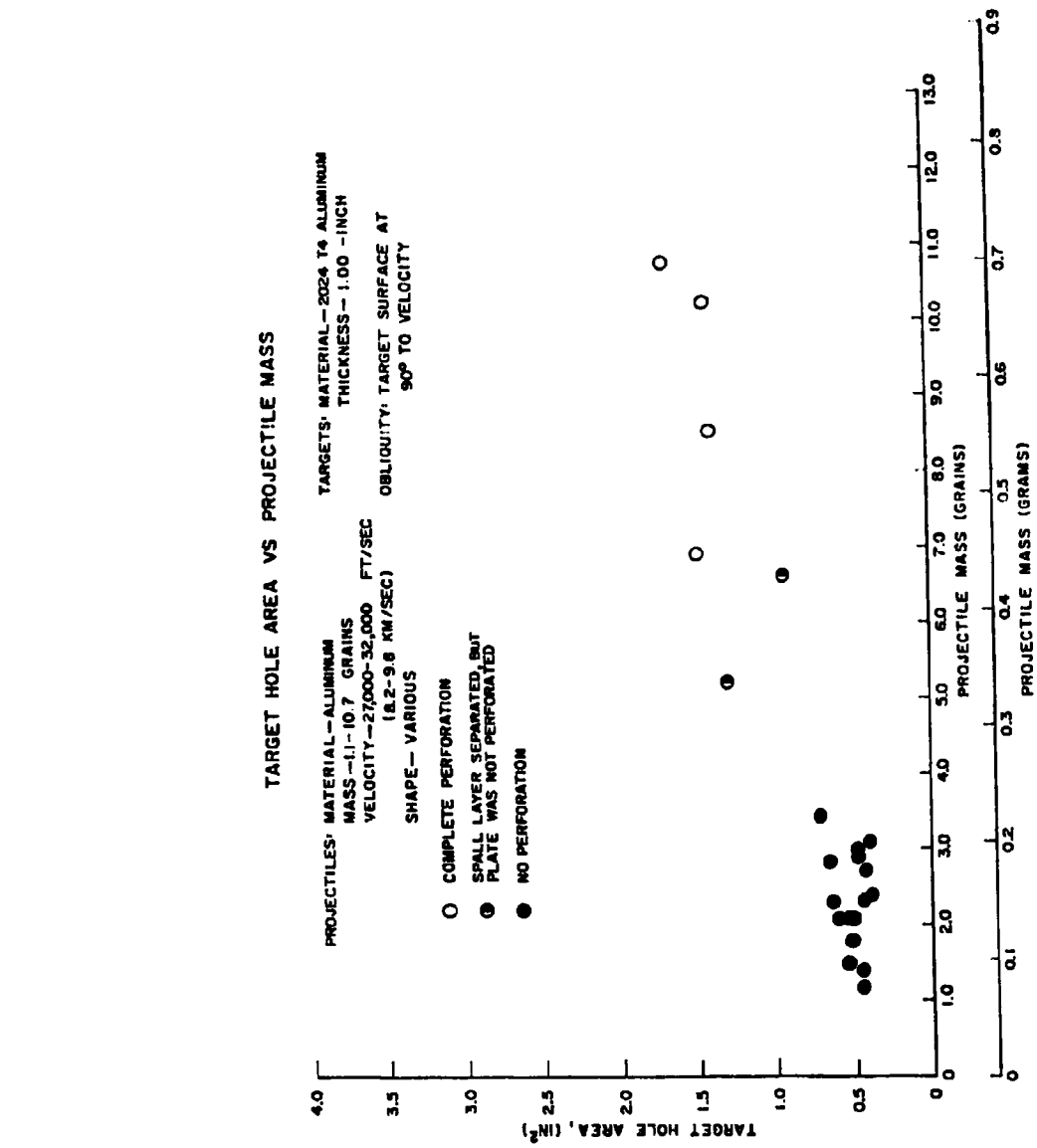
TARGET HOLE AREA VS PROJECTILE MASS
PROJECTILES: MATERIAL—ALUMINUM
MASS—1.1–10.7 GRAINS
VELOCITY—27,000–32,000 FT/SEC
(8.2–9.8 KM/SEC)
SHAPE— VARIOUS
TARGETS: MATERIAL—2024 T4 ALUMINUM
THICKNESS—1.00 -INCH
OBLIQUITY: TARGET SURFACE AT
90° TO VELOCITY
COMPLETE PERFORATION
SPALL LAYER SEPARATED, BUT
PLATE WAS NOT PERFORATED
NO PERFORATION
TARGET HOLE AREA, (IN²)
PROJECTILE MASS (GRAINS)
PROJECTILE MASS (GRAMS)

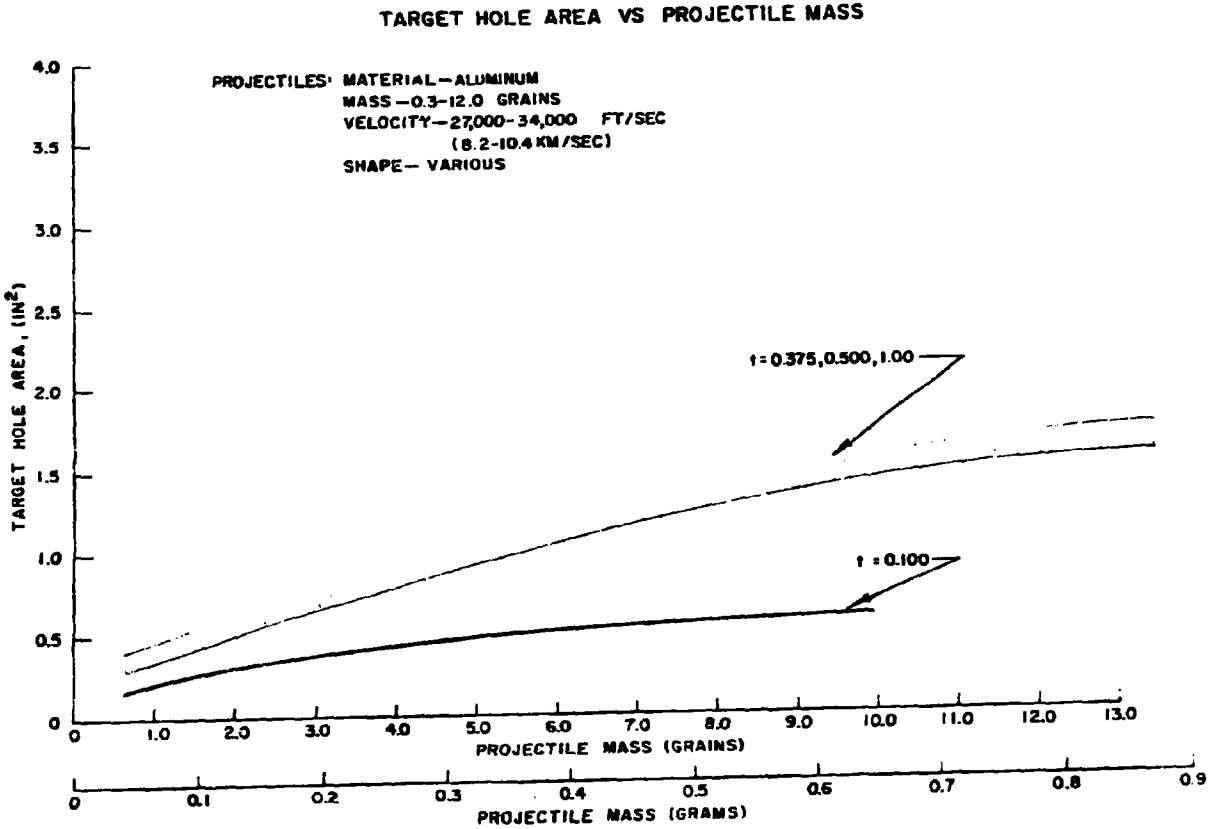
TARGET HOLE AREA VS PROJECTILE MASS
PROJECTILES: MATERIAL—ALUMINUM
MASS—0.3-12.0 GRAINS
VELOCITY—27,000-34,000 FT/SEC
(8.2-10.4 KM/SEC)
SHAPE— VARIOUS
t = 0.375, 0.500, 1.00
t = 0.100
TARGET HOLE AREA, (IN²)
PROJECTILE MASS (GRAINS)
PROJECTILE MASS (GRAMS)

With relatively thick targets, the existence of two distinct modes in the formation of clear holes can be observed. The first of these is the shock-operated crater formation - the second is spallation resulting from interaction of the shock with the rear surface of the target. The two impacts shown in Figure 14 serve to illustrate these modes. In the right-hand impact, the bottom of the crater and the deepest portion of the spall nearly coincide, so that a clear hole is almost formed. In the left-hand impact, no clear hole is formed. However, one or more spall layers was broken loose and ejected, presumably at relatively high velocity. From a vulnerability standpoint it is important to note that even though the target plate successfully resisted complete perforation, the high velocity spall layer would have been very effective in causing damage to internal components, personnel, or other targets behind the initial plate.

For thicker targets, the area of the spalled zone will greatly exceed the area of the clear hole. This is seen in Figure 15.

For ductile targets, such as soft copper, a crater lip forms on the front surface around the periphery of the entrance hole in a thicker target. For more brittle targets, such as the 2024-T4 aluminum used for most of these experiments, extensive spalling occurs on the front surface adjacent to the hole, as is illustrated in Figure 16a. This spalling presumably results from interaction of the shock with the front free surface. Figure 16b shows a case (not untypical) where a very extensive front spall formed, but failed to completely break loose from the target.

C. Perforation Limit

It is usually desirable to know what the characteristics are of a projectile which will just barely perforate a given target. As a rough approximation, it is sometimes assumed that a projectile will just perforate a target whose thickness is 1.5 times the crater depth which the same projectile would have formed in a semi-infinite target of the same material. This rule-of-thumb largely ignores the effect of material strength, which plays a far more important role in the spallation process than it does in crater formation.

As is seen from the legend in Figure 12, only those projectiles above approximately 6.5 grains in mass perforated the 1.000-inch thick targets. From Figure 13, those projectiles above approximately 1.2 grains generally perforated the 0.500-inch targets.

3 TO 12 KM/SEC IMPACTS

3 TO 12 KM/SEC IMPACTS

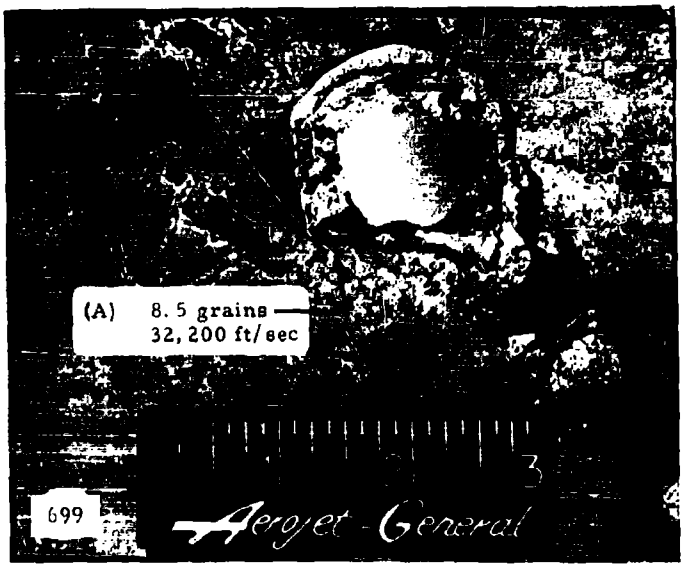

FRONT SURFACE

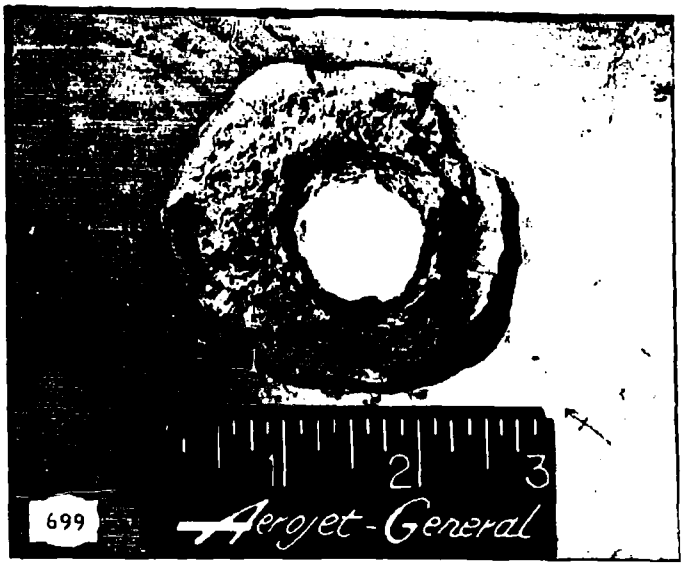

BACK SURFACE

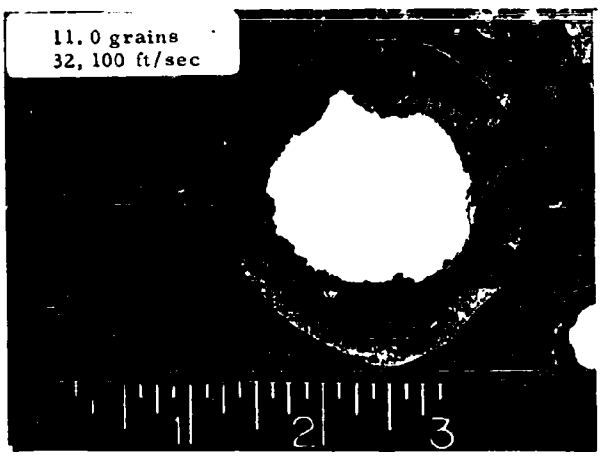

FRONT SURFACE OF TARGET PLATE
(2024-T4 ALUMINUM, 0.375-IN. THICK, 90° OBLIQUITY)

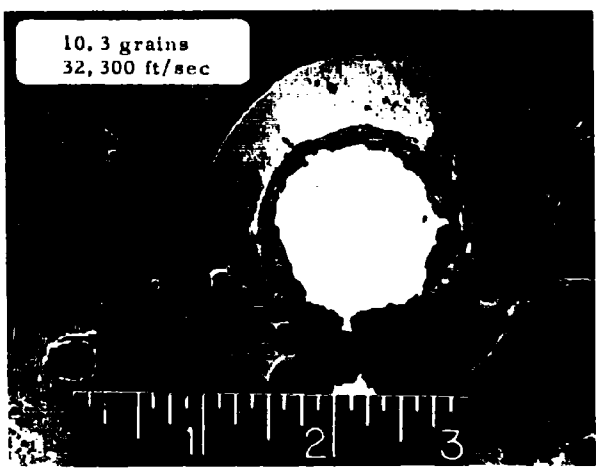

FRONT SURFACE OF TARGET PLATE
(2024-T4 ALUMINUM, 0.500-IN. THICK, 90° OBLIQUITY)

In Figure 17, penetration data are plotted vs projectile mass for impacts of aluminum into 4-inch thick aluminum targets at 8-10 km/sec. (For the projectiles involved, this thickness may be regarded as representative of a semi-infinite target). From these data, it is observed that a 6.5 grain projectile perforates nominally 0.56-inches into the target, and a 1.2 grain projectile perforates about 0.29-inches. Thus, by comparison with the performance of these same mass projectiles in 0.500 and 1.000-inch targets (Figures 11 and 12) we see that they can perforate targets roughly 1.75 times as thick as the penetration into semi-infinite targets. This factor is limited, of course, to 2024-T4 aluminum targets. It may be valid for a wide range of velocities, but our present data only covers a narrow range near 9 km/sec.

Incidentally, as seen in Figures 12 and 13, spallation occurred in all 0.500-inch targets, even with projectiles with masses of somewhat less than 1.0 grains. Spallation also occurred in 1.000-in. targets for projectile masses at least as small as 5 grains. Below this level, bulging without spall separation was observed.

D. Oblique Impacts

When a projectile strikes a target at oblique incidence, the impact area is larger than on a normal target by $1/\sin\theta$, where θ is the angle between the velocity and the target plate surface. If impact area were the only consideration in determining hole area, a given projectile would be expected to produce a larger hole at oblique incidence. In impacts against 0.100-inch aluminum alloy targets at 90°, 50°, and 20° incidence, we did not find any such area relationship to hold. The normal impact data appears in Figure 7, while the 50° and 20° data are shown in Figures 18 and 19. (Note that the projectile area used in these figures is the area on the target, is larger by $1/\sin 50^\circ = 1.3$ for the 50° data and by $1/\sin 20^\circ = 2.9$ for the 20° data.)

The scatter of the 50° data in Figure 18 is greater than was found for the 90° data in Figure 7, but otherwise the data are much the same. The same curve which was drawn on Figure 7 is superimposed on Figure 17 to show the similarity. For the 20° data in Figure 19, even though the scatter is excessive, it is clear that the damage caused by projectiles to targets at 20° obliquity is significantly less than the damage to targets at 90° and 50°.

Target hole vs projectile mass for the same experiments is shown for 90°, 50°, and 20° impact obliquity in Figures 9, 20, and 21. Excessive scatter appears for the 90° data, but the 50° and 20° data appear acceptable. The hole sizes formed at 20° are only slightly smaller than those formed by equivalent masses at 50°.

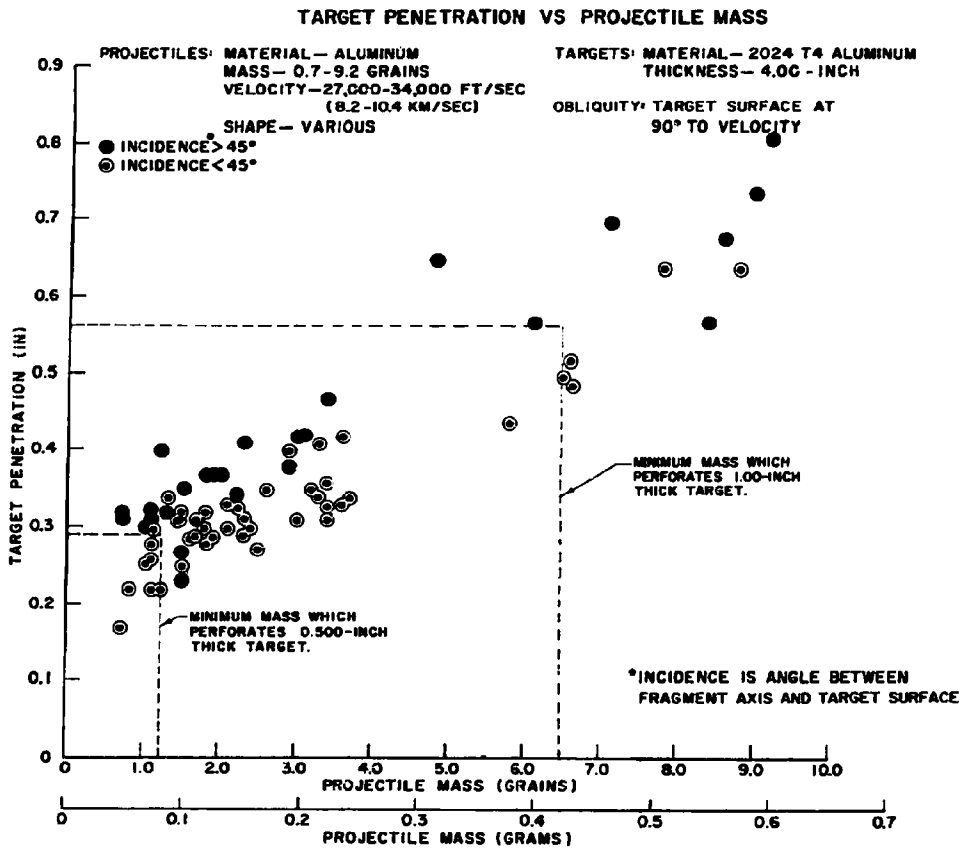

3 TO 12 KM/SEC IMPACTS

TARGET HOLE AREA VS PROJECTILE AREA*

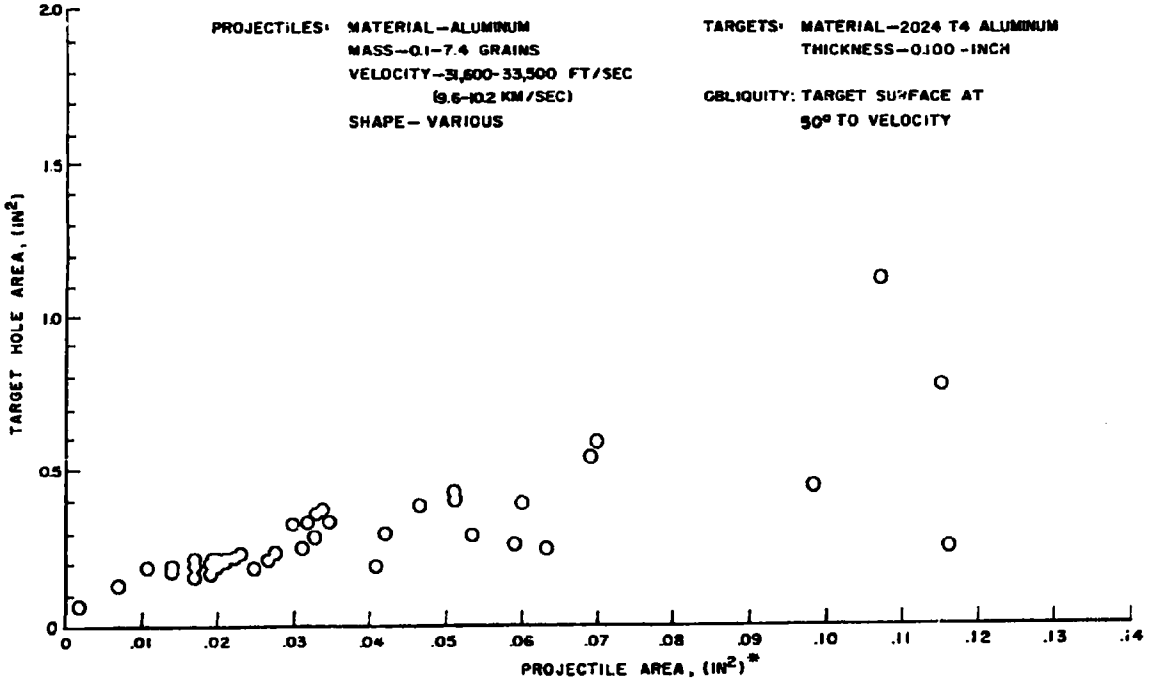

*ON PLANE NORMAL TO VELOCITY

3 TO 12 KM/SEC IMPACTS

TARGET HOLE AREA VS PROJECTILE AREA*

PROJECTILES: MATERIAL—ALUMINUM
MASS—0.3-9.4 GRAINS
VELOCITY—29,600-33,100 FT/SEC
(9.0-10.1 KM/SEC)
SHAPE— VARIOUS

TARGETS: MATERIAL—2024 T4 ALUMINUM
THICKNESS—0.100 -INCH

OBLIQUITY: TARGET SURFACE AT
20° TO VELOCITY

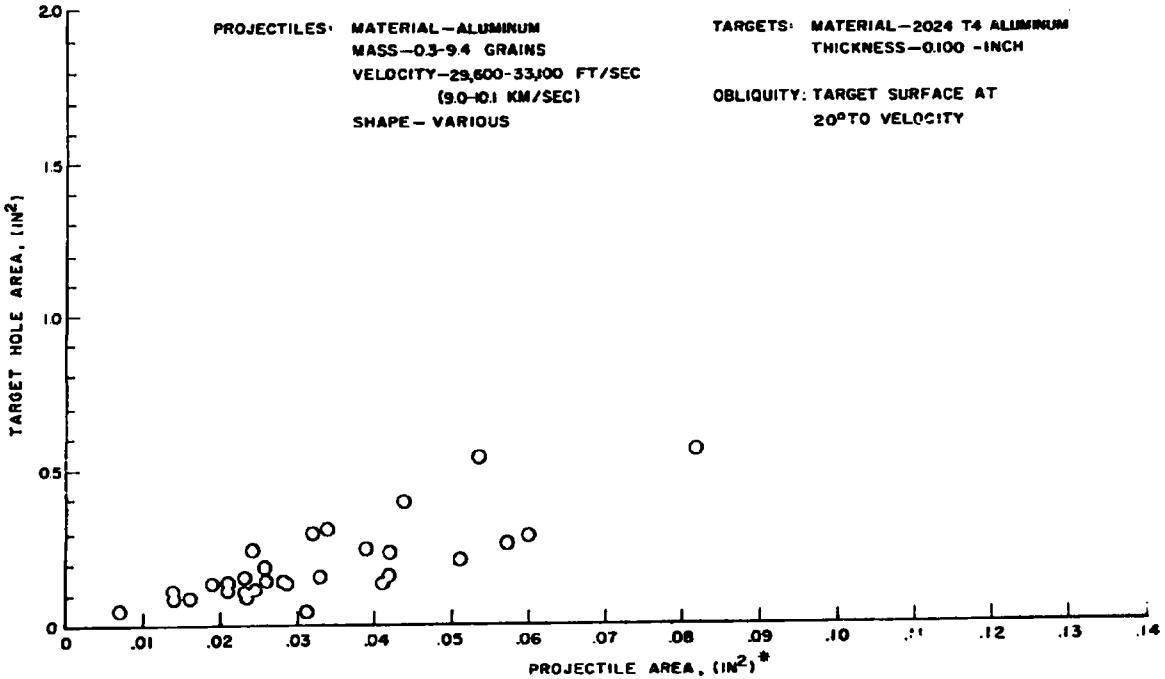

*ON PLANE NORMAL TO VELOCITY

3 TO 12 KM/SEC IMPACTS

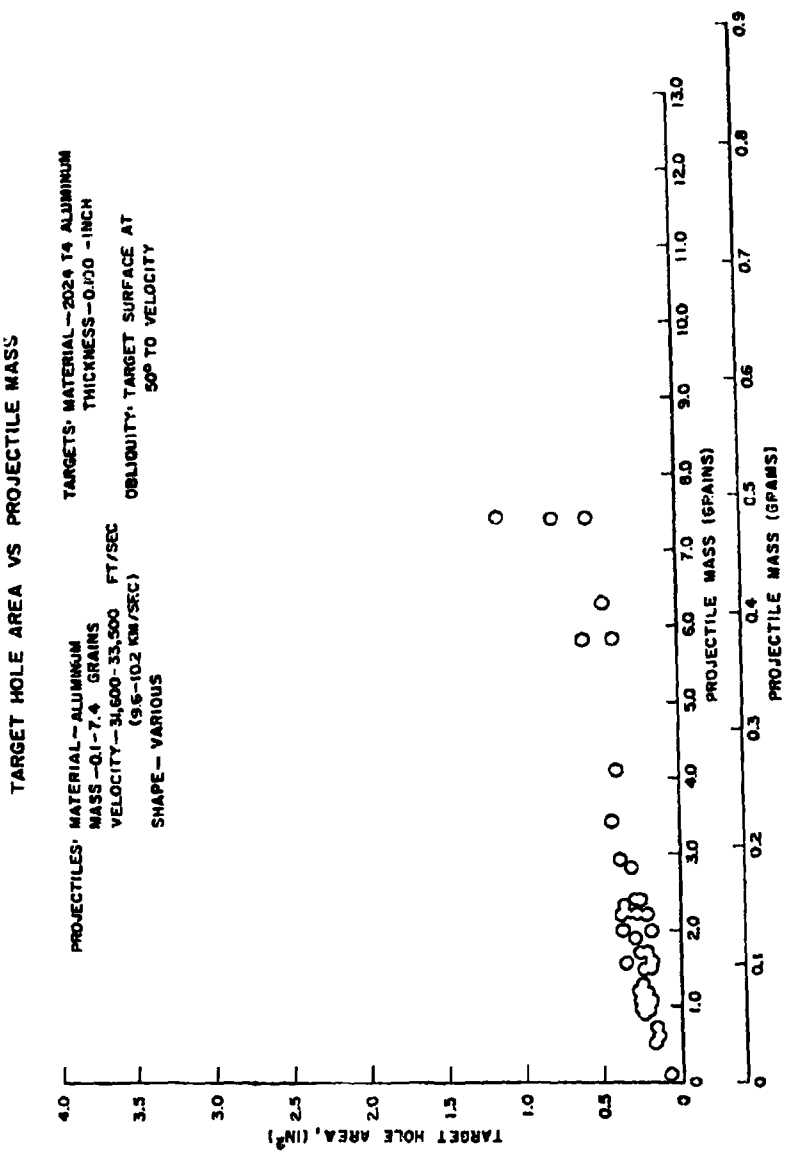
TARGET HOLE AREA VS PROJECTILE MASS
PROJECTILES: MATERIAL—ALUMINUM
MASS —0.1-7.4 GRAINS
VELOCITY—31,600-33,500 FT/SEC
(9.6-10.2 KM/SEC)
SHAPE— VARIOUS
TARGETS: MATERIAL—2024 T4 ALUMINUM
THICKNESS—0.100 -INCH
OBLIQUITY: TARGET SURFACE AT
50° TO VELOCITY
TARGET HOLE AREA, (IN²)
PROJECTILE MASS (GRAINS)
PROJECTILE MASS (GRAMS)

TARGET HOLE AREA VS PROJECTILE MASS

PROJECTILES: MATERIAL—ALUMINUM
MASS—0.3-9.4 GRAINS
VELOCITY—29,600-33,100 FT/SEC
(9.0-10.1 KM/SEC)
SHAPE—VARIOUS

TARGETS: MATERIAL—2024 T4 ALUMINUM
THICKNESS—0.100-INCH

OBLIQUITY: TARGET SURFACE AT
20° TO VELOCITY

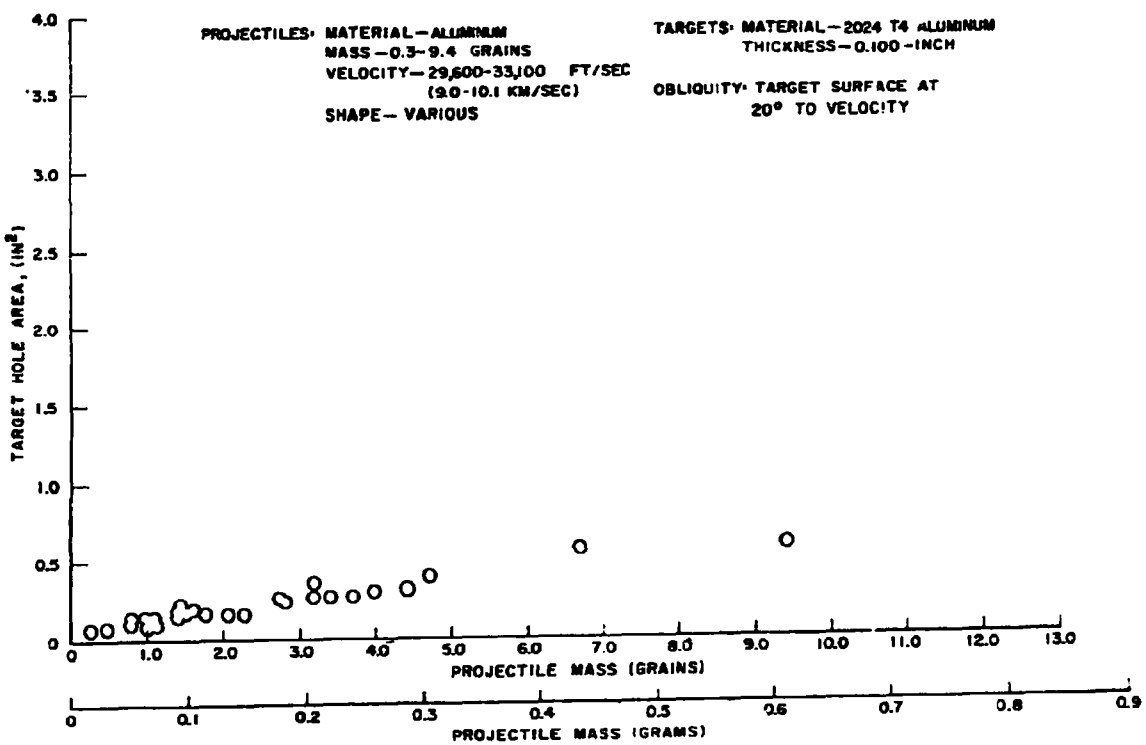

3 TO 12 KM/SEC IMPACTS

While the data on the target hole area vs projectile area plots progressively become more scattered as the obliquity goes from 90° to 50° to 20°, the hole area vs projectile mass plots progressively becomes less scattered, reaching a fairly smooth relationship at 20° obliquity. For impact under such severe conditions of obliquity, projectile mass is clearly more important than area in determining target hole area--even for relatively thin targets.

A surprisingly large portion of the target holes for the 20° incidence impacts are round or nearly-round, as seen in Figure 22.

V. SPECIAL PROJECTILE SHAPES

Projectile shape and orientation at impact exert a strong effect upon thin plates. The effects are most pronounced for extreme shapes, such as rods, flat thin sheets, and distributed mass configurations (hollow cylinders, hollow spheres, etc.). The target plate acceleration technique is particularly well suited for this investigation since it permits nearly unlimited flexibility in the study of shapes and orientations with the projectile mounted stationary in the path of the target plate.

A. Rod Projectiles

Rod projectiles are very effective in penetrating thick targets and multiplate target arrangements. The critical requirement is that the rod axis must be colinear with the relative impact velocity.

Against multiplate targets, the primary interest is in the hole area in the first plate and in the damage sustained by the rod during penetration. A clear illustration of the effect of rod orientation at impact on subsequent breakup is shown in Figures 23 and 24.

In Figure 23 a 1 gram titanium rod with circular cross section and L/D of 10 is shown impacting and penetrating a target consisting of two 0.100-in. aluminum plates 24 inches apart. This rod was launched from a light gas gun and impacted end-on at 3.1 km/sec. The figure shows flash radiographs of the rod in flight before impact on both target plates, and photographs of the target plates after impact. As can be seen, a tumbling results in the rod penetrating the second plate slightly off the end-on orientation. This is further illustrated from the keyhole shape of the hole in the second plate, typical of this type of penetration. Note, however, that the rod reaches the second target plate intact and without any visible

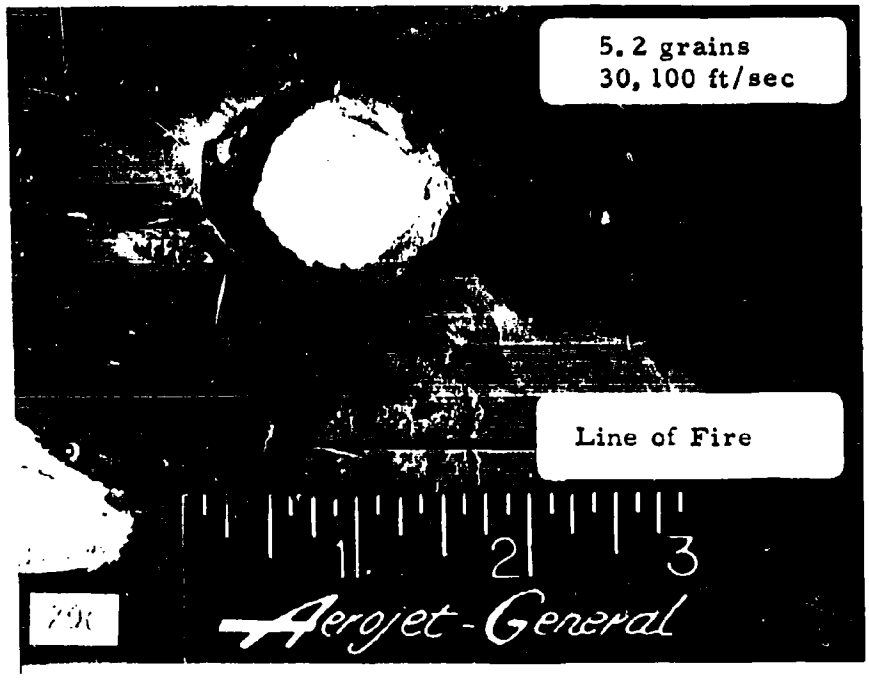

FRONT SURFACE OF TARGET PLATE
(2024-T4 ALUMINUM, 0.375-IN. THICK, 20° OBLIQUITY)

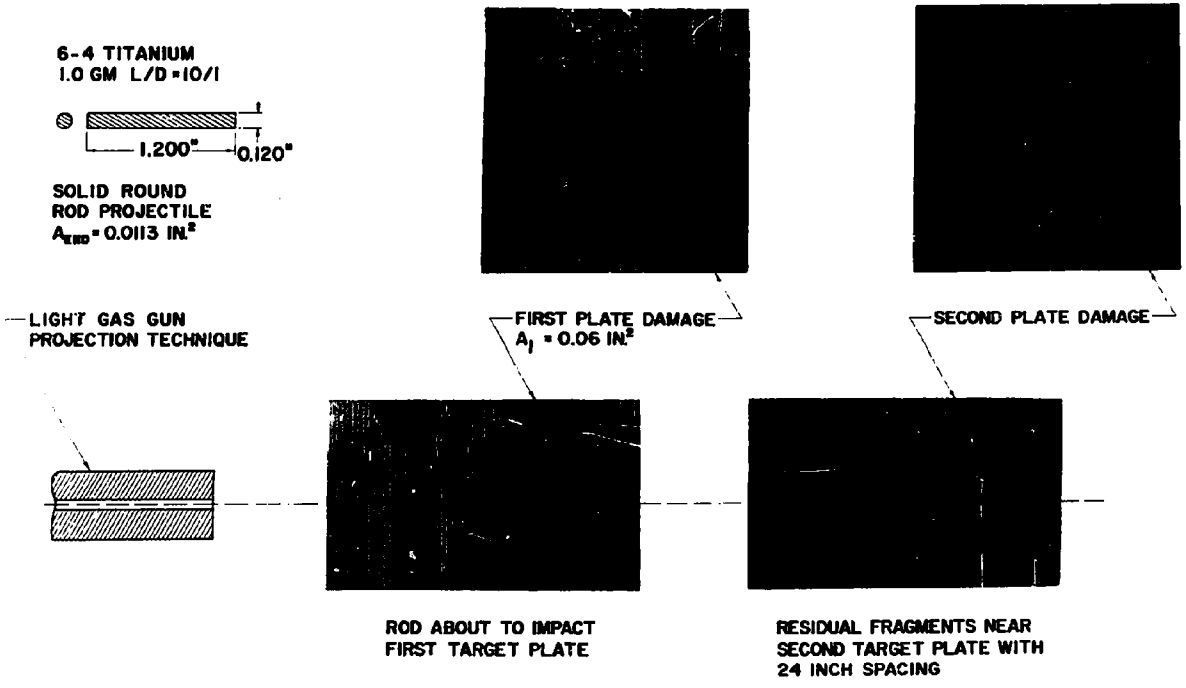

3 TO 12 KM/SEC IMPACTS

3 TO 12 KM/SEC IMPACTS

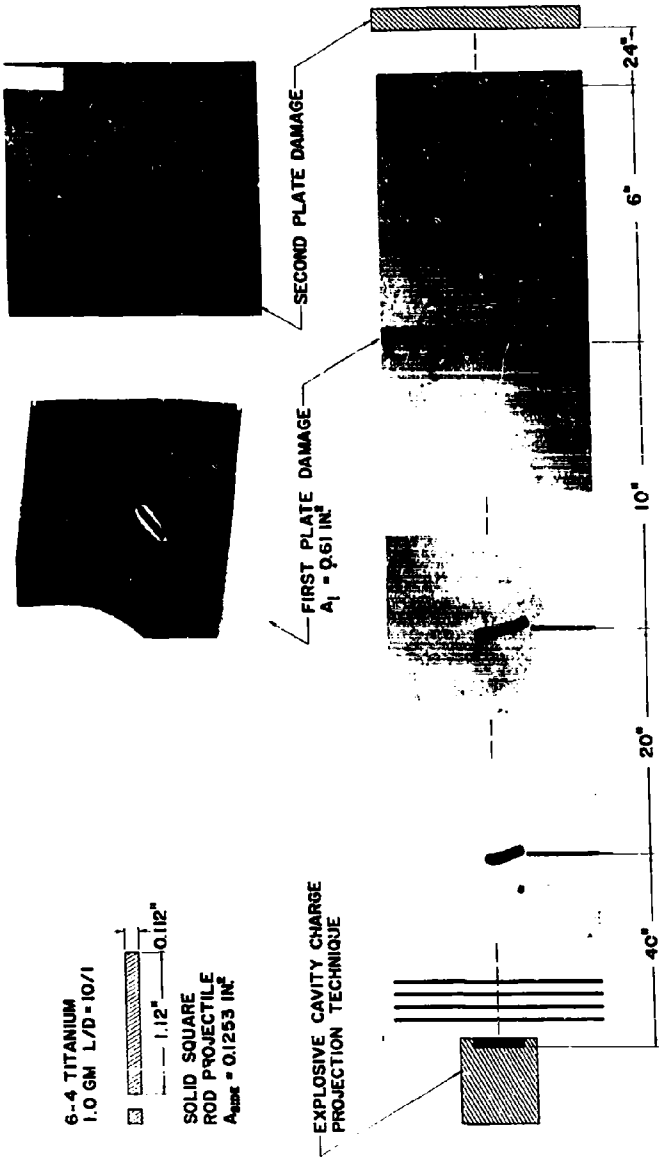

deformation. A short portion of the impacting end of the rod is broken off as a result of each succeeding impact, but this is not visible in Figure 23.

In contrast to the above, Figure 24 shows the complete breakup resulting from a 1 gram titanium rod with square cross section and L/D of 10 impacting side-on against the same target type as that described above. This rod was projected from an explosive cavity charge to an impact velocity of 4.1 km/sec. The sharp contours of the rod prior to impact are clearly shown. This rod, however, is completely fragmented and is incapable of achieving perforation or even significant penetration of the second target plate. The difference in impact effect due to the orientation of rod-shaped projectiles as can be seen, is startling.

It is also worth considering that the relative target-to-projectile thickness ratio vary from approximately 1/10 to 1/1 for the end-on and side-on cases. It has been our experience from other firings in this velocity range that nearly complete projectile breakup is achieved when this ratio is larger than approximately 1/2 depending upon target and projectile materials.

The effects of projectile mass, diameter and length for end-on impacting rods have been studied by impacting flying plate targets (0.10-in. thick aluminum plates) at 3.5 km/sec against stationary projectiles.

The first of these test series involved titanium rods of constant diameter (0.12 in.), with the L/D ratio varying in 10 steps from 1 to 10. It was found that the hole in the target plate was approximately constant in all cases, resulting in an average A_1/A_{0I} ratio of 7.1.

Figure 25 illustrates the effect of varying projectile diameter on A_1/A_{0I} ratio. The projectiles for this test series were aluminum and the targets were the 0.10-in. aluminum flying plates impacting at 3.5 km/sec. Two results are seen from the figure. One is the strongly increasing A_1/A_{0I} ratio with decreasing projectile diameter. This trend has been observed for all projectiles studied to date. The other is the absence of projectile mass or length effect on target hole size. For those firings one series had constant projectile mass (3.1 gram) with varying length and diameter. The other series had constant length (0.131 in.) with varying mass and diameter. As can be seen from Figure 25 the difference between the two series is very small. Each point on the curve represents an average of five shots. From the above it is again evident that the impacting area of the projectile is the major determining factor for the size of holes generated in relatively thin targets.

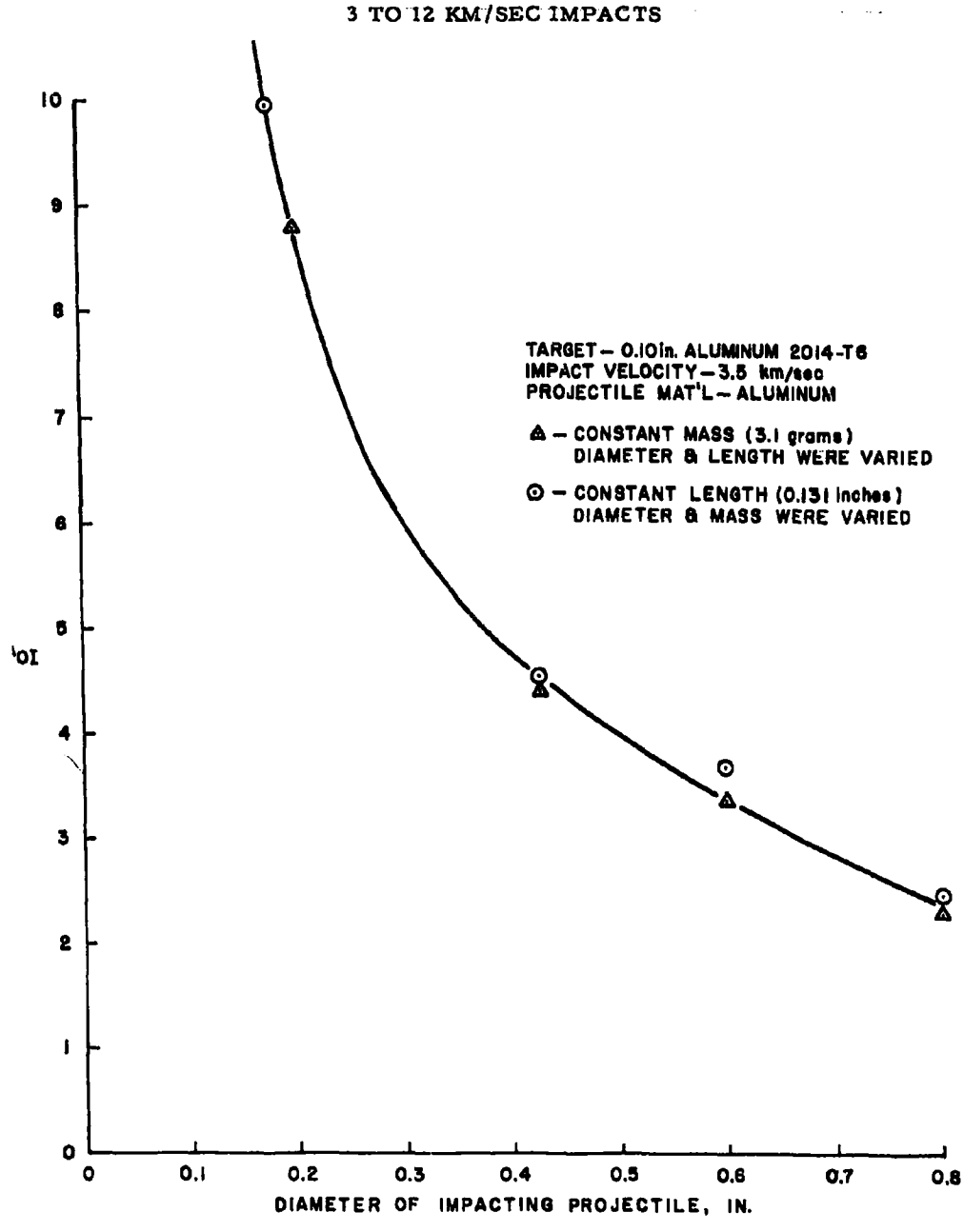
3 TO 12 KM/SEC IMPACTS
TARGET – 0.10in. ALUMINUM 2014-T6
IMPACT VELOCITY – 3.5 km/sec
PROJECTILE MAT'L – ALUMINUM
△ – CONSTANT MASS (3.1 grams)
DIAMETER & LENGTH WERE VARIED
⊙ – CONSTANT LENGTH (0.131 inches)
DIAMETER & MASS WERE VARIED
log I
10
9
8
7
6
5
4
3
2
1
0
0
0.1
0.2
0.3
0.4
0.5
0.6
0.7
0.8
DIAMETER OF IMPACTING PROJECTILE, IN.

Our firings with compact projectiles such as short cylindrical discs have indicated that projectile orientation at impact has a significant effect on the A_1/A_{0I} ratio. When such a projectile impacts flat on the disc surface the A_1/A_{0I} ratio tends to increase. Experimental scatter resulting from orientation and shape variables imparted by the explosive cavity launchers has made it difficult to resolve this question. In an attempt to clarify the effect of front surface shape on the shock strength in the target a series of aluminum rods were impacted by the 0.10-in. aluminum flying plates at 3.5 km/sec. These rods all had an L/D of 10 with a 0.250-in. diameter. Three rod types were studied. These were:

1. Right angle cylinders.

2. Cylinders with conical ends.
   Cone angles of 45°, 27°, 18° and 14° were used.

3. Cylinders with curved ends.
   Curve radii of 0.125 and 0.250-in. were used.

Although some of the configurations are represented by only one firing a strong trend is shown. The A_1/A_{0I} ratios are listed below for the radii and cone angles investigated.

Radius or angle:	∞	0.25	0.125	45°	27°	18°	14°
A_1/A_{0I}:	8.2	8.5	4.9	5.9	5.5	4.1	3.3

While these data are not to be taken as quantitative there seems to be a strong indication of decreasing target hole area with increasing rounding or pointing of the impacting surface. Comparing the data for the infinite and 0.25-in. radii with Figure 25 we see that for the 0.25-in. projectile diameter the curve on Figure 25 gives a value of 7.2. This is close to the values shown above.

As shown in Figure 23 above a rod impacting a thin target end-on will penetrate with very little deformation except for a mass loss from the front end resulting in a shortening of the rod. On several of the aluminum rod front surface firings attempts were made to obtain a flash radiograph of penetration. Figure 26 shows two examples of these tests with a 0.125 in. radius curved (left) and 45° cone shaped (right) front surfaces. The procedure here is to take a static picture before firing; then lower the film cassette slightly to avoid overlapping and finally take the second picture. Having the rods shown before and after firing the same picture

3 TO 12 KM/SEC IMPACTS

also simplified any measurement made from the film. The lack of rod bending or deformation is shown in the figure. It should be remembered, however, that rods are very sensitive to orientation at impact, particularly at these relatively low velocities. A few degrees off normal will, particularly for the sharp-nosed rods, result in keyhole-shaped penetrations in the target plates as well as strong bending for all the rods. It is expected that this bending effect will diminish with increasing impact velocity, but no data in this velocity range are presently available.

B. Foils and Washers

For maximum area damage from a single projectile against a thin target a very thin sheet or foil impacting flat-on would seem to be the most effective. With regard to projectile orientation the presented projectile area, and therefore the maximum hole area in the target, will decrease with changing foil orientation away from the flat-on position. With this change, however, the presented projectile depth, and thus the penetration depth, increases.

To study the minimum thickness necessary for penetration of a specific target (a 0.100-in. aluminum flying plate) a series of thin foils of several materials was investigated. The data obtained are shown in Table II. It is interesting to see that even a 0.0032-in. thick steel foil is capable of complete penetration of an aluminum plate 31 times as thick. This obviously is far in excess of any penetration depth normally achieved at these velocities even with high density compact hypervelocity projectiles. While the same thickness aluminum foil could not match the steel foil performance a 0.016-in. aluminum foil penetrated easily. From the A_1/A_{0I} ratio measured (1.38) it is evident that the minimum thickness was far from reached. The A_1/A_{0I} ratio shown in Table II is indicative of how close one is to the minimum projectile thickness needed for penetration. As an example for the stainless steel sheets we have the following A_1/A_{0I} values:

Thickness, in.:	0.018	0.0075	0.0053	0.0032
0.5 x 0.5 in. sheet:	1.99	1.53	1.09	1.07
1.0 x 1.0 in. sheet:	1.54	1.26	1.05	1.0

Comparison between the two sheet areas again points out the increases in A_1/A_{0I} ratio with decreasing frontal area which has been described previously.

Table II. Impact By Thin Metal Foils at 3.5 Km/Sec.

Material	Mass	L*		t**		A_{OI} Impact Area	A_I	Average Area Loading	ΔL***	A_I/A_{OI}
	(gm)	(cm)	(in.)	(cm)	(in.)	(cm^2)	(cm^2)	($jx10^3/cm^2$)	(cm)	
Aluminum	0.70	2.54	1.0	0.041	0.016	6.45	8.9	0.66	0.18	1.38
	0.18	1.27	0.5	0.041	0.016	1.61	2.62	0.66	0.14	1.63
Aluminum	0.14	2.54	1.0	0.008	0.0032	6.45	No Penetr.	0.13	No Penetr.	No Penetr.
Stainless Steel	2.30	2.54	1.0	0.046	0.018	6.45	9.95	2.18	0.24	1.54
	0.58	1.27	0.5	0.046	0.018	1.61	3.22	2.18	0.21	1.99
Stainless Steel	0.95	2.54	1.0	0.019	0.0075	6.45	8.15	0.91	0.12	1.26
	0.24	1.27	0.5	0.019	0.0075	1.61	2.46	0.91	0.12	1.53
Stainless Steel	0.68	2.54	1.0	0.013	0.0053	6.45	6.78	0.64	0.03	1.05
	0.17	1.27	0.5	0.013	0.0053	1.61	1.75	0.64	0.022	1.09
Stainless Steel	0.41	2.54	1.0	0.008	0.0032	6.45	6.45	0.39	0	1.0
	0.10	1.27	0.5	0.008	0.0032	1.61	1.72	0.39	0	1.07
Titanium	1.18	2.54	1.0	0.038	0.015	6.45	9.19	1.12	0.19	1.42

*Side of square sheet
**Thickness of square sheet
***Difference between side of damage area and side of impacting square sheet

Figure 27 shows three of the stainless steel foils penetrating the aluminum target. The penetration is evident in all three cases.

With the penetrating power of even thin foils established it becomes of interest to see, if distributed mass projectiles in form of, for example, foil washers are capable of the same penetration. Preliminary tests with such projectiles have included 0.020 and 0.025-in. thick stainless steel washers. Pertinent projectile dimensions and resulting target damage are shown in Table III. Only one or two firings of each configuration were made so that no detailed conclusions can be drawn from the data. It seems reasonable to assume that the size of the hole in the washer has no effect on the target damage. The spread in A_1/A_{0I} values for the two washer thicknesses can be assigned to experimental scatter. The trend shown is towards a higher value for the 0.025-in. than the 0.020-in. thick washer. This is consistent with the foil data shown in Table II.

C. Hollow Spheres

A thin-walled hollow sphere has often been proposed as an effective area-cutting projectile. It is particularly desirable due to its insensitivity to orientation at impact. Such projectiles were therefore a natural part of our test program. Due to their particular usefulness, however, the sphere tests are described in a separate paper at this symposium (Reference 2). At this point, it will be sufficient to mention that thin-wall spheres do indeed penetrate effectively. The hollow sphere projectile studies are presently being continued by several investigators.

FLASH RADIOGRAPH SHOWING PENETRATION OF 0.100 INCH ALUMINUM BY 1.0 INCH SQUARE STAINLESS STEEL PROJECTILES

Table III. Impact By Thin Metal Washers at 3.5 Km/Sec.

Material	OD		ID		Thickness		Mass	A_{OI}*	A_I	Average Area Loading	D**	A_I/A_{OI}
	(cm)	(in.)	(cm)	(in.)	(cm)	(in.)	(gm)	(cm^2)	(cm^2)	($jx10^3/cm^2$)	(cm)	
Stainless Steel	1.91	0.75	1.52	0.60	0.051	0.020	0.41	2.90	6.70	2.41	0.40	2.4
Stainless Steel	1.91	0.75	1.27	0.50	0.051	0.020	0.64	2.90	6.08	2.41	0.34	2.1
Stainless Steel	1.91	0.75	0.76	0.30	0.051	0.020	0.97	2.90	6.10	2.41	0.34	2.2
Stainless Steel	1.91	0.75	1.52	0.60	0.064	0.025	0.51	2.90	6.95	2.96	0.42	2.5
Stainless Steel	1.91	0.75	1.27	0.50	1.064	0.025	0.81	2.90	6.30	2.96	0.36	2.3
Stainless Steel	1.91	0.75	1.02	0.40	0.064	0.025	1.03	2.90	7.90	2.96	0.50	2.8

*A_{OI} includes hole area in washer

**Difference between damage area diameter and washer OD

NOTE: These tests were exploratory, and only one or two firings were conducted for each condition. The data are included for comparison with Table II.

REFERENCES

1. K. N. Kreyenhagen, J. E. Ferguson, R. R. Randall, and J. P. Joyce, "Special Explosive Projectors", presented at the Sixth Hypervelocity Impact Symposium.

2. W. H. Dittrich, D. R. Christman, J. W. Gehring, K. N. Kreyenhagen and R. B. Mortensen, "Lethality of Hollow Shapes"(U), presented at the Sixth Hypervelocity Symposium.

THIN PLATE PERFORATION STUDIES WITH PROJECTILES IN THE VELOCITY RANGE FROM 2 TO 5 KM/SEC

by

R. W. Watson, K. R. Becker, and F. C. Gibson

Explosives Research Laboratory
Bureau of Mines
U. S. Department of Interior
Pittsburgh, Pa.

This research is sponsored by the Department of the Army,
Aberdeen Proving Ground, Maryland

THIN PLATE PERFORATION STUDIES

ABSTRACT

The thin plate perforation process has been studied experimentally over the velocity range from 2 to 5 km/sec for two sizes of projectiles. The major research effort was carried out with 2024-T3 aluminum targets using cylindrical steel projectiles having a length-to-diameter ratio of one. However, impacts on other target materials were also studied to delineate the effects of target strength and impact pressure. Particular emphasis was placed on determining the mass, number, and velocity distributions of the particles ejected from the rear surface of the target during the perforation process.

THIN PLATE PERFORATION STUDIES

CONTENTS

	Page
Introduction	212
Procedures and Discussion	213
I. Survey of Impact Damage to Thin and Thick 2024-T3 Aluminum Targets	213
II. Number Distribution	220
III. Mass Distribution	230
IV. Velocity Distribution	235
Concluding Remarks	246
List of References	248

ILLUSTRATIONS

Fig.		
1.	Features of a thin plate perforation and a crater produced in a thick target	215
2.	Cratering efficiency as a function of impact velocity	216
3.	Variation of crater shape with impact velocity.	216
4.	Dependence of perforation entrance diameter on target thickness	218
5.	Plot showing tendency for perforations to be cylindrical for impacts ranging from 2.0 to 5.0 km/sec	218
6.	Variation in exit spall diameter with target thickness	219
7.	Increase in penetration potential with increasing impact velocity	219

CONTENTS (Contd)

Fig.		Page
8.	Experimental set-up for determining the spatial distribution of spall fragments.....	221
9.	Relationship between normalized spall numbers and radial distance from the center of spall impact.....	223
10.	Normalized distribution for target spall particles.....	225
11.	Normalized distribution for projectile remnants.....	225
12.	Effect of projectile size upon the number of target spall particles.....	226
13.	Effect of projectile size upon the number of projectile remnants.....	226
14.	Normalized population density as a function of azimuthal angle.....	228
15.	Effect of impact angle upon displacement angle.	228
16.	Normalized distribution for target spall mass..	231
17.	Normalized distribution for mass of projectile remnants.....	231
18.	Effect of projectile size upon the mass of recovered target spall.....	233
19.	Effect of projectile size upon the mass of recovered projectile remnants.....	233
20.	Effect of target thickness upon average target spall particle size.....	234
21.	Residual projectile velocity as a function of target thickness.....	238

CONTENTS (Contd)

Fig.		Page
22.	Comparison between measured and calculated values of target impulse	238
23.	Excess momentum as a function of impact velocity	240
24.	Forward momentum as a function of target thickness	240
25.	Target impulse as a function of target thickness	242
26.	Ejecta momentum as a function of target thickness	242
27.	Velocity distribution of target ejecta from 3.2 km/sec Scale I impacts	244
28.	Velocity distribution of target ejecta from 3.2 km/sec Scale II impacts	244
29.	Velocity distribution of target ejecta resulting from 5.0 km/sec Scale II impacts	245

THIN PLATE PERFORATION STUDIES WITH PROJECTILES IN THE VELOCITY RANGE FROM 2 TO 5 KM/SEC

INTRODUCTION

The immediate goal of this Bureau of Mines research is to obtain a complete phenomenological description of the thin plate perforation process within the limitations of available projectile accelerators. Data in this area are of immediate value in the formulation of theoretical descriptions of hypervelocity impact phenomena on both finite and quasi-infinite targets. Furthermore, the experimental techniques developed in the course of this work will be applicable to studies at higher impact velocities when suitable projector systems become available.

Since, from the practical point of view, the perforation of lightweight structural alloys is of immediate concern, the major portion of the research was carried out using 2024-T3 aluminum as the basic target material. However, where impact pressure effects required clarification, target materials of higher density were investigated. The experimental results accrued in this investigation can be grouped into four categories: Primary target damage, the number distribution (numbers of spall particles distributed over spatial elements), the mass distribution (mass of spall particles distributed over spatial elements), and the velocity distribution of the material ejected from thin plates during the perforation process.

THIN PLATE PERFORATION STUDIES

PROCEDURES AND DISCUSSION

I. Survey of Impact Damage to Thin and Thick 2024-T3 Aluminum Targets

The research was carried out with two basic explosive projector systems, each of which is characterized by a different projectile mass. One projector, which will be referred to as Scale I, utilized cylindrical steel projectiles having a mass of 0.0235 ± 0.0005 gram. The Scale I projectors can be further subdivided according to projectile velocities of 2.0 km/sec, 3.2 km/sec, and 4.0 km/sec; the latter two systems were developed by two of the authors (1)[1/] while associated with the Carnegie Institute of Technology. The projectiles were 1/16 inch long and 1/16 inch in diameter; the 2.0 km/sec and 3.2 km/sec projectiles were fabricated from Ketos steel drill rod of BHN 200; steel piano wire was used for the 4.0 km/sec projectile.

The second projector, referred to as Scale II, provided a velocity of 3.2 km/sec for a projectile 1/8 inch long and 1/8 inch in diameter, weighing 0.187 gram, made of Ketos steel. The velocity range for the Scale II projectiles was increased by the use of an air-cavity projector designed at the Ballistic Research Laboratories (2); this projector propelled a 0.18 gram steel projectile at a velocity of 5.0 km/sec.

Thick or quasi-infinite targets are defined here as targets of such dimensions that no measurable change in final crater dimension is affected by increasing the size of the target. In tests with 2024-T3 aluminum, it was found that targets having a thickness equal to 3 to 4 times the crater depth and a surface area roughly 25 times that of the crater satisfied these conditions within the accuracy of the crater measurements. Since the

1/ Underlined numbers in parentheses refer to items in the list of references at the end of this report.

current program was principally concerned with a description of behind-target effects, the term "thin target" is generally applied to any target capable of being perforated by a given projectile with a finite probability. For 2024-T3 aluminum, target thicknesses ranged from 3 to 4 times the projectile lengths over the velocity range investigated.

The pertinent variables recorded for thick targets were crater volume, crater depth, and crater diameter; for thin targets, they were entrance and exit diameters of the perforation. In cases where shock spallation was pronounced, the diameter of the spalled area on the back surface of the target was also recorded. The manner in which these variables are defined is illustrated in figure 1 where "thin" and "thick" targets, impacted with Scale II, 3.2 km/sec projectiles are shown.

The pertinent features of these measurements are presented in figures 2 through 7 and can be summarized as follows:

(1) For thick targets, crater volume was found to be proportional to the kinetic energy of the projectile over the velocity range 2 km/sec to 5 km/sec. This is illustrated in figure 2 where crater volume per unit projectile energy is plotted as a function of impact velocity. The apparent discrepancy for the Scale II projectiles can be attributed to the fact that appreciable front surface spallation occurred in these two cases, giving rise to large uncertainties in the volume determinations.

(2) At low impact velocities, the craters are narrow and deep while at velocities approaching the sonic velocity of the target material (5.1 km/sec) the craters approach a hemispherical shape. This is shown in figure 3 where the ratio of the crater depth to the crater diameter is plotted against the impact velocity. The volume-energy dependency and the observation concern-

THIN PLATE PERFORATION STUDIES

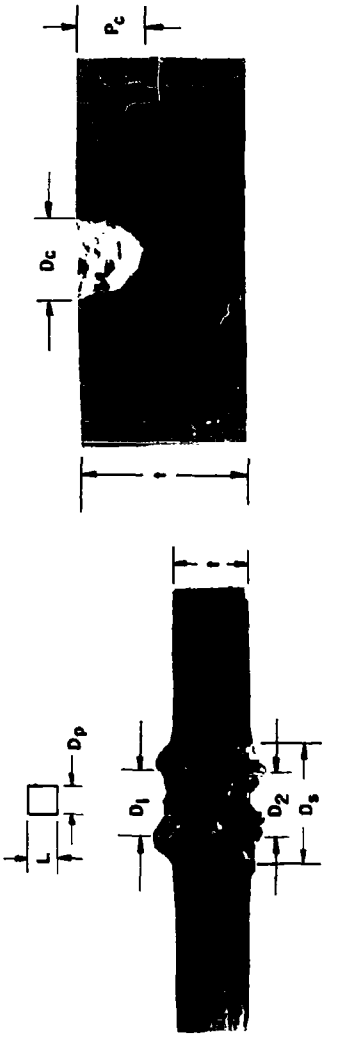

D_p – Projectile Diameter
L – Projectile Length
D_1 – Perforation Entrance Diameter
D_2 – Perforation Exit Diameter
D_s – Spall Diameter
t – Target Thickness
D_c – Crater Diameter
P_c – Crater Depth

FIGURE 1.–Features of a Thin Plate Perforation and a Crater Produced in a Thick Target.

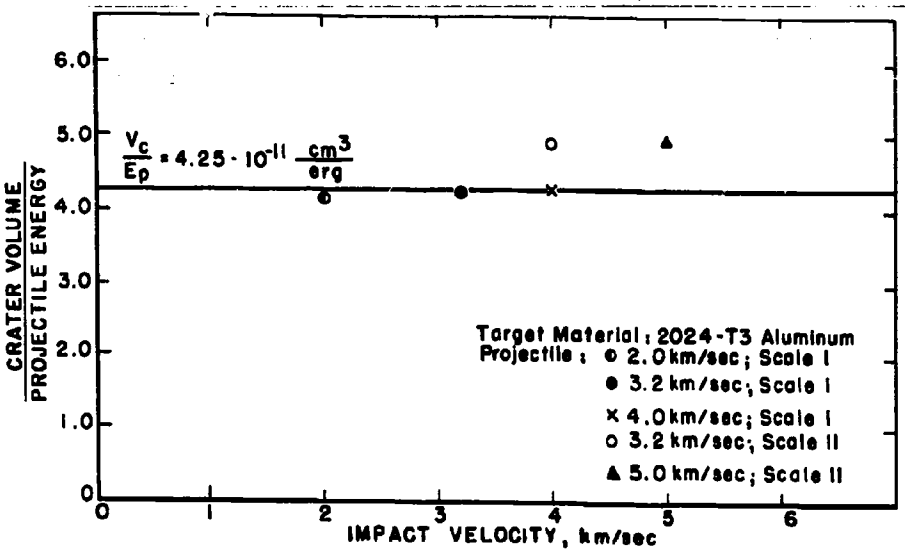

FIGURE 2.—Cratering Efficiency as a Function of Impact Velocity.

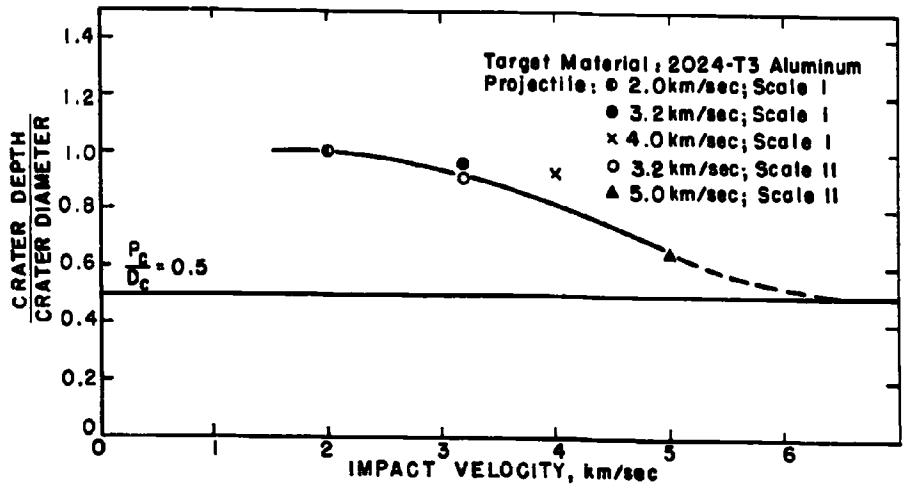

FIGURE 3.—Variation of Crater Shape with Impact Velocity.

ing crater shape are in accord with the results of other investigations for the same range of impact velocities (3,4).

(3) For thin targets having thicknesses in excess of approximately 1.5 times the projectile length, the perforation entrance diameter is independent of target thickness; however, there is a noticeable decrease in entrance diameter for targets of lesser thickness. These features are illustrated in figure 4 where the ratios of the entrance diameters to the crater diameters are plotted as functions of reduced target thickness. Since, as illustrated in figure 5, the perforations are nearly cylindrical, these comments also apply to the exit diameters. The decrease in perforation entrance diameter with diminishing target thickness has been observed for a variety of target materials (5); it has been demonstrated that the perforation diameter for 2S-O aluminum approaches the projectile diameter for targets of thicknesses much less than the projectile length. The results with 2024-T3 aluminum targets show the same trend.

The dependence of exit spall diameter on target thickness is illustrated in figure 6 where the ratio of the spall diameter to the crater diameter is plotted as a function of reduced target thickness for different impact conditions. The results show that, in general, the spall diameter tends to increase with increasing target thickness over the velocity range investigated.

An important feature of these perforation studies is illustrated in figure 7 where, from a practical point of view, the difference in behavior between a thin target and a thick target is delineated. In this plot the ratio T^*/P_c is plotted as a function of impact velocity. The variable T^* is the target thickness for which the expectation of complete perforation by a given projectile becomes negligible; P_c is the crater depth in a semi-infinite target. Values of T^* for a given projectile-target combi-

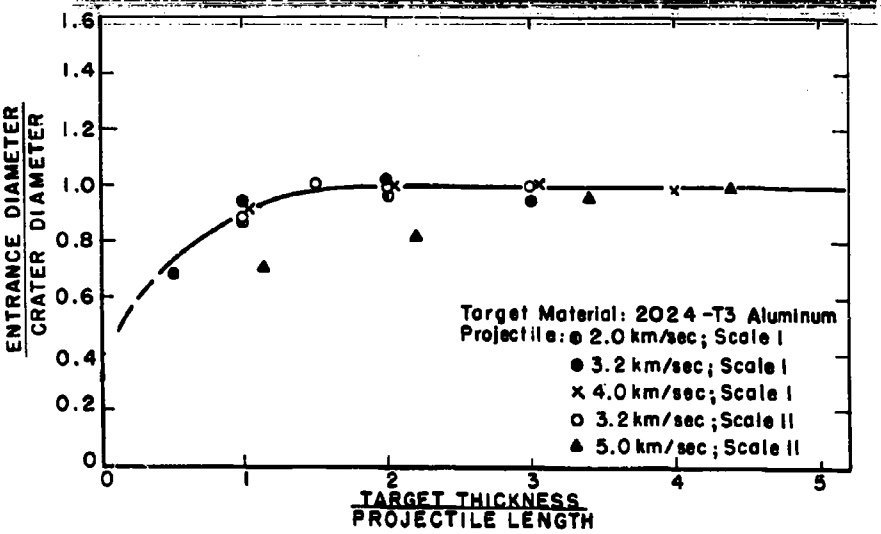

FIGURE 4.- Dependence of Perforation Entrance Diameter on Target Thickness.

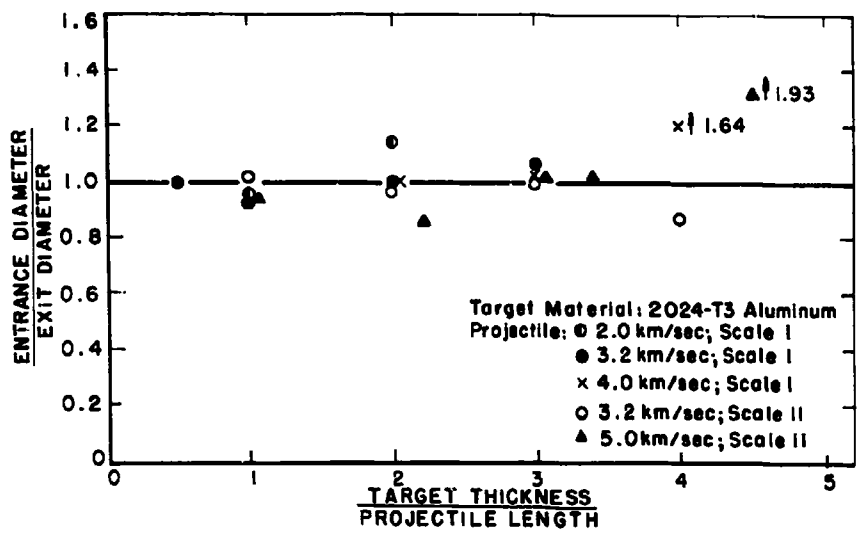

FIGURE 5.- Plot Showing Tendency for Perforations to be Cylindrical for Impacts Ranging from 2.0 to 5.0 km/sec.

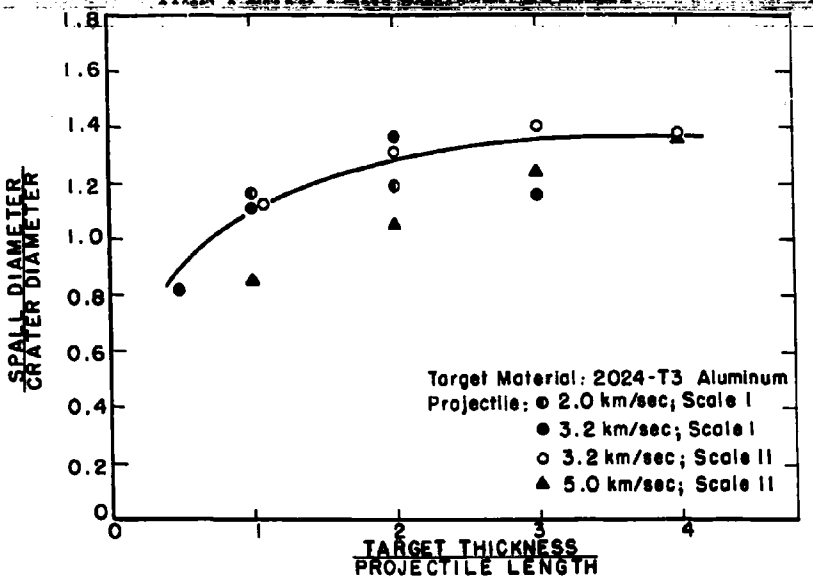

FIGURE 6.- Variation in Exit Spall Diameter with Target Thickness.

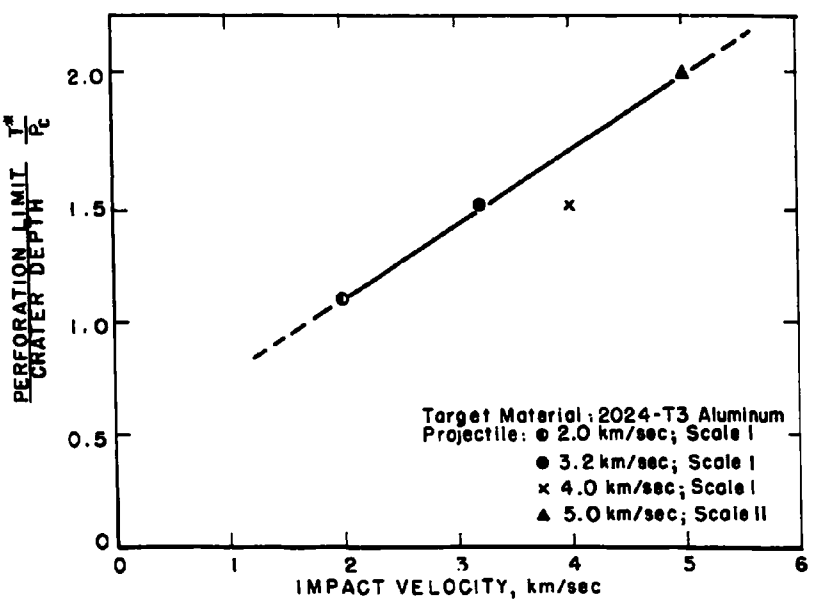

FIGURE 7.- Increase in Penetration Potential with Increasing Impact Velocity.

nation were estimated from the perforation probabilities observed in targets having thicknesses of about T^*. No attempt was made to statistically determine the values of T^*; however, the values used in figure 7 are probably accurate within $\pm$ 5 percent. The results show that the ratio T^*/P_c is a monotonically increasing function of the impact velocity, reaching values in excess of 1.5 for impacts in the 4.0 to 5.0 km/sec region. The significance of this observation is that the magnitude of crater depths in semi-infinite targets does not even closely approximate the penetration capabilities of the projectile through thin targets.

II. Number Distribution

The term "number distribution" refers to the manner in which the spall particles, produced by projectile-target impacts, are spatially distributed behind the target. The experimental technique for determining the distribution is illustrated in figure 8. A witness foil, consisting of 1-mil thick aluminum supported by a backing of fiberboard, was located 6-1/2 inches beyond the target. The witness foil indicated the direction in which individual spall particles were propelled.

For purposes of analysis, the witness foil was laid out in a family of concentric circles whose origin is located on a line through the perforation and normal to the target surface. The number of perforations, found in an element of area, $\Delta r \Delta \phi$, were counted and weighted by the reciprocal of the intercepted solid angle element, $\Delta \Omega$. The weighted count thus has the dimensions - number of fragments per unit solid angle and may be interpreted as representing the population density for a particular solid angle element. The total number of particles (N) is a function of the target thickness, the projectile velocity, and the projectile scale size. A complete reduction of all data at normal incidence is pos-

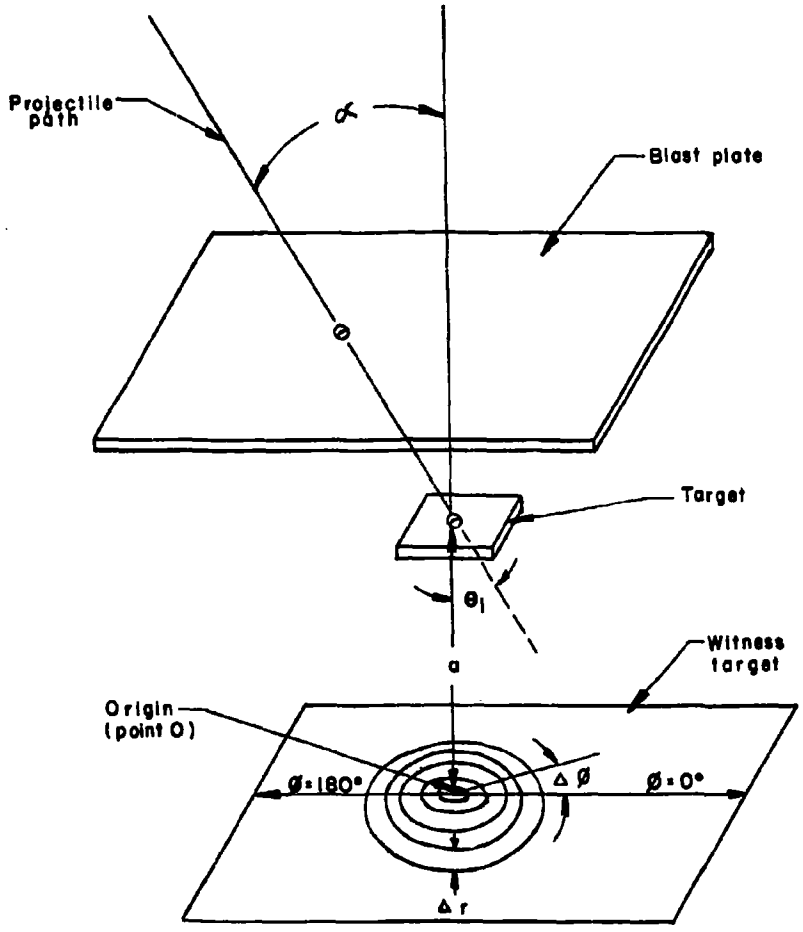

FIGURE 8. – Experimental Set-up for Determining the Spatial Distribution of Spall Fragments.

sible if the population density for each impact data set is multiplied by the factor $\frac{1}{N}$. Thus, the term $\frac{1}{N}\left(\frac{\Delta N}{\Delta \Omega}\right)$ expresses the density of a given element of solid angle as a fraction of the total population.

Number distributions have been determined for impacts on various thicknesses of 2024-T3 aluminum targets with both Scale I and Scale II projectiles over the velocity range 2 km/sec to 5 km/sec. These data are presented in figure 9 which shows $\frac{1}{N}\left(\frac{\Delta N}{\Delta \Omega}\right)$ vs Ω where Ω is a measure of the radial distance from the center of impact. Each data set is an average of several target thicknesses because the distributions for individual target thicknesses did not vary more than the experimental error. Within reasonable limits, the six data sets define one curve; the significance of this is that the percentage of the total number of spall particles found in corresponding elements of space is independent of projectile scale size, target thickness, and projectile velocity. The data for 3.2 km/sec, Scale I projectiles, are from an earlier paper (5). In the earlier work, the normalized distributions for 2024-T3 aluminum, 2S-0 aluminum, magnesium, and lead were found to be essentially the same. Another significant feature of the data deals with the distribution for spall particles having higher penetration capabilities. Data points for these superior particles are identified by stars and are shown to fit the curve as well as any other data point set. The superior group was separated from the aggregate group by filtering out the inferior particles with an additional 7 mils of aluminum foil; about 20 percent of the total population penetrated the filter.

The experimental technique, mentioned earlier, involved counting holes in witness targets and did not provide a distinction between projectile remnants and target spall particles. The desira-

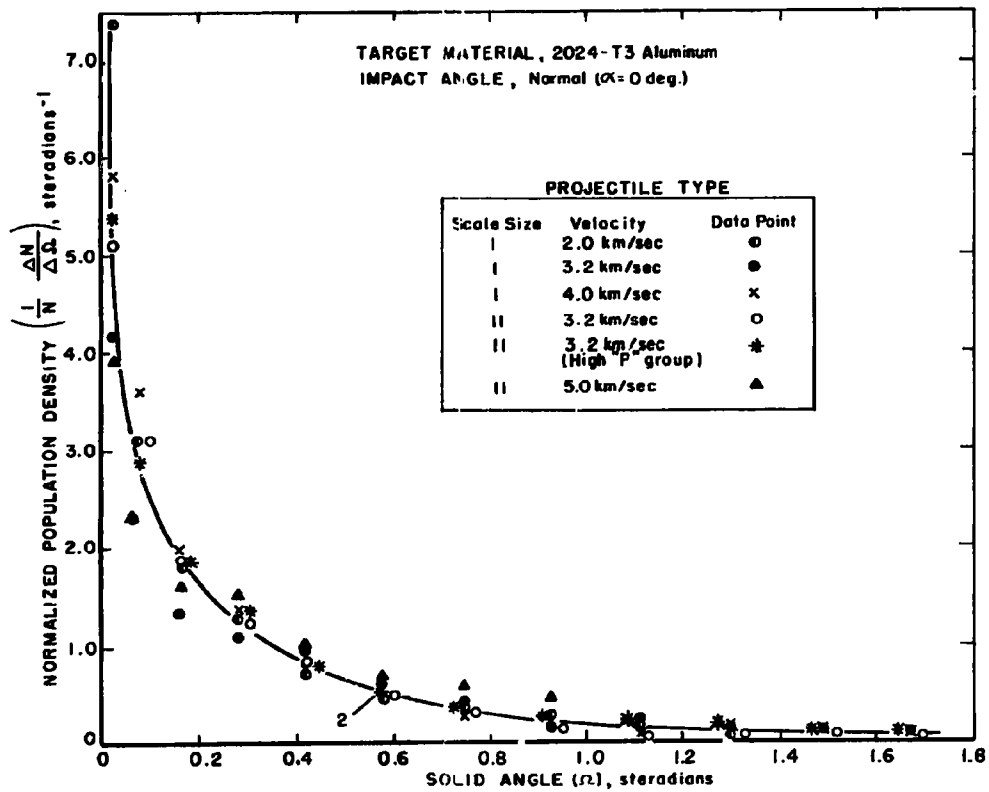

FIGURE 9.- Relationship Between Normalized Spall Numbers and Radial Distance from the Center of Spall Impact.

bility of establishing separate distributions for the two types of particles required analyses by a somewhat more time-consuming technique. A pan of gelatin was substituted for the aluminum witness foil; the gelatin layer was cut, after the impact event, into concentric, annular rings and each ring of gelatin was then dissolved in hot water and the individual particles recovered by filtration. The projectile remnants (steel) are separated magnetically from the target particles (aluminum) and counted. Distribution curves from tests using this technique are shown in figures 10 and 11 for the number of target spall particles and number of projectile remnants respectively.

The two figures show data for three different projectile parameters and illustrate several important points: (1) the percentage of the total number of target spall particles or total number of projectile remains found in a given space element is independent of projectile scale size, projectile velocity, or target thickness; (2) compared to the projectile remains, the target spall particles have a greater tendency to be radially dispersed.

Another interesting feature of these data is the effect of projectile scale size upon the total number of particles produced. The effect is shown in figure 12 for Scale I and Scale II projectiles impacting various thicknesses of 2024-T3 aluminum targets at 3.2 km/sec. The figure is a plot of $\left(\frac{N}{(kL)^2}\right)$ vs $\frac{t}{L}$ where N is the total number of target spall fragments, t is the target thickness, L is the length of the projectile, and k is a constant such that $kL = 1$ for the smaller scale size projectile. This treatment is intended to bring the Scale II data points into coincidence with corresponding Scale I data points. The fact that the second power of kL tends to accomplish this purpose demonstrates that there is a strong tendency for the total number of target spall particles

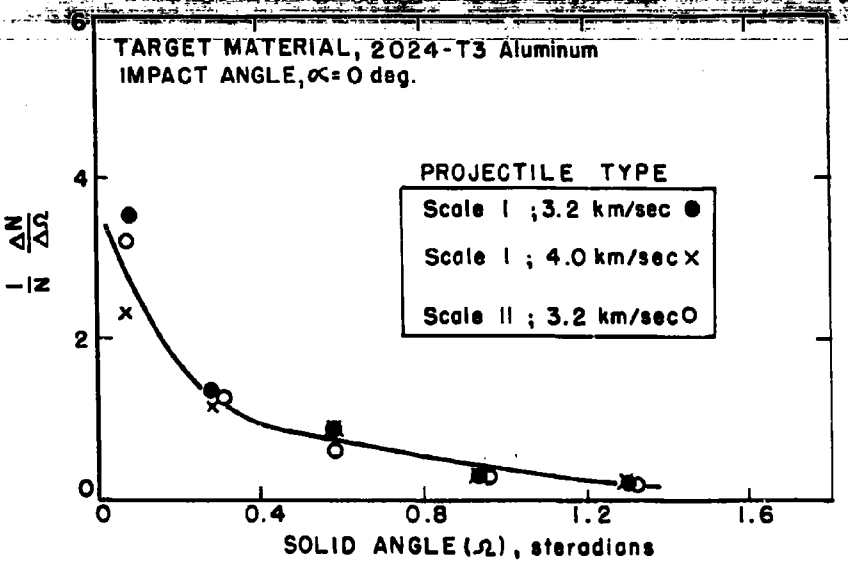

FIGURE 10. – Normalized Distribution for Target Spall Particles.

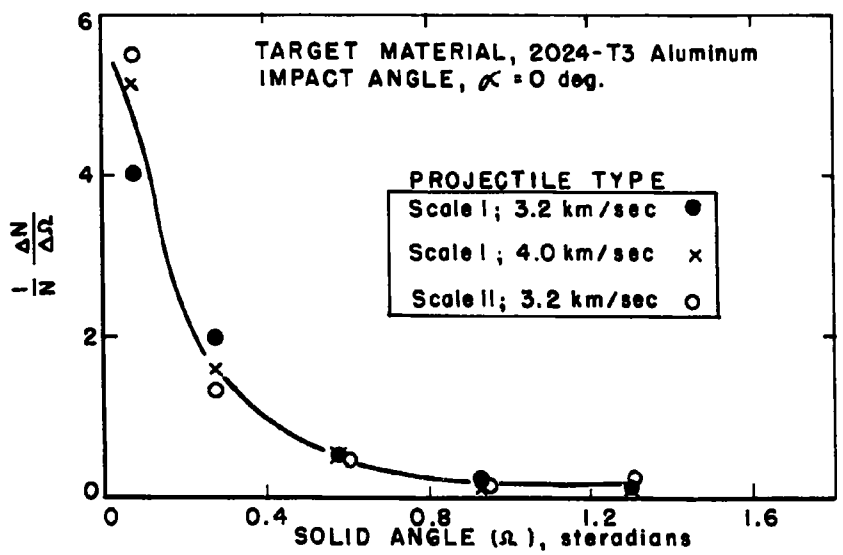

FIGURE 11. – Normalized Distribution for Projectile Remnants.

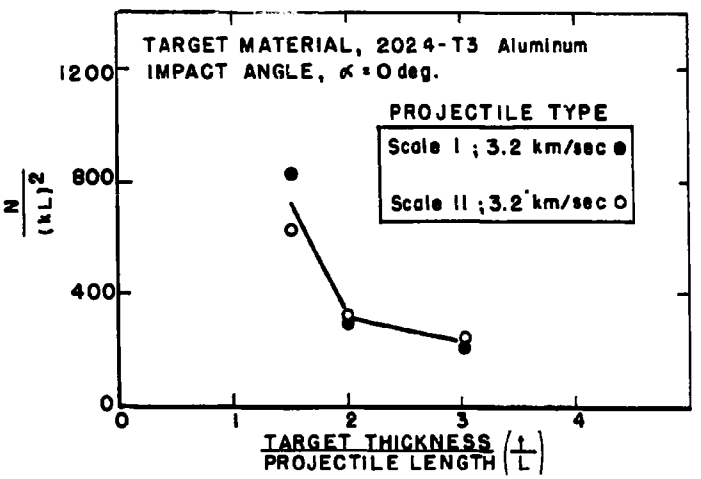

FIGURE 12.- Effect of Projectile Size Upon the Number of Target Spall Particles.

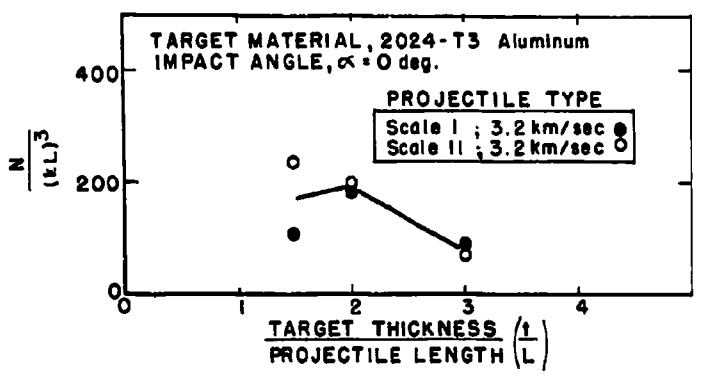

FIGURE 13.- Effect of Projectile Size Upon the Number of Projectile Remnants.

to vary directly with the area of the projectile; this is the case, however, only if the ratio of target thickness to projectile length remains constant.

A somewhat similar treatment is used to demonstrate the scaling effect for the number of projectile remnants produced. These data are presented in figure 13 which shows $\left(\frac{N}{(kL)^3}\right)$ vs $\frac{t}{L}$ where N, in this case, is the total number of projectile remnants. The interpretation here is that the number of projectile remnants produced varies directly with the volume of the projectile, providing the target thickness is scaled with a linear dimension of the projectile.

Data associated with the distributions of numbers of spall particles resulting from oblique impacts on targets have also been obtained. Although a number of significant features of the phenomena are evident, the oblique impact data do not permit as simple an interpretation as data from normal impacts. The added complexities are understandable inasmuch as the center of spall impact does not lie on a line beneath the perforation perpendicular to the target nor on the original line of flight of the projectile; it is found to lie between these two extremes. Hence, the distribution of particles, in terms of the target-witness geometry used for normal impacts, is not independent of the azimuthal coordinate ϕ (see fig. 8).

The dependence of spall numbers upon the coordinate ϕ is illustrated in figure 14 which is a plot of $\frac{1}{N}\frac{\Delta N}{\Delta \phi}$ vs ϕ and may be interpreted as representing the percentage of the total number of particles found to reside in indicated intervals of the angular coordinate ϕ. The plot is for data obtained from Scale I projectiles impacting targets at 60 degrees obliquity (α = 60 degrees). Projectile velocities were 2.0 km/sec, 3.2 km/sec, and 4.0 km/sec.

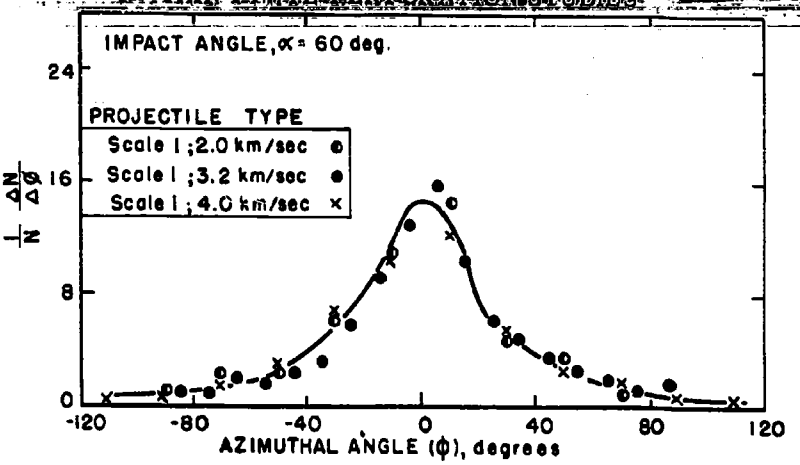

FIGURE 14. – Normalized Population Density as a Function of Azimuthal Angle.

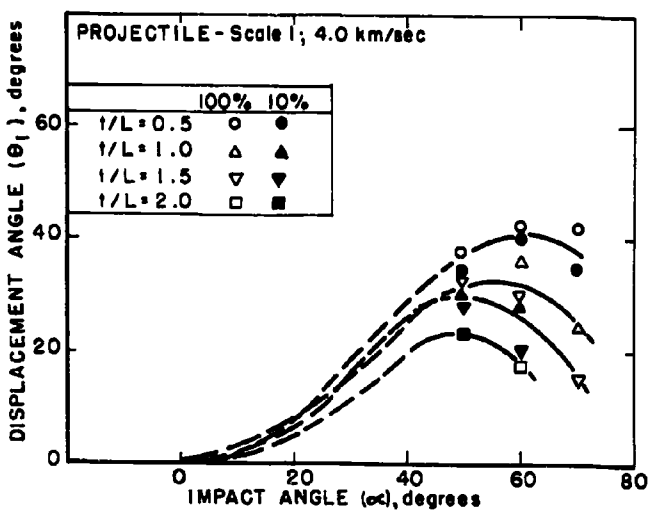

FIGURE 15. – Effect of Impact Angle Upon Displacement Angle.

The data were averaged for several target thicknesses since, again, a target thickness effect was not evident. Several significant features of the data are evident: (1) The spall particles are not dispersed symmetrically about the origin of circles on the witness foil (point 0 in fig. 8); rather, the center of spall impact is displaced radially outward along $\phi \approx 0$ (in the azimuthal direction corresponding to the line of flight of the projectile). (2) The density of spall particles is maximum along $\phi \approx 0$ and diminishes progressively and symmetrically in both the positive and negative angular directions removed from the $\phi \approx 0$. (3) The percentage of the total number of spall particles found in any given element $\Delta \phi$ is independent of target thickness and projectile velocity. A similar independence for 2S-O aluminum, 24S-O aluminum, and 2024-T3 aluminum for one projectile system (3.2 km/sec, Scale I projectile) was demonstrated earlier (5).

The displacements of the centers of spall impact as a function of both impact angle and target thickness are plotted in figure 15. The figure is a plot of displacement angle (θ_1) vs impact angle (α) with target thickness as a parameter; displacement angle is a measure of the displacement of the center of spall population from point 0. The Scale I, 4.0 km/sec projectile, was used to impact 1/32, 1/16, 3/32, and 1/8-inch thick 2024-T3 aluminum targets at 50, 60, and 70 degree impact angles. Target thicknesses are specified relative to the projectile length. An added feature of the plot is that centers of spall populations for the ten percentile group of particles having higher penetration capabilities are shown plotted separately. These data are identified by the designation - 10 percent; the aggregate groups are identified by the designation - 100 percent. Significant features of the plot are

as follows: (1) the displacement angle increases with the impact angle up to impact angle values of between 50 degrees and 60 degrees after which a decrease in displacement angle is noted for further increases in impact angle; (2) displacement angle is always less than impact angle; (3) there is a tendency for the ten percentile group to have lower displacement angles; however, the difference is small and for practical purposes they are interpreted to be the same as those for the aggregate group.

It would seem desirable to make a short comment regarding the peculiar behavior noted in (1) above where displacement angle was found to decrease for values of impact angle greater than about 60 degrees. It is believed that the axis for the envelope of projectile remains and associated target particles flowing through the perforation in the target is different from the axis of target spall produced by shock interactions. The interplay of two such distinct distributions could conceivably cause displacement angle to be a double valued function of impact angle.

III. Mass Distribution

Mass distribution refers to the manner in which the mass contained in the spall envelope is spatially distributed. The collection agent was gelatin, and the data were derived from the same shots used to determine separate particle population distribution for target spall and projectile remnants. Distribution curves take the form $\frac{1}{M}\frac{\Delta M}{\Delta \Omega}$ vs Ω which is similar to the distribution curves for the number of spall particles except that mass rather than numbers is being distributed among the space elements. The data are presented in two plots (figs. 16 and 17) which show $\frac{1}{M}\frac{\Delta M}{\Delta \Omega}$ vs Ω for the target spall mass and the mass of projectile remnants respectively. The plots contain three data point sets representing Scale I, 3.2 km/sec, Scale I, 4.0 km/sec, and Scale

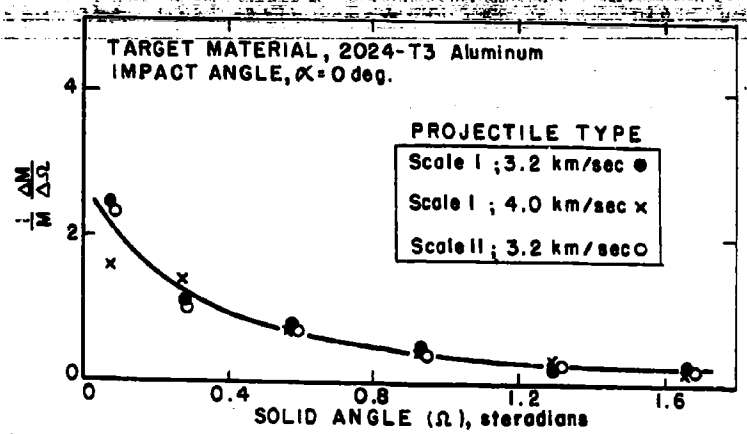

FIGURE 16.- Normalized Distribution for Target Spall Mass.

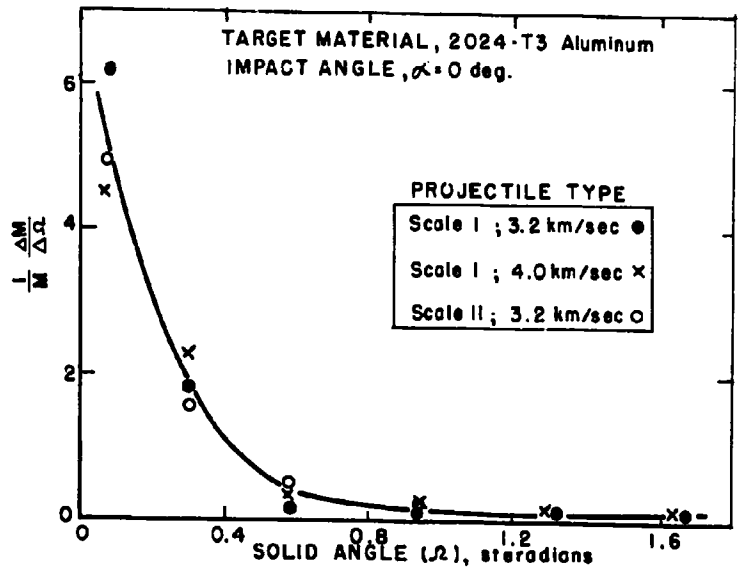

FIGURE 17.- Normalized Distribution for Mass of Projectile Remnants.

II, 3.2 km/sec projectiles that impacted on various thicknesses of 2024-T3 aluminum targets at normal incidence. Individual data points represent an average for several target thicknesses. Significant features of both plots may be summarized as follows: (1) Both distributions are qualitatively similar to the number distribution plots presented earlier, i.e., maximum density is observed at the center of spall impact and decreases radially outward; (2) the mass distribution for projectile remnants differs from the one for target spall particles in that the former shows a substantially greater percentage of the mass distributed nearer the center of spall impact; similar behavior existed for the number distribution data; (3) the percentage of the total amount of mass (target material or projectile remnants) found in any given space element is independent of target thickness, projectile scale size, and projectile velocity; (4) from (1) and (2) it may be concluded that particle size is not particularly dependent upon the space coordinates.

Another set of plots, figures 18 and 19, is presented to indicate reasonable scaling laws for the total mass contained in the envelope of material behind thin targets. The graphs show $\frac{M}{(kL)^3}$ plotted against $\frac{t}{L}$ for the total target spall mass and the mass of projectile remnants respectively. The power of the quantity (kL) is three in these instances and indicates that the total spall mass is proportional to the volume of the projectile providing the target thickness is scaled with the linear dimensions of the projectile. The plots also show that the target spall mass increases with target thickness providing one does not, too closely, approach the maximum penetration capability of the projectile; the mass of recovered projectile remains, however, is independent of target thickness at this particular velocity (3.2 km/sec).

Figure 20 shows the effect of target thickness on spall par-

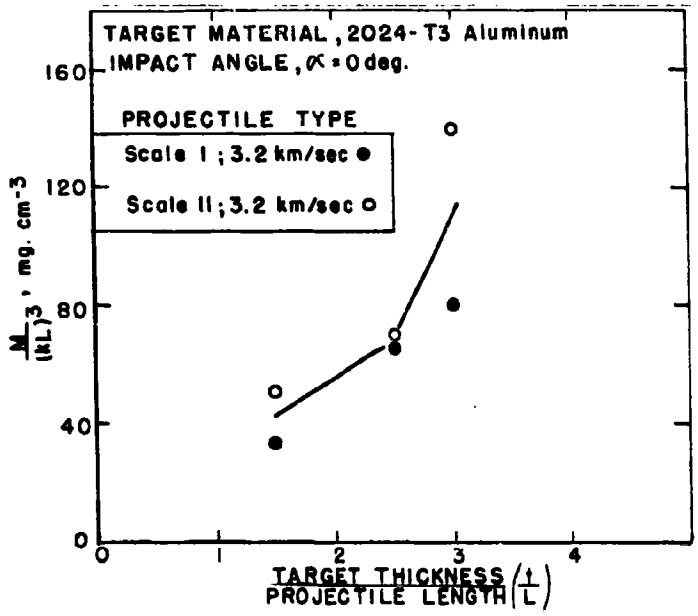

FIGURE 18.- Effect of Projectile Size Upon the Mass of Recovered Target Spall.

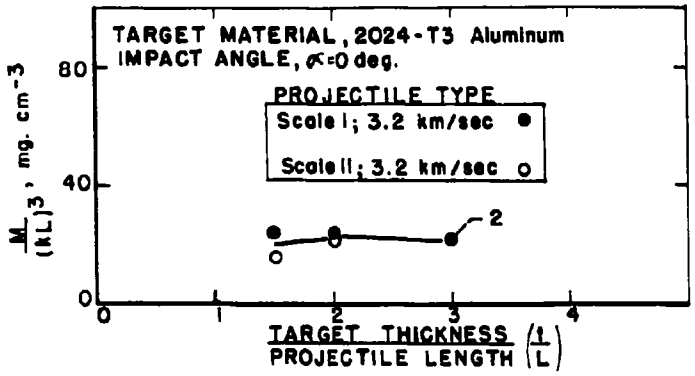

FIGURE 19.- Effect of Projectile Size Upon the Mass of Recovered Projectile Remnants.

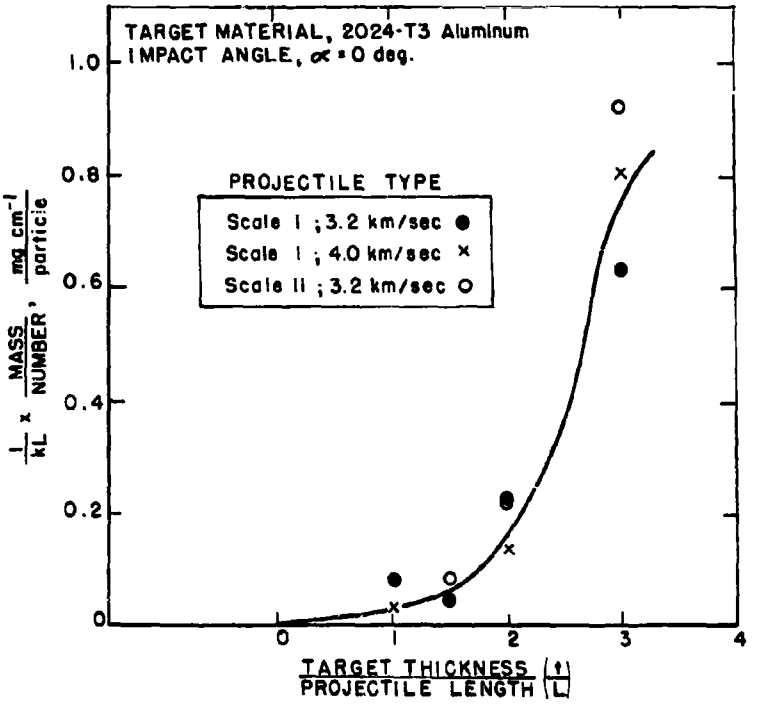

FIGURE 20.- Effect of Target Thickness Upon Average Target Spall Particle Size.

ticle size. The plot is presented in terms of the reduced variables $\frac{1}{kL}$ x mass/number vs $\frac{t}{L}$. The first power of $\frac{1}{kL}$ is the proper reducing factor between these Scale I and Scale II impact data because it has been shown that treatment of the mass data involved the third power and the number data the second power of this factor. It should also be pointed out that the values are unweighted average measures of spall particle size because total mass has simply been divided by total number. Individual data point sets are shown for impacts with 3.2 km/sec Scale I, 4.0 km/sec Scale I, and 3.2 km/sec Scale II projectiles. The character of the plot is interesting from several viewpoints: (1) The average size (mass/particle) of the target spall particles increases drastically with increasing target thickness; the increase amounts to almost an order of magnitude for $\frac{t}{L}$ values ranging from one to three. The change in spall mass and spall numbers with increasing target thickness are in the proper direction for maximum increase in particle size, i.e., spall mass increases while spall numbers decrease. (2) Average spall particle size is proportional to the first power of the scale factor; hence, the Scale II projectiles produce spall particles which are, on the average, twice the size of those produced by Scale I projectiles. (3) The Scale I, 4.0 km/sec data have been included in this plot merely to show that target thickness effect is much more pronounced than the effect from the indicated change in velocity; it is conceivable, however, that a significant velocity effect might be observed if the projectile velocities were substantially different.

IV. Velocity Distribution

The experimental effort directed toward a description of the velocity distribution of the material ejected from thin plates was limited by the small scale size of the projection systems used.

No single experiment has proven adequate for this purpose and, as a consequence, several velocity measuring techniques have been employed. A dual-channel flash X-ray system has been successfully applied to the problem of determining the residual velocity of the emerging projectile material. These measurements coupled with target impulse studies, with a ballistic pendulum, have led to values of total target-spall momentum. A recently developed framing camera technique has proven satisfactory for determining the velocity spectrum of the combined projectile and target spall particles produced by a variety of impact conditions. In this technique, the target spall particles and projectile remains are directed toward a thin aluminum foil viewed by the framing camera. The side of the foil away from the camera is uniformly illuminated by means of an exploding wire used in conjunction with a diffusion screen. When the particles puncture the foil, the event is recorded in the framing camera sequence as a bright flash. The time of occurrence of this event relative to the time of target impact and the distance between the target and the witness foil are then used to calculate an average velocity for each particle observed. By an appropriate choice of framing rate the entire velocity spectrum can be mapped.

The results of the investigations carried out in this area are graphically shown in figures 21 through 29; when considered in their entirety they lead to certain conclusions. The formula

$$v_r = \left[v_o^2 \, e^{-\frac{\rho_t A_f \, z}{m_f}} - \frac{2k}{\rho_t} \left(1 - e^{-\frac{\rho_t A_f \, z}{m_f}} \right) \right]^{1/2}$$

where z = instantaneous depth in the target;

v_r = residual fragment velocity;

A_f = cross sectional area of impacting fragment;

m_f = mass of impacting fragment;

v_o = initial fragment velocity;

ρ_t = target density;

k = target strength factor

derived from previous work with 3.2 km/sec, Scale I projectiles (6) is found to be applicable when the projectile scale size is varied. This is illustrated in figure 21 where the measured values of v_r for both Scale I and Scale II projectiles are plotted as a function of target thickness; a curve calculated from the above formula using the same value of the strength constant k is also shown.

Furthermore, by reasoning that any net impulse transferred to the target, per se, is due to the forces associated with the strength term, k, the residual velocity formula can be used to predict target impulse by first calculating the total momentum lost by the projectile in perforating a given target thickness, z, and then deducting from this value the momentum loss associated with the fluid term in the equation, i.e., k = 0. This method was used to obtain the values represented by the curve which is presented in figure 22 along with measured values of target impulse obtained from ballistic pendulum measurements. The agreement between the measured value and the value calculated on the basis of the above model is very good; however, it should be emphasized that the model is based on the assumption that the projectile suffers little deformation during the perforation process. Flash radiographs indicate that this assumption is no longer valid for steel-aluminum impacts above 4 km/sec.

There is, under certain impact conditions, appreciable momentum associated with the material splashed from the front surface of thin targets; consequently, a simple measure of target impulse and a knowledge of projectile momentum is not sufficient for specifying the momentum of the material carried through the target.

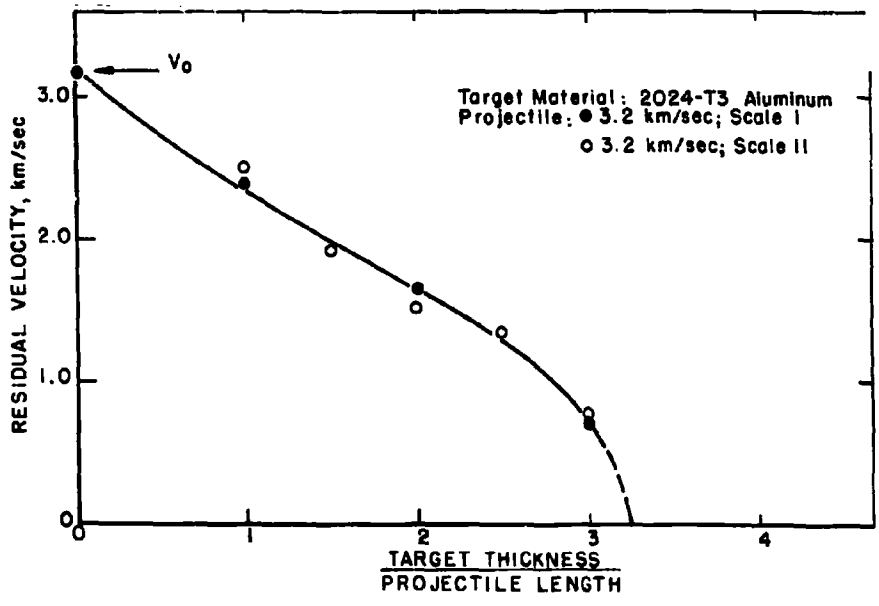

FIGURE 21.- Residual Projectile Velocity as a Function of Target Thickness.

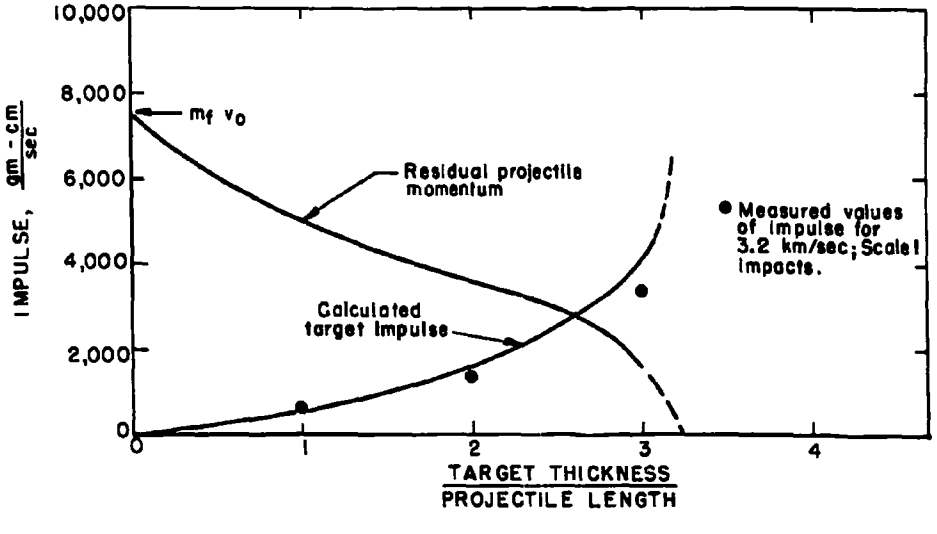

FIGURE 22.- Comparison Between Measured and Calculated Values of Target Impulse.

THIN PLATE PERFORATION STUDIES

Stanyukovich has proposed that above a certain critical velocity the momentum delivered to a target structure is simply related to the kinetic energy of the impacting projectile (7).

Specifically, he equates:

$$J = \frac{BE_o}{\sqrt{\epsilon}}$$

where J = total normal impulse;
E_o = projectile energy;
$\sqrt{\epsilon}$ = target strength;
B = coefficient of proportionality.

A limited number of tests with aluminum, lead, copper, and cadmium targets tend to substantiate the above formulation. These results are presented in figure 23 where the ratio of the total target impulse to the impacting projectile momentum is plotted as a function of reduced impact velocity for a variety of impact conditions. On the assumption that ϵ represents the shear strength of the target, the above formula can be rewritten as:

$$\frac{J}{J_o} = \frac{B}{2\sqrt{\rho_t}} \frac{v_o}{v_s}$$

where J = total normal impulse;
J_o = projectile momentum;
v_o = impact velocity;
ρ_t = target density;
v_s = shear wave velocity;
B = coefficient of proportionality.

Thus, the ratio $\frac{J}{J_o}$ is a linear function of impact velocity reduced

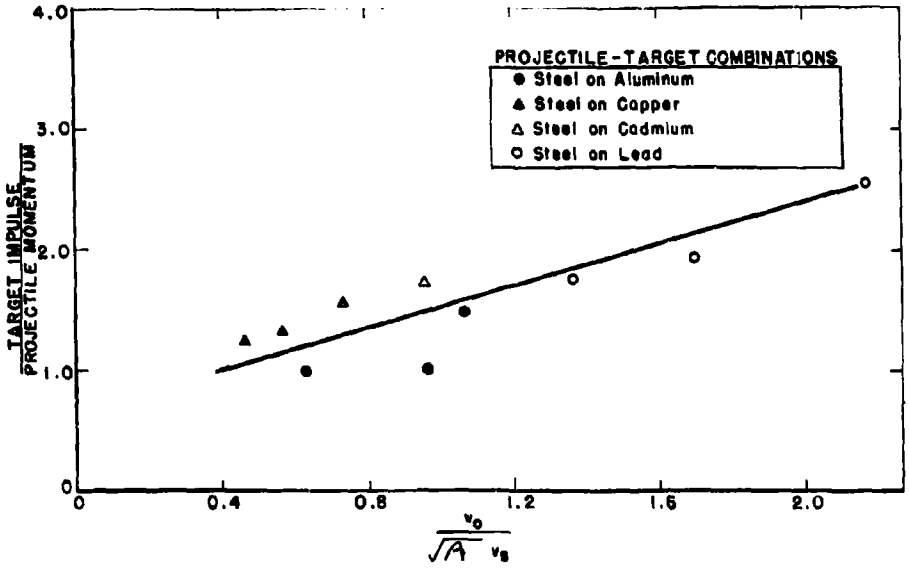

FIGURE 23.- Excess Momentum as a Function of Impact Velocity.

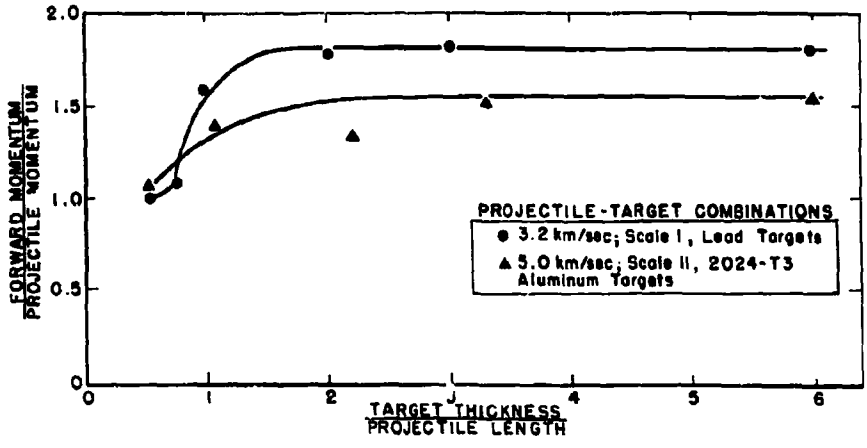

FIGURE 24.- Forward Momentum as a Function of Target Thickness.

by $\sqrt{\rho_t v_s}$. When plotted in this form the data indeed show this linear dependence.

In terms of the thin targets, an interesting and important aspect of the momentum excess phenomenon is illustrated in figure 24 where the experimental results of impulse tests with thin aluminum and lead targets are presented. In these experiments the total forward momentum delivered to the target structure and target spall system was measured as a function of target thickness. For the lead targets, 3.2 km/sec, Scale I projectiles were used; 5.0 km/sec, Scale II projectiles were used in the aluminum tests since this was the only impact arrangement where excess momentum was observed.

The significant feature of this series of tests is the fact that the total forward momentum is essentially independent of target thickness when the latter exceeds one to two times the projectile length. Since, on the basis of hydrodynamic considerations, these values roughly correspond to the primary penetration expected for these target-projectile combinations, the results indicate that the excess momentum imparted to the target-spall system is derived during the hydrodynamic phase of the perforation process.

The practical implication of these observations is illustrated in figures 25 and 26 where the results of impulse studies in 2024-T3 aluminum targets at impact velocities of 3.2, 4.0, and 5.0 km/sec are summarized. The ratio of target impulse to the initial projectile momentum is plotted as a function of target thickness in figure 25. It will be noted that only a small fraction (20 percent or less) of the total forward momentum is absorbed by the target structure for target thickness less than twice the projectile length.

The ratio of total spall momentum to the initial projectile momentum is plotted in figure 26 as a function of target thickness.

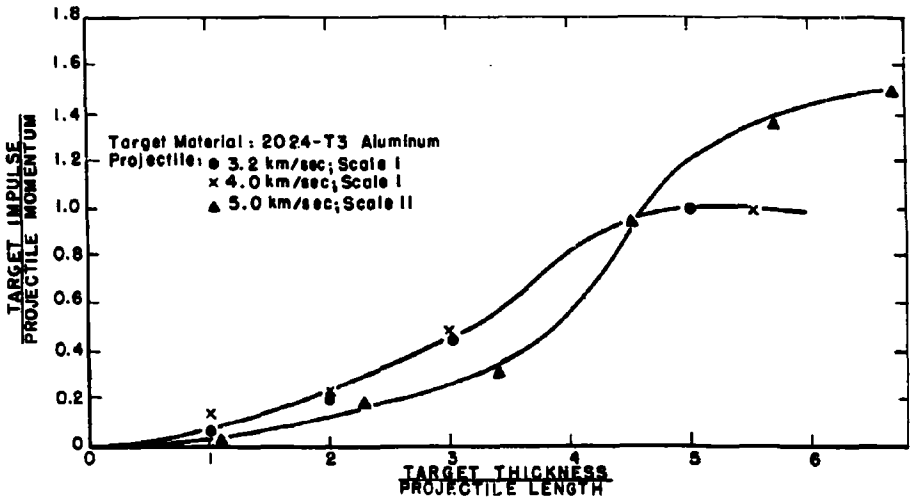

FIGURE 25.- Target Impulse as a Function of Target Thickness.

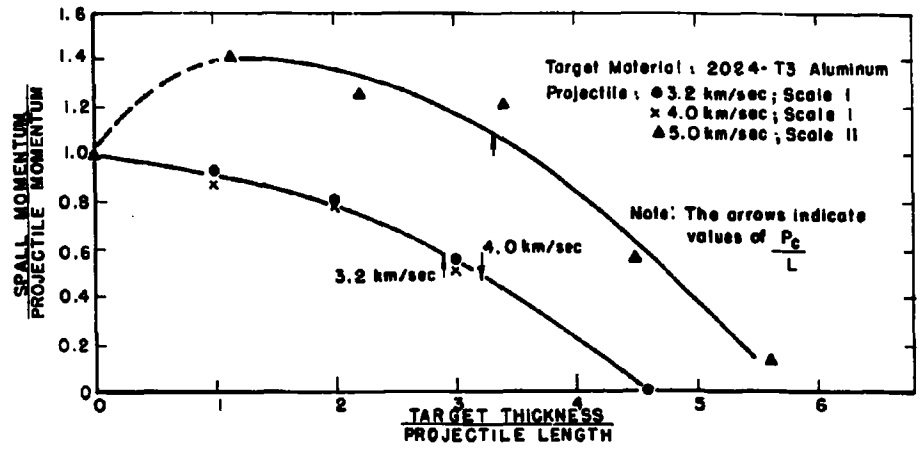

FIGURE 26. - Ejecta Momentum as a Function of Target Thickness.

These results emphasize the fact that a considerable portion of the total forward momentum is contained in the target ejecta system for target thicknesses in excess of the depth of penetration expected in the semi-infinite target configuration; for impacts at 5.0 km/sec, the value of spall momentum is greater than that of the impacting projectile momentum for target thicknesses equal to or less than P_c (crater depth in an infinite target).

The framing camera technique has been used to obtain data relative to the velocity distribution of the individual ejecta particles as a function of target thickness for 3.2 km/sec Scale I, 3.2 km/sec Scale II, and 5.0 km/sec Scale II impacts on 2024-T3 aluminum targets. The results of these experiments are presented in figures 27 through 29 where values of $\frac{\Delta N}{N}\frac{1}{\Delta v}$, which represent the percentage of the total population lying in a velocity increment Δv, are plotted as a function of velocity for various target thicknesses.

The results indicate that for scaled systems (figures 27 and 28) the velocity distributions are similar in that both the maximum spall velocity (intercepts with the velocity axis) and the maxima of the curves (velocity corresponding to the maximum percentage of the total number) nearly coincide.

The velocity distribution curves for different target thicknesses impacted at 3.2 km/sec and 5.0 km/sec show the expected shift in the direction of lower velocity values as the target thickness is increased. The distributions obtained in 3.2 km/sec and 5.0 km/sec Scale II tests with 3/8 inch thick targets tend to show a bimodal form which probably arises from a distinction between the velocities of the projectile remnants (and/or target material driven through the perforation) and spallation resulting from shock interaction at the free surface of the target.

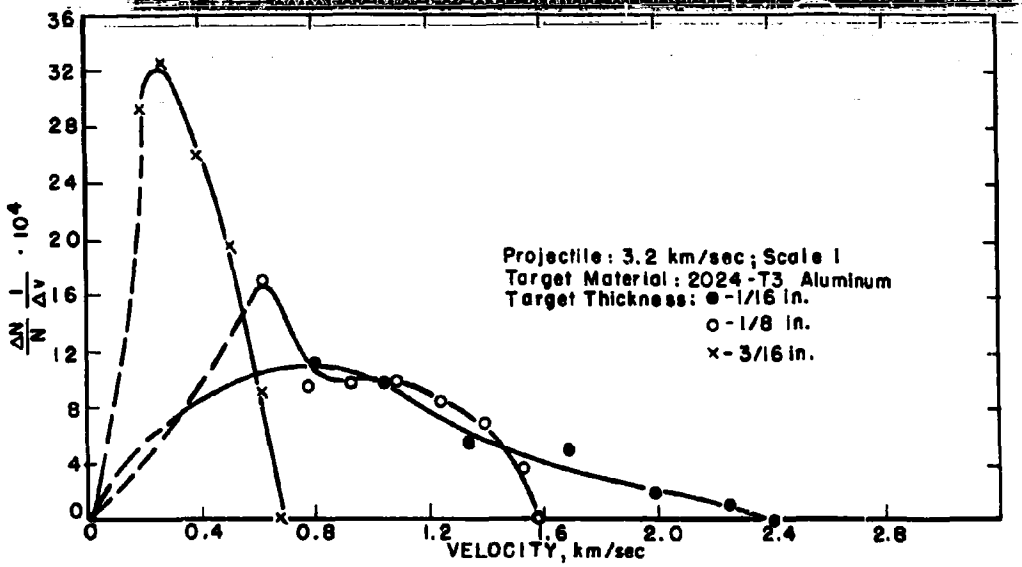

FIGURE 27. - Velocity Distribution of Target Ejecta from 3.2 km/sec Scale I Impacts.

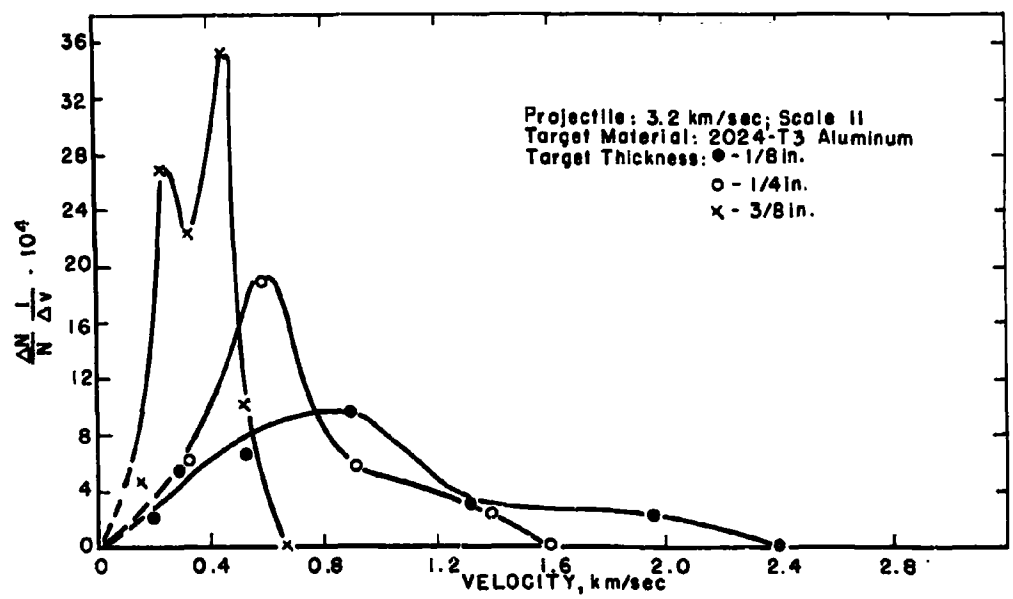

FIGURE 28. - Velocity Distribution of Target Ejecta from 3.2 km/sec Scale II Impacts.

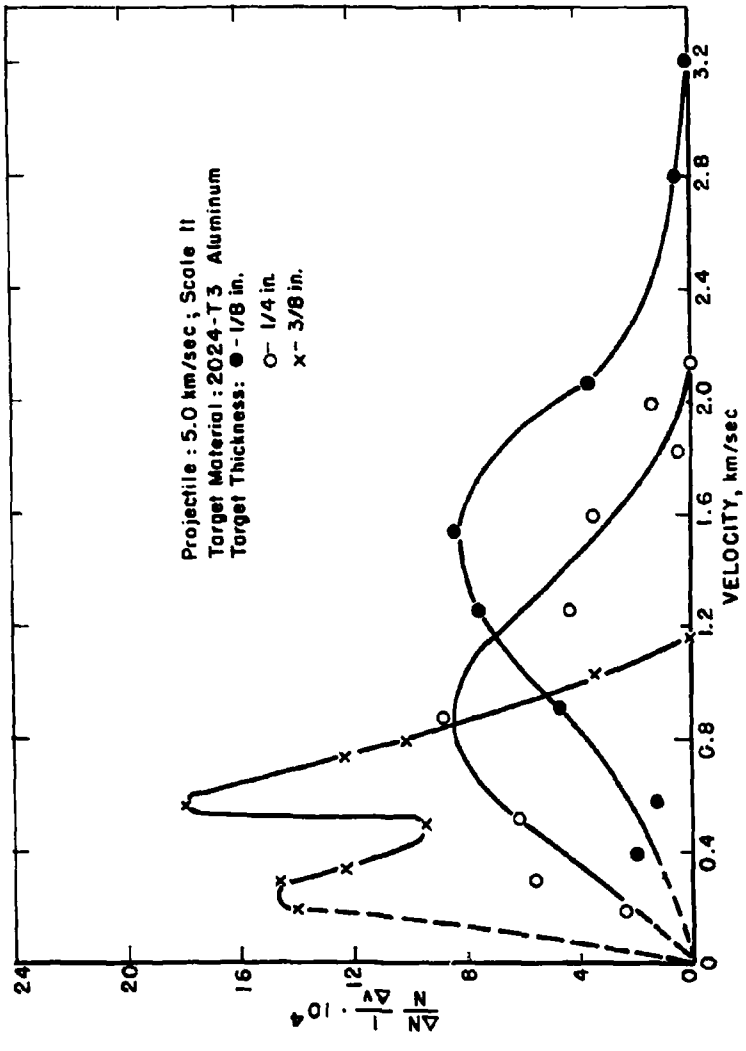

FIGURE 29. - Velocity Distribution of Target Ejecta from 5.0 km/sec Scale II Impacts.

THIN PLATE PERFORATION STUDIES

CONCLUDING REMARKS

The more important aspects of the thin plate perforation process have been investigated over the velocity range from 2 to 5 km/sec. Particular emphasis was placed on studying the spatial, mass, and velocity distribution of rear surface ejecta as the impact velocity, projectile scale size, and the target thickness were varied. A number of simple relationships have been established among these variables. For the case of a nondeforming projectile, it has been shown that residual projectile velocity and target impulse can be predicted on the basis of a simple mathematical model.

The situation is much more complicated where the projectile is seriously deformed. However, the observations relating to the behavior of the target ejecta system indicate the applicability of a simple shock-spallation model. Evidence for this comes from the projectile scale size experiments at 3.2 km/sec where it was found that the mass of target material varied with the cube of the characteristic projectile dimension while the total number of target particles generated varied with the square of the projectile dimension. The formation and subsequent breakup of a back surface spall might lead to these results if proposed spall scaling laws are valid (8). In addition, the number of target particles is found to depend most heavily on target thickness, decreasing markedly as the target thickness is increased. Furthermore, for a given target thickness and projectile scale size, the number of particles is found to increase with impact velocity. This behavior suggests that the number of particles generated in any given impact situation depends primarily on the intensity of the shock wave incident on the rear surface of the target. The general behavior of

the velocity distributions of the ejecta can be described in these same terms.

Further evidence supporting the proposed spall model lies in the observed insensitivity of the spatial distributions of the target ejecta on any of the experimental parameters. Since the ratio of the radial and normal components of velocity of a given particle would depend heavily on the curvature of the impinging shock wave (a slowly varying function of the initial parameters) rather than the incident shock strength (a rapidly varying function of the initial parameters), this observation is also compatible with the proposed model.

REFERENCES

1. Watson, R. W., K. R. Becker, G. M. Bryan, and R. Vitali. Fundamentals of Shaped Charges, Carnegie Institute of Technology, Contract No. DA-36-061-ORD-513, October 31, 1961, pp. 2-12.
2. Kineke, John H. Jr., and Lee S. Halloway. Macro-Pellet Projection with an Air Cavity High Explosive Charge for Impact Studies, BRL Memorandum Report No. 1264, April 1960, 17 pp.
3. Atkins, W. W. Hypervelocity Penetration Studies. Proc. of Fourth Hypervelocity Impact Symposium, April 26-28, 1960.
4. Kineke, John H. Jr. An Experimental Study of Crater Formation in Metallic Targets. Proc. of Fourth Hypervelocity Impact Symposium, April 26-28, 1960.
5. Vitali, R., K. R. Becker, and R. W. Watson. Perforation of Finite Targets by High Velocity Projectiles. Proc. of Fifth Symposium on Hypervelocity Impact, Vol. 1, Part 2, April 1962, pp. 595-596.
6. Watson, R. W. Perforation of Thin Plates by High Velocity Fragments. Proc. of Fifth Symposium on Hypervelocity Impact, October 1961, pp. 587-588.
7. Stanyukovich, K. P. Concerning the Impact of Solids at High Velocities. J. Exptl. Theoret. Phys. (U.S.S.R.) 36, May 1959, pp. 1605-1606.
8. Erkman, John O. Decay of Explosivity-Induced Shock Waves in Solids and Spallings of Aluminum. Third Symposium on Detonation, Princeton University, September 26-28, 1960, pp. 253-266.

A NEW SYSTEM OF PROTECTION FROM HYPERVELOCITY PARTICLES

by

B. W. Reynolds and R. H. Emmons

Goodyear Aircraft Corporation

Akron, Ohio

A NEW SYSTEM OF PROTECTION FROM HYPERVELOCITY PARTICLES

by

B. W. Reynolds* and R. H. Emmons+

ABSTRACT

Rigid and foldable meteroid protection systems for space structures have been experimentally evaluated by Goodyear Aircraft Corporation (GAC). In light of the findings, GAC proposes using a double-wall system incorporating a thin outer wall and a foam spacer attached to an inner structural wall. The foam spacer serves as a mechanical atmosphere tending to absorb and arrest the impacting materials through vaporization.

The GAC experimental tests and data do not support the conclusion of other investigators that the penetration resistance of polymeric materials (flexible fabrics) cannot compare with metals. Significant trends in materials and techniques for protecting against hypervelocity impacts are exhibited.

*Development Engineer, Materials Technology Department, Aeromechanics Technology Division, Goodyear Aircraft Corporation, Akron, Ohio.

+Space Environmentalist, Astronautics Systems Department, Space Systems Division, Goodyear Aircraft Corporation, Akron, Ohio.

PROTECTION FROM HYPERVELOCITY PARTICLES
TABLE OF CONTENTS

Title	Page
INTRODUCTION	253
EXPERIMENTAL DATA	256
BUMPER TEST RESULTS	257
SPACER TEST RESULTS	263
OTHER TEST RESULTS	264
MECHANICAL ATMOSPHERE PROTECTION CONCEPT	264
CONCLUSIONS	274
LIST OF REFERENCES	276
APPENDIX	277

LIST OF ILLUSTRATIONS

Figure	Title	Page
1	Meteoroid Flux in Near-Earth Environment . . .	254
2	Meteoroid Mass-Velocity Relationship	254
3	Schematic of Initial Hypothetical Specimen Configuration (Utilized for Single-, Double-, and Triple-Wall Specimens)	257
4	Hypervelocity Penetration Specimens A-11 through I-1	258
5	Hypervelocity Penetration Specimens I-2 through S-2	259
6	Homogeneous Bumper Impacts	261
7	Heterogeneous Bumper Impacts	262
8	Structural Wall Damage When No Spacer was Used	265
9	Penetrated Foam Weight Comparisons	268
10	Penetration Test Specimens T-2 and U-1.	268
11	Total Penetrated Weight Comparison	269
12	Mechanical Atmosphere Concept	271
13	Foam Penetration Depth	273
14	Protection Concept for Manned Space Structures from Meteoroid Penetration	274

PROTECTION FROM HYPERVELOCITY PARTICLES

INTRODUCTION

Meteoroid protection systems can logically be discussed only after meteoroid environment, damage, and simulation have been studied and evaluated. Only the important facets of these problems are presented in this paper; more extensive details can be found in the references.

Meteoroid environmental characteristics of interest are flux, mass, composition, velocity, and spatial position. Figure 1 presents a summary of meteoroid flux and mass determinations. Unfortunately, there is still a lack of data in the mass regime where the greatest penetration hazard is indicated. A simple function relationship[1a] was tentatively and conservatively selected for preliminary design purposes on vehicles in close earth orbit. The relationship is defined by $F_{>} = 1 \times 10^{-14} m^{-1.38}$, where $F_{>}$ is the number of particles per square meter per second of mass greater than or equal to m in grams.

Meteoroids can be classified into three groups by density. Thus, 90 percent of the total flux, $F_{>}$, consists of 0.5 g/cm^3 particles; 9 percent consists of 2.8 g/cm^3 particles; and 1 percent consists of 7.8 g/cm^3 particles. The low density particles, 0.5 g/cm^3, are believed to be higher density particles held together by fragile porous matrix materials.[2,3,4]

Meteoroid velocity is believed to decrease as the particle mass decreases. A velocity gradation with particle mass is shown in Figure 2. The average perforation hazard meteoroid is believed to have a velocity no less than 50,000 ft/sec relative to any earth-orbiting space vehicle.[5] For expediency, the oversimplification is adopted that the meteoroid flux follows a Poisson distribution.

Two basic types of damage are expected from meteoroid impacts. The smaller micrometeoroid particles striking the outer wall of a space structure tend to erode the surface, thereby causing changes in the optical properties and subsequently affecting the thermal balance of the structure. The larger meteoroid particles may penetrate the space structure and

[a]Superior numbers in the text refer to items in the List of References.

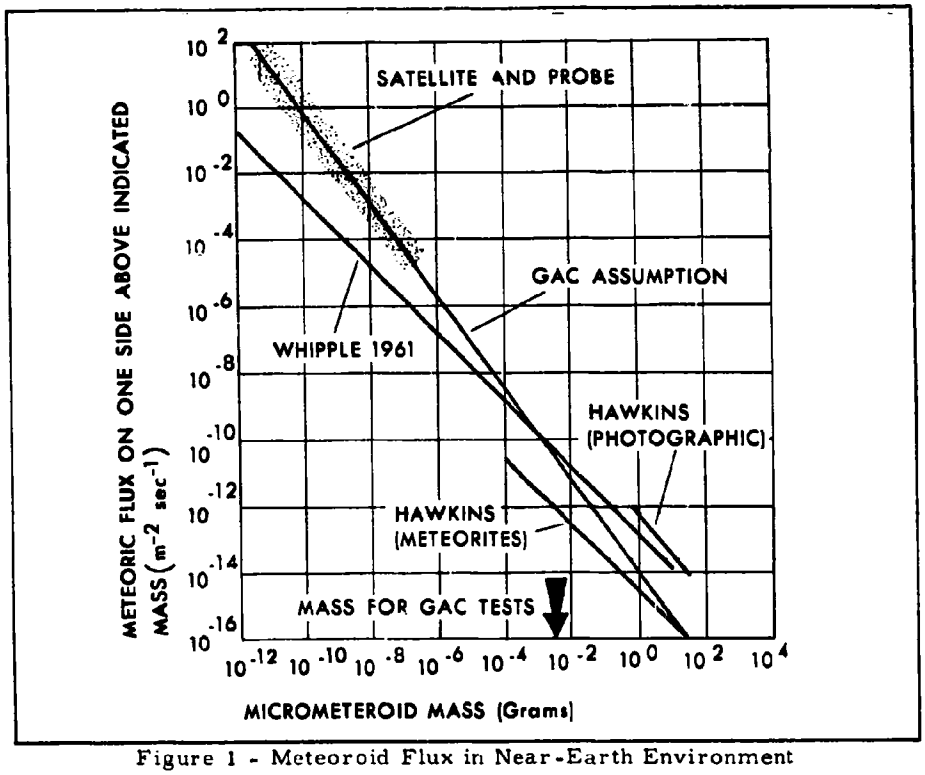

Figure 1 - Meteoroid Flux in Near-Earth Environment

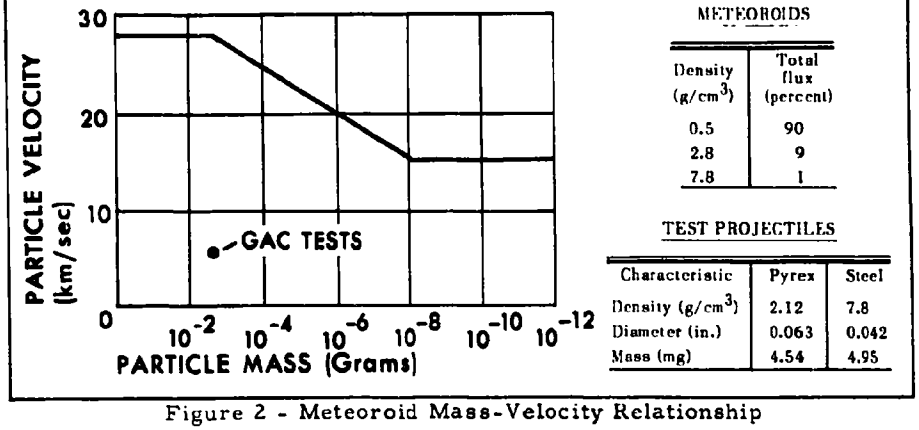

METEOROIDS

Density (g/cm^3)	Total flux (percent)
0.5	90
2.8	9
7.8	1

TEST PROJECTILES

Characteristic	Pyrex	Steel
Density (g/cm^3)	2.12	7.8
Diameter (in.)	0.063	0.042
Mass (mg)	4.54	4.95

Figure 2 - Meteoroid Mass-Velocity Relationship

cause spalling accompanied by or independent of penetration. Impacts by the larger meteoroids subsequently could produce other types of damage to a space structure, such as structural failure, loss of internal pressurizing and life-supporting gases, equipment damage, explosive decompression, and catastrophic atmospheric flash.[3]

This investigation was directed toward the development of external additional protection for both rigid and flexible structural walls, to prevent wall perforation by all meteoroids with masses up to the largest that reasonably could be expected to be encountered during an actual mission. Refer to Figure 2 for a comparison of test projectiles and meteoroids.

Until recently, with the exception of a few scattered points, the maximum published impact velocity appeared to be 12,000 ft/sec for projectiles of known mass. During early 1962, several simulation facilities were found capable of accelerating small spherical projectiles from 1 to 10^{-4} grams to velocities approaching 25,000 ft/sec using light gas guns. Later in 1962, several facilities were established to be capable of accelerating particles to and above 50,000 ft/sec by using exploding foil techniques. Various shaped charge devices accelerate particles to and above 30,000 ft/sec. These facilities require ingenious instrumentation for measuring particle mass just before impact. It can be seen that, if acceleration technique improvement maintains its present pace, adequate simulation of meteoroid particle sizes and velocities will be attained in the near future.[1]

Considerable work is still required in measuring and recording the various phenomena associated with hypervelocity impact. However, instrumentation technology has shown considerable advance. Velocity measurements are made by a variety of techniques. High-speed photography is used for submicrosecond observations of surface phenomena at impact and for observations of such interior behavior as crater enlargement, shock propagation, and fracture in transparent targets. Transient density changes as well as surface and interior processes have been exhibited by flash X-ray photography. Pressure-time profiles during crater formation have been obtained. Impulse measurement by ballistic pendulum techniques, recovery

of particle fragments and residue, and recovery of spall particles are enabling quantitative analyses to be more rigorous. However, no single facility provides all the desirable techniques for complete qualitative and quantitative analysis of hypervelocity impact phenomena.[1]

EXPERIMENTAL DATA

As part of a company-sponsored program for evaluating expandable space and lunar structures consisting of both rigid and flexible materials, Goodyear Aircraft Corporation has experimentally and theoretically investigated hypervelocity terminal effects.

An initial review of impact investigations being pursued indicated that work was proceeding on structural metals and that multiple wall structures were exhibiting considerable promise. However, it was found that other types of materials for the most part were being neglected.

An experimental program was initiated to compare the meteoroid penetration resistance of polymeric materials with the penetration resistance of aluminum materials, to indicate, thereby, the significance and general order of importance for the various experimental parameters, and to thus assist in directing future designs of space vehicles. The hypervelocity firings were conducted for the program by the Armour Research Foundation of Illinois Institute of Technology, on ballistic range No. 2, using 4.54 mg Pyrex and 4.95 mg steel spheres.

Target specimens were designed using the findings of other investigators. Funkhouser, using 12,000 ft/sec, 0.062-in. copper projectiles fired at double-wall, aluminum targets, concluded that 0.01 to 0.02-in. bumpers gave the best penetration protection and that bumper spacing beyond 2 in. was unwarranted. Nysmith and Summers, using 11,000 ft/sec, 1/8-in. Pyrex projectiles fired at multiple wall aluminum targets, concluded that increasing the number of sheets, increasing the wall spacing, and using a spacer of lightweight filler material increased the penetration resistance. Using these results, a hypothesized target specimen design was formulated.

The nomenclature used to describe specimen configuration is given in Figure 3. Initially the hypothetical specimen design for hypervelocity penetration resistance was conceived to function as follows: The bumper serves to fragment the meteoroids which have a mass such as to cause penetration. The spacer positions the outer wall (or walls) and may arrest and absorb the shattered, impacting materials. The inner wall may provide a more economical weight design while performing much the same function as the bumper to fragment and stop meteoroids. The structural wall carries the structural loads. In addition, it also serves as the gas retaining wall for pressurized, manned space structures.

Impacted specimens are shown in Figures 4 and 5. Complete description and test results are shown in the Appendix.

BUMPER TEST RESULTS

The target specimens for the experiments had varied bumper constructions in order to obtain data on homogeneous and composite (heterogeneous) materials with flexible and rigid characteristics.

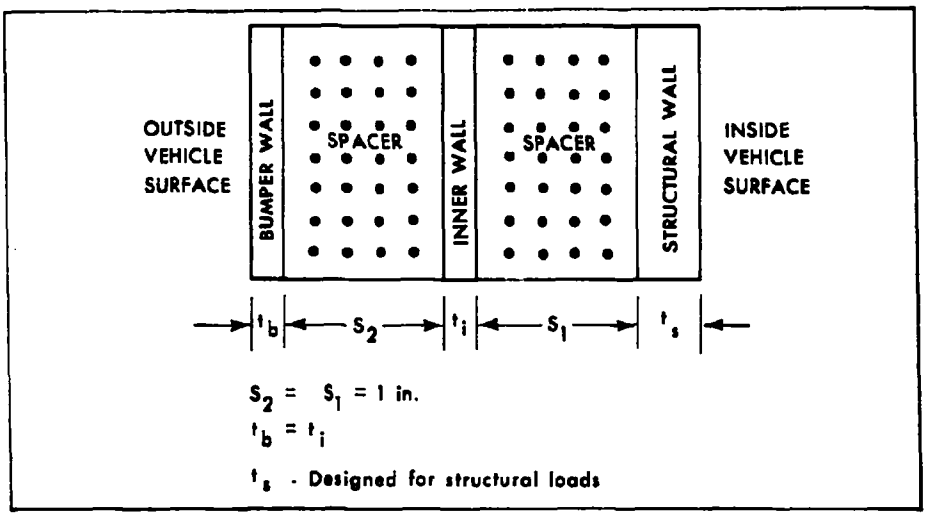

Figure 3 - Schematic of Initial Hypothetical Specimen Configuration (Utilized for Single-, Double-, and Triple-Wall Specimens)

SPECIMEN A-11
VELOCITY - 19,200 FPS
BUMPER - 0.30-PSF ALUMINUM
SPACER - 0.54-PSF ALUMINUM SHEET TRUSS
INTERIOR WALL - 0.30-PSF ALUMINUM
STRUCTURAL WALL - 0.58-PSF ALUMINUM

SPECIMEN B-13
VELOCITY - 19,100 FPS
BUMPER - 0.31-PSF ALUMINUM HONEYCOMB Z PANEL
SPACER - 0.70-PSF ALUMINUM HONEYCOMB TRUSSGRID
INTERIOR WALL - 0.31-PSF ALUMINUM HONEYCOMB Z PANEL
STRUCTURAL WALL - 0.63-PSF ALUMINUM HONEYCOMB Z PANEL

SPECIMEN C-10
VELOCITY - 19,400 FPS
BUMPER - 0.31-PSF ALUMINUM HONEYCOMB Z PANEL
SPACER - 0.62-PSF RIGID POLYURETHANE FOAM
INTERIOR WALL - 0.31-PSF ALUMINUM HONEYCOMB Z PANEL
STRUCTURAL WALL - 0.63-PSF ALUMINUM HONEYCOMB Z PANEL

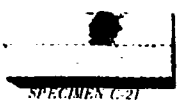

SPECIMEN C-21
VELOCITY - 21,100 FPS
BUMPER - 0.31-PSF ALUMINUM HONEYCOMB Z PANEL
SPACER - 0.62-PSF RIGID POLYURETHANE FOAM
INTERIOR WALL - 0.31-PSF ALUMINUM HONEYCOMB Z PANEL
STRUCTURAL WALL - 0.63-PSF ALUMINUM HONEYCOMB Z PANEL

SPECIMEN D-17
VELOCITY - 19,050 FPS
BUMPER - 0.31-PSF ALUMINUM HONEYCOMB Z PANEL
SPACER - 0.63-PSF RIGID POLYURETHANE FOAM
INTERIOR WALL - NONE
STRUCTURAL WALL - 0.63-PSF ALUMINUM HONEYCOMB Z PANEL

SPECIMEN E-7
VELOCITY - 19,100 FPS
BUMPER - 0.30-PSF ALUMINUM
SPACER - 0.63-PSF RIGID POLYURETHANE FOAM
INTERIOR WALL - NONE
STRUCTURAL WALL - 0.58-PSF ALUMINUM

SPECIMEN E-9
VELOCITY - 20,800 FPS
BUMPER - 0.30-PSF ALUMINUM
SPACER - 0.63-PSF RIGID POLYURETHANE FOAM
INTERIOR WALL - NONE
STRUCTURAL WALL - 0.58-PSF ALUMINUM

SPECIMEN F-4
VELOCITY - 19,800 FPS
BUMPER - 0.42-PSF DACRON-BUTYL
SPACER - 1.00-PSF RUBBER FOAM (SYNTHETIC)
INTERIOR WALL - 0.42-PSF DACRON-BUTYL
STRUCTURAL WALL - 0.59-PSF DACRON-BUTYL

SPECIMEN G-1
VELOCITY - 18,500 FPS
BUMPER - 0.42-PSF DACRON-BUTYL
SPACER - 1.00-PSF RUBBER FOAM (SYNTHETIC)
INTERIOR WALL - NONE
STRUCTURAL WALL - 0.59-PSF DACRON-BUTYL

SPECIMEN G-3
VELOCITY - 19,500 FPS
BUMPER - 0.42-PSF DACRON-BUTYL
SPACER - 1.00-PSF RUBBER FOAM (SYNTHETIC)
INTERIOR WALL - NONE
STRUCTURAL WALL - 0.59-PSF DACRON-BUTYL

SPECIMEN H-5
VELOCITY - 21,400 FPS
BUMPER - 0.17-PSF ALUMINUM
SPACER - 0.2-PSF FLEXIBLE POLYURETHANE FOAM
INTERIOR WALL - NONE
STRUCTURAL WALL - 0.54-PSF ALUMINUM

SPECIMEN H-11
VELOCITY - 12,800 FPS
BUMPER - 0.17-PSF ALUMINUM
SPACER - 0.2-PSF FLEXIBLE POLYURETHANE FOAM
INTERIOR WALL - NONE
STRUCTURAL WALL - 0.57-PSF ALUMINUM

SPECIMEN H-14
PROJECTILE - 0.042 IN. STEEL (4.86 MG)
VELOCITY - 22,500 FPS
BUMPER - 0.17-PSF ALUMINUM
SPACER - 0.2-PSF FLEXIBLE POLYURETHANE FOAM
INTERIOR WALL - NONE
STRUCTURAL WALL - 0.57-PSF ALUMINUM

SPECIMEN I-1
VELOCITY - 12,800 FPS
BUMPER - 0.18-PSF DACRON-NEOPRENE
SPACER - 0.2-PSF FLEXIBLE POLYURETHANE FOAM
INTERIOR WALL - NONE
STRUCTURAL WALL - 0.59-PSF DACRON-NEOPRENE

PROJECTILE FOR ALL SPECIMENS EXCEPT H-14 WAS 0.063-IN. PYREX (4.54 MG).

Figure 4 - Hypervelocity Penetration Specimens A-11 through I-1

SPECIMEN I-2
VELOCITY = 12,800 FPS
BUMPER = 0.18-PSF DACRON-NEOPRENE
SPACER = 0.2-PSF FLEXIBLE POLYURETHANE FOAM
INTERIOR WALL = NONE
STRUCTURAL WALL = 0.87-PSF DACRON-NEOPRENE

SPECIMEN I-5
VELOCITY = 21,800 FPS
BUMPER = 0.17-PSF DACRON-NEOPRENE
SPACER = 0.2-PSF FLEXIBLE POLYURETHANE FOAM
INTERIOR WALL = NONE
STRUCTURAL WALL = 0.60-PSF DACRON-NEOPRENE

SPECIMEN I-8
PROJECTILE = 0.042 IN. STEEL (4.95 MG)
VELOCITY = 22,250 FPS
BUMPER = 0.17-DACRON-NEOPRENE
SPACER = 0.2-PSF FLEXIBLE POLYURETHANE FOAM
INTERIOR WALL = NONE
STRUCTURAL WALL = 0.59-PSF DACRON-NEOPRENE

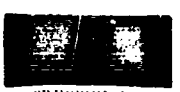

SPECIMEN J-2
VELOCITY = 21,900 FPS
BUMPER = NOT APPLICABLE
SPACER = 0.2-PSF FLEXIBLE POLYURETHANE FOAM
INTERIOR WALL = NONE
STRUCTURAL WALL = 0.61-PSF DACRON-NEOPRENE

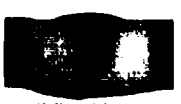

SPECIMEN K-1
VELOCITY = 21,300 FPS
BUMPER = 0.17-PSF FIBERGLASS-SILICONE
SPACER = 0.2-PSF FLEXIBLE POLYURETHANE FOAM
INTERIOR WALL = NONE
STRUCTURAL WALL = 0.26-PSF DACRON-POLYURETHANE

SPECIMEN K-2
VELOCITY = 20,000 FPS
BUMPER = 0.17-PSF FIBERGLASS-SILICONE
SPACER = 0.2-PSF FLEXIBLE POLYURETHANE FOAM
INTERIOR WALL = NONE
STRUCTURAL WALL = 0.26-PSF DACRON-POLYURETHANE

SPECIMEN L-2
VELOCITY = 20,500 FPS
BUMPER = 0.17-PSF ALUMINUM
SPACER = NOT APPLICABLE
INTERIOR WALL = NONE
STRUCTURAL WALL = 0.84-PSF ALUMINUM

SPECIMEN M-3
VELOCITY = 21,200 FPS
BUMPER = 0.18-PSF DACRON-NEOPRENE
SPACER = NOT APPLICABLE
INTERIOR WALL = NONE
STRUCTURAL WALL = 0.89-PSF DACRON-NEOPRENE

SPECIMEN N-1
VELOCITY = 19,300 FPS
BUMPER = 0.18-PSF CX-1046 POLYURETHANE
SPACER = 0.2-PSF FLEXIBLE POLYURETHANE FOAM
INTERIOR WALL = NONE
STRUCTURAL WALL = 0.60-PSF DACRON-NEOPRENE

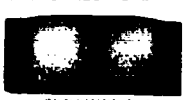

SPECIMEN N-3
VELOCITY = 20,000 FPS
BUMPER = 0.17-PSF CX-1046 POLYURETHANE
SPACER = 0.2-PSF FLEXIBLE POLYURETHANE FOAM
INTERIOR WALL = NONE
STRUCTURAL WALL = 0.60-PSF DACRON-NEOPRENE

SPECIMEN O-1
VELOCITY = 22,250 FPS
BUMPER = 0.17-PSF MYLAR LAMINATE
SPACER = 0.2-PSF FLEXIBLE POLYURETHANE FOAM
INTERIOR WALL = NONE
STRUCTURAL WALL = 0.59-PSF DACRON-NEOPRENE

SPECIMEN P-1
VELOCITY = 20,800 FPS
BUMPER = 0.18-PSF CS-105 COATED RENE 41 WIRE CLOTH
SPACER = 0.2-PSF FLEXIBLE POLYURETHANE FOAM
INTERIOR WALL = NONE
STRUCTURAL WALL = 0.60-PSF DACRON-NEOPRENE

SPECIMEN Q-1
VELOCITY = 21,300 FPS
BUMPER = 0.007-PSF 1 MIL MYLAR
SPACER = 0.2-PSF FLEXIBLE POLYURETHANE FOAM
INTERIOR WALL = NONE
STRUCTURAL WALL = 0.61-PSF DACRON-NEOPRENE

SPECIMEN R-1
VELOCITY = 20,000 FPS
BUMPER = NOT APPLICABLE
SPACER = NOT APPLICABLE
INTERIOR WALL = NONE
STRUCTURAL WALL = 0.90-PSF ALUMINUM

SPECIMEN S-2
VELOCITY = 20,500 FPS
BUMPER = NOT APPLICABLE
SPACER = NOT APPLICABLE
INTERIOR WALL = NONE
STRUCTURAL WALL = 0.92-PSF DACRON-NEOPRENE

PROJECTILE FOR ALL SPECIMENS EXCEPT I-8 WAS 0.063-IN. PYREX (4.54 MG).

Figure 5 - Hypervelocity Penetration Specimens I-2 through S-2

Typical hypervelocity projectile impacts on homogeneous bumper materials are displayed in Figure 6. The homogeneous bumper materials demonstrate the typical lip formation characteristics of hypervelocity impacts in the fluid region, as is shown by the aluminum bumper of specimen E-9. In addition, the polyurethane bumper of N-3 reveals a sunburst pattern suggestive of stress lines about the circular hole and the Mylar bumper of Q-1 shows minor radial cracks.

The typical hypervelocity thin plate hole is shown in cross-section in Figure 6. The outer lip formed on homogeneous bumpers consisted of material raised above the original outside surface around the circular hole. Upon hypervelocity impact a hemispherical crater initially is formed by the impact pressure. Subsequently, the particle and target materials flow along the surface of the expanding crater and are ejected in the opposite direction from that of the projectile. The final ejection of the materials results in the formation of this lip.

The inside surface of homogeneous bumpers exhibited lip formations as pronounced as the outer surface. The inside lip is probably attributable to the bumper material carried with the projectile during the final phase of pushing through the bumper.

The heterogeneous bumpers generally evidenced adhesion or delamination failure about the impact point as shown in Figure 7. There were two exceptions: the René 41-CS-105 bumper of P-1 exhibited minute radial cracks about a circular hole, and Dacron-Neoprene bumpers impacted at 12,800 ft/sec had no noticeable defects about their circular holes. The adhesion and delamination failures can be attributed to the heat generated at impact and to ejection of minute fragments of bumper material immediately after impact. However, the adhesion or delamination failure area about the hole should still be partially effective in fragmenting any impacting meteoroid.

The Z-panel bumpers of C-21 showed pronounced blow-back effects. Z-panels are constructed of a crushed aluminum honeycomb bonded between two thin aluminum sheets. The blow-back and the large area of damage associated with it can probably be explained as being the results of the mechanism of crater growth.

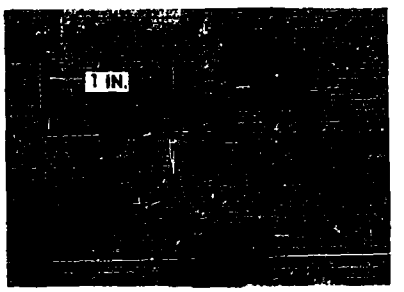

ALUMINUM BUMPER - SPECIMEN E-9

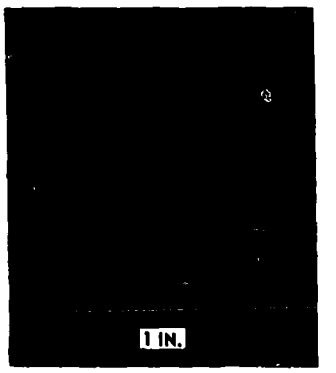

POLYURETHANE BUMPER - SPECIMEN N-3

MYLAR BUMPER - SPECIMEN Q-1

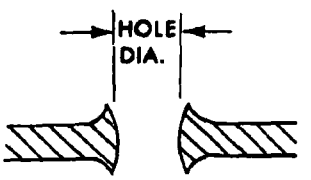

TYPICAL HYPERVELOCITY
THIN-PLATE HOLE

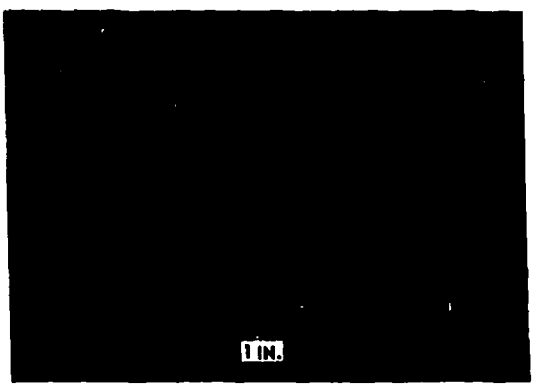

Figure 6 - Homogeneous Bumper Impacts

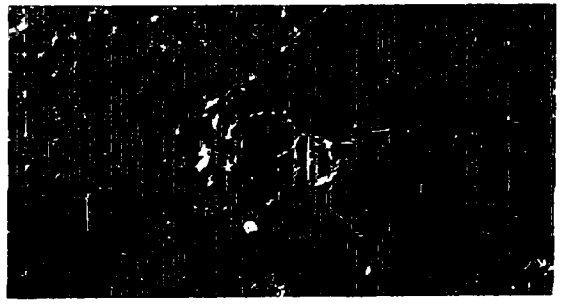

ALUMINUM HONEYCOMB Z-PANEL BUMPER - SPECIMEN C-21

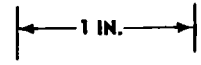

FIBERGLASS-SILICONE BUMPER - SPECIMEN K-2

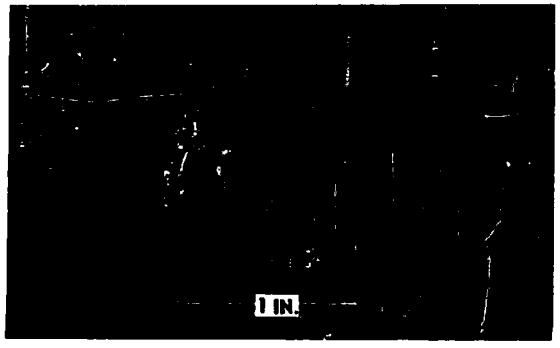

MYLAR LAMINATE BUMPER - SPECIMEN O-1

RENE 41-CS-105 BUMPER - SPECIMEN P-1

Figure 7 - Heterogeneous Bumper Impacts

SPACER TEST RESULTS

The medium that positions the bumper, the interior wall, and the structural wall from one another is identified herein as a spacer. Depending on the spacer material, this medium provides various amounts of additional protection for the structural wall. A foam spacer, for example, serves as a mechanical atmosphere that tends to absorb and arrest the impacting particles through vaporization. Under hypervelocity impact conditions this vaporization of the foam spacer causes cavities of various sizes and shapes to be formed. The size and shape of the cavities are functions of the bumper (material and mass), of the spacer (material and mass), and of the projectile (material, mass, density, and velocity). (Figures 4 and 5.)

The aluminum sheet truss spacer of A-11 reveals widespread pitting and penetration. The aluminum sheet honeycomb trussgrid spacer of B-13 shows twisted, torn, ellipsoidal-shaped damage. The rigid 4 lb/ft^3 polyurethane foam spacer cavities are displayed by C-21 and E-9. The triple-wall Z-panel specimen C-21 displays a cylindrical cavity with a slight indentation of the interior wall, but the 21-mil aluminum bumper specimen, E-9, has a spheroidal cavity in the spacer medium.

The lightweight, 1.2 lb/ft^3, flexible, polyurethane foam spacers were tested using a variety of bumper materials. Two types of cavity formations were observed: ellipsoidal and cylindrical. Specimens H-5, I-5, K-1, N-3, O-1, and P-1 had ellipsoidal shaped cavities. All specimens used a 12-mil aluminum bumper (or its equivalent by weight in other materials).

Cylindrical cavities in the lightweight, flexible, polyurethane foam spacers were attributable to several different test conditions: (1) 12,800 ft/sec Pyrex projectiles, (2) steel projectiles, (3) 1-mil aluminized Mylar, and (4) absence of a bumper.

The cavity shape thus was shown empirically to depend on the effectiveness of the bumper in fragmenting the impacting particles, an ability of the bumper which has been shown to be dependent on the projectile speed and material and bumper mass.

OTHER TEST RESULTS

Specimens L-2 and M-3 shown in Figure 8 were aluminum double-wall and Dacron-Neoprene double-wall specimens of equal weights but having no spacer mediums. The impact side of the structural wall of the aluminum specimen exhibited a series of concentric circular pattern of small pits that were most intense in and on a circle 0.6-in. in diameter and diminished in intensity as the circles grew larger. The reverse side of the metal specimen structural wall had a permanent set that corresponded to the intense pitting on the impact side. The impact side of the structural wall of the fabric specimen showed limited pitting and a change in texture inside a circle 0.5-in. in diameter. No damage was visible on the reverse side of the fabric specimen structural wall.

Two single-wall specimens, S-2 (Dacron-Neoprene fabric) and R-1 (aluminum alloy), of equal weight were also impacted. The specimens sustained approximately equal damage. These single-wall penetrations concisely show the need for additional lightweight protection from the impacting projectile. That additional protection can be provided by foam-spacers with or without a bumper wall will be shown.

MECHANICAL ATMOSPHERE PROTECTION CONCEPT

Bumper and spacer damage is one criterion for evaluating the penetration resistance of impacted constructions, but total depth of penetration into the specimen is considerably more important. A quantitative comparison of penetration resistance for specimens of different designs is obtained by comparing the weight loss per unit area of the specimen to the maximum depth of the penetration.

Table I presents a summary of the penetrated weight of all target specimens by Pyrex projectiles of approximately equal velocities (20,000 ft/sec). The arrangement of specimens lists the most resistant specimen first and subsequent specimens in a descending order of resistance. The totai

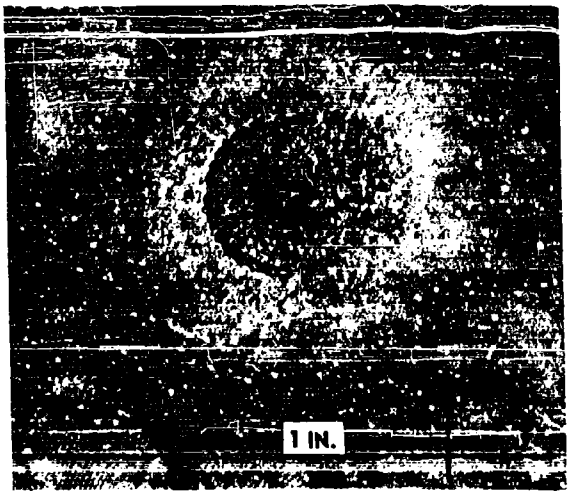

STRUCTURAL WALL IMPACT - SPECIMEN L-2

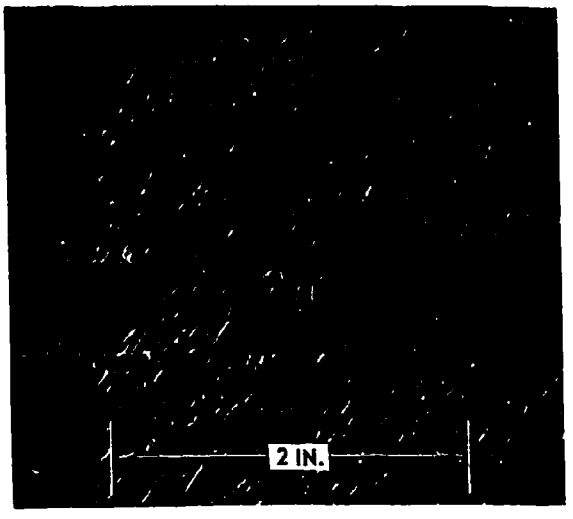

STRUCTURAL WALL IMPACT - SPECIMEN M-3

Figure 8 - Structural Wall Damage When No Spacer was Used

TABLE I - PENETRATED WEIGHT OF TARGET SPECIMENS

Specimen number	Bumper wall		Spacer medium		Projectile			Penetrated weight (lb/ft^2)				Penetration stopped by	
	Material	Weight (lb/ft^2)	Material	Weight (lb/ft^3)	Density (g/cm^3)	Mass (mg)	Velocity (10^3 fps)	Total	Outer wall	Foam	Interior wall	Spacer medium	Interior wall
J-2	None	. . .	Polyurethane foam	1.2	2.12	4.54	21.9	0.20	. . .	0.20	. . .		X
Q-1	1-mil Mylar	0.01	Polyurethane foam	1.2	2.12	4.54	21.3	0.21	0.01	0.20	. . .		X
K-1	Fiberglass-silicone	0.17	Polyurethane foam	1.2	2.12	4.54	21.3	0.33	0.17	0.16	. . .	X	
K-2	Fiberglass-silicone	0.17	Polyurethane foam	1.2	2.12	4.54	20.0	0.34	0.17	0.17	. . .	X	
N-1	Polyurethane	0.16	Polyurethane foam	1.2	2.12	4.54	19.3	0.36	0.16	0.20	. . .		X
P-1	Rene 41-CS-105	0.16	Polyurethane foam	1.2	2.12	4.54	20.8	0.36	0.16	0.20	. . .		X
N-3	Polyurethane	0.17	Polyurethane foam	1.2	2.12	4.54	20.0	0.37	0.17	0.20	. . .		X
O-1	3-ply Mylar	0.17	Polyurethane foam	1.2	2.12	4.54	22.25	0.37	0.17	0.20	. . .		X
H-5	Aluminum 2024T3	0.17	Polyurethane foam	1.2	2.12	4.54	21.4	0.37	0.17	0.20	. . .		X
I-5	Dacron-Neoprene	0.17	Polyurethane foam	1.2	2.12	4.54	21.8	0.39	0.17	0.20	. . .		X
U-1	Aluminum 2024T3	0.32	Rigid polyurethane foam	0.35	2.12	4.54	20.2	0.39	0.32	0.07	. . .	X	
A-11	Aluminum 2024T3	0.30	Aluminum sheet truss	3.4	2.12	4.54	19.2	0.57	0.30	0.27	. . .		X
B-13	Aluminum Z-panel	0.31	Aluminum honeycomb	4.2	2.12	4.54	19.1	0.66	0.31	0.35	. . .		X
L-2	Aluminum 2024T3	0.17	None	. . .	2.12	4.54	20.5	0.71	0.17	. . .	0.54*		X
E-9	Aluminum 2024T3	0.30	Rigid polyurethane foam	4.0	2.12	4.54	20.8	0.72	0.30	0.42	. . .	X	
E-7	Aluminum 2024T3	0.30	Rigid polyurethane foam	4.0	2.12	4.54	19.1	0.75	0.30	0.45	. . .	X	
M-3	Aluminum 2024T3	0.18	None	. . .	2.12	4.54	21.2	0.77	0.18	. . .	0.59*		X
F-4	Dacron butyl	0.42	Flexible latex foam	6.0	2.12	4.54	19.5	0.90	0.42	0.48	. . .		X
F-5	Dacron butyl	0.42	Flexible latex foam	6.0	2.12	4.54	18.85	0.90	0.42	0.48	. . .		X
D-17	Aluminum Z-panel	0.31	Rigid polyurethane foam	4.0	2.12	4.54	19.05	0.92	0.31	0.61	. . .	X	
C-19	Aluminum Z-panel	0.31	Rigid polyurethane foam	4.0	2.12	4.54	19.4	0.93	0.31	0.31	0.31*		X
C-21	Aluminum Z-panel	0.31	Rigid polyurethane foam	4.0	2.12	4.54	21.1	0.93	0.31	0.31	0.31*		X
T-2	Aluminum 2024T3	0.32	Rigid polyurethane foam	6.38	2.12	4.54	19.1	1.06	0.32	0.74	. . .	X	
G-1	Dacron butyl	0.42	Flexible latex foam	6.0	2.12	4.54	16.5	1.20	0.42	0.78	. . .	X	
G-3	Dacron butyl	0.42	Flexible latex foam	6.0	2.12	4.54	19.5	1.20	0.42	0.78	. . .	X	

*Interior wall weight included because of pitting.

penetrated weight of the specimens seems to decrease as the bumper and spacer masses decrease.

The interior wall at times stopped the penetration into various specimens but usually sustained no visible damage. This effect of the inner wall tends to obscure the quantitative evaluation of the impact damage. The effectiveness of the inner wall in stopping penetration is indicated but will necessitate future experiments before its effectiveness can be evaluated.

A plot of penetrated foam weight versus the foam density where the penetration was arrested in the spacer medium is exhibited in Figure 9. Specimen D-17 is excluded because of the relative ineffectiveness of the Z-panel bumper. Specimens G-1 and G-3 are excluded because the foam medium was other than polyurethane. Specimens T-2 and U-1 are shown in Figure 10.

Several very interesting trends and conclusions can be drawn from Figure 9. Specimens U-1, E-7, E-9, and T-1 all have approximately equivalent 2024T3 aluminum bumper masses with different densities of rigid polyurethane foam. The foam penetrated weight decreases with decrease in foam density; this is the same observation derived from Table I. The observed straight line is actually an equation derived in the following manner. The maximum penetration depth observed was experimentally obtained. Its development will be discussed in a later paragraph.

$$\rho(L - 1.27) = 0.416 ,$$

where,

ρ is the foam density (lb/ft^3)

L is the maximum foam penetration depth (in.),

Rearranging,

$$L = 1.27 + \frac{0.416}{\rho} .$$

Multiplying both sides by $\rho/12$ the penetrated surface weight in pounds per square foot is obtained.

$$\frac{L\rho}{12} = 0.106\,\rho + 0.0347 .$$

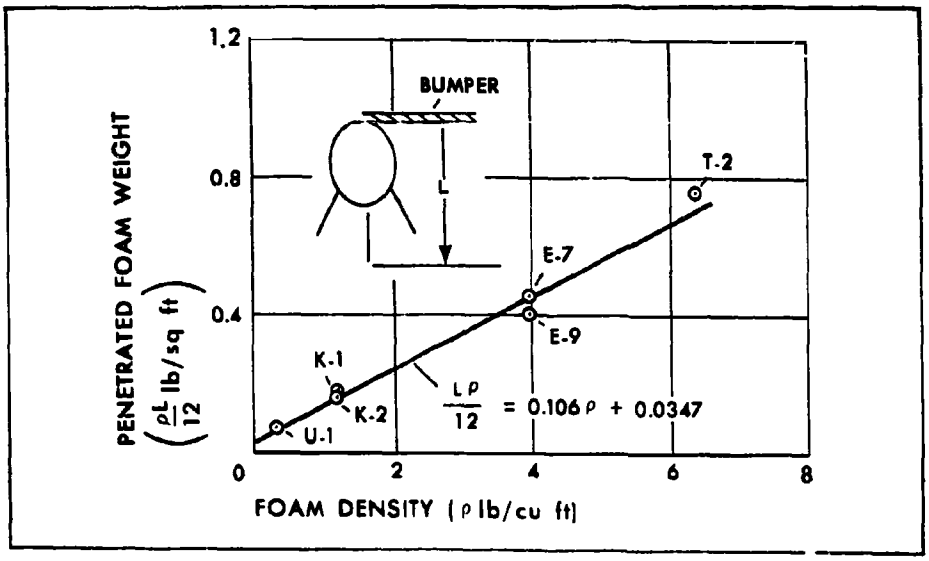

Figure 9 - Penetrated Foam Weight Comparisons

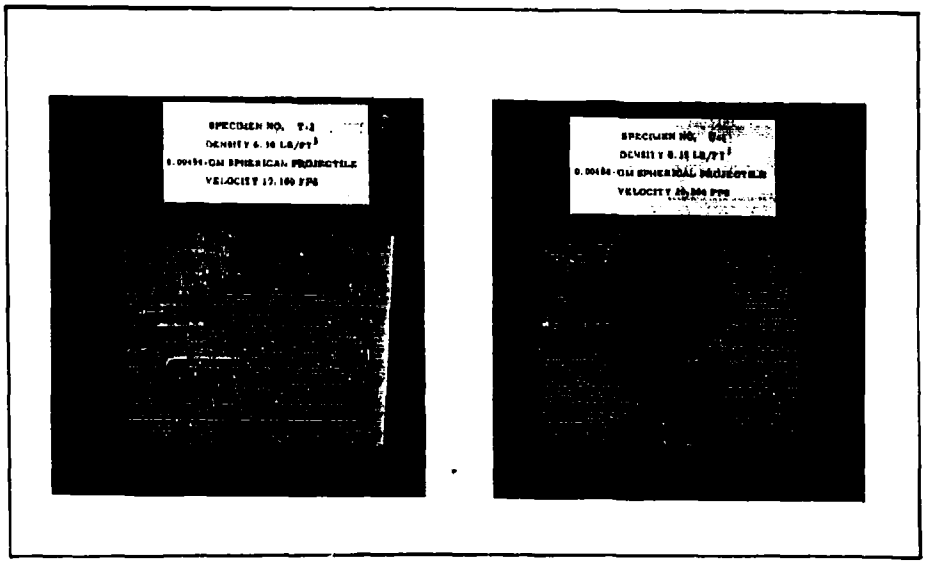

Figure 10 - Penetration Test Specimens T-2 and U-1

Now if specimen K-1 and K-2 are added to the polyurethane foam penetrated weight curve, they fall very closely to the established line. Specimens K-1 and K-2 are constructed of a flexible polyurethane foam spacer and of a fiberglass-silicone bumper having a weight approximately 45 percent of the other specimens shown.

Total depth of penetration versus foam density is presented in Figure 11. This figure includes two additional test points. Specimen H-5 represents an equivalent K specimen with the exception that the bumper was 2024T3 aluminum. Specimen J-2 is also equivalent to H or K with the exception of having no bumper wall. Both H-5 and J-2 should have greater total penetrated weight since the penetration was stopped by the inner wall. Arrows indicate this condition on the curve.

Several conclusions can be drawn from Figure 11. The lower the foam density becomes, the greater the resistance per unit weight. Fiberglass fabric was found to be more effective as a bumper than an aluminum wall of equal weight. Decrease in bumper weight causes a decrease in total penetrated weight.

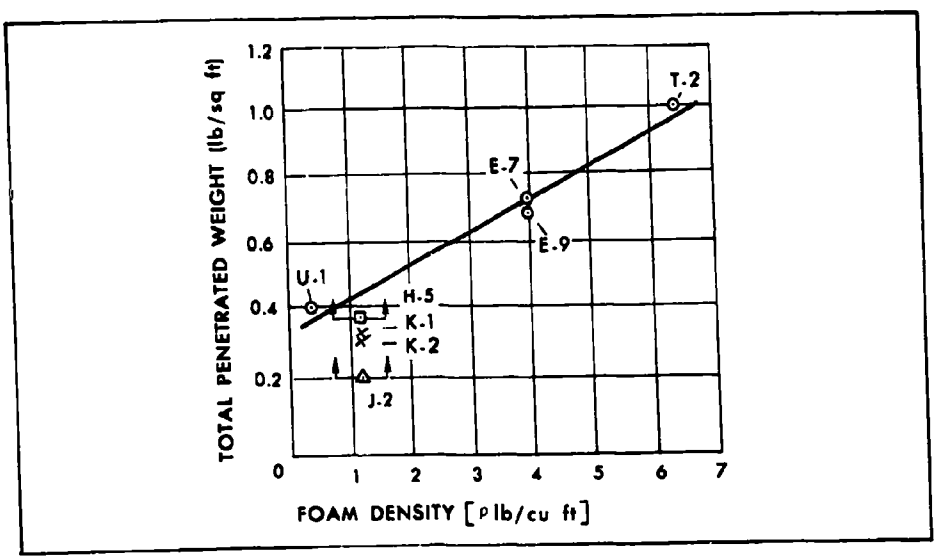

Figure 11 - Total Penetrated Weight Comparison

While it must be emphasized that these conclusions are based on experimental results of certain projectile materials and speeds, the conclusions, nevertheless, merit extensive investigation and study.

Adequately reliable formulas for calculating single sheet thickness required to just stop a given projectile were generally developed for metals and have been experimentally verified to approximately 20,000 ft/sec. The most commonly used formula, developed by NASA, Ames, is

$$t = 3.42 d_P \left[\frac{\rho_P}{\rho_t} \cdot \frac{V}{C}\right]^{2/3},$$

where

t = the plate thickness just to stop a given projectile

d_P = projectile diameter

ρ_P = projectile density

ρ_t = target density

V = projectile velocity

C = velocity of sound in target

As shown in Figure 12, specimen J-2, a spacer of flexible, 1.2 lb/ft^3, polyurethane foam of 2-in. thickness weighing 0.20 lb/ft^2 was able to stop a 21,900-ft/sec, 0.063-in. diameter, 4.54 mg Pyrex projectile having a density of 2.12 gr/cm^3 without visible damage to the structural wall. On the other hand, for an identical projectile and velocity, the single sheet weight of aluminum (as found by the above formula) is 3.14 lb/ft^2. The comparison of 0.20 and 3.14 lb/ft^2 shows an increase in efficiency of penetration resistance for foam by a factor of 15.7 to that of a single-wall aluminum structure.

This ability of foam to absorb and arrest an impacting projectile appears somewhat analogous to the atmospheric dissipation of meteors. The basic

PROJECTILE:
0.0063-IN. PYREX
VELOCITY:
21,900 FPS
SPACER:
0.2 LB/FT^2 FLEXIBLE
POLYURETHANE FOAM

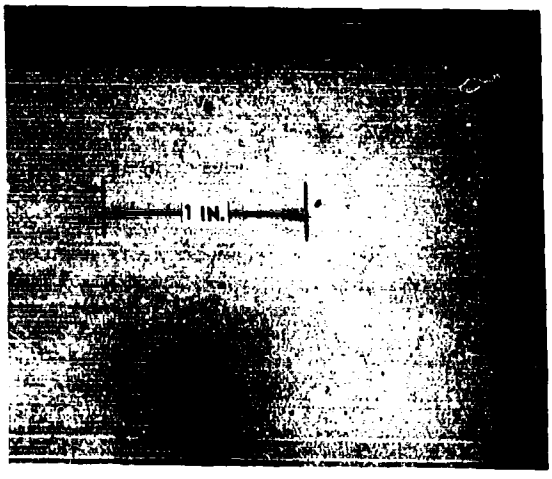

IMPACT SURFACE - SPECIMEN J-2

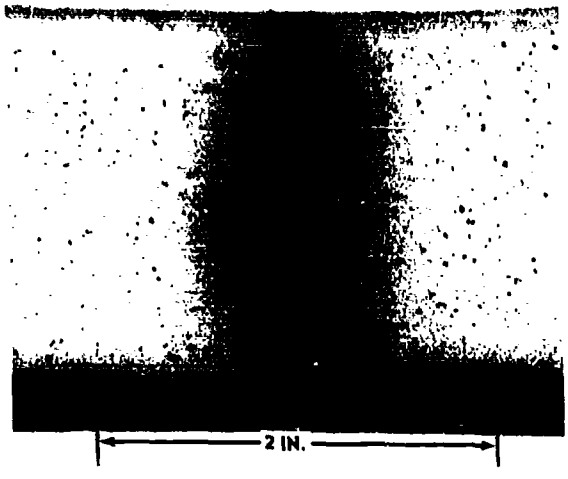

CROSS-SECTION - SPECIMEN J-2

Figure 12 - Mechanical Atmosphere Concept

system of protection from hypervelocity particle impacts by using foam as the essential component, therefore, is identified by Goodyear Aircraft Corporation as a mechanical-atmosphere protection system. The mechanical-atmosphere efficiency factor is expected to increase with impacting velocity increase. The expected increase in efficiency is important since meteoroid impacts for the most part are expected to be above 50,000 ft/-sec.

Experimental work with particle velocities to 22,500 ft/sec showed that the efficiency of the protection system decreased as the impacting particle velocity decreased and as the impacting particle density increased. The decrease in efficiency from these causes is relatively unimportant for a near-earth environment since the average velocities of meteoroids are above 50,000 ft/sec and since massive, steel-like particles are very infrequent.

The use of foams for space structures requires consideration of other factors, such as vibration and shock. The data obtained from vibration and shock tests conducted on 6-in. cubes of rigid polyurethane foam is tabulated in Table II. None of these specimens showed any tendency to disintegrate when severely shock-tested by blows from a 5.4 lb hammer, except for the rigid foam with a density of 1.5 lb per cubic foot that fractured very easily under a slight shock imposed by hand. The test results indicate that flexible foams should be used if foam densities of 1.5 lb/ft^3 or less are required in a structure subject to vibration and shock loads.

TABLE II - RIGID FOAM VIBRATION AND SHOCK TEST DATA

Density (lb/ft^3)	Input (g)	Resonance frequency (cps)	Output (g)	Test time at resonance (min)
6	25	500	350	5
4	25	500	300	5
2.5	25	490	380	5
1.5	25	470	485	5

Skin thickness limitations are often encountered in vehicle designs. The penetration depth of a specimen thus assumes increased significance. The curve of penetrated foam length versus unit weight is presented in Figure 13. At zero foam density the penetrated foam length would be expected to be infinite. At the higher foam densities, above 4 lb/ft^3, the penetrated length remained approximately constant. A hyperbola of the foam $x(y - \alpha) = \beta$ was then empirically fitted obtaining an equation having a standard deviation of 7.6 percent.

$$\rho(L - 1.27) = 0.416 .$$

Additional work is being conducted to further investigate the feasibility of the mechanical-atmosphere protection system. Copper spheres 1/64-in. in diameter and Mylar discs are being fired at velocities ranging from 20,000 to 50,000 ft/sec into foam specimens with and without bumpers. Technical Operations Incorporated of Burlington, Mass., is conducting the firings.

The use of a mechanical atmosphere leads to a re-evaluation of the purpose

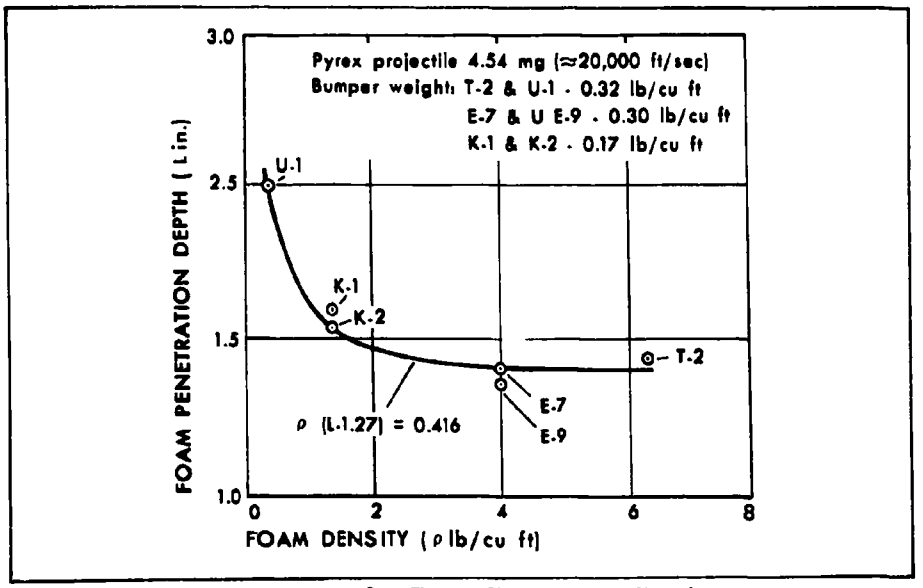

Figure 13 - Foam Penetration Depth

of a bumper wall. An outer wall is required in a space structure utilizing the mechanical-atmosphere protection system (1) to protect the foam during handling, ascent, and deployment operations, (2) to shield the foam from the effects of ultraviolet radiation, and (3) to maintain proper absorptive and emissive characteristics for thermal control.

CONCLUSIONS

The specimen design postulated for meteoroid protection of space structures is shown in Figure 14. The bumper serves as a protective layer for handling purposes and other abrasive conditions. It also serves as an optical coating for thermal balance when in space. Only incidentally does the bumper tend to fragment impacting hypervelocity particles. The foam spacer absorbs, arrests and/or vaporizes the impacting materials; the foam spacer also positions the outer wall (bumper) from the structural wall and offers some thermal balance features. The structural wall

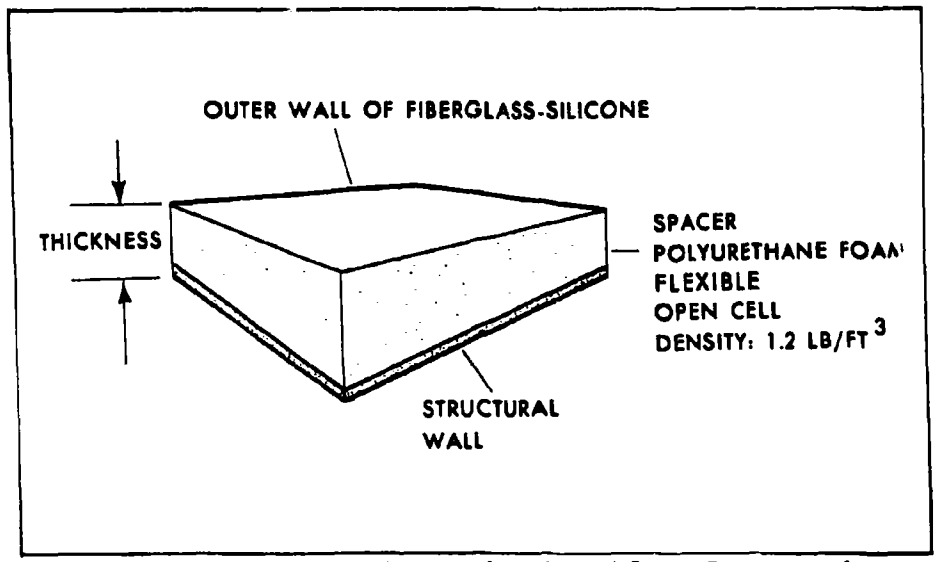

Figure 14 - Protection Concept for Manned Space Structures from Meteoroid Penetration

primarily carries the structural loads and serves as the gas-retaining wall for pressurized, manned space structures.

It was also learned from these initial investigations that:

1. Without a bumper, the foam spacer penetration resistance to Pyrex projectile velocities over 21,900 ft/sec was comparable to or better than the resistance of equal weight aluminum structures. The foam spacer exhibited an efficiency by weight 15.7 times that of a single aluminum wall.
2. Both rigid and flexible foam spacers, as mechanical atmospheres, tend to absorb and arrest impacting materials through vaporization.
3. When foam spacers were absent, aluminum structural walls sustained greater damage than equivalent weight fabric walls against 20,000 ft/sec Pyrex projectiles.
4. An aluminum sheet bumper is superior to an equal weight Z-panel of crushed aluminum honeycomb against 20,000 ft/-sec Pyrex projectiles.
5. A fiberglass-silicone bumper is superior to an equal weight Z-panel of crushed aiuminum honeycomb against 20,000 ft/-sec Pyrex projectiles.
6. Failures about the impact holes for some nonmetals indicate that bumpers should be made of homogeneous materials or of high-temperature composites.
7. The use of a bumper for fragmenting hypervelocity particles requires re-evaluation if foam is used as an absorbing medium.

Goodyear Aircraft is persuing theoretical and experimental efforts to provide a more rigorous investigation of the mechanical atmosphere system of protection from meteoroid impacts. Such an investigation is in keeping with the considerable promise of polymeric materials revealed by the present experimental hypervelocity terminal efforts.

LIST OF REFERENCES

1. Reynolds, B. W. - "Effects of Hypervelocity Particle Impact on Composite Materials for Expandable Structures Applications," GER-10663, Akron, Ohio, Goodyear Aircraft Corporation, August 1962.

2. Whipple, Fred L. - "Dust and Meteorites," Astronautics, August 1962.

3. Thompson, A. B., and Gell, C. F. - "Meteoroids as a Hazard in Space Flight - A Survey of Present Information," (Astronautics Division, Chance-Vought Corporation, Dallas, Texas). American Rocket Society, Space Flight Report to the Nation, October 9-15, 1961, New York, ARS 2138-61.

4. Davidson, J. R., and Sandorff, P. E. - "Environmental Problems of Space Flight Structures, Part I, Meteoroid Hazard," Preliminary Draft, March 1962.

5. Whipple, Fred L. - "The Meteoritic Risk to Space Vehicles," Vistas in Astronautics - By First Annual Air Force Office of Scientific Research Astronautic Symposium, 1958.

6. Funkhouser, John O. - "A Preliminary Investigation of the Effect of Bumpers as a Means of Reducing Projectile Penetration," NASA TN-D-802, Langley Research Center, Langley Field, Va., National Aeronautics and Space Administration, Washington, D.C., April 1961.

7. Nysmith, C. R., and Summers, J. L. - "Preliminary Investigation of Impact on Multiple Sheet Structures and an Evaluation of Meteoroid Hazard to Space Vehicles," NASA TN-D-1039, Ames Research Center, Moffett Field, California, National Aeronautics and Space Administration, Washington, D.C., September 1961.

APPENDIX

HYPERVELOCITY IMPACT SPECIMEN DESCRIPTION AND TEST RESULTS

HYPERVELOCITY IMPACT SPECIMEN DESCRIPTION AND TEST RESULTS

HYPERVELOCITY PUNCTURING OF SELF-SEALING STRUCTURES

NSL 63-53
MARCH 1963

Available from NASA and OTS as N63-15390. Ref.: Scientific and Technical Aerospace Reports (STAR), Vol. 1, No. 12, p. 865.

Prepared by

PHILIP J. D'ANNA
MEMBER
RESEARCH STAFF
SPACE MATERIALS LABORATORY

L. ROTH
VICE PRESIDENT AND MANAGER
RESEARCH DEPARTMENT

NORTHROP SPACE LABORATORIES
1111 EAST BROADWAY HAWTHORNE, CALIFORNIA

HYPERVELOCITY PUNCTURING OF SELF-SEALING STRUCTURES*

By Philip J. D'Anna
Member of Research Staff - Space Materials Laboratory
Northrop Space Laboratories

SUMMARY

The concept of self-sealing structures is proposed as a promising and highly reliable technique for minimizing air leakage due to meteoroid induced punctures to pressurized space vehicle compartments. Three mechanical and two chemical self-sealing concepts are presented. Details are given on the development of one of the mechanical concepts in which an elastomer is used as the self-sealing constituent. Both panel configuration and elastomer response to hypervelocity puncturing need to be considered in order to obtain a successful self-sealing panel. A correlation is then shown to exist between dynamic elastomer response characteristics required for successful sealing, and pertinent static and dynamic material properties. It is proposed that the static material property correlation be used as a preliminary screening tool for candidate elastomers while dynamic testing, preferably by hypervelocity puncturing, be used for the final evaluation. In conclusion, the air leakage rate through panels punctured by 1/8-inch diameter steel spheres at velocities to 7,000 fps were found to vary from zero leakage to 1.4 lbs/day for a driving pressure of 14.7 psi. This compares with a leakage rate of 260 lbs/day for a hole the same diameter as the pellet used in puncturing the self-sealing panels.

INTRODUCTION

The loss of irreplaceable fluids caused by meteoroid induced punctures during either long duration, near earth space missions, or those extending great distances from the earth, presents a major problem to the designer of future manned or unmanned space vehicles.

*This paper reports a portion of the findings resulting from a NASA sponsored research program (NASr-102) entitled "Self-Sealing Structures for Control of the Meteoroid Hazard to Space Vehicles" - Norm Mayer, Project Monitor, NASA Headquarters, Washington, D. C.

Among the structural techniques that have been proposed for minimizing this hazard the bumper shield--or multiple wall structure--concept is currently the favorite among space vehicles designers. Experiments conducted with multiple wall structures, at both private and government ballistic facilities (References 1, 2, 3), have demonstrated that this technique will improve the penetration resistance of a structure over that of an equivalent weight single sheet configuration. Although this technique may prevent penetration or injection of projectile and shield fragments into the interior of a space vehicle, damage to the inner shell may be severe enough to cause fracturing or puncturing of the shell with the result that air leakage will occur. Furthermore, should spallation of the inner shell material occur, the crew may be exposed to a spray of impact induced particles. The possible types of meteoroid impact damage to the inner shell of a spaced sheet structure are illustrated in Figure 1. The "ballistic limit" as used in this illustration is the critical projectile velocity which causes damage of the inner shell that results in air leakage from the pressurized compartment.

A more promising and highly reliable technique for limiting the loss of a space vehicle's atmosphere due to meteoroid punctures is that of the Self-Sealing Structure. In this concept, the inner pressurized shell of a space vehicle, either with or without a bumper shield, is made with the capability of self-sealing after being punctured by a meteoroid. A few possible configurations by which such a self-sealing structure may be integrated into a space vehicle design are illustrated in Figure 2. In configuration "A" of Figure 2, the structural skin of the self-sealing shell will resist penetration by the smaller dust particles found in space. Some larger particle may conceivably puncture the shell and inject impact induced material into the interior of the space vehicle. In this latter case, however, the puncture would self-seal thereby preventing leakage of air from the pressurized cabin. This configuration could be used in unmanned pressurized compartments or in areas where an occasional penetration by a meteoroid could be tolerated.

Local shielding, as illustrated in configuration "B" could be used in areas highly sensitive to particle penetration, such as the crew's working and sleeping quarters or other areas where critical instruments or equipment may be made inoperative by meteoroid induced particle impacts.

PUNCTURING OF SELF-SEALING STRUCTURES

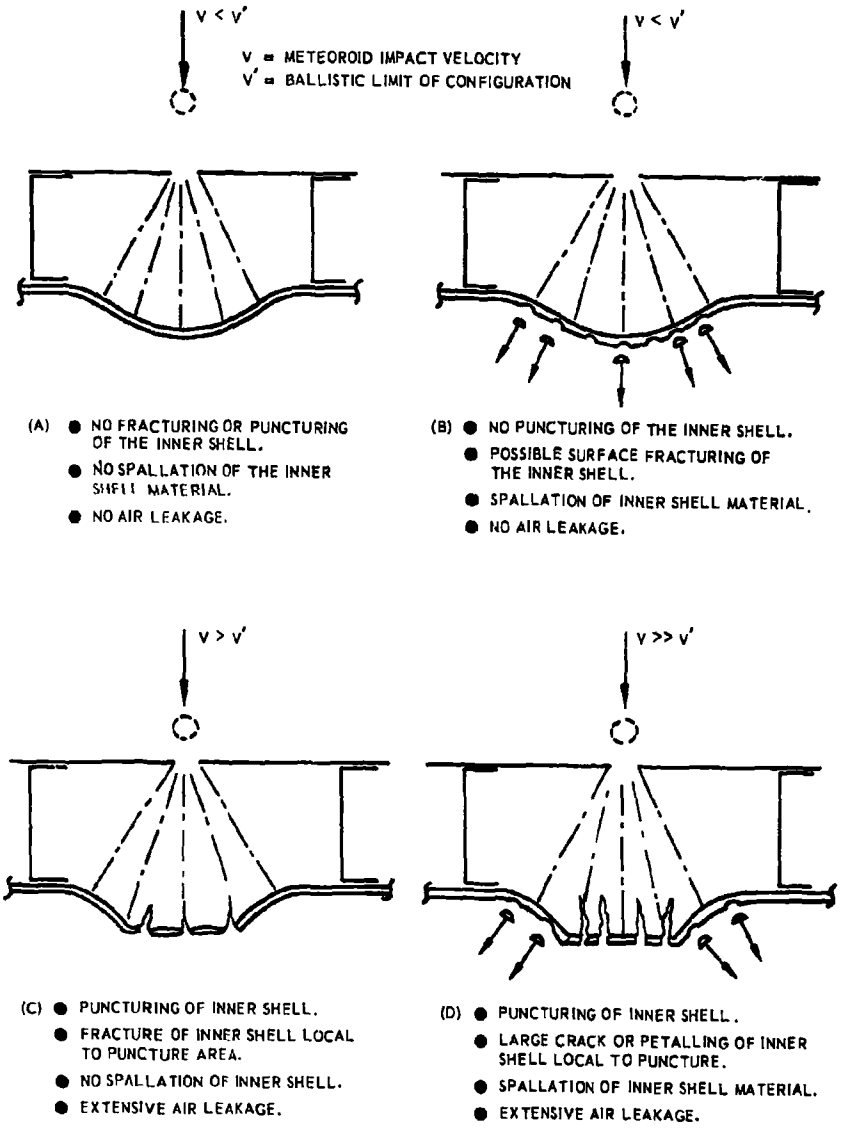

FIGURE 1 VARIOUS TYPES OF METEOROID IMPACT DAMAGE TO SPACED SHEET STRUCTURES

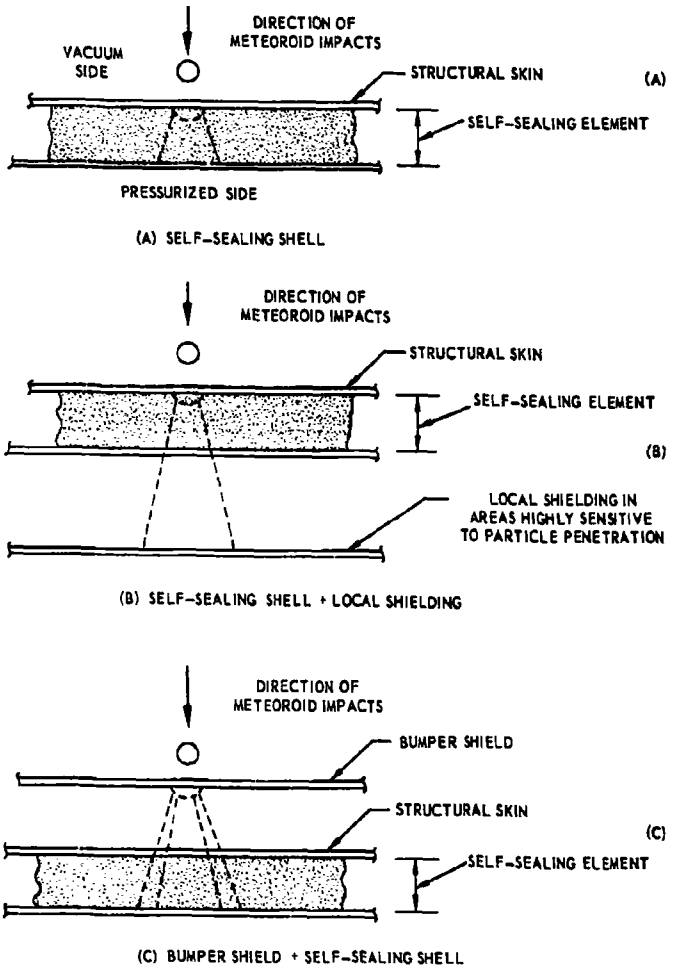

FIGURE 2 SELF-SEALING WALL CONFIGURATIONS FOR SPACE VEHICLE APPLICATION

Configuration "C" illustrates the concept in which the best features of the bumper shield and self-sealing wall are combined to give a highly reliable system possessing both high penetration resistance and high self-sealing capability.

SELF-SEALING STRUCTURE CONCEPTS

The theory of operation of the self-sealing structure is based on a self-sealing material or mechanism which is either attached to or forms an integral part of the structural shell of the pressurized compartment that is to be protected.

Upon puncture of the shell, a self-sealing action is initiated either by the dynamic imbalance due to the escaping fluids, by stored energy in an elastomer, or by a chemical reaction resulting from the dynamic action of the penetrating particle bringing together materials that will foam, swell, or cure and set upon contact or exposure to the space environment (vacuum and/or radiation).

During the course of Northrop's NASA-sponsored program on self-sealing structures, five self-sealing panel configurations--two chemically activated and three mechanically activated--were fabricated and their self-sealing capabilities experimentally verified by puncturing with both 1/8-inch diameter steel and lead spheres at velocities up to 7,000 fps. This paper will, however, be limited to the discussion of the hypervelocity testing and evaluation of one of the mechanically actuated concepts, namely, the Honeycomb-Core-Elastomer Concept. The other concepts will only be described to the extent that their basic characteristics and principles of operation will be delineated. A detailed description and evaluation of these other concepts, including test results, may be found in Reference 4.

CHEMICAL CONCEPTS

Catalyst-Membrane Configuration. The basic details of this concept, and pertinent parameters, are illustrated in Figure 3. In this configuration, a double-wall panel is divided into two compartments by a thin impermeable membrane. One compartment contains an uncured elastomer compound while the other contains a catalyst for curing the elastomer. The principle of operation is that, upon penetration by a meteoroid, the membrane will be punctured, allowing the components to mix and initiate a chemical

reaction to form a solid (cured) mass of elastomeric material and thereby effect a seal. The dynamic mixing action of the puncturing projectile is sufficient, in most cases, to effect a seal along the projectile entry path sealing the punctures through both panel faces and separating membrane.

A number of uncured RTV silicones were tested with the most successful (RTV-60) completely sealing in less than 10 seconds.

Catalyst-Bag Encapsulation Configuration. The basic details of this concept, and pertinent parameters, are illustrated in Figure 4. In this configuration, the elastomer curing agent is encapsulated in polyethylene bags, and the bags dispersed between two layers of uncured elastomer. The principle of operation is that upon penetration by a meteoroid, one of the polyethylene bags will be punctured thereby releasing the catalyst which will cure and set the uncured elastomer local to the projectile entry path to effect a seal.

MECHANICAL CONCEPTS

Elastomeric Spheres Configuration. The basic details of this concept, and pertinent parameters, are illustrated in Figure 5. In this configuration, the panel is of double-wall construction with the space between the walls filled with loosely packed elastomeric spheres. If, for structural reasons, a corrugated core panel is required, the spheres may be packed in the channels formed by the corrugations and the face sheets.

Puncturing of this panel creates a pressure differential across the opening which draws a ball into the puncture of the outer wall (vacuum side) to effect a seal. Should the puncture diameter be larger than the spheres, two or more may bridge the gap and either seal the hole, or substantially reduce the leakage rate.

Precompressed Elastomer Configuration. The basic details of this concept, and pertinent parameters, are illustrated in Figure 6. In this configuration, the panel is a corrugated core sandwich in which the channels are filled with a precompressed elastomer. The fabrication of this panel is accomplished by partially filling the channels, formed by the corrugations and face sheets, with an uncured natural rubber which expands upon curing to completely fill the space between the face sheets with a precompressed elastomer. The amount of compression preload is governed by the amount of

PUNCTURING OF SELF-SEALING STRUCTURES

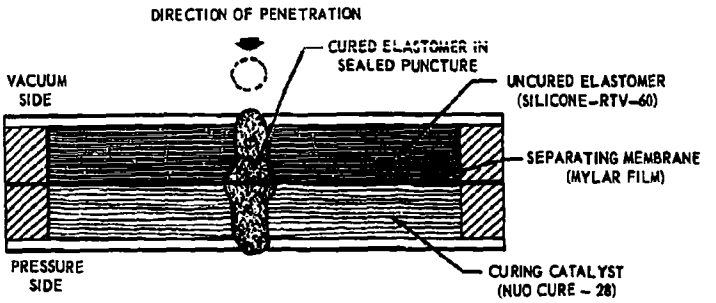

PERTINENT PARAMETERS

- COMPARTMENT SIZE FOR CHEMICAL COMPONENTS
- PROPER MIXING OF COMPONENTS
- CHEMICAL REACTION TIME AFTER PUNCTURE
- VISCOSITY OF CHEMICAL COMPONENTS

FIGURE 3 SELF-SEALING PANEL CHEMICAL CONCEPT - CATALYST-MEMBRANE CONFIGURATION

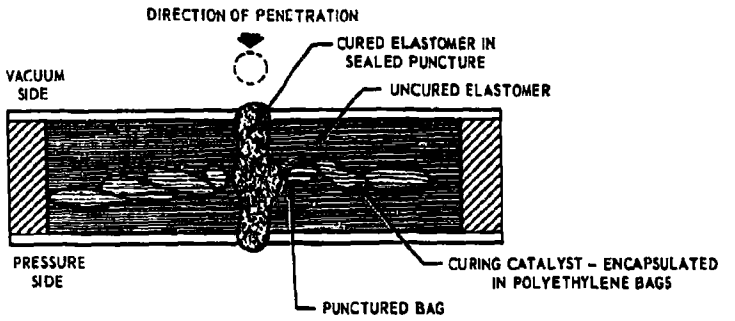

PERTINENT PARAMETERS

- SIZE OF CURING CATALYST ENCAPSULATING BAGS
- PROPER MIXING OF COMPONENTS
- CHEMICAL REACTION TIME AFTER PUNCTURE
- VISCOSITY OF CHEMICAL COMPONENTS

FIGURE 4 SELF-SEALING PANEL CHEMICAL CONCEPT - CATALYST-BAG ENCAPSULATION CONFIGURATION

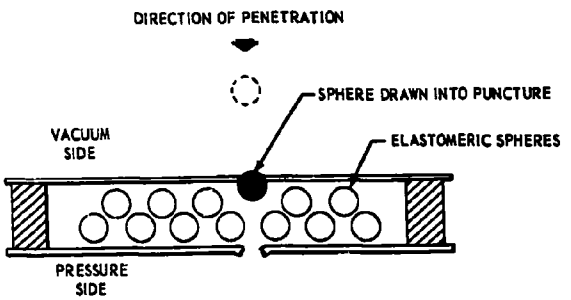

PERTINENT PARAMETERS

- HOLE GEOMETRY
- TYPE OF DAMAGE TO PROJECTILE ENTRY FACE
- DIAMETER OF ELASTOMERIC SPHERES
- HARDNESS OF ELASTOMERIC SPHERES
- DRIVING FORCE (PRESSURE DIFFERENTIAL) TO MOVE SPHERES

FIGURE 5 SELF-SEALING PANEL MECHANICAL CONCEPT - ELASTOMERIC SPHERES CONFIGURATION

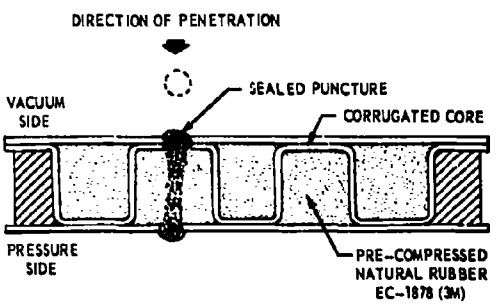

PERTINENT PARAMETERS

- PRE-COMPRESSION STRESS IN ELASTOMER
- POROSITY OF EXPANDED ELASTOMER
- MATERIAL LOSS FOLLOWING PUNCTURING

FIGURE 6 SELF-SEALING PANEL MECHANICAL CONCEPT - PRE-COMPRESSED ELASTOMER CONFIGURATION

uncured rubber used, and the ratio of its unconfined volume expansion (when cured) to that permitted by the panel configuration.

Upon puncturing of this panel, the relieved compression preload, local to the projectile entry path, mechanically moves the surrounding elastomer to close the puncture and effect a seal.

Honeycomb Core-Elastomer Configuration. The basic details of a successful configuration of this concept are illustrated in Figure 7. The panel configuration consists of a double-wall honeycomb core sandwich with the core cells filled with an elastomer sealant. This sealant is rigidly confined between the inner face of the space vehicle's structural shell and an impervious nonmetallic backup sheet.

The principle of operation for this concept is based on limiting the destructive energy dissipation of the penetrating projectile and damage to the panel and sealant so that any resulting punctures will be sealed by the dynamic mechanical response of the elastomer.

EXPERIMENTAL TESTING AND CONCEPT EVALUATION

Initial experimentation during the development of successful self-sealing structures revealed the advantages of using elastomers, instead of other materials, in various panel configurations. However, the fact that not all configurations sealed indicated that the proper combination of material properties and panel configuration was required for successful sealing. Therefore, the evaluation of the Honeycomb Core Elastomer Concept self-sealing panel configuration was conducted in two phases. In Phase I, we evaluated the panel configuration and geometrical parameters and determined the contribution of each panel component to effective self-sealing. In Phase II, we evaluated the sealant material and determined the pertinent dynamic material properties and mechanical response characteristics required for obtaining successful sealing. The hypervelocity puncturing of the panel specimens, at velocities to 7,000 fps, was accomplished with the Northrop Particle Accelerator (Figure 8) in which 1/8-inch diameter steel spheres are propelled down a 2-foot long barrel by an explosive gun powder discharge from a modified 25 calibre rifle cartridge. Projectile velocity measurements were

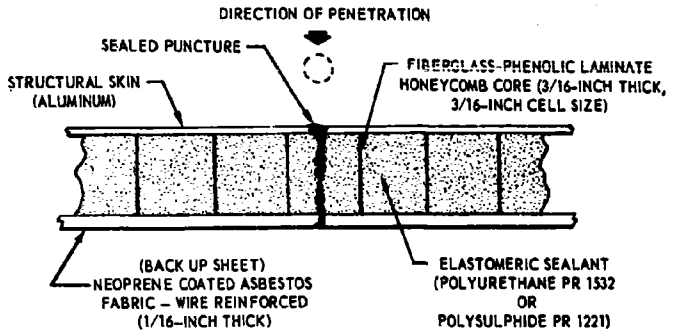

PANEL CONFIGURATION REQUIREMENTS

- RIGIDLY CONFINE SEALANT MATERIAL
- MAINTAIN BONDED AND STRUCTURAL INTEGRITY OF PANEL
- NON-DESTRUCTIVE IMPACT ENERGY ABSORPTION & DISSIPATION
- MINIMIZE LOSS OF SEALANT MATERIAL

FIGURE 7 SELF-SEALING PANEL MECHANICAL CONCEPT – HONEYCOMB CORE – ELASTOMER CONFIGURATION

obtained by means of a velocity detector to start and stop a Hewlett-Packard electronic counter. The gun barrel is enclosed in one end of a transparanet plexiglass chamber while the other end has an opening for mounting of the test panel. The test panel was mounted to form an air tight seal with the chamber. The chamber was then evacuated to between 0.4 and 0.5 Torr to give a pressure differential across the specimen of approximately one atmosphere. The sealability of the panel, after puncturing, was determined by checking for air leakage around the projectile exit area of the backup sheet.

Panel Configuration Evaluation. During the initial development of this concept, various combinations of materials and panel configurations were tested until successful self-sealing was obtained. Examination of these early results indicated that the sealing effectiveness of this concept was sensitive to the following panel configuration parameters:

- Addition and bonding of pellet entry face sheet to panel,
- Elastomer sealant used to fill the honeycomb core cells.
- Cell size of honeycomb core (height and diameter).
- Type of material used as the pellet exit sheet (backup sheet) of the panel.
- Type of adhesive and quality of bond for bonding the various components of the panel.

Following the initial success of this concept, the contribution by each panel component to effective self-sealing was evaluated by the hypervelocity puncturing of panel configurations from which one or more components were eliminated or their material configuration altered. The results from this phase of the evaluation revealed the following:

- Pellet Entry Face Sheet. This sheet limits the impact damage to the sealant by preventing or minimizing fractures and cratering of the pellet entry face of the sealant. In the configurations tested in which this face sheet was either eliminated or left unbonded on the panel, more cratering damage to the sealant resulted.

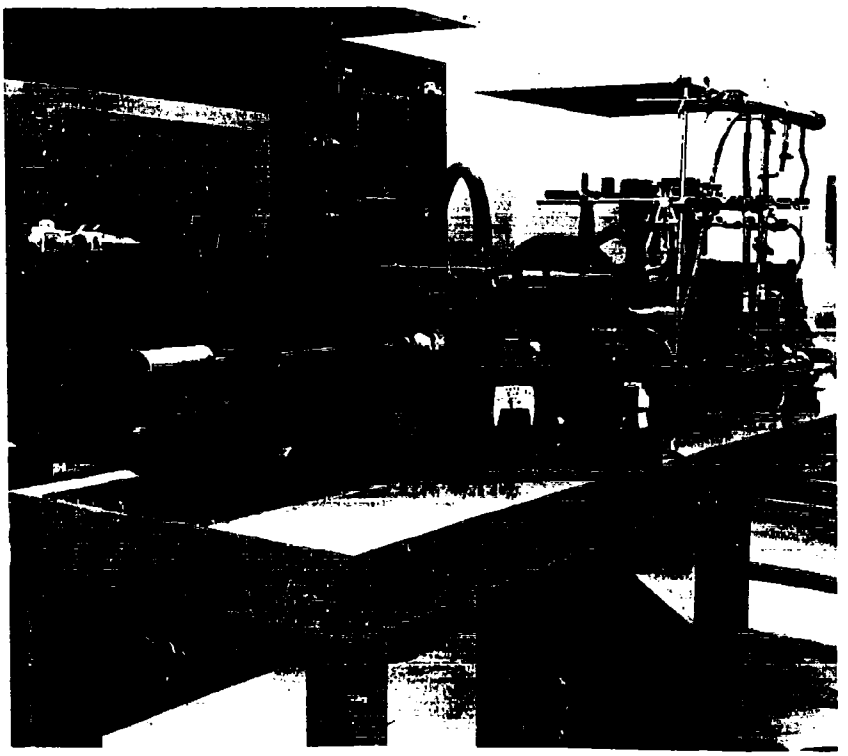

FIGURE 8 NORTHROP PARTICLE ACCELERATOR FOR THE HYPERVELOCITY PUNCTURING OF SELF-SEALING PANEL SPECIMENS

- Elastomeric Sealant. This is the key component which performs the actual self-sealing in a successful panel configuration. A successful elastomer responds to hypervelocity puncturing by permitting passage of the pellet, without excessive fracturing or loss of material, local to the pellet entry path, and then rebounds back to seal the hole. From our sealant evaluation program, we found two materials which most consistently gave successful self-sealing action. These were Polyurethane PR 1532 and Polysulfide PR 1221.

- Honeycomb Core. The honeycomb core, besides addition structural strength to the panel, provides a cell structure for rigidly confining the sealant. This improves material rebound and encourages nondestructive energy dissipation while localizing damage to both the sealant and surrounding structure.

  A core cell size (cell diameter and cell depth) of from 1.5 to 2 times the pellet diameter was found to give the lightest configuration consistent with effective self-sealing response.

  A reinforced plastic honeycomb core was found to be a better nondestructive energy dissipater than a metallic core. When an aluminum honeycomb core was used, extensive damage local to the pellet entry path and excessive leakage occurred.

  Eliminating the honeycomb core from the panel configuration resulted in less consistent sealing and greater sealant damage, particularly in those configurations in which "fracture prone" sealant materials were used.

- Backup Sheet. A reinforced neoprene rubber or plastic laminate backup sheet completes the panel sandwich, aids in the energy absorption of the puncturing pellet, and minimizes damage and loss of sealant material by shock wave reflection phenomena such as spalling.

  When an aluminum backup sheet was used, petalling of the sheet local to the pellet exit hole, excessive loss of material by spalling and unsuccessful

sealing resulted. Figure 9 illustrates the damage sustained by both metallic and nonmetallic backup sheets after being punctured by a 1/8-inch diameter steel pellet.

Bonding Integrity. It was found that best results were obtained when the components of the panel were bonded together with the same material as the elastomer used in the honeycomb core cells. Poor bonding at the interfaces of the sealant with the core cell walls or facing sheets resulted in unbonding of these components from the sealants, local to the pellet entry path, and unsuccessful sealing.

HYPERVELOCITY PUNCTURING OF ELASTOMERS

The mechanical response of materials to hypervelocity puncturing is essentially a high speed loading or high strain rate phenomenon. Elastomers, in general, are sensitive to strain rate but exhibit the desired characteristics of recovery from mechanical deformation after strains of 100 percent or more.

Based on observations resulting from the ballistic testing of elastomer type structures, one can postulate a model to describe the dynamic action during the hypervelocity puncturing of elastomers. A proposed model is illustrated in Figure 10. At impact, as illustrated in (A) of Figure 10, initial penetration is accompanied by exceedingly high pressures local to the impact point. Next, a compression wave propagates at the point of impact compressing and accelerating the elastomer to make room for the penetrating pellet. At the same time, a compression wave backs up into the pellet, at a velocity somewhat higher than that in the elastomer, encouraging early pellet fragmentation and decelerating it so that it moves along a common boundary with the accelerating elastomer. At (B), incipient cracks have started to form local to the pellet elastomer interface, while some elastomer material has been ejected outward from the area of impact. As the pellet begins to decelerate, a shock wave detaches from the common boundary and proceeds into the elastomer ahead of the penetrating pellet. At (C), as the volume of action increases, the initial high pressures drop and assist the further breakup of the pellet. Next, cracks begin to develop in the elastomer permitting displacement of material and passage of the pellet. As the compression wave encounters the rear free surface of the

0.021 INCH ALUMINUM (2024-T3) BACKUP SHEET

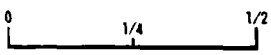

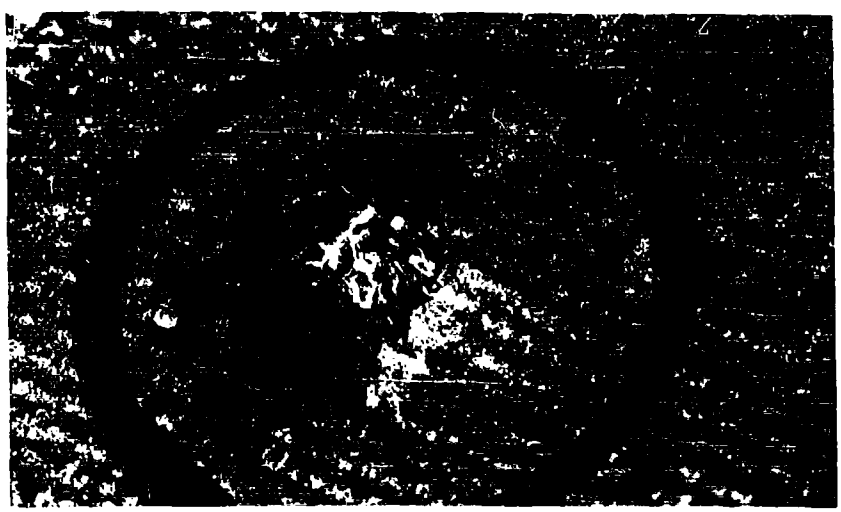

1/16-INCH WIRE REINFORCED NEOPRENE RUBBER BACKUP SHEET

FIGURE 9 HYPERVELOCITY PUNCTURING DAMAGE TO THE PELLET EXIT FACE OF SELF-SEALING PANELS

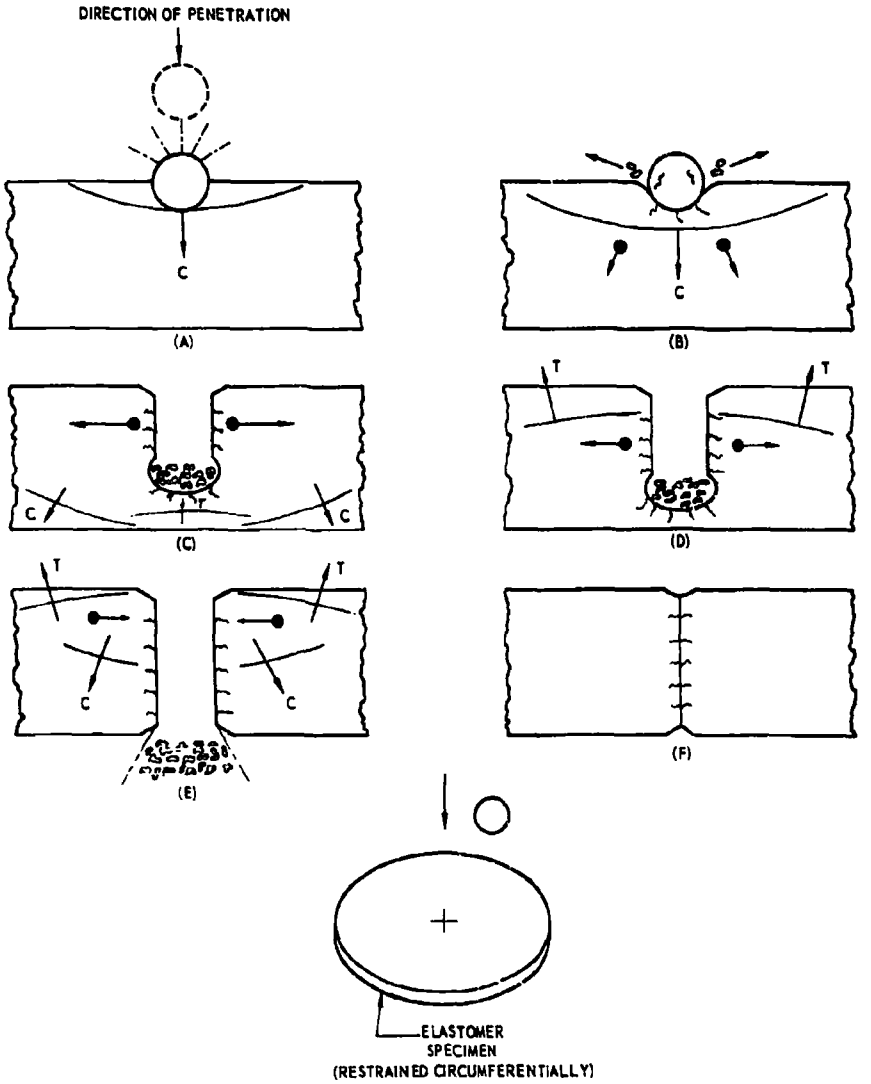

FIGURE 10 MODEL FOR THE HYPERVELOCITY PUNCTURING OF ELASTOMERS

elastomer, it is reflected back into the material as a tension wave at which time, as shown in (D), incipient spalling and material tear out is initiated.

At (E), the tension forces (resulting from the tension wave) with the assistance of the pellet fragments breaking through the rear face of the elastomer, induce spalling and material tear out. Af (F), the pellet has completely penetrated the elastomer and the material local to the pellet entry path, now relieved of its preload compressive stresses (initially precompressed by the dynamic action of the penetrating pellet), rebounds to close the hole. Residual damage to the elastomer includes cratering at the pellet entry face, minute fractures local to the pellet entry path and spalling plus some material tear out at the pellet exit face. Depending on the extent and type of pellet fragmentation, some material loss along portions of the pellet entry path may also occur.

ELASTOMER MATERIAL EVALUATION

The response of the elastomer sealant to both the static and dynamic effects of the natural and induced environment will determine their self-sealing effectiveness when used in a composite configuration. Based on essentially static and environmental considerations, the following material parameters are considered to be significant:

- Cohesive strength (shear).
- Cured state of elastomer.
- Resistance to degradation by the material environment, e.g., radiation and vacuum.
- Resistance to degradation by the induced environment, e.g., pressure, extreme temperature, mechanical loads, contained fluid of pressurized compartment.
- Permeability to contained fluid of pressurized compartment.
- Odor and toxicity of degradation products.
- Fire resistance and burning characteristics.

In addition, results from the hypervelocity puncturing of slugs of various candidate sealant materials (both with and without backup sheets), and completed panel configurations, plus a rational analysis of the puncturing action, established that the following dynamic characteristics were required for effective self-sealing.

- Minimum material removal local to the pellet entry path and sealant boundary interfaces, e.g., cratering and spalling.
- Minimum crack propagation local to the pellet entry path and sealant boundary interfaces.
- Minimum radial permanent deformation local to the pellet entry path.
- Maximum material rebound to permit pellet entry path closure.
- Maximum nondestructive energy absorption and dissipation.

The two sealant materials (Polyurethane PR 1532 and Polysulfide PR 1221), which produced consistent successful panel configurations, came the closest to satisfying all the above requirements. The less successful sealants were found to be deficient in one or more of these requirements. This is dramatically illustrated in Figure 11 where the hypervelocity puncturing damage to a successful sealant specimen (Polysulfide PR 1221) is compared to that sustained by a less successful specimen (Silicone DC 521). It is interesting to note that the "fracture prone" sealant DC 521 propagates many cracks radially from the pellet entry path while the polysulfide does not. The backup sheet is seen to minimize the damage to the pellet exit face of the polysulfide. However, though the silicone specimen sustained less material removal with the backup sheet, crack propagation local to the pellet exit area was still extensive.

As part of the elastomer evaluation program, an attempt was made to establish a correlation between the material's dynamic characteristics require for self-sealing, and some static or dynamic material property. The static and quasi-static material properties selected for possible correlation were:

- Hardness (Durometer A) (Instantaneous values).
- Hardness change between instantaneous and equilibrium values--an index of material flow under stress.
- Shear strength
- Tensile modulus
- Secant modulus (tensile) ratio--an index of material flow under stress
- Lupke resiliency--an index of internal energy dissipation at low strain rates.

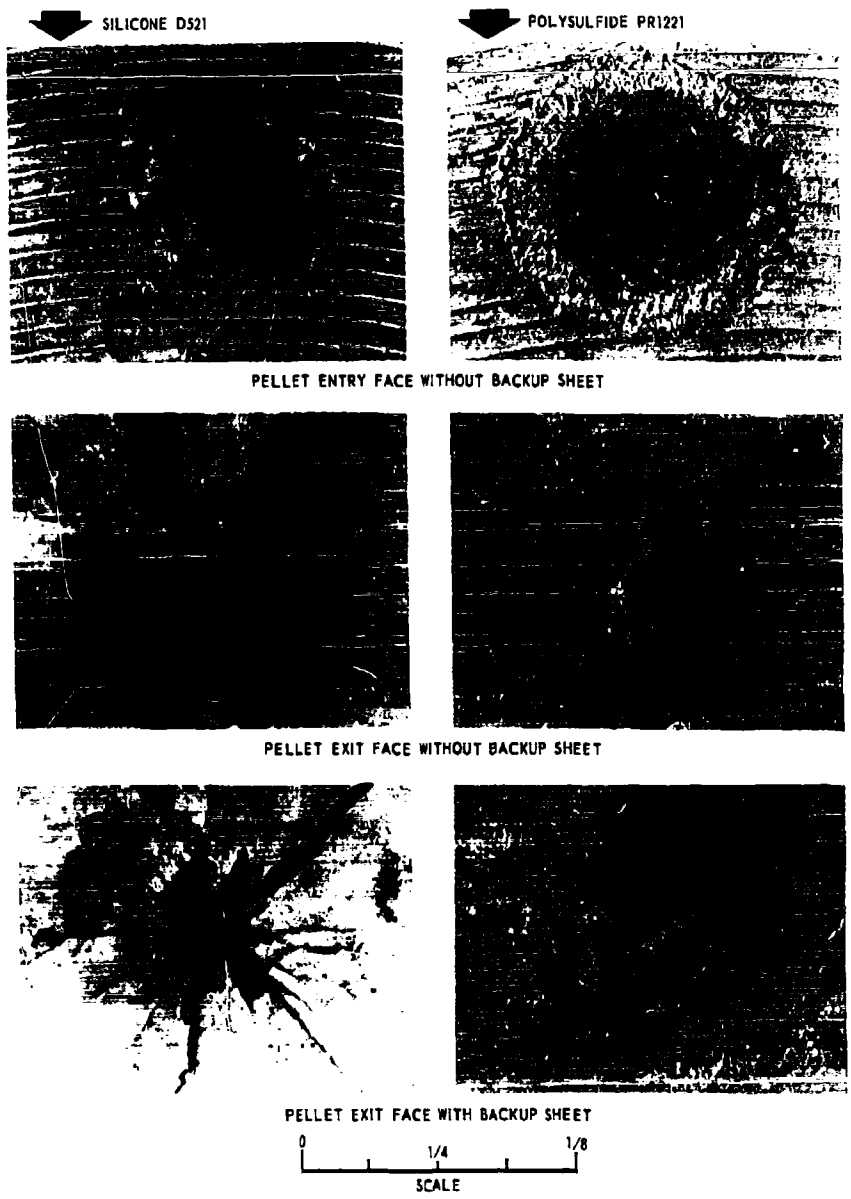

FIGURE 11 HYPERVELOCITY PUNCTURING DAMAGE TO SEALANT TEST SPECIMENS WITHOUT AND WITH NEOPRENE BACKUP SHEET

Standard ASTM procedures were used in determining the Durometer hardness and tensile modulus (except that a strip specimen was used in place of the "dumbbell" specimen). Both instantaneous and equilibrium values were recorded in the hardness tests. Two plate tests were used to determine shear strength. The Lupke resilience tester is a pendulum tester which measures energy absorption empirically by means of the percent rebound of the pendulum striking the elastomer target (1 7/8-inch diameter X 5/8-inch thick) from a fixed height.

The dynamic material properties selected for correlation were:

- Dynamic Modulus (in-phase)--a measure of elastic material response at high strain rates.
- Dynamic Loss Factor--an index of internal energy dissipation at high strain rates.

These dynamic material properties were determined by exciting a sealant specimen, on an electrodynamic shaker, with a sinusoidal load input at frequencies up to 2,000 cps. The test setup and pertinent test parameters are illustrated in Figure 12. Further details on this test procedure and method of analysis may be found in Reference 4.

EVALUATION OF TEST RESULTS

The static and dynamic (hypervelocity puncturing and electrodynamic shaker) tests were conducted for the two most successful sealants and some others, mostly silicones, which did not prove as successful. Hypervelocity puncturing of both sealant specimens and of panel configurations demonstrated that Polyurethane PR 1532 and Polysulfide PR 1221 sustained the minimum impact damage and gave the best self-sealing response of all materials tested. These were followed by the silicones in the following order of increasing impact damage: RTV-20, RTV-11, DC 521, and RTV-60.

A relative rating of those static and dynamic properties which demonstrated a correlation which desired dynamic characteristics for effective self-sealing is given in Table 1. Based upon these test results and their evaluation, the following was determined:

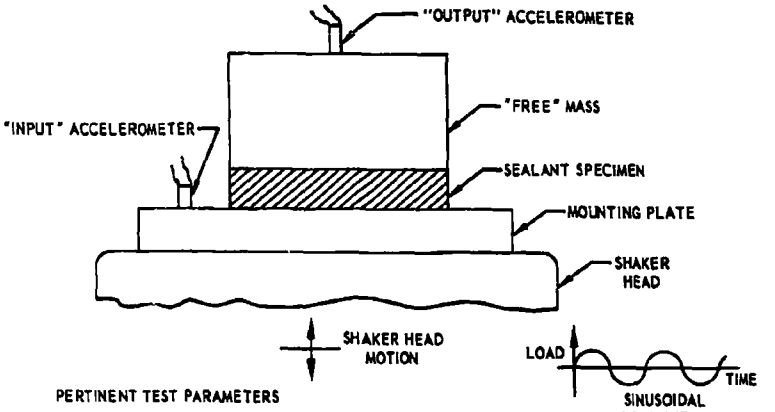

PERTINENT TEST PARAMETERS

g_i = INPUT "g" – LOAD TO SHAKER HEAD

g_o = OUTPUT "g" – LOAD TO "FREE" MASS = "g" – LOAD INPUT TO SPECIMEN

$\frac{g_o}{g_i}$ = TRANSMISSIBILITY

δ = PHASE ANGLE BETWEEN g_i AND g_o

ϕ = PHASE ANGLE BETWEEN STRESS (σ) AND STRAIN (ϵ)

E' = IN-PHASE MODULUS = $\frac{\sigma'}{\epsilon}$ WHERE σ' IS THE COMPONENT OF THE STRESS IN PHASE WITH THE STRAIN

E'' = OUT OF PHASE MODULUS = $\frac{\sigma''}{\epsilon}$ WHERE σ'' IS THE COMPONENT OF THE STRESS 90° OUT OF PHASE WITH THE STRAIN

L = LOSS FACTOR = $\frac{E''}{E'}$ = TAN ϕ

FIGURE 12 SHAKER TEST SET-UP FOR DETERMINING DYNAMIC PROPERTIES OF SEALANTS

No correlation is indicated between self-sealing capability of the elastomer sealants tested and

- o Tensile modulus (at low strain rates).
- o Durometer hardness.

A definite correlation exists between desired dynamic characteristics for effective self-sealing action and the following material properties:

- o Energy absorption and dissipation as determined by the Lupke resiliency and electrodynamic shaker tests.
- o Stress relaxation or material flow as determined by the Secant modulus ratio and hardness change.
- o Dynamic modulus as determined by the electrodynamic shaker tests.
- o Shear strength as determined by the lap shear test.

From these results it has been concluded that a combination of simple tests such as the Lupke resiliency, lap shear, and stress relaxation may be used for the preliminary screening of candidate sealant materials for use in self-sealing structures. However, final evaluation should be determined by testing at high strain rates by such methods as the electrodynamic shaker tests or by hypervelocity puncturing at velocities approaching actual service conditions. Results obtained, for this program, from the hypervelocity puncturing tests at velocities to 7000 fps will be verified at an outside ballistic facility at velocities to 20,000 fps. Since 7000 fps is above the minimum velocity required for hypervelocity puncturing action in an elastomer* it is expected that the conclusions arrived at from our initial tests will remain valid.

*The "hypervelocity regime" for an elastomer is considered to be the velocity of sound in the elastomer (5000-6000 fps) or higher.

TABLE 1

RELATIVE RATING OF STATIC AND DYNAMIC PROPERTIES OF SELECTED SEALANTS AND CORRELATION WITH DESIRED DYNAMIC CHARACTERISTICS

	*	*	RATING BY		*	*	*
						ELECTRODYNAMIC SHAKER TESTS	
SEALANT MATERIAL	DESIRED DYNAMIC CHARACTERISTICS (SEE NOTE 1)	LUPKE RESILIENCY	SECANT MODULUS RATIO (SEE NOTE 2)	HARDNESS CHANGE (SEE NOTE 3)	SHEAR STRENGTH (PSI)	DYNAMIC MODULUS	DYNAMIC LOSS FACTOR
PR 1532	1	1	0.68	11	2	1	1
PR 1221	2	2	0.64	18	1	2	2
RTV-20	3	3	1.28	0	3	3	3
RTV-11	4	5	1.00	0	4	–	–
DC 521	5	4	1.00	0	–	4	4
RTV-60	6	6	1.16	0	5	–	–

NOTES:

1. AS DETERMINED FROM HYPERVELOCITY PUNCTURING TESTS OF SEALANT SPECIMENS AND PANEL CONFIGURATIONS CONTAINING EACH SEALANT.
2. SECANT MODULUS RATIO = $\frac{\text{SECANT MODULUS AT 50\% STRAIN}}{\text{SECANT MODULUS AT 25\% STRAIN}}$
3. THE DIFFERENCE BETWEEN THE IMMEDIATE AND EQUILIBRIUM HARDNESS READING (DUROMETER A).

*A RATING OF 1 INDICATES THE MATERIAL POSSESSING THE HIGHEST DESIRED VALUE OF THE INDICATED PROPERTY; A RATING OF 2, THE SECOND HIGHEST, AND ETC.

The final evaluation, following the hypervelocity puncturing of completed panel configurations, was to check for sealability with the leak detector apparatus illustrated in Figure 13. The pressure in the air chamber with the panel attached to the open end is initially at 14.7 psi at the start of data recording. The flow rate through the puncture is then determined from the pressure decay vs. time data obtained as the chamber air escapes through the puncture into the vacuum flask.

The air leakage rates (with a driving pressure of 14.7 psi across the puncture) for some of our more successful panel configuration, have varied from zero leakage to 1.4 pounds per day. This compares with an optimistic (minimum) leakage rate of 260 pounds per day for an assumed 1/8-inch diameter puncture resulting from impacts by 1/8-inch diameter projectiles to either single thickness skins or the inner shell of a spaced structure. The actual puncture size and leakage rates in these instances will be greater than the figure indicated, due to the fact that the hole size in a punctured sheet is always greater than the projectile diameter and the possibility of leak provoking fractures local to the hole. Therefore, even for those panel configurations that did not completely seal, a decided advantage over the non-self-sealing type of structure is indicated.

The panel weights for the configurations tested varied from 1.7 to 2.0 lbs/ft^2. No serious attempt at reducing the weight of these panels has been made at this time. However, the panel and elastomer depth required for effective sealing is a function of the puncturing projectile diameter. Therefore, it is reasonable to assume that thinner and lower weight panel configurations would prove as effective in a realistic meteoroid environment where the meteoroids with the highest probability of impacting a space vehicle are smaller in diameter than the pellets used in our hypervelocity tests.

In conclusion, it should be added that the more promising chemical self-sealing panel concepts currently under development, are initially domonstrating greater consistency in completely sealing upon being punctured than the Honeycomb-Core-Elastomer configurations. Therefore, successful development of these concepts should further enhance the cause of the self-sealing structure philosophy as a promising technique for minimizing air leakage due to meteoroid induced punctures.

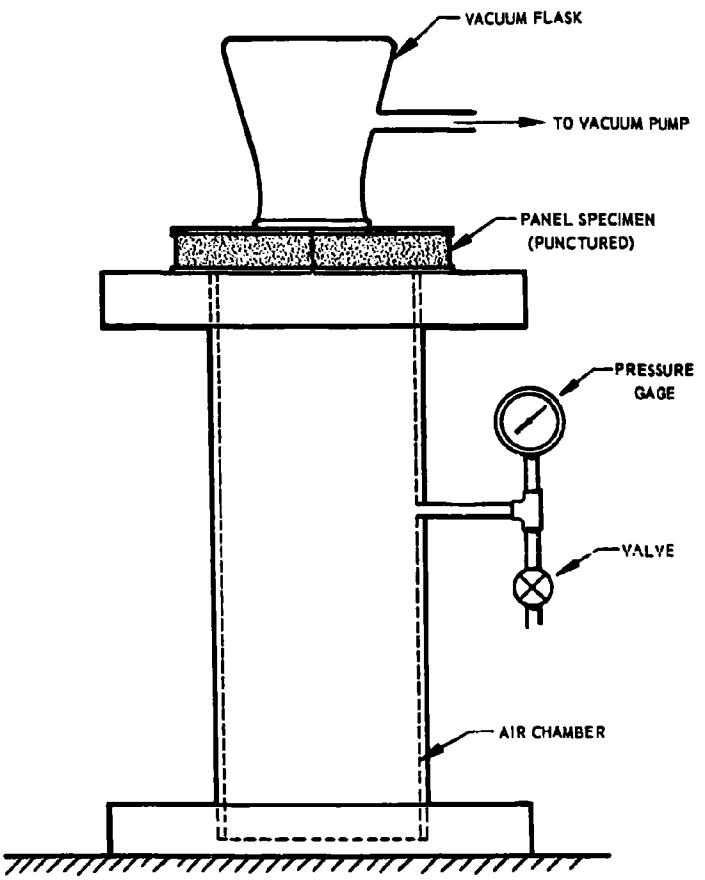

FIGURE 13 LEAK DETECTION APPARATUS

The author wishes to acknowledge the valuable assistance of his co-workers at the Northrop Space Laboratories for performing the experiments and generating the data that were used in the preparation of this paper.

REFERENCES

1. Wallace, R. R., Vinson, J. R. and Kornhauser, M., "The Effects of Meteoroids and Hypervelocity Projectiles on Multi-Walled Space Vehicle and Missile Structures," General Electric Company, T.I.S. 60 SD 464, December 1960.

2. Eichelberger, R. J. and Gehring, J. W., "Effects of Meteoroid Impacts on Space Vehicles," ARS Report 2030-61, October 1961.

3. Nysmith, R. C., Summers, J. L., "An Experimental Investigation of the Impact Resistance of Double-Sheet Structures at Velocities to 24,000 Feet Per Second" NASA TN D-1431, September 1962.

4. D'Anna, P. J., Heitz, R. M., Piechocki, J. J., Hunter, R. W., Jenkins, R. K., "Self-Sealing Structures for Control of the Meteoroid Hazard to Space Vehicles." Final Report NASA Contract NASr-102, March, 1963. (Northrop Technical Memorandum NSL 62-132-3)

AN INVESTIGATION OF THE PENETRATIONS OF HYPERVELOCITY PROJECTILES INTO COMPOSITE LAMINATES*

by

A. R. McMillan

ABSTRACT

This paper will describe the results of an experimental research program aimed at determining the damage that would be inflicted upon a composite laminated target by the impact of a hypervelocity projectile. The experimental program was conducted on the Ballistics Range facilities of the GM Defense Research Laboratories in Santa Barbara, California. Targets were impacted under simulated operating conditions at velocities up to 26,000 feet per second with glass and aluminum projectiles weighing from 0.015 to 0.05 grams. In the experiments such target design variables as thickness, material composition, and temperature were considered.

The aim of the research program was to obtain data related to broad concepts of design showing the damage sustained by generic complex targets under impact conditions typical of an operating environment.

*Work described in this paper carried out under NASA Contract No. NASW-468 and ARPA Contract No. ARPA/Nonr. 3891-(00) (X).

LIST OF FIGURES

Figure 1	.22 Cal. Accelerated-Reservoir Light-Gas Gun
Figure 2	Velocity Stations and Impact Chamber
Figure 3	Impact Chamber
Figure 4	Effect of Target Thickness on Penetration and Spall, for Flat Targets
Figure 5	Depth of Penetration vs. Target Thickness, for Flat Targets
Figure 6	Depth of Penetration vs. Target Diameter, Constant Wall Thickness
Figure 7	Effects of Laminates on Penetration and Spall, for Flat Targets
Figure 8	Depth of Penetration vs. Weight of Target, for Flat Laminates
Figure 9	Impact Crater in Typical Radiator Section
Figure 10	Projectile Size Effects, Aluminum with HS-25 Liner Targets
Figure 11	Target Temperature Effects, Aluminum with HS-25 Liner Targets
Figure 12	Impact Angle Effects, Aluminum with HS-25 Liner Targets
Figure 13	Impact Angle Effects, Columbium Targets - No Liner
Figure 14	Target Material Effects
Figure 15	Armor Thickness Effects, Columbium Targets
Figure 16	Liner Effects, Aluminum Targets
Figure 17	Internal Tube Damage
Figure 18	Typical Impact Crater Section, Aluminum with HS-25 Liner Target
Figure 19	Armor-Liner Interface Photomicrographs, Ref. Figure 18

PENETRATION INTO COMPOSITE LAMINATES

INTRODUCTION

Within the past two years, the techniques for projection of hypervelocity projectiles and for observation of the effects of impact have been considerably improved[1,2]. The projectile capabilities that have been achieved cover the entire range of mass of primary concern in space travel, and the velocities extend well into the lower portion of the range of interest. A physical description of the mechanism of crater formation in simple targets under hypervelocity impact is now possible, and the model that has been evolved from the combined theoretical and experimental studies by many researchers has been illustrated schematically in Reference 1. Several attempts have been made to develop a complete theory to describe hypervelocity impact[3,4,5]; however, these approaches have limitations in that they treat relatively simple structures.

Very little information is available to the designer on the damage that might be inflicted upon a complex structure by a hypervelocity impact. In consideration of this problem, a two-fold experimental research program was initiated to: (a) assess the impact damage by a hypervelocity fragment against a variety of space vehicle designs under simulated

operating conditions and (b) to assess the damage caused by a fragment which would perforate the shell or which would eject small particles of debris from the rear of the target. In these cases, the target could then be treated as a thin target in the analysis of the effects of hypervelocity impact[6]. Because of the paucity of information regarding impact damage to a complex structure, the test variables included the velocity, size, and material of the impacting projectile, selected target materials such as aluminum, copper, polyethylene, and columbium, as well as the structural design and environment in which the materials are being used.

EXPERIMENTAL TECHNIQUES

Description of Range and Monitoring Instrumentation

All of the tests to date were conducted on a ballistics range, which is fully described in GM DRL Report ER 62-201A[7]. The basic equipment consists of a gun, a 20 foot free-flight range, and an impact chamber. The 0.22" caliber accelerated-reservoir light-gas gun is shown in Figure 1. With the accelerated-reservoir light-gas gun, it is possible to launch cylindrical plastic models to velocities of 10 km/sec, or saboted metal or glass spheres to velocities of 8.6 km/sec. The projectile is launched into the flight range and travels through a surge chamber (in which the

model is separated from the sabot) then into the velocity chamber. Here, the position and time of flight of the projectile are recorded at each of three spark shadowgraph stations (Figure 2). The measurements of time and distance between stations serve to determine the velocity of the projectile along its trajectory and, in particular, at the target. The accuracy of the impact velocity determined in this manner is better than 1%. The model flight is terminated in a specially-constructed impact chamber (Figure 3) which has several viewing ports. Three large windows are located in opposite sides of the target area, and many smaller windows are located on the front and top of the chamber. The full-size door acts as the rear wall of the chamber to allow easy insertion and removal of the targets. The targets are held by a mount sitting on two rails on the floor of the chamber. This design allows placement of the target at a uniform longitudinal position with respect to the viewing ports. The target chamber has provisions for heating targets and controlling the test medium. The range is also equipped with an air scrubber to allow impact of toxic materials. A Beckman & Whitley Model 192 framing camera capable of framing rates of 1.4 million frames per second, and four channels of flash x-ray are available for diagnostic experiments related to the impact phenomena.

Target Preparation and Damage Assessment

The assessment of target damage to any target is complex and requires precise definition. Prior to testing any of the targets, each target was classified according to both material properties and by examination of the condition of the material. Since some of the tests were aimed at simulating actual operating conditions, many targets were annealed for eight hours at the test temperature of 700°F. This pre-treatment procedure was significant in that the aluminum targets undergo a phase change at 700°F after several hours anneal, resulting in reducing the Brinell Hardness Number from a nominal 52 to a value to 36 at room temperature. The BHN is used here as a measure of the strength of the material; hence, the lower the BHN, the more damage is caused on impact[1, 6]. Following the shot, the targets were cooled to room temperature and the damage assessed.

EXPERIMENTAL OBSERVATIONS

The possible number of laminated structures which could be used in a vehicle hull is almost unlimited; hence, it is not feasible to explore, experimentally, more than the generic combinations of materials. To

evaluate the impact effects on laminated structures, it is necessary to have a basis of comparison. To provide this basis of comparison, a series of tests was performed to determine the effects of varying the thickness of a simple target, Figure 4. The thickness of a group of 2024-T3 aluminum targets was varied from 0.005" to semi-infinite. Aluminum projectiles of 1/8" diamater were fired at an average velocity of 7.4 kilometers per. second with variation in actual velocities of not more than 2%. For the thick targets, a typical hemispherical crater was formed. As the thickness of the target was reduced, the succeeding targets first exhibited fracturing and bubbling then spall due to the intense pressure pulse beneath the actual crater. As the thickness was further reduced, the target was completely perforated. This series of tests made possible the evaluation of the constants in the equation

$$T_p = a\, P_\infty \qquad \text{(1)}$$

where

T_p = the thickness of target required to prevent perforation or spall

P_∞ = penetration in a semi-infinite target

a = constant (for particular conditions of impact velocity, target material and projectile material)

PENETRATION INTO COMPOSITE LAMINATES

Perforation occurred for thicknesses of 0.456" or 1.78 P_{∞} . Spall occurred for thicknesses up to 0.50" or 1.95 P_{∞} . Spall was here defined as complete detachment of a portion of the rear face of the target. In thicknesses up to 0.584" or 2.28 P_{∞} the rear face of the target was still bubbled and fractured below the surface, although no metal was detached from the target. The results of these tests are shown in Figure 5, a comparison of penetration versus thickness of the target. The thickness required to prevent perforation, $> 1.78\ P_{\infty}$, and the thickness required to prevent spall, $> 1.95\ P_{\infty}$, are greater for this target-projectile combination than estimated in References 1 and 3.

A series of tests was also performed to establish the effect of target shape on penetration and spall. Glass projectiles 3/32" diameter (0.016 grams) were impacted at 7.5 kilometers per second on targets where the shape was varied from a flat plate to a small hollow cylinder. The wall thickness of each shape was held constant. Figure 6, a plot of penetration versus the reciprocal of inside diameter, shows the strong effect of shape on penetration. The flat plate was completely perforated and the large diameter tube spalled on the inside, while the smaller tubes showed only dimpling on the inside surface.

PENETRATION INTO COMPOSITE LAMINATES

Since internal spall can be extremely lethal even in the absence of complete penetration, several experiments were conducted to investigate techniques of preventing spall by using properly selected materials. One of the important parameters to be considered is the acoustic resistance $G = \rho_t C$, where ρ_t is the density of the target materials and C is the shock wave velocity in the target under the conditions encountered. By mismatching the acoustic resistances of a laminate, the shock wave can be divided with a portion of the energy being reflected back into the first layer of the laminate and the remainder being transmitted into the second layer. In this manner, it is possible to break up and attenuate the shock wave in a laminate and avoid spall that would occur in an equal weight homogeneous structure[8].

To examine the effect that a laminate can have on penetration and spall, a variety of laminates were impacted under the same conditions as the 0.50" 2024-T3 aluminum target (Figure 4). Figures 7 and 8 show the results of replacing a simple target by a laminate. Two copper-aluminum laminates of the same weight per unit area as the 0.50" 2024-T3 plate were impacted. With .040" of copper bonded to the rear face of the aluminum, the aluminum was not spalled or perforated. However, the copper was detached, split open and spalled. Reversing this laminate and placing the

copper on the front face of the aluminum, the result of the impact was similar to that obtained with the simple aluminum target except that the total penetration was greater. The copper was detached from the aluminum and the rear face of the aluminum spalled.

The 0.50" aluminum target was then replaced by an aluminum-polyethylene laminate of the same weight per unit area. In this case, the aluminum was perforated, yet the 0.130" of polyethylene on the rear face was only bent with no perforation or spall.

Finally a target was tested in which the thickness of the polyethylene was increased to 0.255" and the thickness of aluminum decreased to 0.331" (thus reducing weight and maintaining the same over-all thickness). This target represents 81% of the weight per unit area of the 0.50" 2024-T3 target and the other laminates. In this case, the aluminum was perforated and a portion of the spall from the aluminum penetrated the polyethylene and lodged in it. This represents a marginal situation or the "ballistic limit" for this projectile and velocity, wherein an increase in the thickness of the aluminum would effect a defeat of the projectile (or conversely, an increase in projectile energy would defeat the target).

PENETRATION INTO COMPOSITE LAMINATES

Reference is again made to Figure 8, showing a plot of penetration versus weight per unit area of target. The penetration into the aluminum-copper laminate is about the same as that into the simple aluminum plate, while the penetration into the aluminum-polyethylene laminate was the greatest, there was no damage to the rear surface. Although the al-poly laminate is amenable to a space vehicle hull, the ballistic limit shown for the aluminum-polyethylene laminate in Figure 7 is of no use to the radiator designer, who, because of temperature considerations, cannot use the heat sensitive polyethylene liner.

One concept of a radiator structure proposed uses both a laminate and a cylindrical shape to afford protection against damage that might be inflicted by a meteoroid impact. To permit high temperature operation, the laminate consists of a cast 356 aluminum armor (0.400" thick) covering a Haynes Stellite #25 cobalt alloy liner (0.020" thick). The crater shown in Figure 9 was caused by a 1/8" diameter glass sphere (0.038 grams) impacting at 7.01 km/sec. The crater (0.3" deep) did not perforate the coolant carrying tube; yet, the intense shock induced beneath the crater caused the liner tube to be dimpled, thus constricting the I.D. of the tube. This particular shot was fired at room temperature, hence

the aluminum armor behaved in a semi-brittle fashion evidenced by the brittle spallation around the periphery of the crater. This phenomena will later be compared to that obtained with the target at an operating temperature of 700°F.

Note the complex nature of defining the extent of damage to this laminated target. The target itself offers many variables; size, composition, condition at time of impact and shape. The size, shape, composition and impact velocity of the projectile are further variables. To test the effect of these design variables, a number of qualitative comparisons have been made, and are shown in Figures 10 through 17. On each of the Figures, the average projectile velocity is shown for brevity. The actual measured velocity did not vary from this average velocity by more than $\pm$ 2%. These comparisons of the experimental variables will be numerically assessed later in Table I.

First, consider the mass scaling effects by comparing the damage caused by impact of two glass sphere projectiles, one 3/32" diamater, the second 1/8" diameter, each impacting an aluminum-armored HS-25 radiator at a velocity of 7.1 km/sec (Figure 10). These projectiles

weigh 0.016 and 0.040 grams respectively and, therefore, fall into the meteoroid mass-frequency distribution area of interest for radiators[9]. The target was at an environmental operating temperature of 715°F. It can be seen in Figure 10 that this radiator target provided an assessment of the marginal protection afforded by this configuration. The 1/8" glass sphere perforated the aluminum armor and the HS-25 liner tube, while the 3/32" glass sphere did not perforate the armor, but merely caused dimpling of the inner liner. Hence, under these conditions of target temperature and projectile impact velocity, the ballistic limit of this configuration can be defined as a projectile mass between 0.016 to 0.04 grams.

Although it was shown in Reference 1 that by increasing the target temperature one could achieve greater damage to a simple metal target, it was not known how the increased temperature would affect a composite such as those selected for these tests. Therefore, 1/8" glass spheres were fired at a velocity of 7.1 km/sec into each of two targets, one at room temperature, the other at 700°F (Figure 11). In both cases, the radiator complex was perforated. In the case of the target at room temperature, however, the perforation was marginal in comparison to

the target at 700°F which was severely damaged with a 1/4" hole having been punched through the HS-25 liner. In addition, the target at room temperature exhibited evidence of brittle spalling around the periphery of the crater indicative of the greater hardness of the material. The increased damage of a target, resulting from the lower strength at higher temperatures, has been accounted for in some empirical relationships describing hypervelocity cratering.

The next variable known to seriously affect the damage sustained by a target under hypervelocity impact is that of the attacking angle of the projectile to the target. In Figure 10 the results of a 3/32" glass sphere impacting normal to the radiator target were shown. Figure 12 compares the damage sustained to the radiator by 3/32" glass spheres impacting at angles of 15° and 68° from the normal (note that the photographs were taken normal to the resultant crater).

Several important results should be pointed out. First, both of the craters are approximately hemispherical, thus assuring that the impacts were typical of the hypervelocity impact regime. Secondly, the depths of penetration (and, of course, the resulting crater volumes)

decrease as the angle of attack increases. These results are in agreement with several other investigations[1,10] and can be accounted for empirically by measuring the energy of the attacking projectile in terms of its normal component of velocity. Hence, as the angle of obliquity is increased, the normal component of energy of the projectile diminishes with the cosine of the angle of attack. So long as the minimum normal velocity of the projectile does not fall below that required for hypervelocity cratering, the resultant crater will, in general, be a hemisphere, although much reduced in volume.

This phenomena of reduced penetration under oblique impact was also observed for columbium radiator targets (Figure 13). Columbium is of particular interest to the space radiator designer because of its high strength properties at very high temperatures. Since columbium has a melting point of 4474°F (ASM Metals Handbook, 8th Ed.), it is of particular interest for use in advanced radiator systems having operating temperatures near 2000°F.

One serious drawback against the use of columbium in a space radiator is the density of the material, 8.57 grams per cc. compared to

aluminum, 2.7 grams per cc. The designer must, therefore, consider the protection afforded by a radiator complex of equal weight per unit length. This comparison is made in Figure 14, showing the protection afforded by an all-columbium radiator versus that afforded by the aluminum-armored HS-25 lined radiator tube. Note that the all-columbium radiator was perforated, while the aluminum - HS-25 structure was not.

Obviously, it would be possible to use an all-columbium system and prevent damage to the internal fluid by increasing the thickness and thus the "ballistic limit" of the radiator tube (Figure 15). Two choices are then left to the designer: First, by increasing the wall thickness of the material one can prevent perforation as shown in Figure 15. In order to hold this increase in weight to a minimum, however, the second variable, the I. D. of the tube, was diminished to 1/4 that of the columbium tube shown in Figure 14. The results of Figure 15 thus indicate the effects of two variables; first, the thickness of the armor, and secondly, the benefit to be derived by decreasing the tube I. D.

Not only has it been observed that by decreasing the I. D. of the coolant-carrying tube one can prevent spalling or perforation into the

inner tube, but also it has been found that a ductile, yet tough, inner liner will prevent spallation of metal into the coolant-carrying tube. Obviously a perforation will permit the cooling fluid to leak from the radiator. Spallation of metal particles is certainly a more subtle damage than a complete perforation, yet in many cases could be equally devastating[10]. Metal particles in the fluid could cause damage and failure of the liquid circulating pumps.

Recalling the beneficial effects of a polyethylene liner (Figure 7), the comparable effects of an inner liner in a radiator which must withstand 700°F can be seen in Figures 16 and 17. In Figure 16, one target was lined with Haynes Alloy No. 25 liner; the second target had no liner, but the aluminum armor was made thicker, thus keeping the weight constant. The inner HS-25 liner, although severely dimpled, prevented spalling of metal into the coolant-carrying tube. In Figure 17, the effects of an inner tube are shown in close-up photographs; first, for the case of an all-columbium tube without a liner in which severe spalling occurred; and secondly, for the case of the aluminum-armor HS-25 tube radiator complex in which no spalling, just dimpling of the inner wall, occurred. Again, it should be noted that this comparison is made for approximately equal weight per unit length of radiators. Note also that the aluminum HS-25 radiator complex did not

spall, even though it had been struck by a 1/8" glass sphere. It can be concluded, therefore, that a tough inner liner is of utmost importance in preventing spall particles from being ejected into the coolant-carrying fluid. Sections of the crater made after impact are shown later in Figure 18 and clearly depict the manner in which the HS-25 liner restricts the breaking away or flaking of the spalled particles.

ASSESSMENT OF DAMAGE TO RADIATOR TARGETS

The complexity of the target and the many types of damage that can be effected on the complex target prevent a brief evaluation of the damage by simply stating the depth of penetration or the diameter of the crater that has been made. It was seen in Figures 10-17 that the many projectile and target variables each act in its own significant way to establish the final damage to the target. Such parameters as the target temperature, angle of attack, target material, thickness of the armor, effects of the armor on the inner liner, and the target shape itself, all contribute to the final damage to the target. It is not sufficient, therefore, to merely observe the crater and to measure the depth of penetration, since in many cases spalling has been caused under the crater and particles have been ejected from the rear of the target. On the other

hand, it was observed in many cases that the tough HS-25 liner used in some of the radiator targets could be dimpled just as the polyethylene was seen to do in Figure 7. Dimpling can completely constrict the tube, thus preventing fluid flow, yet the target would not be perforated, nor would any fragments be ejected into the internal tube. It was suspected, however, that when the HS-25 tube was badly dimpled, delaminating would take place between the HS-25 tube and the aluminum armor, thereby reducing the heat transfer properties of the radiator section.

It was necessary, therefore, to section each and all of the targets after impact in order to examine and to assess the details of the damage that had been effected. A typical impact crater section of an aluminum radiator target with an HS-25 liner is shown in Figure 18. Here, the spalling of the armor material beneath the crater itself can be clearly seen, in addition to the dimpled HS-25 liner and the delaminating that has occurred between the liner and the armor. Of a much more subtle nature is the delaminating that has occurred at a distance far removed from the dimpled section itself. A close-up view of points A and B in Figure 18 can be seen in Figure 19. Here at a magnification of 120X and 300X, respectively, the crater section at points A and B can be seen in detail. At point A, severe delaminating has occurred due to the fact that the liner

was pulled away from the armor, and the bonding material failed. Section B shows another interesting observation. Here, it is believed that some delaminating is not associated with the formation of the crater, but rather, a failure of the bond during fabrication of the radiator section. The different coefficients of expansion of aluminum and HS-25 no doubt resulted in a poor bond, since this effect was observed to some degree in all of the target sections prior to conducting the impact experiments.

COMPARISON OF EXPERIMENTAL OBSERVATIONS WITH ESTABLISHED EMPIRICAL RELATIONSHIPS

It was pointed out early in the report that there does not exist any detailed mathematical formulation by which to predict the damage by a hypervelocity fragment complex target. The theoretical approaches of Bjork, Riney, Kirchner and others have made significant advances in the analytical approach; however, the treatments do not account in detail for the effects of increased target temperature, effect of variations in the alloy of the target, impacts at angles of obliquity, and the spalling and delaminating of thin and composite targets. A number of empirical relationships have been offered in the literature which do permit at least an approximation of the damage which might occur under limited conditions.

Two such empirical relationships that appear to hold under a wide variety of impact conditions, and which allow for the effects of target temperature and the angle of projectile impact, were given by Eichelberger and Gehring[1] and by Charters and Summers[11].

Rewriting those two relationships we have the forms:

From Reference 1

$$\frac{P}{d_p} = \frac{\left(\frac{12 \times 10^{-9} \frac{E}{B} \cos^2\theta}{2\pi}\right)^{1/3}}{d_p} \quad \text{----------(cgs units) -- (2)}$$

and from Reference 11

$$\frac{P}{d_p} = 2.28 \left(\frac{\rho_p}{\rho_t}\right)^{2/3} \left(\frac{V \cos\theta}{C_t}\right)^{2/3} \quad \text{----------} (3)$$

where

P = depth of penetration

E = energy of projectile

B = Brinell Hardness No. (varying with target temp.)

θ = angle of impact (measured from the normal)

ρ_p = projectile density

ρ_t = target density

V = projectile velocity

C_t = velocity of sound in target

and d_p = diameter of projectile

Regarding the use of these two relationships, two comments are made: (a) Eichelberger and Gehring's Equation (2) was derived from the relationship $V = 4 \times 10^{-9} E/B$, where V is crater volume in cm^3, E is projectile kinetic energy in ergs, and B is target hardness in standard BHN. This latter relationship applies to meteoroid impact conditions, where velocities can be expected to be in the range of 10 to 70 km/sec. Hence, Equation (1) is subject to the same conditions. At lower impact velocities, a factor T is added to the relationship; T being of the primary penetration phase of crater formation. This factor, T, is proportional to $(\rho_p / \rho_t)^{1/2}$, and is independent of velocity. Therefore, as velocity increases and the contribution of projectile energy is increased, the contribution of T to the total penetration becomes negligible.

(b) Charters and Summers in a paper following Reference 11 (See Reference 12) use a combination of Equation (3) and a simple model of the impact process to derive another damage formula. This equation shifts the emphasis from the speed of sound to the strength of the target material and is given by

$$\frac{P}{d_p} = 1.50\left(\frac{\rho_p}{\rho_t}\right)^{1/3}\left(\frac{\rho_p V^2}{2S_t}\right)^{1/3} \qquad \text{----------} \quad (4)$$

where S_t is assumed to be a constant deformation strength of the target material. Unfortunately, the values of S_t are not well known for conditions relevant to hypervelocity impact. However, Charters and Summers suggest that an impact experiment be conducted and, from Equation (4) and the measured crater depth, a value of S_t be derived. This value can then be used to predict damage in the same target material but for a variety of impact conditions.

Referring again to Equations (2) and (3), the numerical values of the predicted depths of penetration were calculated for several typical targets and the resulting values are tabulated in Table I. The relationships of Equations (2) and (3) predict depths of penetration in semi-infinite

targets but do not provide predictions for the penetration into thin targets or laminates. A comparison of the predicted penetrations in 2024-T3 aluminum with the actual penetrations shows a reasonable approximation to the measured value in the case of the 0.50" target. The 0.456" target which was perforated shows a much greater penetration than predicted (Figure 4). In both cases spall occurred, but could not be predicted on the basis of the simple predictions without a knowledge of the constant "a" in Equation (1).

The evaluation of equi-protection schemes is of utmost importance to the design engineer, who must also consider the problems of fabrication, structural design, and, in the case of radiator design, thermal properties[13]. In comparing the effects of varying target temperatures and of varying angle of impact, the corrections allowed in the Equations (2) and (3) permit reasonable approximations to the actual measured values (Table I). Note that in the case of targets 6 and 12 (Fig. 11), the 1/8" glass sphere perforated the radiator section, yet the calculated depths of penetration did not exceed the thickness of the original section. In the case of the aluminum target No. 38 (Figure 16) and the columbium target No. 31

(Figure 13) spalling was observed, yet, here again, the predicted depth of penetration did not meet the thickness of the target section. These results show that a relatively thin target can be perforated through a process of spalling out a section immediately under the actual crater.

Although the depth of penetration in targets 9 and 5 (Figures 12 and 10 respectively) exceeded the predicted depth required to cause spalling and partial perforation, no damage other than dimpling was effected to the inner tube. This effect is attributed to the ability of the HS-25 liner to absorb the energy of the shock through slight deformation of the tube (Figure 17) just as the polyethylene was deformed in the aluminum-polyethylene laminate (Figure 7). Without the inner liner the aluminum armor is spalled, resulting in debris being ejected into the internal fluid. The phenomena of spalling and perforation is amplified in the case of a flat plate target over that of the cylindrical target section. The proximity of the free surfaces in the cylindrical targets results in a more rapid attenuation of the pressure pulse; consequently, the cylindrical targets offer more resistance to penetration than the flat plate configuration (Figure 6).

CONCLUDING REMARKS

An attempt has been made in this report to alert the design engineer to the many target design parameters that affect the ability of a composite vehicle structure to prevent hypervelocity impact damage. Although it is impossible to test all, or even a small percentage, of the many suggested vehicle structures, an insight can be gained from the experimental results presented herein, of the behavior of several generic targets under projectile impact and intense impulsive loads.

It has been demonstrated that steps can be taken to prevent spall other than merely increasing the structure thickness. By employing carefully selected materials, a laminate can be constructed such that it will provide the equivalent protection of a greater weight of homogeneous material. A variation in the structure shape can also afford greater protection than provided by an equivalent flat structure. The laminated space radiator segments are an application of these protection devices and provide an example of a structure that is extremely resistant to spall. These are, of course, only a few of the possible steps that may prove beneficial in providing protection against hypervelocity impact but do afford an indication of the weight savings that may be realized.

REFERENCES

1 Eichelberger, R. J., and Gehring, J. W., "Effects of Meteoroid Impacts on Space Vehicles", ARS Journal, October 1962, Vol. 32, No. 10, pp. 1583-1591.

2 Curtis, J. S., and Gehring, J. W., "Protection Techniques", paper presented at the Symposium on Structural Dynamics Under High Impulse Loading, Dayton, Ohio, Sept. 17-18, 1962.

3 Bjork, R. L., "Effects of a Meteoroid Impact on Steel and Aluminum", The Rand Corp. Paper P-1662, 1958. Presented at the Tenth International Astronautical Congress, London, 1959, Springer-Veilag, Vienna.

4 Riney, T. D., "Theory of High Speed Impact", General Electric Final Report on MSVD Req. No. 214-796, Contract No. AF 08(635)-1713, Eglin Air Force Base, Florida, Dec. 1961.

5 Rae, W. J., and Kirchner, H. P., Progress Reports on "A Study of Meteoroid Impact Phenomena", Cornell Aeronautical Lab., Inc., Buffalo, New York, Sept. 1962.

6 Maiden, C. J., "Experimental and Theoretical Results Concerning the Protective Ability of a Thin Shield Against Hypervelocity Projectiles", paper to be presented at the Sixth Symposium on Hypervelocity Impact, April 30, May 1 and 2, Cleveland, Ohio.

7 General Motors Defense Research Laboratories, "Research Facilities of the Aerospace Operations Department", ER 62-201A, GM DRL, Santa Barbara, California.

8 Rinehart, J. S., "Practical Counter-Measures for the Prevention of Spallation", Colorado School of Mines Research Foundation Report AF-SWC-TR-60-7 to Air Force Special Weapons Center, Albuquerque, New Mexico, 1960.

9 Loeffler, I. J., Lieblein, Seymour, and Clough, N., "Meteoroid Protection for Space Radiators" paper presented at the ARS Space Power Systems Conference, Santa Monica, California, Sept. 1962, ARS Paper No. 2543-62.

10 Bryan, G. M., "Oblique Impact of High Velocity Steel Pellets on Lead Targets", Proceedings on the Fifth Symposium on Hypervelocity Impact, Vol. 1, Part 2, April 1962, pp. 511-534.

11 Charters, A. C., and Summers, J. L., "High Speed Impact of Metal Projectiles in Targets of Various Materials", Proceedings of Third Hypervelocity Impact Symposium, Armor Research Foundation, Chicago, Illinois, 1958.

12 Charters, A. C., and Summers J. L., "Some Comments on the Phenomena of High Speed Impact", Proceedings of the Decennial Symposium, White Oak U.S. Naval Ordnance Laboratory, 1959.

13 Gehring, J W., and Lieblein, Seymour, "Preliminary Results on Effects of Hypervelocity Impacts on Space Radiator Tubes," Paper presented at the ARS Space Power Systems Conference, Santa Monica, California, Sep 1962, ARS Paper No. 2544-62

Target No., See Figs. 10-16	Projectile	Target Material	Target Temperature	Angle of Impact	$\frac{P}{d}$ Calculated Eq. 2 (I)	$\frac{P}{d}$ Calculated Eq. 3 (II)	$\frac{P}{d}$ Measured Value	
. 5	3/32" glass	0.4" Al + 0.020" HS-25 Liner	700°F	0°	3.08	3.40	3.26	Effect of varying target material. Figs. 10 & 15.
34	3/32" glass	0.25 Columbium	700°F	0°	1.75	1.82	2.40	
6	1/8" glass	0.4" Al + 0.020" HS-25 Liner	Rm. Temp.	0°	2.21	2.48	Perf.	Effect of varying target temperature, Fig. 11.
12	1/8" glass	"	700°F	0°	2.99	3.34	Perf.	
7	3/32" glass	"	700°F	68°	1.64	1.83	1.35	Effect of varying angle of impact, Fig. 12
9	3/32" glass	"	700°F	15°	3.07	3.40	3.36	
	1/8" Al.	0.50" 2024-T3	Rm. Temp.	0°	1.82	2.53	2.24	Effect of varying target composition, Figs. 4 and 7.
	1/8" Al.	.456" 2024-T3 .130" polyethylene	Rm. Temp.	0°	1.82	2.53	3.64	

TABLE I

COMPARISON OF CALCULATED AND MEASURED PENETRATION DEPTHS

GAS MANIFOLD
POWDER CHAMBER
PUMP TUBE
HIGH PRESSURE COUPLING
LAUNCH TUBE

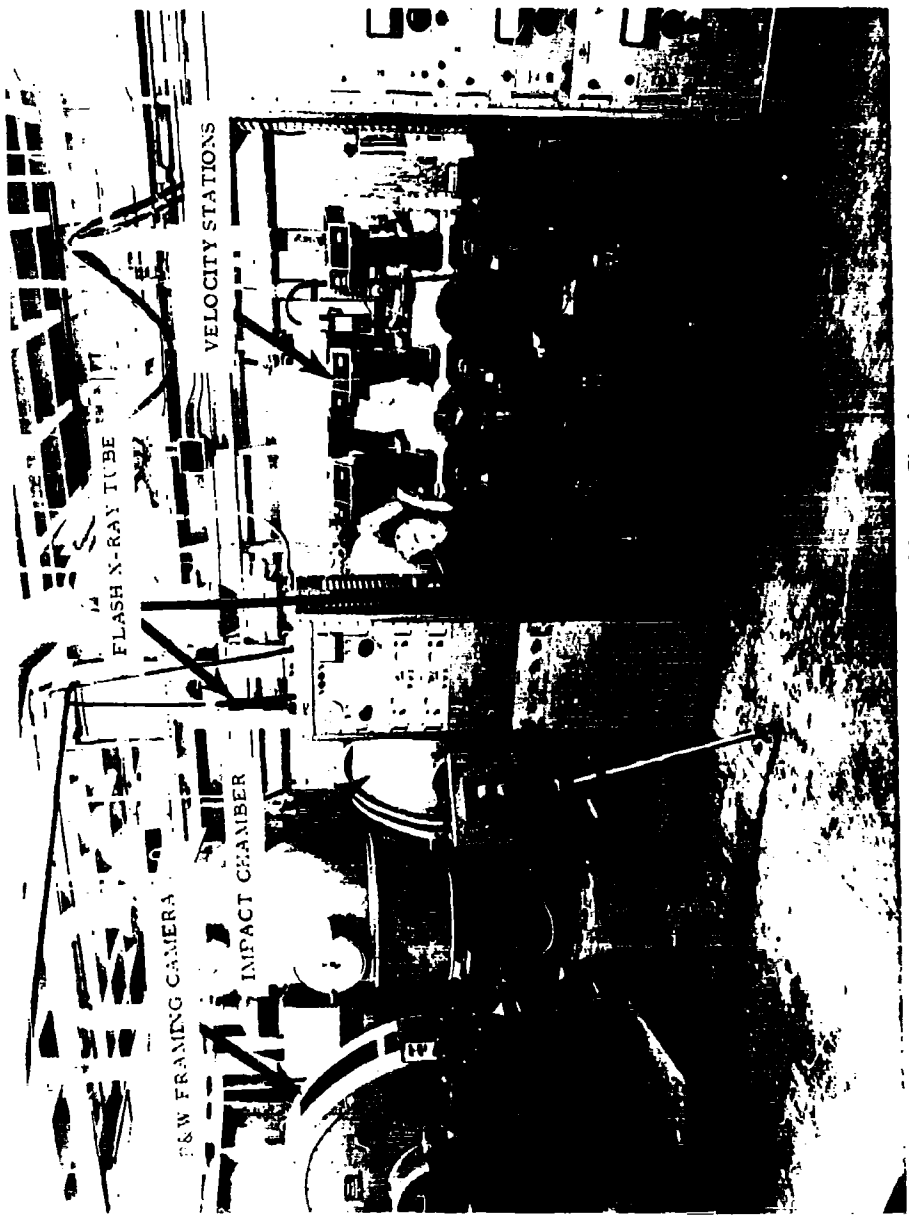

Figure 2 Velocity Stations and Impact Chamber

Figure 3 Impact Chamber

2024-T3 AL. TARGETS
1/8" 2017 AL. SPHERES, 0047 gm.
7.4 km/sec

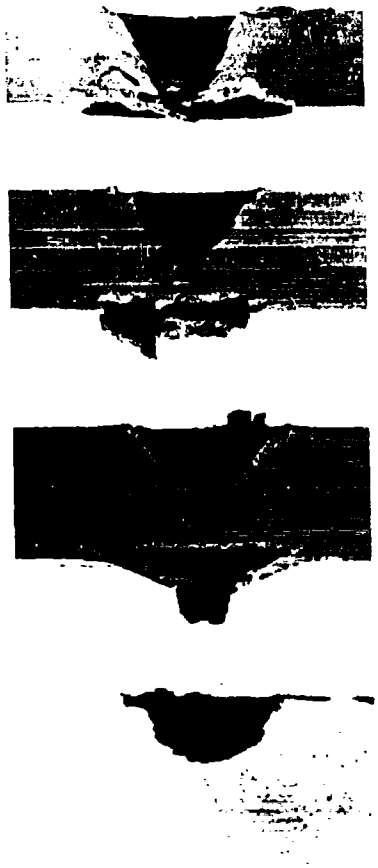

t = 0.40"
p = HOLE

t = 0.50"
p = 0.28"

t = 0.56"
p = 0.27"

t = SEMI-INFINITE
p = 0.26"

Figure 4 Effect of Target Thickness on Penetration and Spall, for for Flat Targets

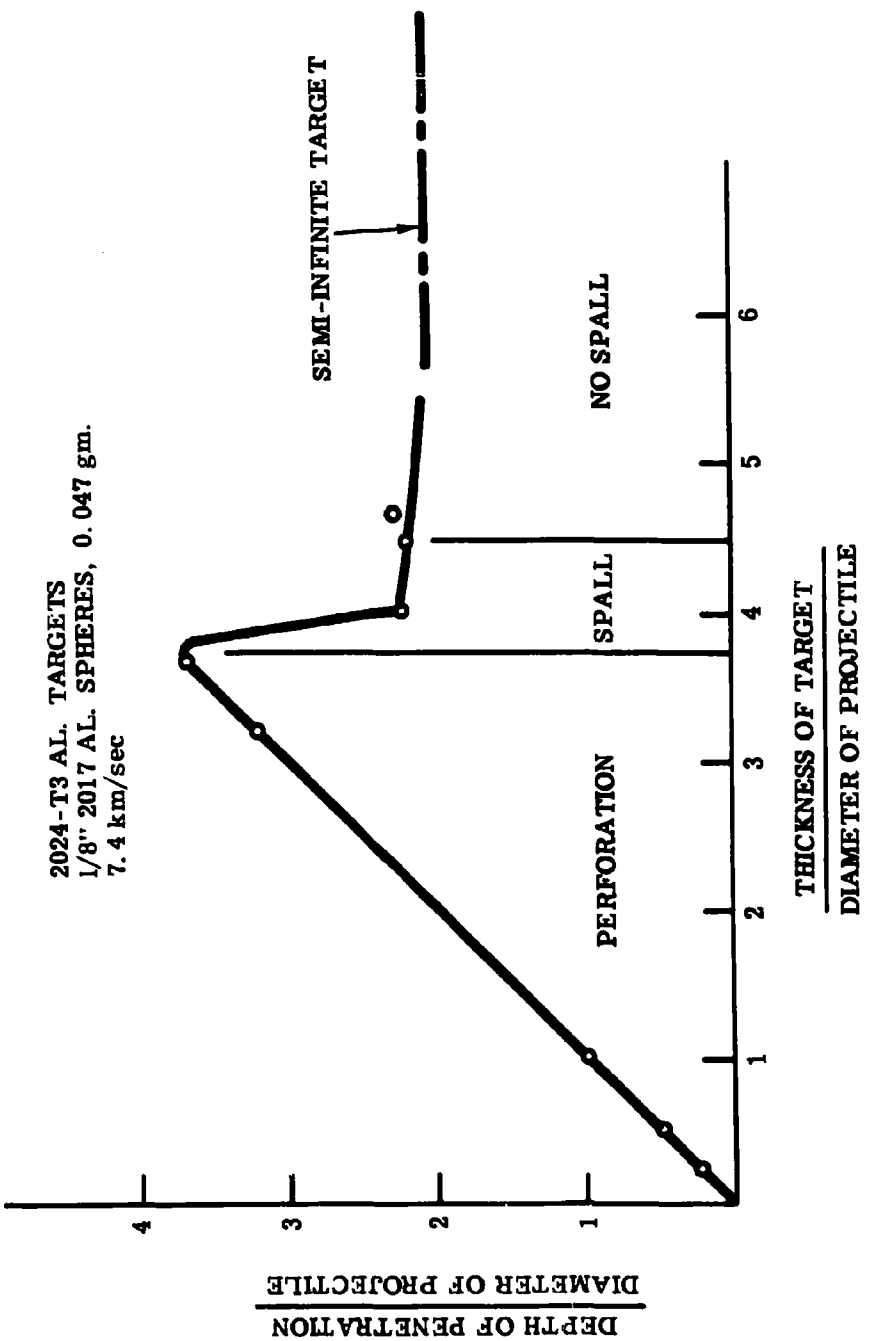

Figure 5 Depth of Penetration vs. Target Thickness, for Flat Targets

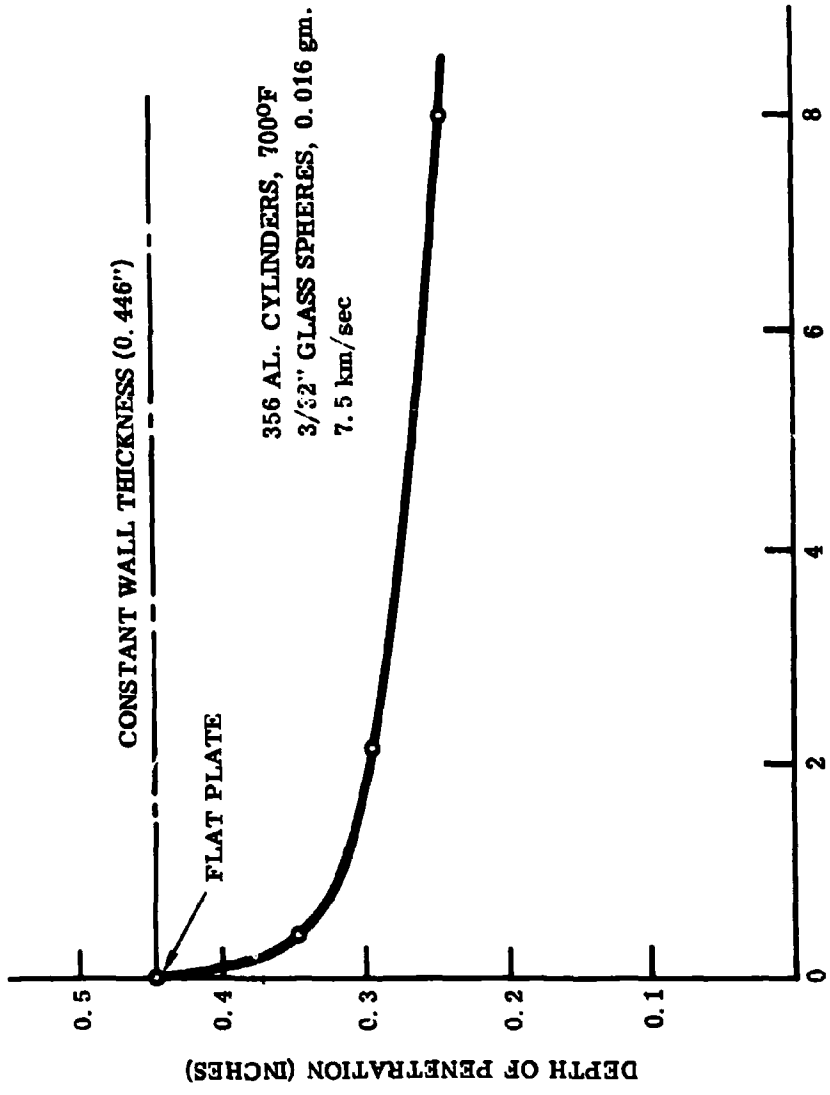

Figure 6 Depth of Penetration vs. Target Diameter, Constant Wall Thickness

PENETRATION INTO COMPOSITE LAMINATES

ALL TARGETS EQUAL WEIGHT PER UNIT AREA, 3.4 GM/CM^2
1/8" 2017 AL. SPHERES, 0.047 GM. 7.4 KM/SEC

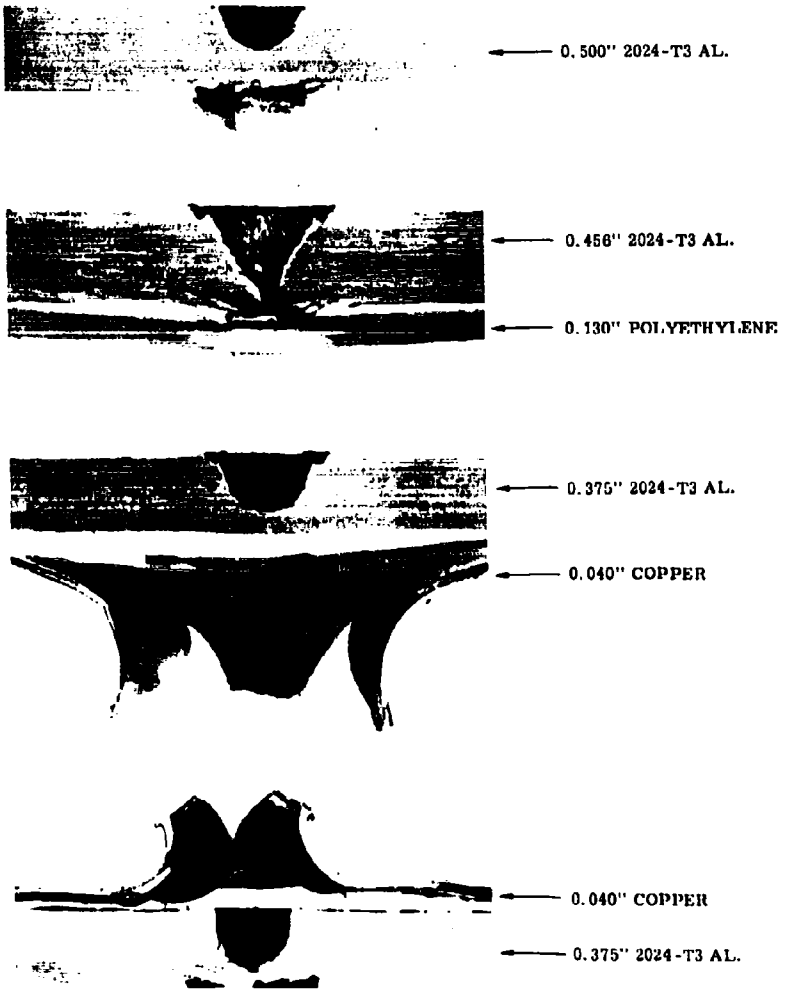

Figure 7 Effects of Laminates on Penetration and Spall, for Flat Targets

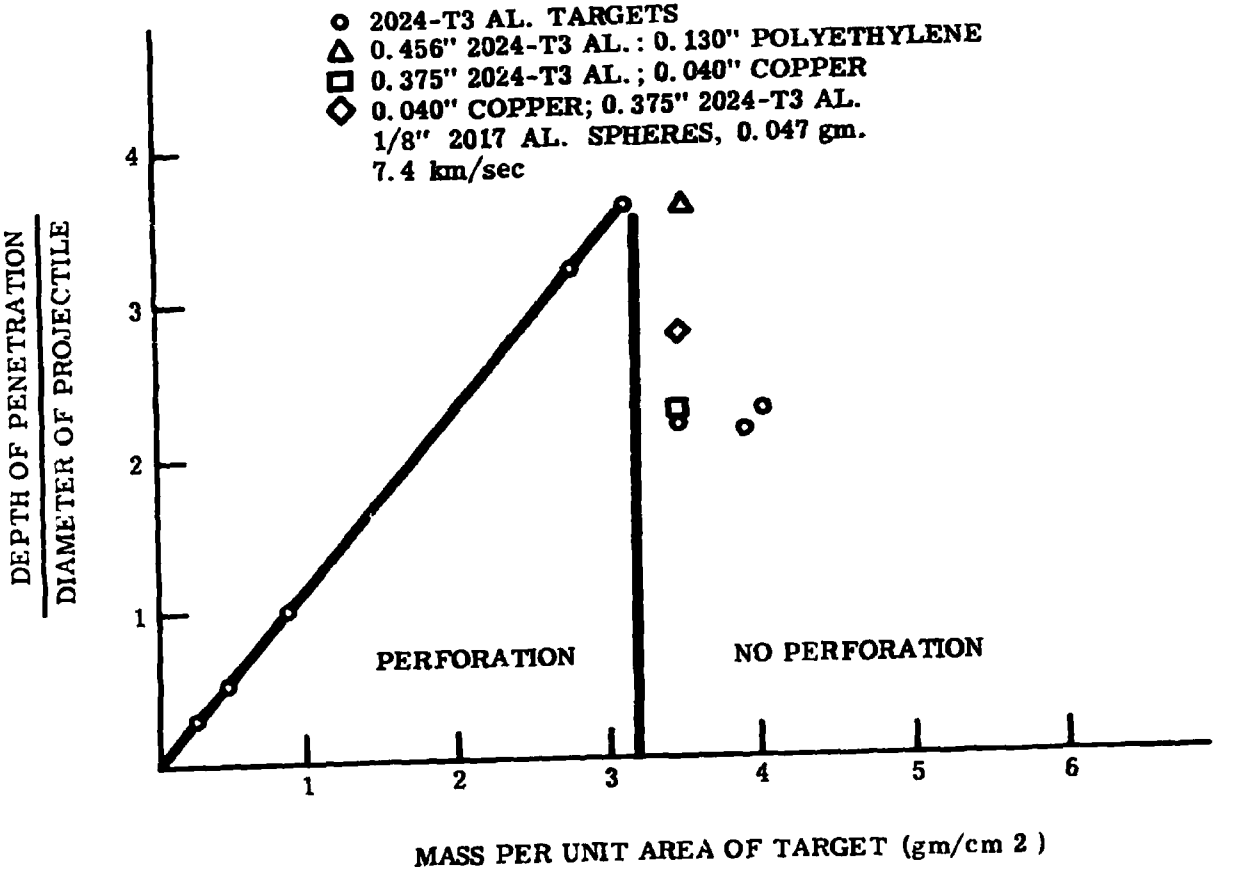

Figure 8 Depth of Penetration vs. Weight of Target, for Flat Laminates

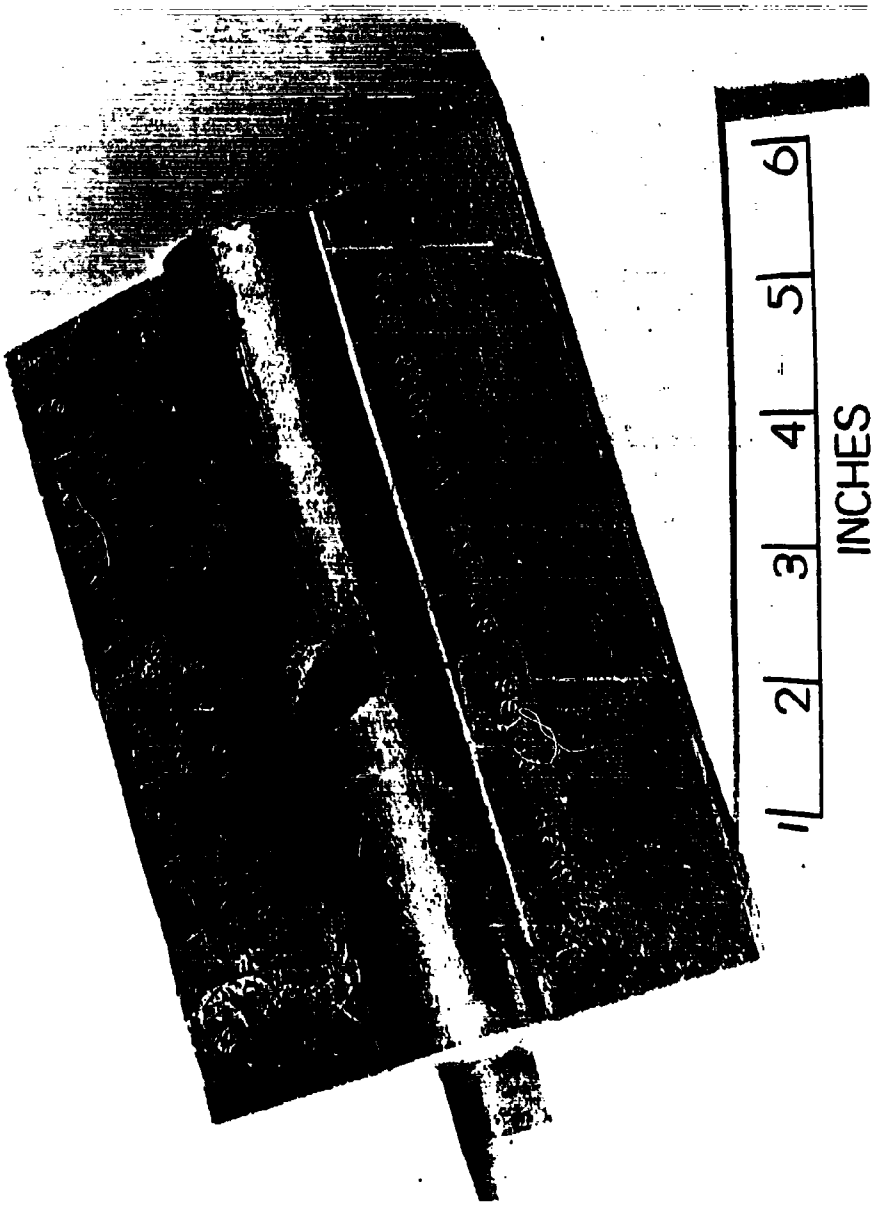

Figure 9 Impact Crater in Typical Radiator Section

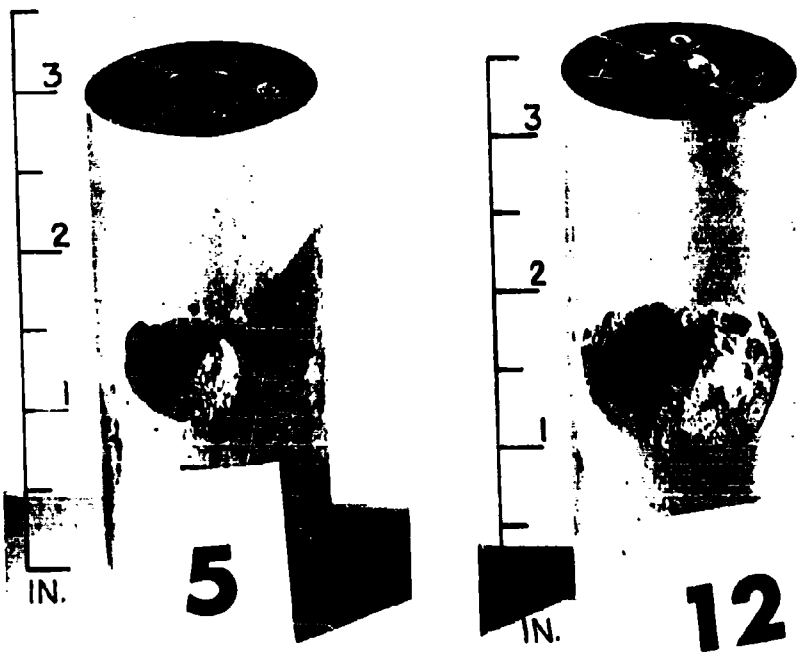

3/32" GLASS SPHERE
NO PERFORATION
PENETRATION = 0.31"

1/8" GLASS SPHERE
PERFORATED

$\overline{V}$ = 7.08 km/sec
715°F

Figure 10 Projectile Size Effects, Aluminum with HS-25 Liner Targets

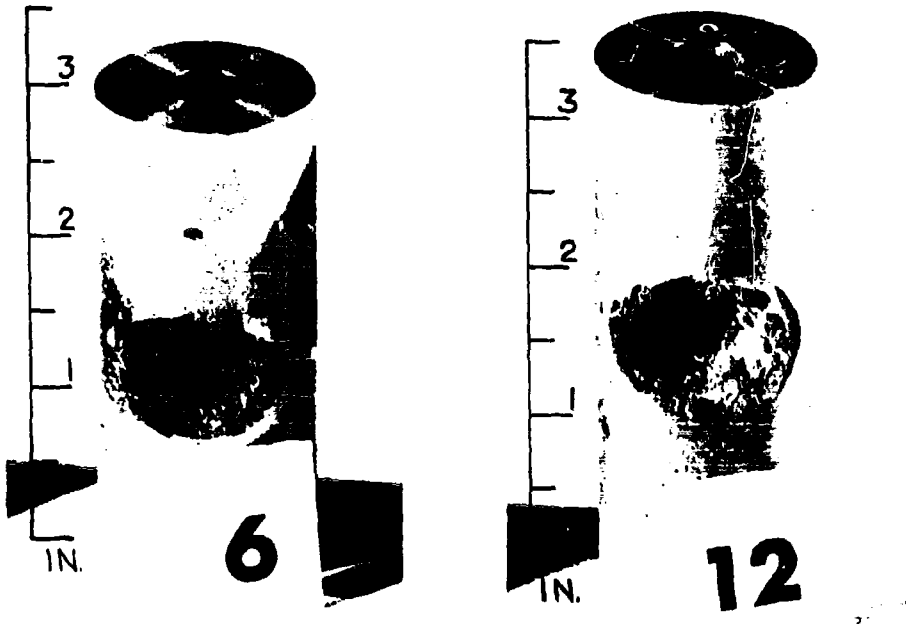

ROOM TEMPERATURE
BHN 53
PERFORATED

700°F
BHN=20
PERFORATED

1/8" GLASS SPHERE
$\overline{V}$ = 7.10 km/sec

Figure 11 Target Temperature Effects, Aluminum with HS-25 Liner Targets

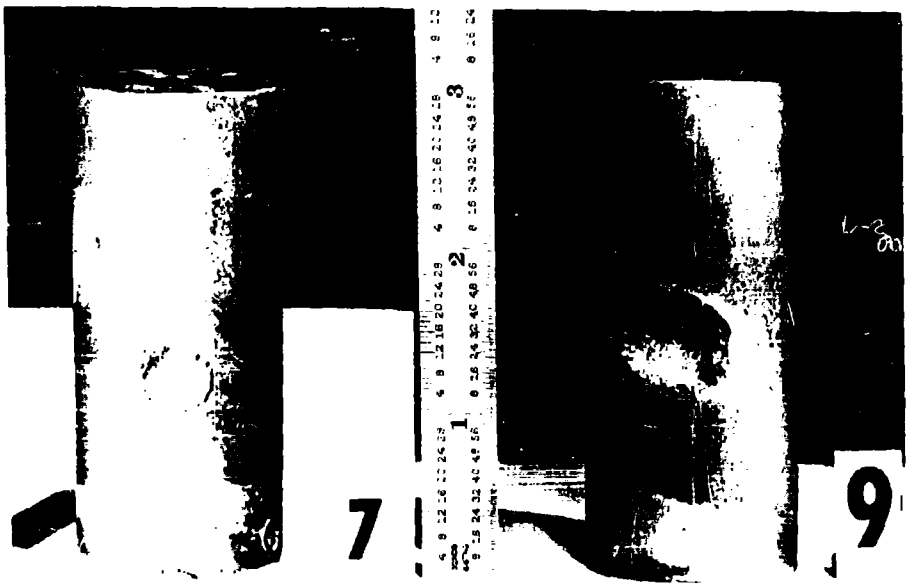

68° FROM CENTER
NO PERFORATION
PENETRATION; 0.13"

15° FROM CENTER
NO PERFORATION
PENETRATION; 0.34"

3/32" GLASS SPHERE
$\bar{V}$ = 7.44 km/sec
700°F

Figure 12 Impact Angle Effects, Aluminum with HS-25 Liner Targets

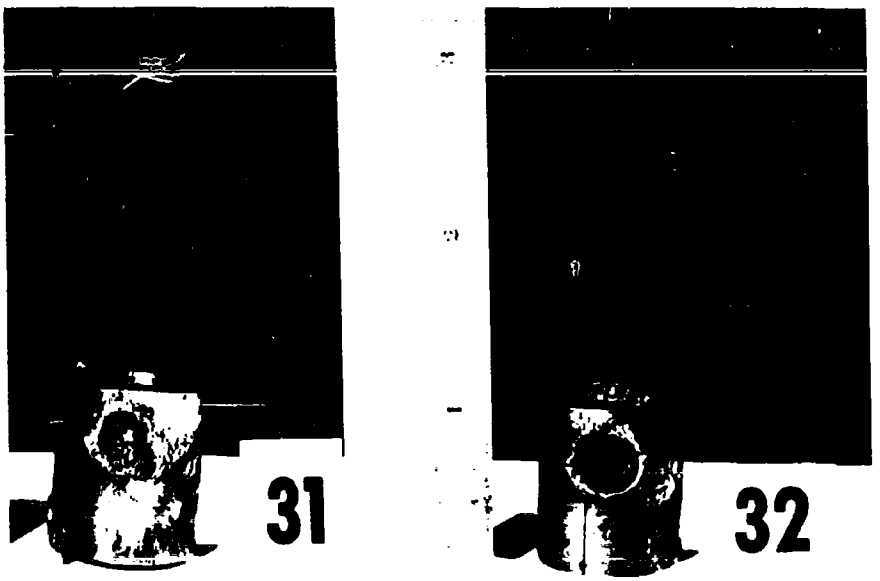

40° FROM CENTER
NO PERFORATION

12° FROM CENTER
PERFORATED

3/32" GLASS SPHERE

$\overline{V}$ = 7.81 km/sec

700°F

Figure 13 Impact Angle Effects, Columbium Targets - No Liner

PENETRATION INTO COMPOSITE LAMINATES

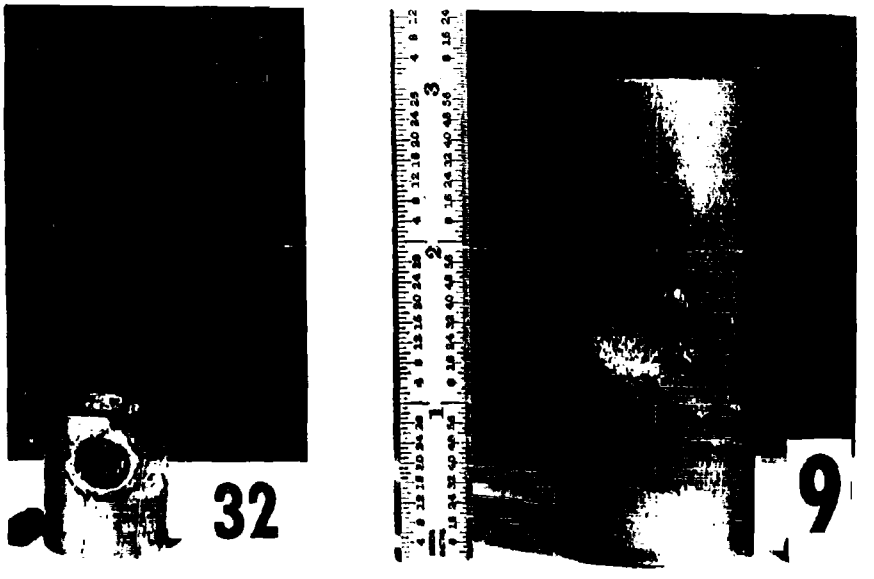

200" COLUMBIUM
PERFORATED

400" AL. ARMOR, HS-25 LINER
NO PERFORATION

3/32" GLASS SPHERE
$\overline{V}$ = 7.56 km/sec
700°F

(APPROXIMATELY EQUAL WEIGHT
PER UNIT LENGTH OF RADIATOR)

Figure 14 Target Material Effects

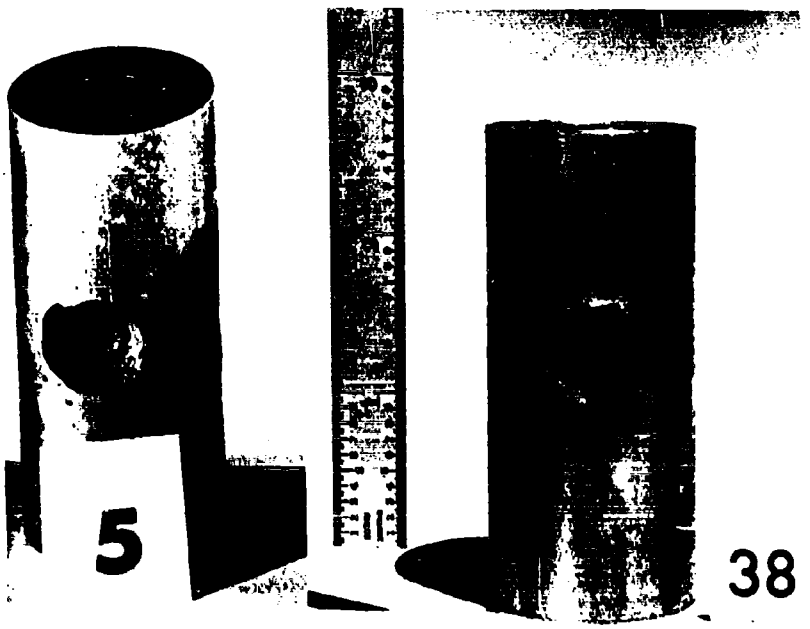

0.40" Al. ARMOR 0.02" HS-25 LINER
NO SPALL ON INSIDE
NO PERFORATION

0.47" Al. ARMOR, NO LINER
SPALL ON INSIDE
NO PERFORATION

3/32" GLASS SPHERE
$\overline{V}$ = 7.50 km/sec
715°F

Figure 16 Liner Effects, Aluminum Targets

PENETRATION INTO COMPOSITE LAMINATES

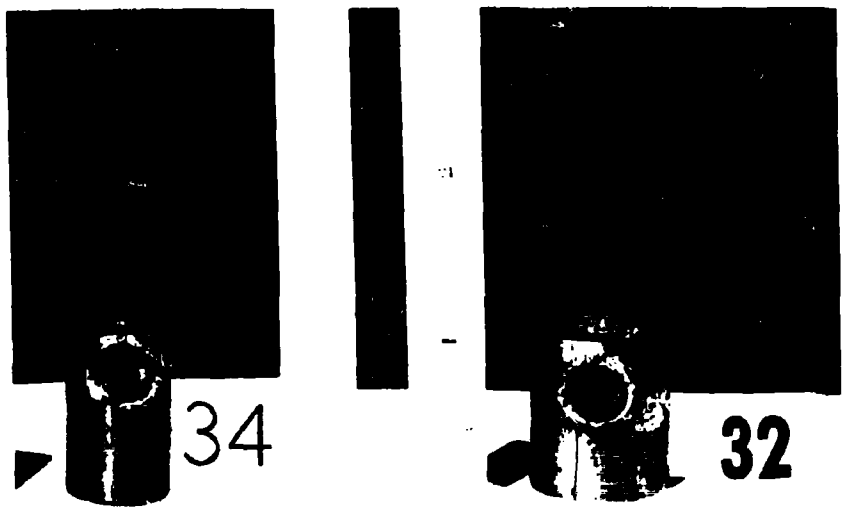

0.25" THICK WALL 0.12" ID
NO PERFORATION

0.20" THICK WALL 0.47" ID
PERFORATED

3/32" GLASS SPHERE

$\bar{V}$ = 7.37 km/sec

700°F

Figure 15 Armor Thickness Effects, Columbium Targets

PENETRATION INTO COMPOSITE LAMINATES

ALL COLUMBIUM 0.20" THICK WALL
NO PERFORATION
3/32" GLASS SPHERE

0.40" AL. ARMOR, 0.02" HS-25 LINER
NO PERFORATION
1/8" GLASS SPHERE

$\overline{V}$ = 7.52 km/sec
700°F

(APPROXIMATELY EQUAL WEIGHT
PER UNIT LENGTH OF RADIATOR)

Figure 17 Internal Tube Damage

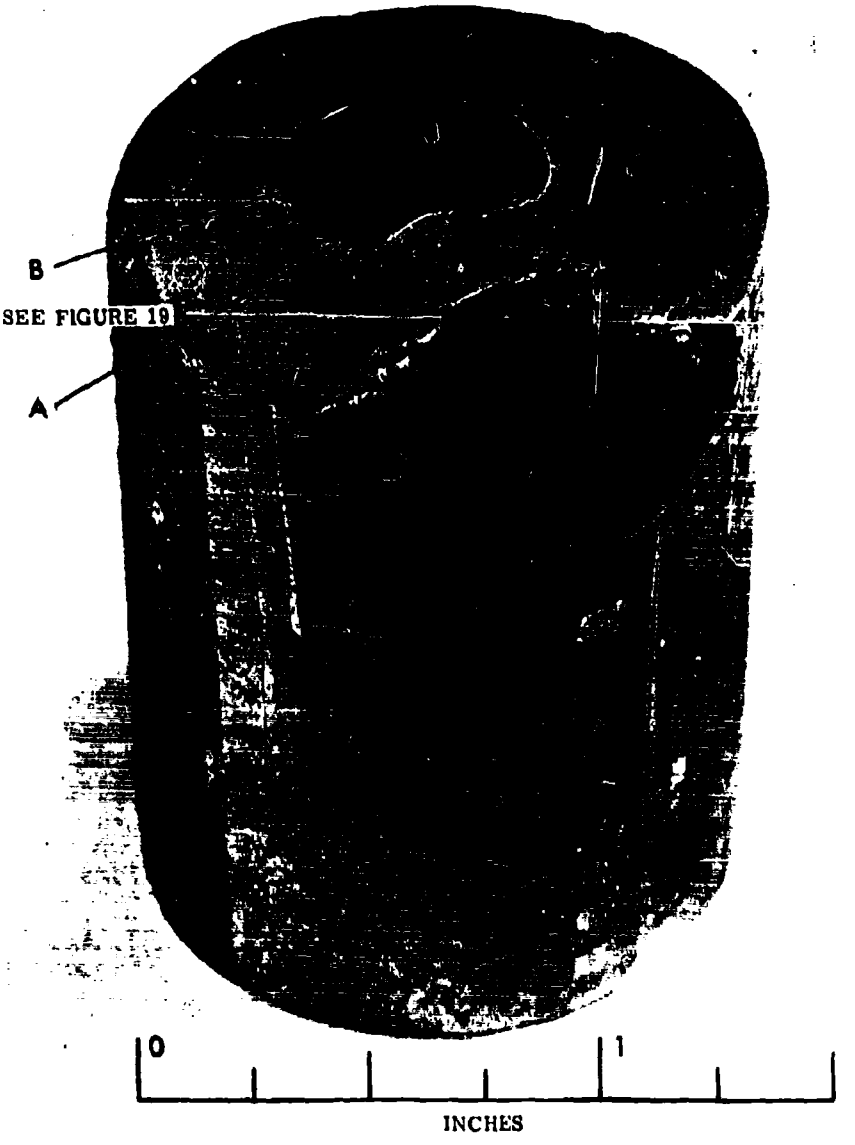

Figure 18 Typical Impact Crater Section, Aluminum with HS-25 Liner Target

SECTION B (300X)

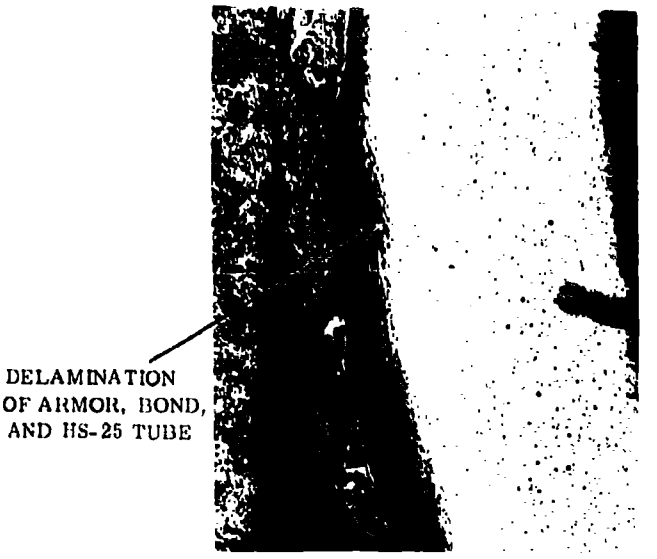

SECTION A (120X)

Figure 19 Armor-Liner Interface Photomicrographs, Ref. Figure 18.

METEOROID EFFECTS ON NUCLEAR ROCKET SPACE VEHICLE MISSION SUCCESS

by

William H. Sterbentz

Loren L. Long

METEROID EFFECTS ON SPACE VEHICLES

ABSTRACT

The results of an analysis of the effects of meteoroids on nuclear-rocket vehicles for three missions are presented. The probability of failure to complete a lunar mission is negligible for an unprotected nuclear rocket wherein the nuclear stage is used only to accelerate the payload spacecraft to the desired earth-lunar transfer velocity. However, if such an unprotected nuclear rocket is also used to retro fire the payload into lunar orbit, there is a 2% probability of failure to successfully complete the mission.

In the case of the nuclear orbital transfer vehicle, the unprotected vehicle probability of failure due to meteoroid damage for a single 15-day mission is about 10% with a virtual certainty to fail to achieve a desired lifetime of 30 to 50 missions. A shield of 0.02-inch aluminum around the liquid hydrogen propellant tank reduces the probability of failure to less than 0.5% for a single mission for both the lunar and orbital vehicles. However, the shield thickness should be increased to about 0.20 inch for the orbital transfer vehicle and results in maximum vehicle lifetime payload. It is further evident that a meteoroid shield of such thickness and large weight should be integrated into the tank design to provide solar thermal radiation insulation to reduce propellant boiloff and to increase structural stiffness.

METEROID EFFECTS ON SPACE VEHICLES

INTRODUCTION

Nuclear rocket propelled space vehicles will be operational about the turn of this decade. Because of the marked superiority of nuclear rocket performance to that of chemical rockets, mission flight plans in many applications may be expected to be quite different from those of present, more conventional, chemical rocket systems. For example, the nuclear rocket used as the third-stage of a boost vehicle from earth can also be used very effectively to retro fire a payload vehicle into a lunar orbit. Thus, the very large nuclear rocket liquid-hydrogen propellant tank and engine are transported to lunar orbit and the danger of meteoroid damage to the system becomes of concern.

Several factors govern the need for and design of meteoroid shielding for space vehicles. The first factor, already mentioned, is the mission; and this factor is particularly significant with nuclear rocket vehicles because of their large size and, in some cases, long time exposure to meteoroids. Three fundamentally different nuclear rocket missions will be used to illustrate this significant mission effect. The second factor involves knowledge of meteoroid population in space, meteoroid capability of penetrating space vehicle structures, and the criticality of any penetrations to the successful completion of the mission. The third factor concerns the cost of meteoroid protection, in terms of reduced payload, to increase the probability of mission success. The second and third factors will be analyzed for the three nuclear rocket missions and will result in certain fundamental definitions of meteoroid shielding design and mandatory meteoroid penetration technology requirements.

SYMBOLS

The following symbols are used in this paper.

A	area exposed to meteoroid impact
D	pellet diameter
H	Brinell hardness
K_1, K_2	constants
P	probability
p	depth of penetration into a semi-infinite target
t	time
V	velocity
δ	thin plate thickness
ρ	density
ϕ	meteor flux above an indicated meteoroid mass

Subscripts

C	component
C_1, C_2, etc	component (1), component (2), etc.
C_N	component (N)
D	damage
F	failure
o	equivalent unprotected thin-plate target
P	penetration
S	strike
Sh	shield
T	target
v	vehicle

METEROID EFFECTS ON SPACE VEHICLES

NUCLEAR ROCKET MISSIONS

The nuclear rocket is basically a very large vehicle even when applied as the third-stage of a space vehicle. For example, a 4000-megawatt nuclear rocket engine applied as the third-stage propulsion system on an Advanced Saturn V class launch vehicle would properly be matched to a 250,000-pound liquid hydrogen propellant tank. Such a possible space vehicle is shown in Figure 1. This nuclear rocket vehicle consists of a nuclear-powered third stage employing a nominal 4000-megawatt nuclear rocket engine boosted to near earth orbit by the chemical first two-stages of the Saturn V/N rocket vehicle. The chemical stages are the S-IC first stage and the S-II second stage. The complete space vehicle stands 386 feet high exclusive of the payload abort system and is 33 feet in diameter. The nuclear stage and payload section is about 165 feet long.

Three missions will be used to illustrate the effect of mission flight plan on meteoroid shield design requirements. The first and second missions considered, manned lunar missions, are shown in Figure 2. In both cases, the nuclear rocket stage and payload are boosted into low earth orbit of about 100-nautical mile altitude by the first- and second-stage chemical rockets of the Saturn V/N. After an appropriate system check-out accomplished in earth orbit, the nuclear rocket engine is fired until the proper earth-lunar transfer velocity is achieved. At this point, one of two mission flight plans may be adopted. The first case involves separation of the manned payload from the nuclear stage upon achieving the earth-lunar transfer velocity. In this case, the nuclear-stage propellant has been exhausted and the spent stage will enter a solar orbit and the manned payload vehicle will complete the lunar mission without further need of the nuclear rocket.

The live nuclear stage in this mission would have been exposed to the meteoroid hazard for about 4 to 5 hours.

TYPICAL OPERATIONAL CONFIGURATION

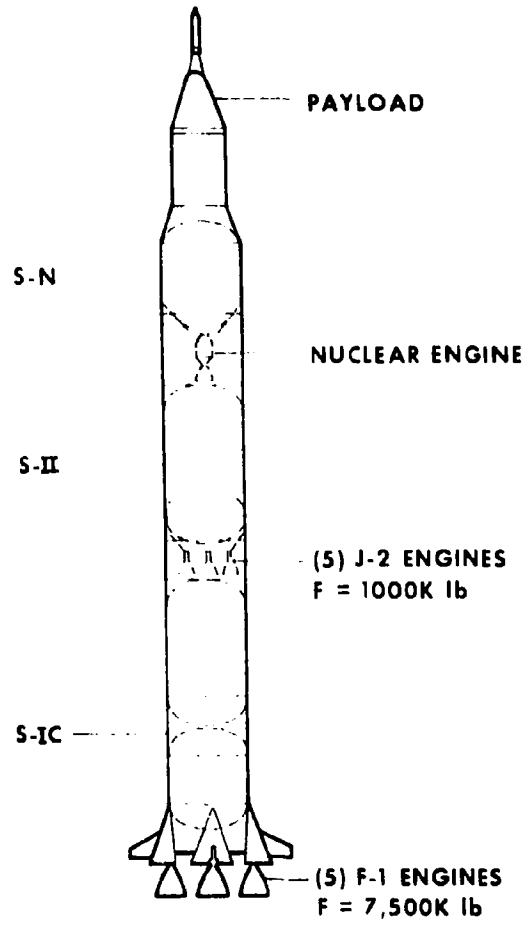

Figure 1

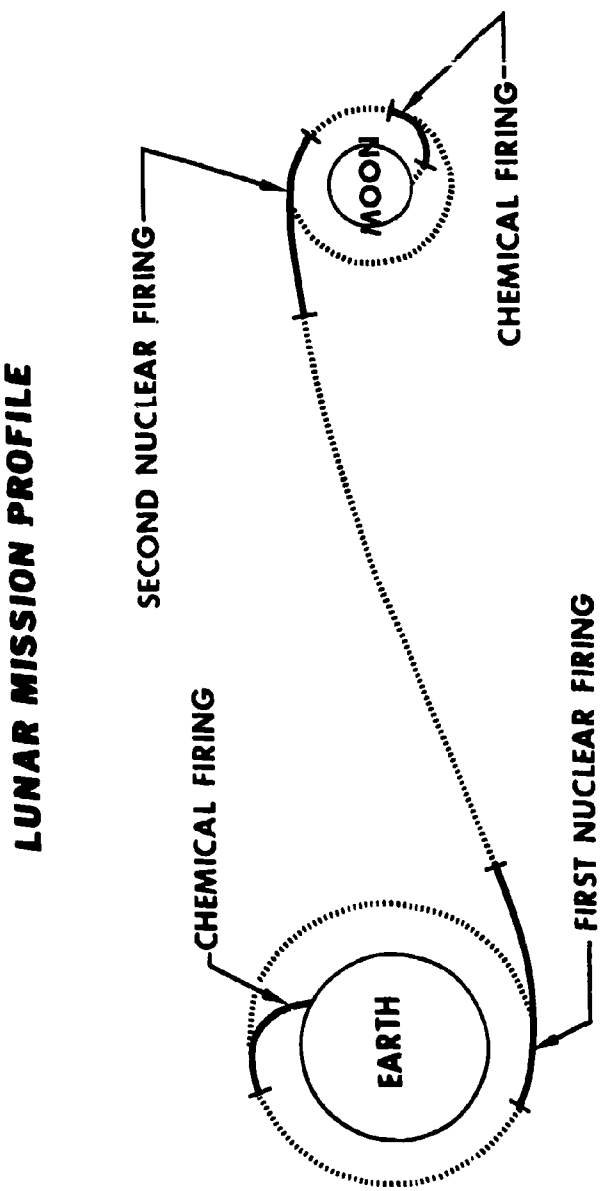
LUNAR MISSION PROFILE
SECOND NUCLEAR FIRING
CHEMICAL FIRING
MOON
CHEMICAL FIRING
CHEMICAL FIRING
EARTH
FIRST NUCLEAR FIRING

Figure 2

In the second lunar mission, the nuclear stage contains sufficient remaining propellant to retro fire the nuclear stage and payload into an appropriate lunar orbit. Thus, upon achieving the desired earth-lunar transfer velocity, the nuclear rocket engine is shut down after an appropriate engine cooldown cycle has been completed. The nuclear rocket stage and payload will then proceed to the moon in a 60- to 70-hour transfer flight time. Upon arriving at the moon, the nuclear stage is restarted to retro-fire the nuclear stage and payload into an appropriate lunar orbit. The payload section is then separated from the nuclear stage and completes the manned-lunar-landing mission with chemical propulsion systems. The nuclear stage is no longer used for the mission after this point in time and may be either left in orbit about the moon or may be restarted and fired into a solar orbit for final disposal.

Figure 3 shows the nuclear rocket and payload as it would appear in earth orbit just prior to firing into the earth-lunar transfer trajectory. Figure 4 shows the nuclear rocket and payload in orbit about the moon. The nuclear rocket engine is in an after-cooling condition, the stage retrorockets are firing, and the payload chemical propulsion system has been fired and separated from the nuclear stage for the final landing approach.

From Figures 3 and 4, it is apparent that the propellant tank of the nuclear rocket stage presents by far the largest exposed area to meteoroid impact. The nuclear rocket engine and other accessories, for example the attitude control system, are relatively small. In addition, a major portion of the exposed area of the nuclear rocket engine consists of relatively thick materials difficult for most meteoroids to penetrate.

The third mission to be considered for the nuclear rocket space vehicle is the orbital transfer mission shown in Figure 5. The vehicle would be similar to that shown in Figure 3. The purpose of the orbital transfer vehicle is to provide an efficient method for transferring large payloads from one earth orbit to another. The nuclear orbital transfer vehicle after being initially placed in a parking orbit would be fueled and

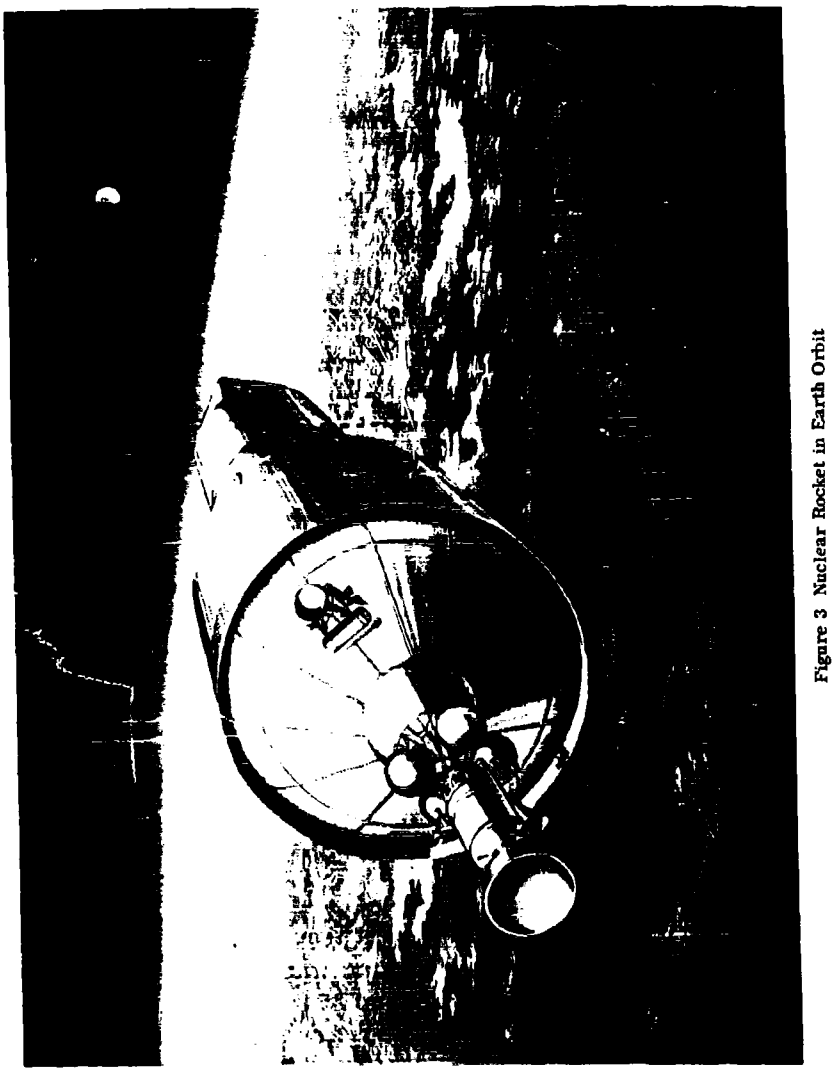

Figure 3 Nuclear Rocket in Earth Orbit

Figure 4 Nuclear Rocket in Lunar Orbit

ORBITAL TRANSFER VEHICLE
Mission Profile
THIRD NUCLEAR FIRING
FIRST NUCLEAR FIRING
CHEMICAL FIRING AND RENDEZVOUS
FOURTH NUCLEAR FIRING
SECOND NUCLEAR FIRING

provided with payload by means of a chemical launch system. The chemical launch system would boost a propellant tanker into orbit and rendezvoused with the orbital transfer vehicle. Similarly, a payload section would be launched and rendezvous with the orbital transfer vehicle. The nuclear orbital transfer vehicle would be used to transfer the payload to a higher altitude orbit in the same or an inclined plane to the parking orbit. Because of the very high specific impulse of the nuclear rocket engine, payloads can be more efficiently transported to orbit by this technique than by other techniques or by chemical rocket vehicles. The nuclear orbital transfer vehicle after placing the payload in the appropriate orbit, which might be a manned orbiting space station, for example, would return to the parking orbit either with an earth return payload or to pick up a new payload and propellant at a later time. Such a vehicle would make from 30 to 50 missions during its lifetime. Considering that a single mission would take from 5 to 15 days to complete, the vehicle would be exposed to meteoroid impact and damage for a year or more. Thus, we have three basically different nuclear rocket space vehicle missions: one a single 1 to 5-hour use of the nuclear rocket; one a single 3-day use of the nuclear rocket, and the other a large number of single missions and a vehicle lifetime span of approximately one year or more. These missions will be used to illustrate mission effects on the meteoriod shielding problem.

PROBABILITY OF VEHICLE FAILURE

Increasing the protection for a nuclear rocket vehicle to meteoroid damage for either of the lunar missions will result in increased probability of successfully completing the mission. This increased reliability, however, is obtained at the cost of decreasing payload as a result of the increased stage inert weight through provision of a meteoroid shield. The orbital transfer vehicle, on the other hand, must consider not only single mission payload costs, but also the lifetime mission payload cost. Increasing protection of this vehicle against meteoroid damage results not only in increasing single mission reliability, but also increases the probable vehicle lifetime. Thus, increasing meteoroid protection decreases the single mission payload as it does for the lunar mission vehicles, but at the same time will increase the vehicle

lifetime payload. To obtain specific values of payload costs for increased reliability, a systematic technique for evaluating the probability of failure of a vehicle due to meteoroid damage must be applied.

The technique employed consists basically of determining the probability of vehicle failure due to meteoroid damage as given by Eq. (1). The probability of vehicle failure is simply the sum of the failure probabilities of individual components which make up the complete vehicle.

$$P_{VF} = P_{C_1F} + P_{C_2F} + P_{C_3F} + \ldots + P_{C_NF} \tag{1}$$

The probability of component failure due to meteoroid damage is given in Eq. (2) and, it is the product of the probability of a meteoroid striking a component, the probability of a meteoroid penetrating a component, and the probability of a meteoroid having struck and penetrated a component to cause the vehicle to fail to complete its mission.

$$P_{C_NF} = \left(P_S P_P P_D\right)_{C_N} \tag{2}$$

Probability of Striking

Consider first the question of the probability of a meteoroid to strike any particular component of the nuclear rocket vehicle. Shown in Figure 6 is a nuclear rocket vehicle in earth orbit. In this study, it was assumed that the variation in meteoroid flux, velocity, and mass with respect to orientation of the vehicle is negligible. Under these conditions, the probability of the meteoroid to strike any component of the nuclear rocket vehicle can be given by Eq. (3).

$$P_S = 1 - e^{-\phi A_C t} \tag{3}$$

PROBABILITY TO STRIKE

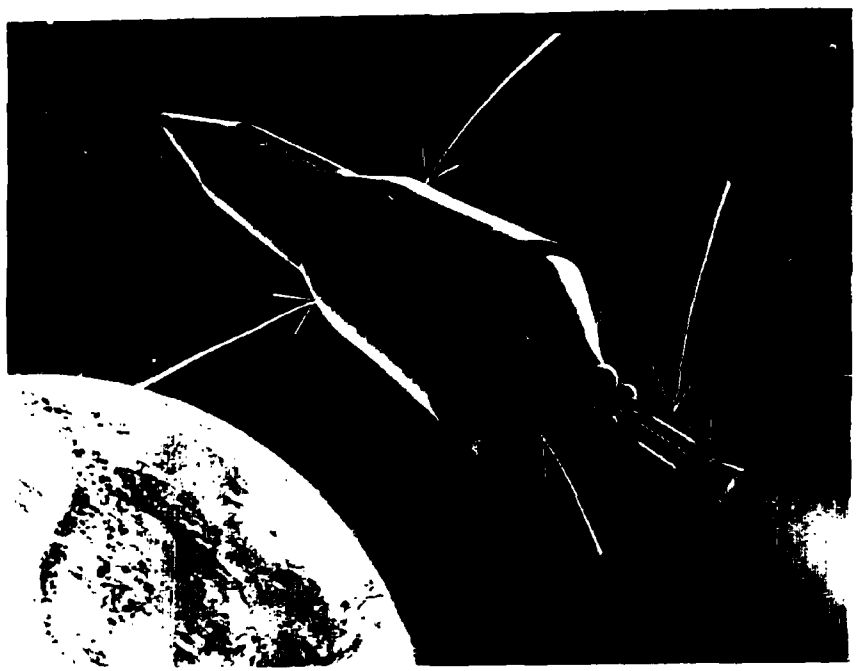

$$(P_S)_{C_n} = 1 - e^{-\phi A_C t}$$

Figure 6

Equation (3) shows that the probability to strike a component is a function of the meteoroid flux, the area of the component exposed to meteoroids, and the time for which the component is exposed.

Meteoroid flux has been measured in experiments of various Explorer and Vanguard satellites, particularly in the micrometeoroid range. The larger and heavier meteoroids have been measured by photographic and radar techniques. Figure 7 shows these data and Dalton's (Ref. 1) empirical correlation of these data. These values of meteoroid flux have been used in this analytical study. The exposed area of each component is, of course, given from nuclear rocket vehicle design. The time of exposure to meteoroid impact is a function of the mission flight plan.

Probability of Penetrating

The probability of penetrating any component that has been struck by a meteoroid has been estimated for the technology available on hypervelocity impact phenomena. The probability of penetrating a component that has been struck by a meteoroid will be either zero or unity, depending upon whether the meteoriod has or has not penetrated the component.

Figure 8 presents the Herrmann and Jones correlation (Ref. 2) relating pellet penetration into a semi-infinite target as a function of the pellet impact velocity. The Herrmann and Jones equation is given by Eq. (4)

$$\frac{p}{D} = K_1 \ln \left[1 + \frac{\rho_T V^2}{K_2 H_T} \right] \tag{4}$$

Two correlations with experimental data obtained at the NASA (Ref. 3) are shown. These experimental data were obtained with various diameter (1/16 to 3/16 inch) copper pellets impacting aluminum and steel targets. The Herrmann and Jones equations correllate reasonably well with lower velocity experimental data and the higher velocity theoretical predictions of Bjork (Ref. 4).

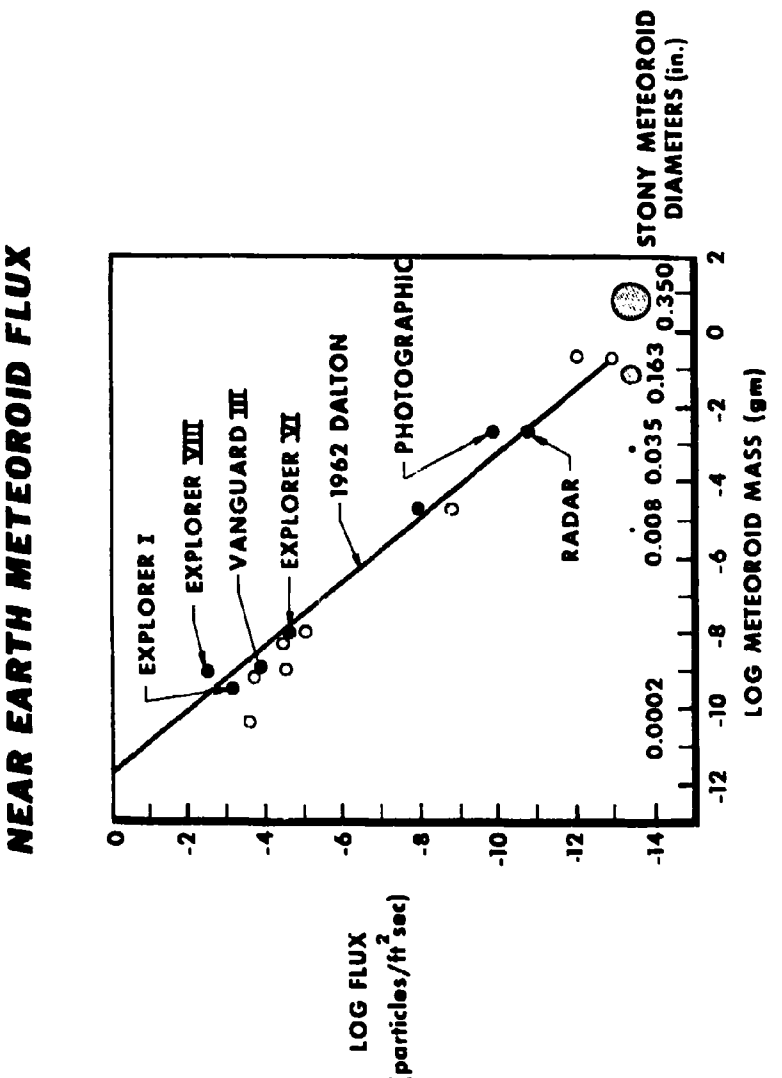
NEAR EARTH METEOROID FLUX
EXPLORER I
EXPLORER VIII
VANGUARD III
EXPLORER XI
1962 DALTON
PHOTOGRAPHIC
RADAR
STONY METEOROID DIAMETERS (in.)
0.0002
0.008
0.035
0.163
0.350
LOG METEOROID MASS (gm)
LOG FLUX (particles/ft² sec)
0
-2
-4
-6
-8
-10
-12
-14
-12
-10
-8
-6
-4
-2
0
2

Figure 7

CORRELATION OF THICK TARGET DATA AND THEORY

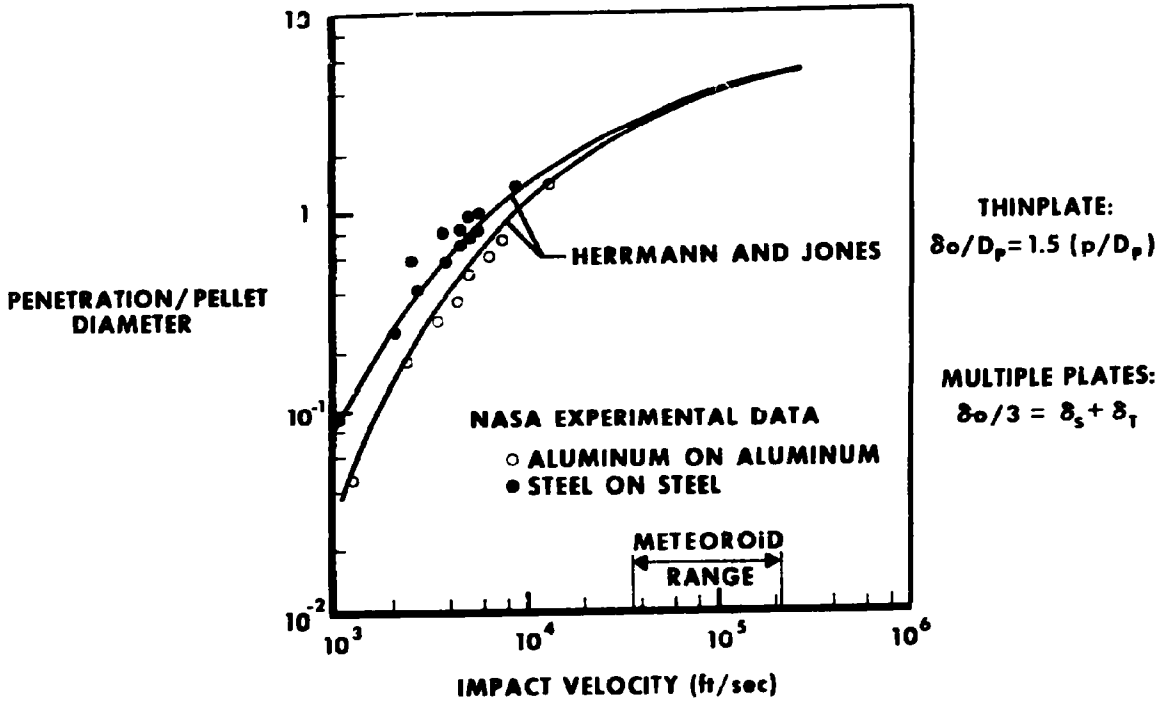

Figure 8

The Herrmann and Jones equation as given by Eq. (4) was used as a fundamental expression for predicting the depth of penetration of a meteoroid impacting a space vehicle. However, impacting meteoroids which would penetrate a component of a nuclear rocket space vehicle require the application of thin-plate and multiple-plate penetration technology. In this respect, the equations of Herrmann and Jones are modified in accordance with Eqs. (5) and (6) which relate semi-infinite target data and theory to thin plate and multiple plate penetrations. These correlations were suggested by Bjork (Ref. 4), Kinard et al. (Ref. 5), and Humes et al. Ref (6).

$$\frac{\delta_o}{D} = 1.5\left(\frac{p}{D}\right) \tag{5}$$

$$\frac{\delta_o}{3} = \delta_{Sh} + \delta_T \tag{6}$$

Figure 9 shows the penetration depth as a function of pellet velocity of copper pellets on an aluminum semi-infinite target, both with and without a thin aluminum meteoriod shield. As can be seen, imposing a meteoroid shield between the impacting pellet and the target significantly reduces the total penetration. The Herrmann and Jones equation prediction is shown by the solid line curve for the semi-infinite target data, but in this case indicates about a 20% discrepancy with experimental data. Application of the thin plate and multiple plate penetration correlation [Eqs. (5) and (6)] to the Herrmann and Jones Eq. (4) yields the second curve shown on Figure 9. The relative magnitude of the predicted effects of interposing a thin aluminum shield are about the same as the experimentally observed effects. However, the predictions are still about 20% too low in the range up to 22,000 feet per second. In this study, experimental data, where available, were used in conjunction with the Herrmann and Jones equations, and the Herrmann and Jones equations were used independently where experimental data were lacking.

The penetration phenomena requires the knowledge of meteoroid velocity. Reference 1 presents an analysis of available meteoriod velocity data as a function of meteoroid

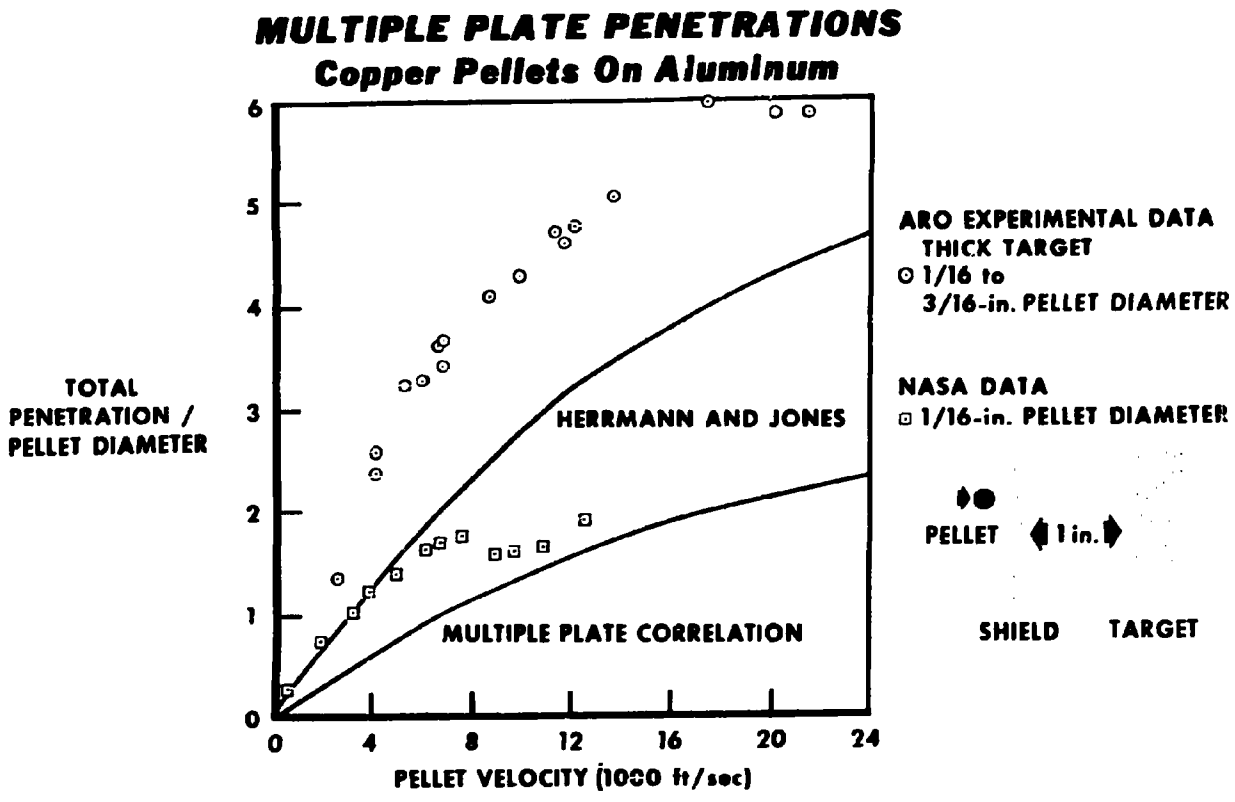
MULTIPLE PLATE PENETRATIONS
Copper Pellets On Aluminum
TOTAL PENETRATION / PELLET DIAMETER
0
1
2
3
4
5
6
0
4
8
12
16
20
24
PELLET VELOCITY (1000 ft/sec)
HERRMANN AND JONES
MULTIPLE PLATE CORRELATION
ARO EXPERIMENTAL DATA
THICK TARGET
1/16 to
3/16-in. PELLET DIAMETER
NASA DATA
1/16-in. PELLET DIAMETER
PELLET
1 in.
SHIELD
TARGET

Figure 9

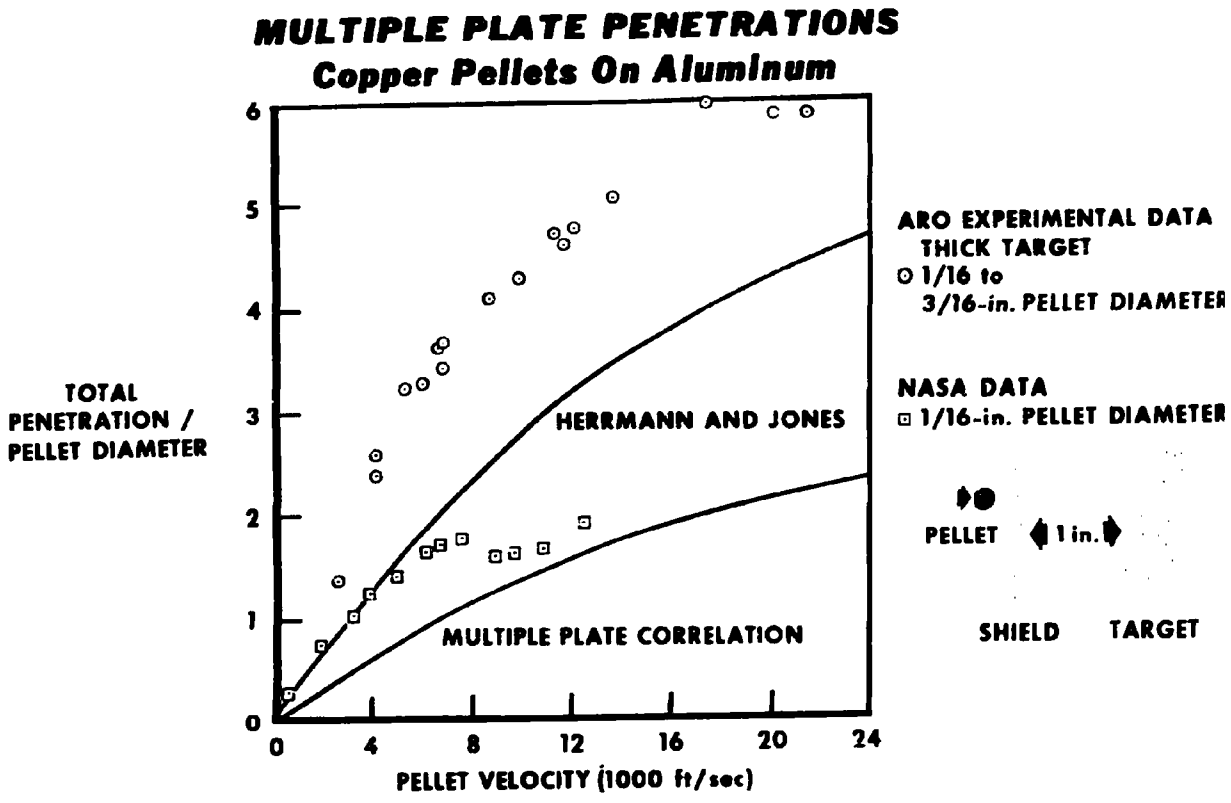
MULTIPLE PLATE PENETRATIONS
Copper Pellets On Aluminum
TOTAL PENETRATION / PELLET DIAMETER
0
1
2
3
4
5
6
0
4
8
12
16
20
24
PELLET VELOCITY (1000 ft/sec)
HERRMANN AND JONES
MULTIPLE PLATE CORRELATION
ARO EXPERIMENTAL DATA
THICK TARGET
1/16 to 3/16-in. PELLET DIAMETER
NASA DATA
1/16-in. PELLET DIAMETER
PELLET
1 in.
SHIELD
TARGET

Figure 9

mass, indicating a cursory correlation between meteoroid velocity and mass. This correlation is presented in Figure 10 and was used in this study.

Probability of Critical Damage

The last probability factor required is that of determining the criticality of component failure due to meteoroid penetration on the vehicle mission success. This was determined from an engineering failure mode analysis. The procedure is schematically illustrated in Figure 11, which shows a nuclear rocket vehicle and payload. The nuclear rocket vehicle has been broken into component areas of various criticality to mission success. Certain areas, such as the aft stage skirt and portions of the interstage area between the propellant tank and the payload, are not critical to meteoroid damage. Other areas, such as the nuclear rocket engine, attitude control system, and pressurization tanks, are extremely critical to the success of the mission should they be penetrated by a meteoroid. The propellant tank itself, because of its extremely large area, is actually the governing component to the success of the mission. The propellant tank consists of two volumes, one being the ullage space and the other containing the propellant. Should the meteoroid penetrate the tank below the liquid level, data from Ref. 7 indicates a high probability of tank rupture. Should the meteoroid penetrate the ullage space, on the other hand, a simple penetration would likely occur and, depending upon the size hole and the time at which the penetration occurred, may or may not cause the mission failure. These data and techniques were applied to the vehicles shown in Figures 4 and 5 and the missions shown in Figures 3 and 5.

PROBABILITY OF FAILURE AND PAYLOAD COSTS

Figure 12 shows a cut away of the liquid hydrogen propellant tank and reveals its basic design. The tank consists of an aluminum wall approximately 0.250 inch thick, to which is bonded an internal foam insulation about 1.5 inches thick, and a hydrogen vapor varrier. Longitudinal stiffeners spaced about 9 inches apart, externally

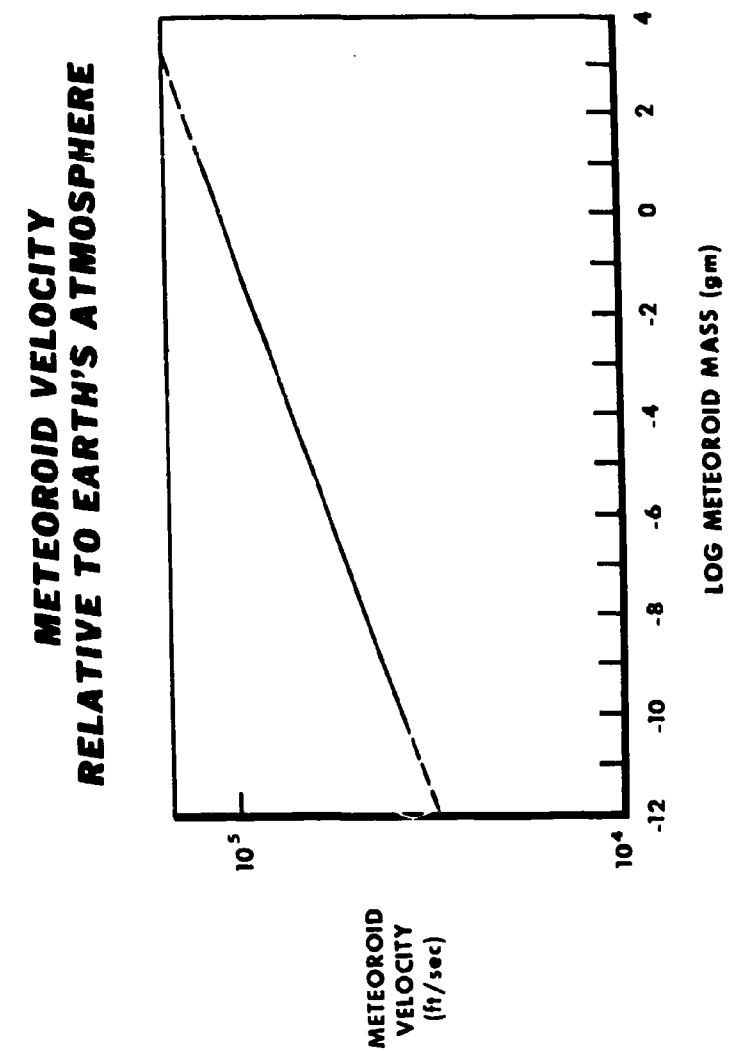
METEOROID VELOCITY
RELATIVE TO EARTH'S ATMOSPHERE
METEOROID VELOCITY (ft/sec)
10^5
10^4
-12
-10
-8
-6
-4
-2
0
2
4
LOG METEOROID MASS (gm)

Figure 10

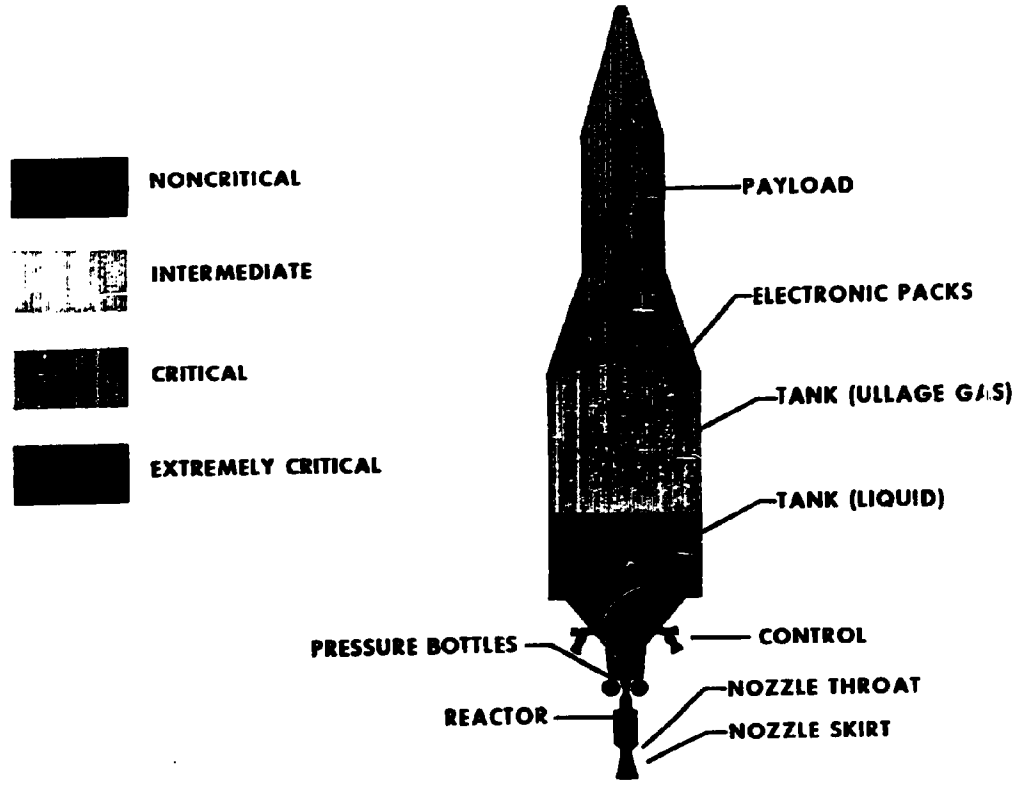
CRITICALITY OF COMPONENT FAILURE
NONCRITICAL
INTERMEDIATE
CRITICAL
EXTREMELY CRITICAL
PAYLOAD
ELECTRONIC PACKS
TANK (ULLAGE GAS)
TANK (LIQUID)
CONTROL
PRESSURE BOTTLES
NOZZLE THROAT
REACTOR
NOZZLE SKIRT

Figure 11

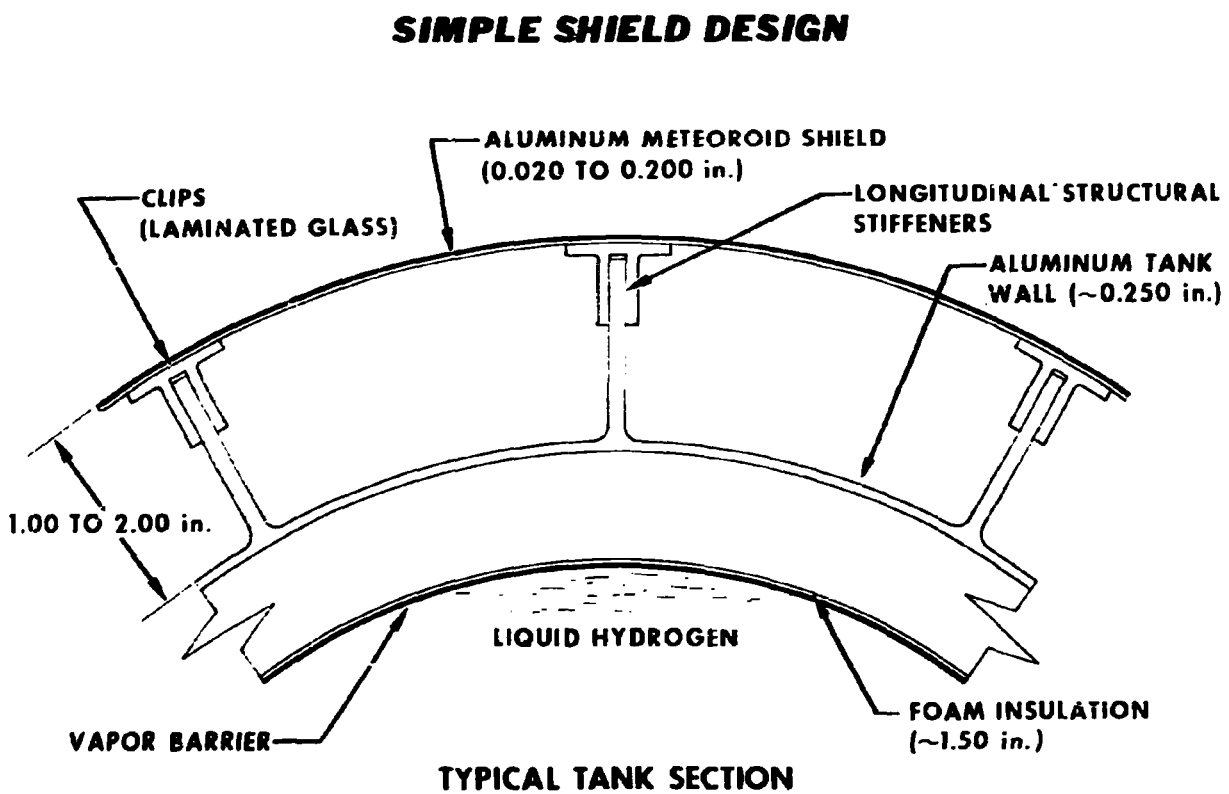
SIMPLE SHIELD DESIGN
ALUMINUM METEOROID SHIELD
(0.020 TO 0.200 in.)
CLIPS
(LAMINATED GLASS)
LONGITUDINAL STRUCTURAL
STIFFENERS
ALUMINUM TANK
WALL (~0.250 in.)
1.00 TO 2.00 in.
LIQUID HYDROGEN
VAPOR BARRIER
FOAM INSULATION
(~1.50 in.)
TYPICAL TANK SECTION

Figure 12

around the tank, complete the outside contour of the tank wall. Meteoroid shields of varying thicknesses from 0.02 to 0.2 inch were applied to the exterior of the tank and attached to the longitudinal stiffeners. The results of the investigation are shown in Figures 13 and 14.

Figure 13 shows the probability of failure of the nuclear vehicle on a lunar or orbital transfer mission by meteoroid damage. The results of the study revealed that when an unprotected nuclear stage is disposed of upon achieving the desired earth-lunar transfer velocity at earth departure (4- to 5-hour nuclear stage exposure to meteoroid damage case), the probability of failure to complete the mission due to meteoroid impact on the nuclear stage is negligible. However, an unprotected nuclear rocket vehicle on a 3 day lunar mission has a probability of failure due to meteoroid damage of about 2%. Furthermore, an unprotected orbital transfer vehicle has a single mission probability of failure of 10% by virtue of the fact that this mission is of nominal 15 days duration. The unprotected orbital transfer vehicle is obviously unsuited to the mission requirements as indicated by the rapid increase in probability of failure as the number of missions increases. Application of an aluminum shield of as small as 0.02 inch thick decreases the probability of failure for a single mission to less than 0.5% for both the lunar and orbital transfer vehicles. However, the orbital transfer vehicle should have a reasonable lifetime of approximately 30 to 50 missions. If the probability of failure in this lifetime is to be held to less than 1%, then an aluminum meteoroid shield greater than 0.2 inch thick would be required.

Figure 14 shows the payload cost of such meteoroid protection for a probability of success of 99% for an orbital transfer vehicle. The single mission payload capability of the orbital transfer vehicle is about 200,000 pounds, and if a shield thickness approaching 0.2 inch is used, approximately 20,000 pounds of inert weight would be added and is directly subtractable from the payload. Two significant conclusions can be deduced from this result. One is shown on Figure 14 which presents the vehicle lifetime payload as a function of the number of missions and required shield thicknesses to achieve the probability of success of 99%. It can be seen that the vehicle lifetime payload steadily

PROBABILITY OF FAILURE BY METEOROID DAMAGE

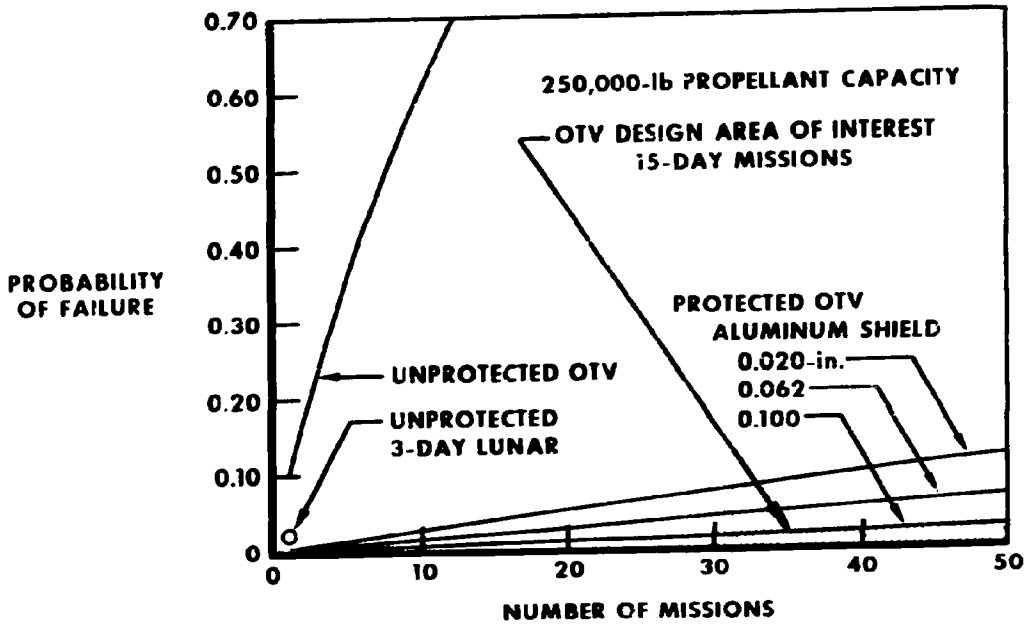

Figure 13

EFFECT ON PAYLOAD

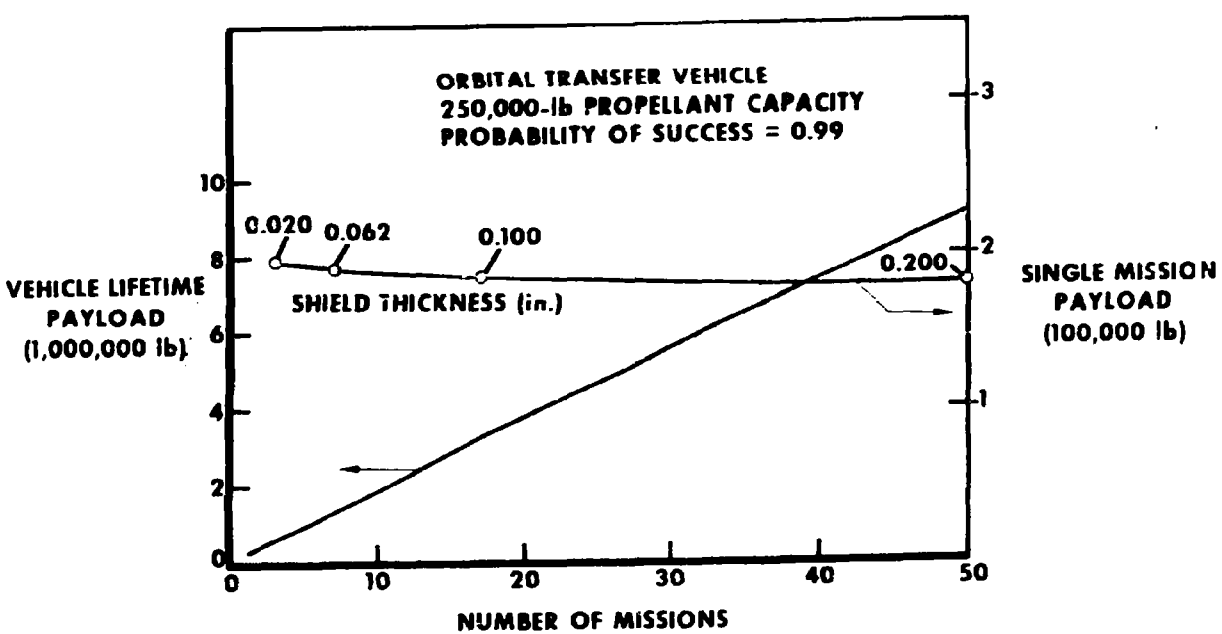

Figure 14

increases with the number of missions in spite of the fact that the single mission payload decreases as the required shield thickness and resulting inert weight increases. The second is that the required meteoroid shield is of such thickness and weight that it can serve a number of functions in addition to providing meteoroid protection to the vehicle. First, the shield itself may be integrated into the vehicle structural design to provide additional structural stiffness to the vehicle. Second, by dividing the meteoroid shield into three or four individual shields significant solar thermal radiation insulation can be obtained, reducing propellant boiloff. A conceptual design incorporating these features is shown in Figure 15. Specific tradeoffs among these various factors are presently being investigated, but indications are clear at this point that the true cost of providing meteoroid protection to space vehicles can be less than that shown in Figure 14.

CONCLUDING REMARKS

The results of the study have indicated a number of important areas of required research in meteoroid shield and penetration phenomena. They are as follows:

1. Data are sketchy regarding the meteoroid characteristics of flux, mass, density, velocity, and distribution. Of particular need are data revealing the characteristics of the heavier meteoroids (10^{-4} grams and heavier).
2. Additional research is required in both theoretical and experimental areas of thin-plate and multiple-plate penetration phenomena, particularly at velocities in excess of 30,000 feet per second.
3. Data are required regarding pellet-penetration of tanks of liquid and gaseous hydrogen revealing the nature of resulting tank rupture. Both the compressibility of liquid and gaseous hydrogen and the extremely low temperature conditions imposed by liquid hydrogen are significant parameters requiring evaluation.
4. Additional detailed design of meteoroid shields which have been integrated into the vehicle structural design must be made, giving recognition to the solar thermal radiation protection and tank structural stiffness available through proper use of meteoroid shielding.

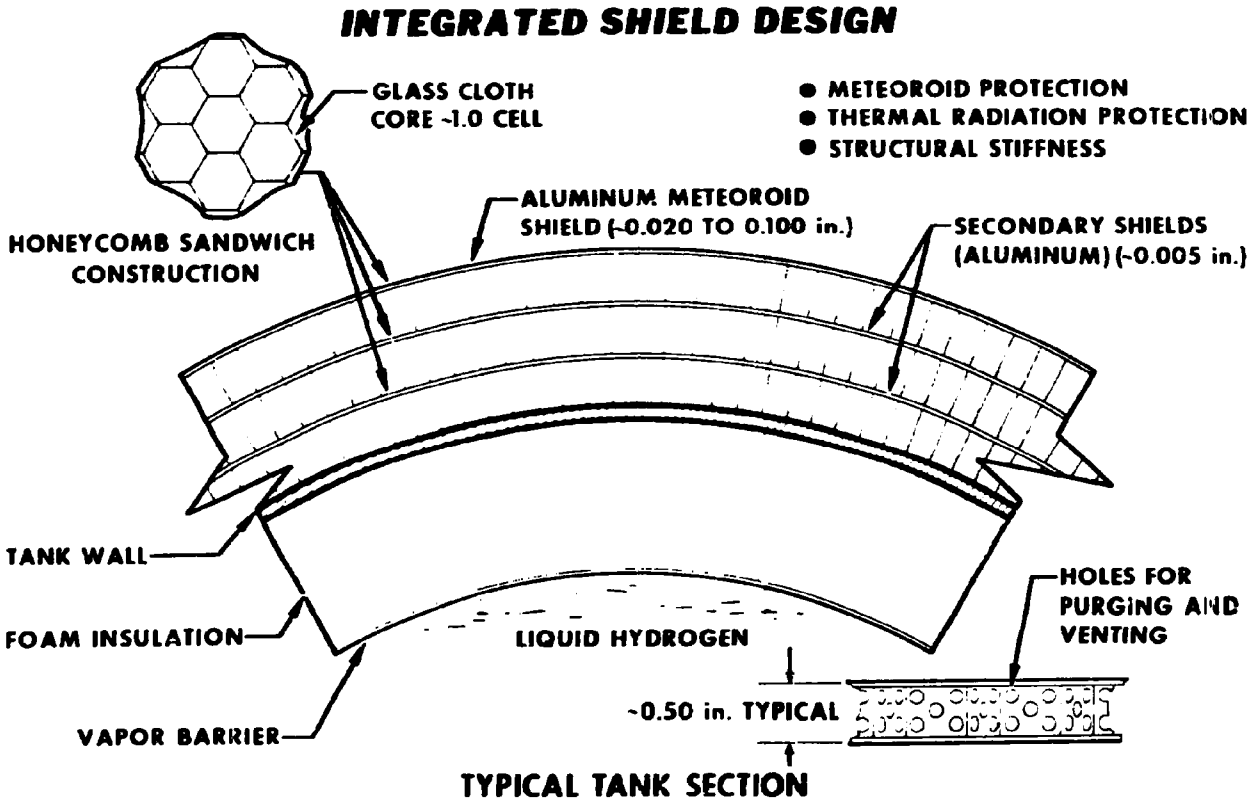
INTEGRATED SHIELD DESIGN
GLASS CLOTH
CORE ~1.0 CELL
● METEOROID PROTECTION
● THERMAL RADIATION PROTECTION
● STRUCTURAL STIFFNESS
ALUMINUM METEOROID
SHIELD (~0.020 TO 0.100 in.)
SECONDARY SHIELDS
(ALUMINUM) (~0.005 in.)
HONEYCOMB SANDWICH
CONSTRUCTION
TANK WALL
FOAM INSULATION
VAPOR BARRIER
LIQUID HYDROGEN
HOLES FOR
PURGING AND
VENTING
~0.50 in. TYPICAL
TYPICAL TANK SECTION

Figure 15

REFERENCES

1. Dalton, C. C.: Meteoroid Hazard to Space Vehicle in Orbit Near the Earth: A Functional Interpretation of the Information For Design and Operations Decisions. NASA TM X-789, December 1962.

2. Herrmann, W. and Jones, A. H.: Correlation of Hypervelocity Impact Data. Proceedings of the 5th Symposium on Hypervelocity Impact. Vol. 1, Part II, April 1962.

3. Collins, R. D., Jr. and Kinard, W. H.: The Dependency of Penetration on the Momentum Per Unit Area of the Impacting Projectile and the Resistance of Materials to Penetration. NASA TN D-238, May 1960.

4. Bjork, R. L.: Meteoroids Versus Space Vehicles. Report P-1963, The RAND Corp., April 4, 1960.

5. Kinard, William H., Lambert, C. H., Jr., Schryer, David R., and Casey, Francis W., Jr.: Effect of Target Thickness on Cratering and Penetration of Projectiles Impacting at Velocities to 13,000 Feet Per Second. NASA Memo 10-18-58L, 1958.

6. Humes, D., Hopko, R. N, and Kinard, W. H.: An Experimental Investigation of Single Aluminum "Meteor Bumpers."

7. Stepka, Francis S.: "Investigation of Impact By High Velocity Particles Into Liquid-Filled Tanks." Prepared for the ASM Engineering Quarterly, August 1962.

THIN PLATE PERFORATION AND PROTECTION

SUMMARY

by
Dale M. Davis, PE
Weapons Laboratory
Detachment 4, ASD
Eglin AFB, Fla

SUMMARY - PERFORATION AND PROTECTION

INTRODUCTION

When the Sixth Hypervelocity Impact Symposium was planned, it was divided into four sessions, namely: Techniques, Theory, Experimentation, and Application. Based on past experience, this was a logical division; however, this year for the first time, there was a large number of papers presented which dealt with other than homogeneous quasi-infinite targets. That is, there were many papers dealing with penetration of thin plates, spaced plates, and composite targets. As a result when the committee met after the symposium, they reorganized the papers into the more practical breakdown reflected in these proceedings.

It is fitting that this Summary should be prepared by the Air Force, particularly by Detachment 4, ASD. The Air Force has a specific interest in projection techniques as the necessary tools to accomplish a job, and in the penetration of thick and quasi-infinite targets both for academic reasons and to aid in understanding the more realistic cases of penetration. However, our real interest is in the application of the knowledge of hypervelocity impact phenomena to the defensive and offensive problems of defending our aerospace vehicles and devising means of defeating those which are a threat to our security.

The information presented in this assemblage of papers contains the best and most up-to-date treatment of fragment lethality against finite targets available in the UNCLASSIFIED literature.

DISCUSSION

Of the ten papers which precede this Summary, I will discuss the last nine, as Dr. Zernow's Introductory Paper was not available. The nine were arranged in order by the symposium committee, beginning with the papers on Theory and ranging through Experimentation to Application. Of course, they cannot all be clearly separated into one of these categories, some encompassing more than one group.

The first three reports to be considered contain theoretical treatments of hydrodynamic impact into thin plates. As might be expected, all three approaches are different - also, the results are different. To readers experienced in this field, this does not come as any surprise; to those newcomers, it should serve to point out the extreme complexity of the problem and the effect of making various assumptions on "negligible" factors.

SUMMARY - PERFORATION AND PROTECTION

Mr. Krauss's treatment is a two-dimensional analysis, which considers the often-neglected factor of radial velocity. The simplifying assumptions which were made are: (1) target and projectile are of the same material, (2) target and projectile behave as viscous fluids (hardness and strength neglected), and (3) compressibility of both target and projectile is ignored. Of these three, the first will not contribute error to the solution, but will limit its application. The second can be shown by experiment to introduce significant error - at least in the velocity range where we have experimental techniques available for confirmation. The magnitude of errors contributed by the third assumption cannot be determined at this time. The mathematical formulation presents equations which are capable of solution in several degrees, the solution presented is a first-order approximation. Perhaps this first approximation is as accurate, in comparison with the real case, as can be assured from the assumption of the initial conditions, without resorting to emperical constants to correct for strength, etc?

Mr. Sandorf, in his development of meteoroid bumper design criteria develops a one-dimensional solution of optimum bumper thickness. He considers several bumper and projectile materials at the interesting velocities of 20,000 fps (typical of weapons application) and 100,000 fps (typical of meteoroid impact). The assumption is made that optimum thickness of shield is that which will subject the entire projectile to shock load before the rarefaction wave from the unbounded rear target surface "cancels" the impact pressure. The results tabulated for optimum bumper thickness at 20,000 fps impact velocity are about one-half of that concluded by Maiden in his paper - however, agreement to within a factor of two is not bad in this relatively new area. Perhaps some of this disagreement could be attributed to edge effects in the unbounded projectile. Interestingly, Sandorf's figures for 100,000 fps essentially agree with Maiden's for velocities around 30,000 fps.

Mr. Maiden, in his paper, discusses data on an experimental and theoretical study of bumper plate effectiveness in protecting space vehicles. The experimental program considered the effect of several factors, varied singly. These factors are shield thickness, shield material, shield strength, and impact velocity. Following his discussion of experimental data, Mr. Maiden evolves a rather complete theoretical treatment of thin-plate penetration effects. After discussing the theoretical effect of the same variables covered in the experimental program, he goes on to compare the theory with experimental data and points out discrepancies and possible explanations. The fact that Mr. Maiden had access to such a wealth of valid experimental data makes this paper extremely valuable in understanding impact effects on bumper plates.

The paper by Messrs. Mortensen, Ferguson, Joyce and Kreyenhagen contains an analysis of the largest single collection of thin-plate impact data available at this time. Several types of projectiles are considered, notably discs of L/D ratio one-third and irregular chunky fragments formed from shaped-charge jets. Velocities range to near-40,000 fps, the higher velocities being obtained with the shaped-charge

jets. Because of the nature of the technique, the exact mass and condition of the impacting projectile are not known; however, it is closely estimated by flash radiography, and since it is the only available data in this velocity range, it is of significant value.

Messrs. Watson, Becker, and Gibson present an emperical study of penetration effects upon targets near the penetration limits of the projectiles considered. The paper discusses the number, mass, and velocity distribution of projectile mass and target ejecta. The velocity range considered is 6,000 to 15,000 fps. The work is unique and especially interesting since it covers the normally unpredictable transition range where steel projectile penetration into aluminum targets varies from kinetic theory on the low end to hydrodynamic at the upper end.

Messrs. Reynolds and Emmons discuss an experimental evaluation of spaced plate protection techniques. Basically, they consider the impact of Pyrex and steel particles into target configurations consisting of thin plates separated by foam and honeycomb structures. Two specific points of special significance are brought out within the limits tested: (1) the protective efficiency increased essentially linearly with decreasing bumper thickness and foam density, and (2) Fiberglas fabric was more efficient as a bumper than was aluminum.

In his paper concerning self-sealing structures, Mr. D'Anna discusses both chemical and mechanical sealants for structural vehicles. The study is both analytical and experimental. This is a different approach to the same problem discussed in earlier papers by Maiden and Reynolds and Emmons. It would appear that if weight were the deciding factor the self-sealing structures might lose out to the spaced plates. Also, the experimental work by D'Anna was conducted at only 7,000 fps, which is not in the true hypervelocity range. At impact velocities which are in excess of the shock velocities in the target materials, the effects may be significantly different than those observed.

Mr. McMillan's work is representative of an area in which increased emphasis will be placed in the future. It is valid, well-controlled experimental data on hypervelocity impact into realistic targets. The fact, as evidenced in earlier papers, that we cannot yet obtain valid, theoretical predictions of impact effects into simple targets precludes, for the time being, our ability to predict the effects reported in this paper. Much more work of this kind is needed to even obtain a good empirical understanding.

Messrs. Sterbentz and Long discuss the meteoroid threat to the success of the nuclear rocket mission. Two possible designs for the protection and structure of the liquid hydrogen tank are given. The paper points out the need for more impact data on multiple thin targets.

SUMMARY - PERFORATION AND PROTECTION

In summary, a large amount of data has been presented on impacts into thin targets, indicative of the growing interest in this area.

AUTHORS

Atkins, W. W. . . . . Vol. 4, p. 385
Baer, Paul G. . . . . Vol. 1, p. 41
Baker, J. R. . . . . Vol. 1, p. 175
Barbarek, Louis A. C. . . . . Vol. 4, p. 395
Becker, K. R. . . . . Vol. 3, p. 207
Bjork, R. L. . . . . Vol. 2, p. 1
Brown, J. M. . . . . Vol. 4, p. 1
Calvit, H. H. . . . . Vol. 2, p. 229
Carey, Charles A. . . . . Vol. 4, p. 271
Chandler, R. L. . . . . Vol. 4, p. 37
Chapman, R. L. . . . . Vol. 1, p. 317
Charters, A. C. . . . . Vol. 1, p. 1
Christman, D. R. . . . . Vol. 4, p. 101
Coley, R. B. . . . . Vol. 4, p. 345
Condon, J. J. . . . . Vol. 1, p. 175
Cox, C. M. . . . . Vol. 4, p. 193
D'Anna, Philip J. . . . . Vol. 3, p. 281
Dailey, James J. . . . . Vol. 4, p. 329
Davids, N. . . . . Vol. 2, p. 229
Davis, Dale M. . . . . Vol. 4, p. 151
. . . . . Vol. 3, p. 387
Donardo, B. Pat . . . . . Vol. 2, p. 577
Dittrich, W. H. . . . . Vol. 4, p. 101
Donaldson, Coleman duP. . . . . Vol. 4, p. 305
Eckerman, J. . . . . Vol. 1, p. 247
Eichelberger, R. J. . . . . Vol. 2, p. 683
Emmons, R. H. . . . . Vol. 3, p. 249
Engel, Olive G. . . . . Vol. 2, p. 337
Ferguson, J. E. . . . . Vol. 1, p. 349
. . . . . Vol. 3, p. 157
Frilchtenicht, J. F. . . . . Vol. 2, p. 591
Gates, D. F. . . . . Vol. 1, p. 155
Gault, D. E. . . . . Vol. 2, p. 367
. . . . . Vol. 2, p. 419
Gaydos, George M. . . . . Vol. 4, p. 167
Gehring, J. W. . . . . Vol. 2, p. 627
. . . . . Vol. 4, p. 101
Gibson, F. C. . . . . Vol. 3, p. 207
Giroux, Richard . . . . . Vol. 3, p. 141
Glass, C. M. . . . . Vol. 2, p. 401
Goodman, E. H. . . . . Vol. 2, p. 543
Halperson, S. M. . . . . Vol. 2, p. 525
Harms, D. E. . . . . Vol. 1, p. 317
Harrity, Edmund M. . . . . Vol. 4, p. 167

Heitowit, Ezra D. . . . . Vol. 2, p. 419
Heyda, James F. . . . . Vol. 2, p. 321
Howell, William G. . . . . Vol. 1, p. 305
Ipson, Thomas W. . . . . Vol. 1, p. 305
Johnson, O. T. . . . . Vol. 2, p. 229
Joyce, J. P. . . . . Vol. 1, p. 349
Kineke, John H., Jr. . . . . Vol. 3, p. 157
Kinslow, Ray. . . . . Vol. 2, p. 457
Kirchner, Henry P. . . . . Vol. 2, p. 513
Kraus, H. . . . . Vol. 2, p. 273
Kreyenhagen, K. N. . . . . Vol. 2, p. 163
Kronman, S. . . . . Vol. 3, p. 13
Lane, D. C. . . . . Vol. 4, p. 101
Lamcke, Bo . . . . . Vol. 4, p. 21
Liles, C. D. . . . . Vol. 4, p. 373
Long, Loren L. . . . . Vol. 1, p. 107
Luttrell, J. L. . . . . Vol. 2, p. 543
MacCormack, R. W. . . . . Vol. 3, p. 357
Maiden, C. J. . . . . Vol. 2, p. 157
Margolis, P. K. . . . . Vol. 2, p. 367
McKay, W. L. . . . . Vol. 2, p. 613
McMillan, A. R. . . . . Vol. 3, p. 69
Merendino, A. . . . . Vol. 4, p. 1
Mobley, C. . . . . Vol. 1, p. 247
Moore, H. J. . . . . Vol. 3, p. 309
Mortensen, R. B. . . . . Vol. 1, p. 331
Nysmith, C. Robert . . . . . Vol. 2, p. 401
Perrachino, Mario A. . . . . Vol. 2, p. 367
Placesi, R. . . . . Vol. 3, p. 157
Pond, R. B. . . . . Vol. 4, p. 101
Porter, C. D. . . . . Vol. 4, p. 345
Rae, William J. . . . . Vol. 2, p. 577
Randall, R. R. . . . . Vol. 4, p. 235
Recht, Rodney F. . . . . Vol. 1, p. 155
Reynolds, B. W. . . . . Vol. 2, p. 401
Richards, L. G. . . . . Vol. 1, p. 175
Vol. 2, p. 163
Vol. 1, p. 349
Vol. 1, p. 305
Vol. 3, p. 249
Vol. 2, p. 513

Riney, T. D. . . . . Vol. 2, p. 195
Rhea, W. A. . . . . Vol. 4, p. 345
Rockowitz, Murray . . . . . Vol. 4, p. 271
Sandorff, P. E. . . . . Vol. 3, p. 41
Seigel, A. E. . . . . Vol. 1, p. 195
Slattery, J. C. . . . . Vol. 2, p. 591
Smith, Horace C. . . . . Vol. 1, p. 81
Sorenson, G. P. . . . . Vol. 1, p. 317
Stein, Samuel D. . . . . Vol. 4, p. 167
Sturbonis, William H. . . . . Vol. 3, p. 357
Summers, James L. . . . . Vol. 2, p. 577
Swift, H. F. . . . . Vol. 1, p. 175
. . . . . Vol. 1, p. 375
Thorn, F. N. . . . . Vol. 4, p. 193
Tillotson, J. H. . . . . Vol. 2, p. 59
Vitale, Richard . . . . . Vol. 2, p. 457
Walsh, J. M. . . . . Vol. 2, p. 59
Warnke, M. I. . . . . Vol. 2, p. 627
Watmough, D. . . . . Vol. 4, p. ...
Watson, R. W. . . . . Vol. 3, p. 207
Wilkins, Mark J. . . . . Vol. 2, p. 141
Zarrow, L. . . . . Vol. 3, p. 1
Zimmerman, F. J. . . . . Vol. 4, p. 47
Zimney, H. N. . . . . Vol. 4, p. 345